Stockholm
University

Shells and filament in flows

VIPIN AGRAWAL

ISBN XXX-XX-XXXX-XXX-X

Printed in Sweden by Universitetsservice US-AB, Stockholm 2022
Distributor: NORDITA, Department of theoretical physics, Stockholm University

To my mother, brother,
and to the memories of my father

> *Yet each of us has the indisputable impression that the sum total of his own experience and memory forms a unit, quite distinct from that of any other person. He refers to it as 'I'. What is this 'I'? If you analyze it closely you will, I think, find that it is just a little bit more than a collection of single data (experiences and memories), namely the canvas upon which they are collected. And you will, on close introspection, find that what you really mean by 'I' is that ground stuff upon which they are collected. You may come to a distant country, lose sight of all your friends, may all but forget them; you acquire new friends, and you share life with them as intensely as you ever did with your old ones. Less and less important will become the fact that, while living your new life, you still recollect the old one. 'The youth that was I', you may come to speak of him in the third person, indeed the protagonist of the novel you are reading is probably nearer to your heart, certainly more intensely alive and better known to you. Yet there has been no intermediate break, no death. And even if a skilled hypnotist succeeded in blotting out entirely all your earlier reminiscences, you would not find that he had killed you. In no case is there a loss of personal existence to deplore. Nor will there ever be.*
>
> — **Erwin Schrödinger**
> What is life?, 1944

ABSTRACT

The motivation to study elastic structures such as filaments and shells stemmed from its application in the construction of tall buildings, bridges etc. Interest in this field has rekindled in the past decades due to growing interest in understanding biological materials and because of possible applications in nanoscience and medicine. This also poses new challenges as the biological materials show both solid and fluid-like behavior, and in addition they are active. In this thesis, we study the mechanical properties of shells and filament and their interaction with fluid. The thesis is divided into two themes. First, how to model nano-vesicles and how are the mechanical properties of a spherical shell is affected if they are thermal and active? Second, can non-linear interaction between fluid and filament generate turbulence and hence mixing in the Stokes flow?

To model nano-vesicles, we develop an open-source software package – MeMC. The MeMC models nano-vesicles as an elastic objects. It interprets the force-distance data generated by indentation of biological nano-vesicles by atomic force microscopes and uses Monte Carlo simulations to compute elastic coefficients of a nano-vesicle Further, we use this code and break the detailed balance in Monte Carlo simulation – thereby driving the shell active and out of thermal equilibrium – to study the effect of activity on mechanical properties of elastic shells, in particular, buckling. Such a shell typically has either higher (active) or lower (quiescent) fluctuations compared to one in thermal equilibrium depending on how the detailed balance is broken. We show that for the same set of elastic parameters, a shell that is not buckled in thermal equilibrium can be buckled if turned active. Similarly, a shell that is buckled in thermal equilibrium can unbuckle if turned quiescent. Based on this result, we suggest that it is possible to experimentally design microscopic elastic shells whose buckling can be optically controlled.

In the next part of the thesis, we visit the problem of mixing in Stokes flow using elastic filament. As it is known, the flow of Newtonian fluid at low Reynolds number is, in general, regular and time-reversible due to absence of nonlinear effects. For example, if the fluid is sheared by its boundary motion that is subsequently reversed, then all the fluid elements return to their initial positions. Consequently, mixing in

microchannels happens solely due to molecular diffusion and is very slow. Here, we show, numerically, that the introduction of a single, freely floating, flexible filament in a time-periodic linear shear flow can break time reversibility and give rise to chaos due to elastic nonlinearities, if the bending rigidity of the filament is within a carefully chosen range. Within this range, not only the shape of the filament is spatiotemporally chaotic, but also the flow is an efficient mixer. We model the filament using the bead-rod model. We consider two different models for the viscous forces: (a)they are modeled by the Rotne–Prager tensor. This incorporates the hydrodynamic interaction between every pair of beads. (b)we consider only the diagonal term of the Rotne–Prager tensor which makes the viscous forces local. In both of these cases, we find the same qualitative result: the shape of a stiff filament is time-invariant – either straight or buckled for large enough bending rigidity; it undergoes a period-n bifurcation (n = 2,3, 4, etc) as the filament is made softer; becomes spatiotemporally chaotic for even softer filaments. For case (a) but not for (b) we find that the chaos is suppressed if bending rigidity is decreased further. For (b), in the chaotic phase, we show that the iterative map for the angle, which the end–to–end vector of the filament makes with the tangent its one end, has period three solutions; hence it is chaotic.

SVENSK SAMMANFATTNING

Motiveringen att studera elastiska strukturer som filament och skal härrörde från dess tillämpning vid konstruktion av höga byggnader, broar etc. Intresset för detta område har återuppstått under de senaste decennierna på grund av ett växande intresse för att förstå biologiska material och på grund av möjlig tillämpning inom nanovetenskap och medicin. Detta innebär också nya utmaningar eftersom de biologiska materialen uppvisar både fast och flytande beteende, och dessutom är de aktiva. I denna avhandling studerar vi de mekaniska egenskaperna hos skal och filament och deras interaktion med vätska. Uppsatsen är uppdelad i två teman. För det första, hur man modellerar nano-vesiklar och hur påverkas de mekaniska egenskaperna hos ett sfäriskt skal om de är termiska och aktiva? För det andra, kan icke-linjär interaktion mellan vätska och filament generera turbulens och därmed blanda i Stokes-flödet?

För att modellera nanovesiklar utvecklar vi ett mjukvarupaket med öppen källkod – MeMC. MeMC modellerar nanovesiklar som ett elastiskt föremål. Den tolkar kraftavståndsdata som genereras av indragning av biologiska nano-vesiklar med atomkraftmikroskop och använder Monte-Carlo-simuleringar för att beräkna elastiska koefficienter för en nanovesikel. Vidare använder vi den här koden och bryter den detaljerade balansen i Monte-Carlo-simulering – därigenom driver skalet aktivt och ur termisk jämvikt – att studera effekten av aktivitet på de mekaniska egenskaperna hos elastiska skal, i synnerhet buckling. Ett sådant skal har typiskt antingen högre (aktiva) eller lägre (vila) fluktuationer jämfört med ett i termisk jämvikt beroende på hur den detaljerade balansen bryts. Vi visar att för samma uppsättning elastiska parametrar kan ett skal som inte är buckligt i termisk jämvikt bucklas om det aktiveras. På samma sätt kan ett skal som spänns i termisk jämvikt lossna om det blir vilande. Baserat på detta resultat föreslår vi att det är möjligt att experimentellt designa mikroskopiska elastiska skal vars knäckning kan styras optiskt.

I nästa del av avhandlingen tittar vi på problemet med att blanda in Stokes-flödet med hjälp av elastiskt filament. Som bekant är flödet av newtonsk vätska vid lågt Reynolds-tal i allmänhet regelbundet och tidsreversibelt på grund av frånvaron av 3 icke-linjära effekter. Till exempel, om vätskan klipps av genom sin gränsrörelse som därefter reverseras, så återgår alla vätskeelementen till sina initiala positioner. Följaktligen sker blandning i mikrokanaler enbart på grund av molekylär diffusion och är mycket långsam. Här visar vi, numeriskt, att införandet av en enda, fritt flytande, flexibelt filament i ett tidsperiodiskt linjärt skjuvflöde kan bryta tidsreversibiliteten och ge upphov till kaos på grund av elastiska olinjäriteter, om glödtrådens böjstyvhet ligger inom ett noga utvalt sortiment. Inom detta område är inte bara formen på glödtråden rumsligt kaotisk, utan även flödet är en effektiv blandare. Vi modellerar glödtråden med pärlstavmodellen. Vi beaktar två olika modeller för de viskösa krafterna: (a) de är modellerade av Rotne–Pregor-tensoren. Detta inkluderar den hydrodynamiska interaktionen mellan varje par av pärlor. (b) vi betraktar endast den diagonala termen för Rotne–Pregor-tensorn som gör de viskösa krafterna lokala. I båda dessa fall finner vi samma kvalitativa resultat: formen på ett styvt filament är tidsinvariant - antingen rak eller bucklig för en tillräckligt stor böjstyvhet; den genomgår en period-n bifurkation (n = 2,3, 4, etc) när glödtråden görs mjukare; blir rumsligt kaotiskt för ännu mjukare filament. För fall (a) men inte för (b) finner vi att kaoset undertrycks om böjstyvheten minskar ytterligare. För (b), i den kaotiska fasen, visar vi att den iterativa kartan för vinkeln, som glödtrådens ände-till-ände vektor gör med tangenten sin ena ände, har period tre lösningar; därför är det kaotiskt.

ACKNOWLEDGEMENT

> *No man is an island.*
>
> **— John Donne**

This quote by John Donne was right to the point. I am lucky to be connected to many in my life who keeps me from being 'rifted'. They have directly or indirectly helped me to reach towards the goal – what is known as *doctorate in philosophy*. This achievement may seem very small in the big vast universe, but to some, this achievement means a universe.

Despite the peaks and valleys, the past four and a half years overall have been very formative years of my life, both academically and personally. As I write this sitting in my cozy office at NORDITA, I can almost relive the past and hear all the memories swirling around me, asking me to thank so many people. Although next few pages is an injustice to show my gratitude towards everyone but let me give it a fair try.

Dhrubaditya Mitra

It will not be an overstatement if one says that "a person is nothing but the summation of all the teachings." In my supervisor, Dhrubaditya Mitra (Dhruba), I have found that teacher and a friend. With Dhruba, it's been a privilege to witness incredible passion towards research and teaching, insatiable curiosity, remarkable energy as well as empathy and care. I thank him for all the fruitful discussions and patiently answering all the naive questions. The work presented in my thesis undoubtedly would not have been possible without his supervision. I like to acknowledge him not for just the successful results but his abilities to keep the research interesting during all the failures. All of this does not overshadow his efforts in shaping me as a disciplined, sincere and careful student. In the end, I thank him for being a wonderful supervisor who provided me a psychological support in difficult times.

NORDITA Colleagues, collaborators and committee members

I would like to start this long list of names with my co-supervisor, Supriya Krishnamurthy. I shall always regret the fact that we were not able to collaborate on more projects except one. However I have enjoyed by being an assistant for her course on statistical mechanics. Her abilities to teach in systematic and orderly way has always captivated me. I am also thankful to my mentor, Thors Hans Hansson, for his precious time to make all the administrative formalities easier for me. On the same note, I would also like to acknowledge the HR department at NORDITA who always offered a great support. Especially Hans Mühlen for being a tech wizard and not letting me or anyone at NORDITA worry about anything related to technical problems. With them and Ralf, I enjoyed organising NORDITA day.

I would like to express my gratitude towards my licentiate and pre-defense committee members. I thank Ralf, Cristobal, Anne-Virgine for going through the previous version of my thesis and all the useful scientific comments which has helped me not only in my research but has also improved my writing. Thanks to Sten, Michael Odelius, Mark Stockett and Per-Erik for all the general comments on my thesis. Further, I am deeply thankful to have an amazing group of scientists in my final thesis committee. With few of them, I have had a privilege to have scientific discussions during schools and conferences. This special shout out goes to Gerhard Gompper, Paulo Arratia, Joakim Stenhammar and Luiza Anghuleta. I also thank Alain Goriely for agreeing to visit NORDITA for my PhD defence.

I thank all the post-docs who has helped me during my PhD studies. Thank you, Vikash, whose mere presence in the office has taught me a lot about physics and programming. Working with him has unquestionably expedited my research in the last year of PhD. I thank Navaneeth for helping me in early days of PhD by teaching me Stokesian dynamics and Akshay Bhatnagar for clarifying general doubts in physics and also helping me during my sickness. I also thank Prabal for all the white-board discussion and his lessons on eigenvalues, eigenvectors. I would never forget all the political discussion with him and Dhruba together which made NORDITA an even more enjoyable place. A special thank to Marc Suñé Simon for lending me all the books on elasticity and letting me bug him time to time for the doubts.

Next, I thank my collaborators. First, Sreekanth for the discussions on non-equilibrium statistical mechanics and also being my first friend in Stockholm. I am also thankful to him for introducing me to other Indian gang in Stockholm. Second, Hanna,

Fredrik and Apurba for allowing me to be a part of the work on exosomes. A special thank to Hanna for teaching me the workings of Atomic force microscope. Third, I thank my Indian collaborators Shubhrokoli and Ayan with whom I have had an honor to publish an article.

Now thanking other PhD students at NORDITA – Anthony, Ludovico and Bart – for creating a nice and warm atmosphere in the institute to fellow PhD students. I would like to thank the movie group, including but not limited to, Kristain, Luca, Francesco and Sankalp for bringing out a nice culture in NORDITA. A special thank to Prabal again who started this. Although I have been very lousy at joining the movies but I have had fun sharing pizza and wine whenever I joined.

I would like to thank technical and computational division of Stockholm university specially Mikica, who has helped me setting up my account on SU HPC facilities. Additionally, Mikica has been my mentor at fysikshow who taught me most of the experiments. Having fysikshow with him has been nothing other than a fun expedition.

Friends

A heartfelt thanks goes out to all the friends that I made in the past few years. Amidst the ups and downs of life, these years have been incredible for me with some great friendships. Without them this chapter of my life would have unfolded very differently. Let me start with my Lappis gang. I thank Laura, Ajinkya, Vivek, Ana, Neeraj, Kunal, Vikash, Chalke and Prim for celebrating all the joyous things together and tolerating me in my worst. With a subset of these friends, I have also had the pleasure of having coffee/chai (almost) everyday and had great philosophical, spiritual and political discussions. I would like to thank my old Lappis corridor mates – Asams, Einar, Aja, Tanya and Jorge– for all the gathering, poker games and parties that we have had together. Next shout out goes to the badminton friends and members of RaketSportsKlubb, Hari, Satish, Saurabh, Aravind, Sneha, Pankaj, Aayush, Kunal and Daniel for all the nice badminton games and parties afterwards. I also thank all the other friends from Albanova, including but not limited to, Ram, Megha, Tien-Tien, Kasturie, Martina – with whom I have shared most of my lunch time.

This section is definitely incomplete without lauding my old friends for motivating me to choose research career. I would like to acknowledge Prince, Bhargav, Mainak, Goenka, Chaitanya, Aglave, Shashank and Mayank for the same and also for being

in touch and continuting the same level of friendship even after so many years. I also thank my childhood friends, Khandelwal, Mangal, Gupta, Rudra, Swetcha, Lakshman and Sanil. Their support in one way or another helped me to go through each and every stage of my educational and professional career.

Family

Of all the things I am thankful for, my gratitude towards family rises to top. As a kid, I once read these lines:

> Parents are like a bow, and children like arrows. The more the bow bends and stretches, the farther the arrow flies. I fly, not because I am special, but because they stretched for me.

Now, as I have grown past my teenage years, I have understood the truth behind these lines. I have my mother, Kanta Devi, whose struggles of life has always been balanced with a thought of her kids having a so called great future. Even though, unfortunately my father is not present today, he was my first teacher. Starting from card games to algebra, he taught me a lot before his untimely and early demise. There is no doubt that I still share his passion in mathematics and science. I want to thank my elder brother, Manoj Agrawal, who has made great sacrifices in his life for the well being of all the siblings. He has been an inspiration to me to pursue mathematics and science at high school which has led me to this moment. From buying me the first book on alphabets till this date he has always been there for me. I thank my sisters, Seema and Vinita, for their unconditional love and instilling a great culture of excellence from childhood. A special thanks to Seema di for being the only bread earner of the family in the difficult financial situations. I thank Pooja di as well who has indirectly helped me to achieve my academic goals. I also thank my sister-in-law, Rekha, who has always been supportive of my decisions, brother-in-laws, Anand, Chandramohan for their interest in my scientific work, and love to my nephews – Hardik, Divyansh, Ronak.

LIST OF PAPERS

The following papers, referred to in the text by their Roman numerals, are included in this thesis.

PAPER **I:** **MeMC: A package for Monte Carlo simulations of spherical shells**
Vipin Agrawal, Vikash Pandey, Hanna Kylhammar, Apurba Dev and Dhrubaditya Mitra, *Journal of Open Source Software*, 7(74), 4305.
DOI: 10.21105/joss.04305
Link: https://doi.org/10.21105/joss.04305

PAPER **II:** **Active buckling of pressurized spherical shells : Monte Carlo Simulation**
Vipin Agrawal, Vikash Pandey and Dhrubaditya Mitra, *arXiv preprint*, arXiv:2206.14172. 2022 Jun 28.
Link: https://doi.org/10.48550/arXiv.2206.14172

PAPER **III:** **Chaos and irreversibility of a flexible filament in periodically driven Stokes flow**
Vipin Agrawal and Dhrubaditya Mitra, *Physical Review E* **106**, 025103 – 12 August 2022.
DOI: 10.1103/PhysRevE.106.025103
Link = https://link.aps.org/doi/10.1103/PhysRevE.106.025103

PAPER **IV:** **Flexible filament in time-periodic viscous flow: shape chaos and period three**
Vipin Agrawal and Dhrubaditya Mitra, *arXiv preprint*, arXiv:2210.04781. 2022 Oct 10.
Link: https://doi.org/10.48550/arXiv.2210.04781

The following paper is not included in the thesis:

PAPER **V:** **Quantitative analysis of non-equilibrium systems from short-time experimental data**
Sreekanth K. Manikandan, Subhrokoli Ghosh, Avijit Kundu, Biswajit Das, Vipin Agrawal, Dhrubaditya Mitra, Ayan Banerjee and Supriya Krishnamurthy, *Communications Physics*, **4(1)**, pp. 1–10 (2021)
Link: https://doi.org/10.1038/s42005-021-00766-2

AUTHOR'S CONTRIBUTION

The following papers, referred to in the text by their Roman numerals, are included in this thesis.

PAPER **I:** My colleague and I wrote the code together. I performed the test cases. I contributed in writing the paper.

PAPER **II:** I was involved in designing the research. I performed simulation, analyzed the data. I wrote the paper along with my colleagues.

PAPER **III:** My supervisor and I designed the research. I wrote the code, performed simulations and analyzed the data. My supervisor shepherded the paper writing.

PAPER **IV:** I designed the problem, performed simulations, analyzed the data. I contributed in writing the paper.

The following paper is not included in the thesis:

PAPER **V:** I wrote down the optimization code to find maximum entropy generation rate. I performed the analytical calculation to find velocity profile around the bubble.

LICENTIATE THESIS CONTRIBUTION

The work presented in this thesis builds upon the work in licentiate thesis (defended on 7^{th} December 2021). Of the papers included in the thesis, paper I were part of licentiate. In each chapter, the contribution from the licentiate thesis is as follows:

- Chapter **6**: This chapter was included in the licentiate. It has been taken verbatim.
- Chapter **7**: This chapter was a part of the licentiate thesis but section 7.5 is new.
- Chapter **8**: Introduction of this chapter is new. Other parts of the section has been taken from the licentiate but modified upto certain extent.
- Chapter **1–4** and **9** do not have any contribution from licentiate thesis.

CONTENTS

LIST OF FIGURES

Part I

Thesis overview

1

INTRODUCTION AND MOTIVATION

> *Although not everyone is mindful of it, all cell biologists have two cells of interest: the one they are studying and Escherichia coli.*
>
> **— F. Neidhardt**

In this thesis, we study the elastic properties of shells and filament and their interactions with fluid. The motivation is threefold. First, because of their ubiquity in biological systems [1, chapter 10, 11], second, they pose very interesting and challenging phenomena due to the inherent nonlinearities [2, 3] and third, because of their applications in nano-technology and medicine [4, 5, 6, 7, 8, 9].

From biological point of view, filaments are the basis for many biological phenomena. Such as microorganismal swimming [10, 11], network of filaments which make up cytoskeleton of an eukaryotic cells [12] (see Fig. 1.1(a)) hunting and swimming of protozoans, (see Fig. 1.1(d) [13]) and dynamics of actin filaments and DNA [14, 15]. Similarly, shells and membranes are also one of the hallmark feature of cellular life. For example, the building block of life, a cell has a membrane that separates it from the rest of the world [1, chapter 11]. This gives rise to many interesting biological phenomena such as the mechanism of internalizing or secreting the large extracellular molecules by cells (endocytosis and exocytosis, see Fig. 1.1(c)) [16] and budding – a form of asexual reproduction of plant etc Fig. 1.1(b). At even smaller level in the length scale, a cell produces a lot of nano-vesicles e.g. exosomes. Which are essentially a building block of inter-cell communication. It is evident that, studying the elasticity of biological materials will help us understanding these biological phenomena. However it poses new challenges mainly because these materials show both solid and fluid like behavior [17], and in addition they are active [18].

In elasticity, the dynamical variable is the displacement of a point from its undeformed position. If this displacement is small and the stress-strain response

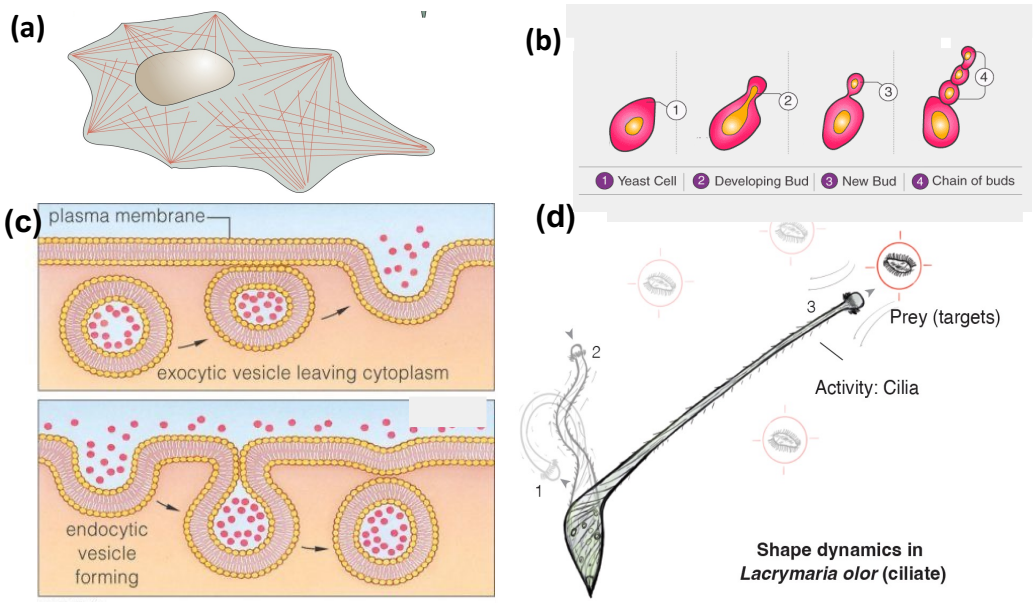

Fig. 1.1.: **(a)** Cytoskeleton in an eukaryotic cell. **(b)** Budding in Yeast. **(c)** Illustration of exocytosis and endocytosis. **(d)** Hunting for prey in the single-celled ciliate using long cellular protrusion. Figures adapted and reprinted with permission from [19, 20, 1, 21].

(constitutive relation) of a body is linear – which is true for most solid materials except e.g, foams – elasticity is a linear problem [2, 3]. But if the displacement is large then even for linear constitutive relation the elastic response can be nonlinear. Canonical examples of such problems are two-dimensional membranes or shells in three dimensional space or one-dimensional filaments in two or three dimensional space (see chapter 1 of [22], chapter 2 of [3]). Hence nonlinear elasticity plays a crucial role in understanding the biological phenomena stated above.

From an application-oriented point of view, the study of elastic objects have wide applications. We list a few of them here.

1. Red blood cells (RBC) get harder due to malaria – studying the interaction of elastic body such as RBC and blood flow could help us in developing new affordable microfluidic devices to detect malaria [23].

2. Micro-robots are used for the localized delivery of drugs or for brachytherapy – treatment by placing a radioactive source near tumors [6].

3. Exosomes of ovarian cancer contain different set of proteins and micro RNAs as compared to the normal exosomes of cancer-free individuals [24]. Expressing pan proteins in lesser amount over the membrane, can in principal change

the elastic modulii of exosomes. Based on this, an early detection of cancer is possible.

4. One of the most-used methods to determine the elastic moduli of microscopic shells is to measure their force distance curves while poking them with an atomic force microscope (AFM) and then interpreting the data in the light of the theory of elastic shells [25, 26, 27, 28, 29, 30, 31].

5. Synthetic nano-vesicles can be turned active if irradiated with certain frequency of light [32, 33]. We show that the buckling of such vesicle depends on the activity of the shell [34]. Based on this, it may be possible to drive flows at microscopic scales by repeating buckling and unbuckling of shells.

6. Flow at low Reynolds number is linear and time-reversible. Consequently, such flows are non-mixing [35]. We show that the introduction of a single freely-floating filament can give rise to chaos and hence mixing in the fluid [36].

1.1 Thesis outline

This thesis focuses on two important themes. First, elastic properties of shells and second, the elastic interaction of filament and the fluid.

In **chapter 2**, we review the basic concepts of elasticity of three-dimensional bodies. In **chapter 3** , we give an overview of elasticity of plates. We formulate the expression for bending and stretching energy of plates using the concepts in three-dimensional elasticity. In **chapter 4**, we discuss the kinematics and mechanics of shells. In chapter 5, we discuss the recent literatures about the effect of thermal fluctuations on mechanical properties of shells particularly buckling. We also summarize the work from paper I [37]– *MeMC: a package for Monte Carlo simulation of spherical shells*– where we have developed an open source package for Monte Carlo simulation of spherical shells and paper II [34] – *active buckling of pressurized spherical shells: Monte Carlo simulation* – where we show how by driving the shell out-of-equilibrium can make it buckle at lower or higher pressure.

In **chapter 6**, we move to filaments. We formulate the expression for energy of filament and subsequently discuss the Euler-Bernoulli equation. **chapter 7** is dedicated to revise the fundamentals of Stokes flow i.e. the flow at zero Reynolds number. Here we introduce the mixing problem in Stokes flow. We also review the concepts of Stokesian dynamics. In **chapter 8**, we discuss recent literature about filament in Stokes flow and summarize our work in paper III [36] – *chaos*

and irreversibility of a flexible filament in periodically driven Stokes flow – and paper IV [38] – *flexible filament in time-periodic viscous flow: shape chaos and period three* – where we put forward an idea that the nonlinear elasticity of the filament can give rise to chaos and hence mixing in Stokes flow.

References

[1] Rob Phillips, Jane Kondev, Julie Theriot, Hernan G Garcia, and Nigel Orme. *Physical biology of the cell*. Garland Science, 2012.

[2] LD Landau and EM Lifshitz. *Mechanics*. Vol. 1. Course of Theoretical Physics. Oxford, England: Pergamon Press Ltd., 1969.

[3] Basile Audoly and Yves Pomeau. "Elasticity and geometry". In: *Peyresq Lectures On Nonlinear Phenomena*. World Scientific, 2000, pp. 1–35.

[4] Todd M Squires and Stephen R Quake. "Microfluidics: Fluid physics at the nanoliter scale". In: *Reviews of modern physics* 77.3 (2005), p. 977.

[5] Chia-Yen Lee, Chin-Lung Chang, Yao-Nan Wang, and Lung-Ming Fu. "Microfluidic mixing: a review". In: *International journal of molecular sciences* 12.5 (2011), pp. 3263–3287.

[6] Bradley J Nelson, Ioannis K Kaliakatsos, and Jake J Abbott. "Microrobots for minimally invasive medicine". In: *Annual review of biomedical engineering* 12 (2010), pp. 55–85.

[7] Ch Gao, E Donath, S Moya, V Dudnik, and H Möhwald. "Elasticity of hollow polyelectrolyte capsules prepared by the layer-by-layer technique". In: *The European Physical Journal E* 5.1 (2001), pp. 21–27.

[8] Vernita D Gordon, Xi Chen, John W Hutchinson, et al. "Self-assembled polymer membrane capsules inflated by osmotic pressure". In: *Journal of the American Chemical Society* 126.43 (2004), pp. 14117–14122.

[9] Gerard Adriaan Vliegenthart and Gerhard Gompper. "Mechanical deformation of spherical viruses with icosahedral symmetry". In: *Biophysical journal* 91.3 (2006), pp. 834–841.

[10] Geoffrey Ingram Taylor. "Analysis of the swimming of microscopic organisms". In: *Proceedings of the Royal Society of London. Series A. Mathematical and Physical Sciences* 209.1099 (1951), pp. 447–461.

[11] Eric Lauga and Thomas R Powers. "The hydrodynamics of swimming microorganisms". In: *Reports on Progress in Physics* 72.9 (2009), p. 096601.

[12] Michael J Shelley. “The dynamics of microtubule/motor-protein assemblies in biology and physics”. In: *Annual review of fluid mechanics* 48 (2016), pp. 487–506.

[13] Bruce Alberts. *Molecular biology of the cell*. WW Norton & Company, 2017.

[14] DJ Smith, EA Gaffney, and JR Blake. “Modelling mucociliary clearance”. In: *Respiratory physiology & neurobiology* 163.1-3 (2008), pp. 178–188.

[15] Markus Harasim, Bernhard Wunderlich, Orit Peleg, Martin Kröger, and Andreas R Bausch. “Direct observation of the dynamics of semiflexible polymers in shear flow”. In: *Physical review letters* 110.10 (2013), p. 108302.

[16] Gerald Bergtrom. “Cell and Molecular Biology: What We Know & How We Found Out (Annotated iText)”. In: (2015).

[17] Hiroshi Noguchi and Gerhard Gompper. “Dynamics of fluid vesicles in shear flow: Effect of membrane viscosity and thermal fluctuations”. In: *Physical Review E* 72.1 (2005), p. 011901.

[18] F S Gnesotto, F Mura, J Gladrow, and C P Broedersz. “Broken detailed balance and non-equilibrium dynamics in living systems: a review”. In: *Reports on Progress in Physics* 81.6 (2018), p. 066601.

[19] http://lifeofplant.blogspot.com/2011/04/endocytosis-and-exocytosis.html.

[20] Deepak Krishnamurthy and Manu Prakash. “Emergent Programmable Behavior and Chaos in Dynamically Driven Active Filaments”. In: *bioRxiv* (2022).

[21] https://byjus.com/biology/budding/.

[22] LD Landau and EM Lifshitz. “Theory of Elasticity,(Pergamon Press, Oxford, 1986)”. In: ().

[23] Dmitry A Fedosov, Hiroshi Noguchi, and Gerhard Gompper. “Multiscale modeling of blood flow: from single cells to blood rheology”. In: *Biomechanics and modeling in mechanobiology* 13.2 (2014), pp. 239–258.

[24] Allison Beach, Huang-Ge Zhang, Mariusz Z Ratajczak, and Sham S Kakar. “Exosomes: an overview of biogenesis, composition and role in ovarian cancer”. In: *Journal of ovarian research* 7.1 (2014), pp. 1–11.

[25] Mathias Buenemann and Peter Lenz. “Elastic properties and mechanical stability of chiral and filled viral capsids”. In: *Physical Review E* 78.5 (2008), p. 051924.

[26] Dominic Vella, Amin Ajdari, Ashkan Vaziri, and Arezki Boudaoud. “The indentation of pressurized elastic shells: from polymeric capsules to yeast cells”. In: *Journal of the Royal Society Interface* 9.68 (2012), pp. 448–455.

[27] Daan Vorselen, Fred C MacKintosh, Wouter H Roos, and Gijs JL Wuite. “Competition between bending and internal pressure governs the mechanics of fluid nanovesicles”. In: *Acs Nano* 11.3 (2017), pp. 2628–2636.

[28] Daan Vorselen, Melissa C Piontek, Wouter H Roos, and Gijs JL Wuite. “Mechanical characterization of liposomes and extracellular vesicles, a protocol”. In: *Frontiers in molecular biosciences* 7 (2020), p. 139.

[29] Sara Cavallaro, Federico Pevere, Fredrik Stridfeldt, et al. “Multiparametric profiling of single nanoscale extracellular vesicles by combined atomic force and fluorescence microscopy: correlation and heterogeneity in their molecular and biophysical features”. In: *Small* 17.14 (2021), p. 2008155.

[30] JP Michel, IL Ivanovska, MM Gibbons, et al. “Nanoindentation studies of full and empty viral capsids and the effects of capsid protein mutations on elasticity and strength”. In: *Proceedings of the National Academy of Sciences* 103.16 (2006), pp. 6184–6189.

[31] CI Zoldesi, IL Ivanovska, C Quilliet, GJL Wuite, and A Imhof. “Elastic properties of hollow colloidal particles”. In: *Physical Review E* 78.5 (2008), p. 051401.

[32] P Girard, J Prost, and P Bassereau. “Passive or active fluctuations in membranes containing proteins”. In: *Physical review letters* 94.8 (2005), p. 088102.

[33] P Manneville. “Turbulent patterns made simple?” In: *Journal of Fluid Mechanics* 796 (2016), pp. 1–4.

[34] Vipin Agrawal, Vikash Pandey, and Dhrubaditya Mitra. “Active buckling of pressurized spherical shells: Monte Carlo Simulation”. In: *arXiv preprint arXiv:2206.14172* (2022).

[35] Hassan Aref, John R Blake, Marko Budišić, et al. “Frontiers of chaotic advection”. In: *Reviews of Modern Physics* 89.2 (2017), p. 025007.

[36] Vipin Agrawal and Dhrubaditya Mitra. “Chaos and irreversibility of a flexible filament in periodically driven Stokes flow”. In: *Physical Review E* 106.2 (2022), p. 025103.

[37] Vipin Agrawal, Vikash Pandey, Hanna Kylhammar, Apurba Dev, and Dhrubaditya Mitra. “MeMC: A package for Monte Carlo simulations of spherical shells”. In: *Journal of Open Source Software* 7.74 (2022), p. 4305. URL: https://doi.org/10.21105/joss.04305.

[38] Vipin Agrawal and Dhrubaditya Mitra. *Flexible filament in time-periodic viscous flow: shape chaos and period three*. 2022. arXiv: 2210.04781 [cond-mat.soft].

2

THREE DIMENSIONAL ELASTICITY

> *ut tensio, sic vis*
> *(as the extension, so the force)*
>
> — **Robert Hooke**
> 1678

The theory of elasticity deals with materials that, in the presence of mechanical stress, depart from their 'natural' configuration. In this chapter, we discuss the fundamental equations of elasticity in three dimensions. First, we introduce the fundamental notions.

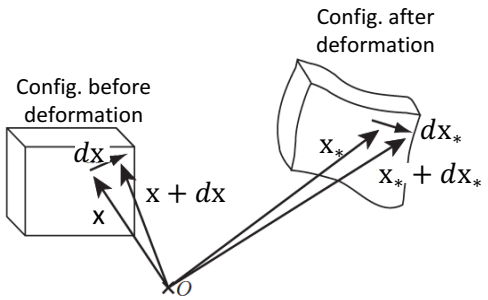

Fig. 2.1.: **Configuration of an elastic body** before and after deformation. Two nearby material points on the body before deformation at $\mathbf{x}$ and $\mathbf{x} + d\mathbf{x}$, moves to $\mathbf{x}_*$ and $\mathbf{x}_* + d\mathbf{x}_*$ after the deformation. Figure adapted and reprinted with permission from [1].

2.1 Strain

Consider a solid body as shown in Fig. 2.1. Let us take two nearby points at $\mathbf{x} \equiv \{x^1, x^2, x^3\}$ and $\mathbf{x} + d\mathbf{x}$ on the body, which moves to $\mathbf{x}_* \equiv \{x_*^1, x_*^2, x_*^3\}$ and $\mathbf{x}_* + d\mathbf{x}_*$ respectively after the deformation. Let us define

$$\boldsymbol{u}(\mathbf{x}) = \mathbf{x}_* - \mathbf{x}, \tag{2.1}$$

where $\boldsymbol{u}(\mathbf{x})$ is the displacement of the point at $\mathbf{x}$ due to deformation. The small line element $d\mathbf{x}$ changes to $d\mathbf{x}_*$,

$$d\boldsymbol{u}(\mathbf{x}) = d\mathbf{x}_* - d\mathbf{x}. \tag{2.2}$$

In general, this change can be due to translation, rotation or stretching/compression. Translation and rotation do not contribute to the elastic energy. Hence the elastic energy only depends on: [1, section 2.2] [2, section 1]:

$$(d\mathbf{x}_*)^2 - (d\mathbf{x})^2 = (d\mathbf{x} + d\boldsymbol{u})^2 - (d\mathbf{x})^2 \tag{2.3a}$$

$$= 2e^{\alpha\gamma} dx^\alpha dx^\gamma, \tag{2.3b}$$

$$\text{where} \qquad e^{\alpha\gamma} = \frac{1}{2}\left(\frac{\partial u^\alpha}{\partial x^\gamma} + \frac{\partial u^\gamma}{\partial x^\alpha} + \frac{\partial u^\mu}{\partial x^\alpha}\frac{\partial u^\mu}{\partial x^\alpha}\right). \tag{2.3c}$$

Here $e^{\alpha\gamma}$ is the strain tensor, the Greek indices go from 1 to 3 and Einstein summation is implied.

Note that $e^{\alpha\gamma}$ is a symmetric tensor of rank two by its construction so it can be represented by 3×3 symmetric matrix. The eigenvectors of a symmetric matrix are orthogonal. These eigenvectors are called the principal axes of strain tensor – let us denote them by $\tilde{x}^1, \tilde{x}^2, \tilde{x}^3$. In the coordinate system of principal axes, the strain tensor is diagonal. We denote the diagonal entries as $\tilde{e}^{11}, \tilde{e}^{22}, \tilde{e}^{33}$ – these are called principal strains [1, section 2.2]. We rewrite Eq. (2.3)(a,b):

$$(d\mathbf{x}_*)^2 = \left(\delta^{\alpha\gamma} + 2e^{\alpha\gamma}\right) dx^\alpha dx^\gamma, \tag{2.4a}$$

$$= \left(1 + 2\tilde{e}^{\alpha\gamma}\right) \delta^{\alpha\gamma} d\tilde{x}^\alpha d\tilde{x}^\gamma \tag{2.4b}$$

$$= (1 + 2\tilde{e}^{11}) d\tilde{x}^1 d\tilde{x}^1 + (1 + 2\tilde{e}^{22}) d\tilde{x}^2 d\tilde{x}^2 + (1 + 2\tilde{e}^{33}) d\tilde{x}^3 d\tilde{x}^3, \tag{2.4c}$$

$$= d\tilde{x}_*^\alpha d\tilde{x}_*^\alpha, \tag{2.4d}$$

where $d\tilde{x}_*^1 = \sqrt{1 + 2\tilde{e}^{11}} d\tilde{x}^1$, and similarly for other two directions. This shows that any elastic deformation of a body can locally be represented as a combination of

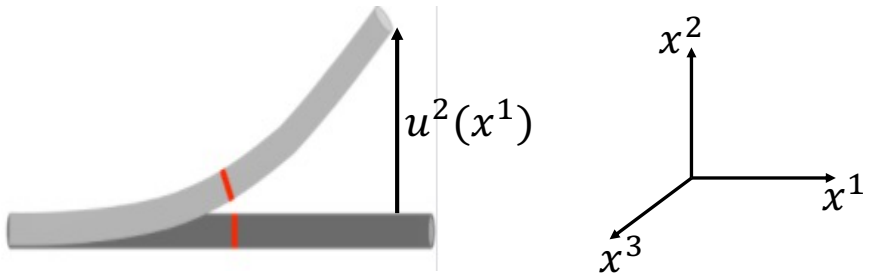

Fig. 2.2.: **A rod** along x^1 direction with the tip displacement as $u^2(x^1)$.

extension and compression along the principal axes. The relative extension along principal axis $\tilde{x}^1$ is:

$$\frac{d\tilde{x}^1_* - d\tilde{x}^1}{d\tilde{x}^1} = \sqrt{1 + 2\tilde{e}^{11}} - 1 \approx \tilde{e}^{11}, \tag{2.5}$$

and similarly for other two directions.

2.1.1 Small strain

As described earlier, the strain tensor has three principal axis at any point in the elastic material. Let us choose three distances along these three principal axis and consider deformations of the body, for which the changes in these distances are small compared with the distances themselves. In other words, relative extension or compression along any principal axis is much less than 1, hence so are principal strains. Consequently, in the frame of Cartesian coordinates also, we can drop the nonlinear term in Eq. (2.3)(b) to get:

$$e^{\alpha\gamma}_{\text{lin}} = \frac{1}{2}\left(\frac{\partial u^\alpha}{\partial x^\gamma} + \frac{\partial u^\gamma}{\partial x^\alpha}\right). \tag{2.6}$$

The subscript lin is for the strain tensor in the small deformation regime.

In some cases, even for small strains, all the nonlinear terms can not be ignored. For example, consider an undeformed rod along the x^1-axis as shown in Fig. 2.2. The rod is deformed as shown in the same figure. Clearly the tip of the rod moves by a considerable amount of distance. Nevertheless the local compression and the extension in the rod is small. Let u^2 be the vertical displacement of every point in the rod. Here, the derivative $\partial u^2/\partial x^1$ is comparable to unity and the nonlinear terms involving this derivative can not be ignored in the expression of strain tensor. This illustrates that for a one-dimensional object embedded in two or three dimensions, or for a two-dimensional object embedded in three dimension, even in the regime of

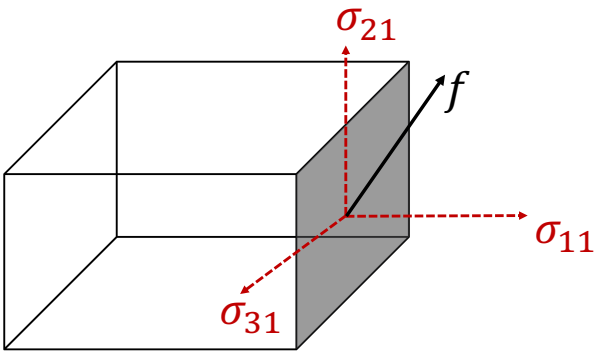

Fig. 2.3.: The force on the face parallel to $x^2 - x^3$ plane due to rest of the body is f. Stress σ on the face has three components along all the three axis.

small deformation, the nonlinearity in strain tensor is significant. We discuss these cases for filament and shells in the subsequent chapters.

2.2 Stress

Take a solid body in mechanical equilibrium and apply external forces to deform it. Now consider a small volume element inside the body as shown in Fig. 2.3. Without any loss of generality, we take the volume element as a rectangular parallelepiped with faces parallel to Cartesian coordinate axis. Due to deformation, at microscopic level, the arrangement of molecules is changed. This gives rise to *internal forces*. These forces act through the faces of the volume element. Now consider the face parallel to $x^2 - x^3$-plane as shown in Fig. 2.3. We define stress as force across the face, per unit area of that face. The stress will be a 2nd rank tensor or a 3×3 matrix [3, chapter 31]. We further assume that Hooke's law holds, such that for small strain, stress is proportional to strain [2, section 4]. In the most general form,

$$\sigma^{\alpha\beta} = E^{\alpha\beta\gamma\delta} e^{\gamma\delta}, \tag{2.7}$$

where $\sigma^{\alpha\beta}$ is second-rank stress tensor and $E^{\alpha\beta\gamma\delta}$ is the fourth-rank tensor of elastic modulii of the material.

2.2.1 Lamé coefficients

If the elastic material is isotropic then the tensor $E^{\alpha\beta\gamma\delta}$ must be invariant under rotation and reflection. Hence it is described by two elastic coefficients [3, chapter 31]

$$E^{\alpha\beta\gamma\mu} = \lambda\delta^{\alpha\beta}\delta^{\gamma\mu} + \mu(\delta^{\alpha\gamma}\delta^{\beta\mu} + \delta^{\alpha\mu}\delta^{\beta\gamma}), \tag{2.8}$$

which are called the Lamé coefficients. Substituting Eq. (2.8) in Eq. (2.7), we get

$$\sigma^{\alpha\beta} = \lambda e^{\mu\mu}\delta^{\alpha\beta} + 2\mu e^{\alpha\beta}. \tag{2.9}$$

2.2.2 Elastic energy

To construct the elastic energy of the system, we must follow certain rules. First, the energy should not be function of displacement field $\boldsymbol{u}$, but its gradient – This ensures that translating a body from one point to another does not change the stored elastic energy. Second, it should be quadratic in any deformation to ensure that the energy function has a minima. Third, it should be scalar. Such an energy function is constructed as the linear combination of $\sigma^{\alpha\beta}\sigma^{\alpha\beta}, \sigma^{\alpha\beta}e^{\alpha\beta}, e^{\alpha\beta}e^{\alpha\beta}$. We use Eq. (2.9) to replace $\sigma^{\alpha\beta}$ in terms of $e^{\alpha\beta}$. In an isotropic material obeying the Hooke's law, this leads to the following expression for the total elastic energy

$$\mathcal{H} = \int_V H dV, \tag{2.10}$$

where

$$H = \frac{1}{2}\lambda e^{\mu\mu}e^{\mu\mu} + \mu e^{\alpha\gamma}e^{\alpha\gamma}, \tag{2.11}$$

is the energy per unit volume, and V is the volume. Here λ and μ are known as the Lamé coefficients [1].

2.2.3 Bulk modulus, Young's modulus and Poisson ratio

Let us represent the strain tensor as the sum of pure shear and a hydrostatic compression. Pure shear alters the shape of a body but do not change its volume whereas hydrostatic compression causes a change in volume but no change in the shape. We rewrite the identity $e^{\alpha\gamma}$ as:

$$e^{\alpha\gamma} = \left(e^{\alpha\gamma} - \frac{1}{3}\delta^{\alpha\gamma}e^{\mu\mu}\right) + \frac{1}{3}\delta^{\alpha\gamma}e^{\mu\mu}. \tag{2.12}$$

Here, the first term on the right hand side is strain due shear deformation, as it does not cause any change in the volume of the body whereas the second term is due to hydrostatic compression.

Substituting Eq. (2.12) in (2.11)

$$\begin{aligned} H &= \mu \left(e^{\alpha\gamma} - \frac{1}{3}\delta^{\alpha\gamma} e^{\mu\mu} \right)^2 + \frac{1}{2} K e^{\mu\mu} e^{\mu\mu}, \\ K &= \lambda + \frac{2}{3}\mu. \end{aligned} \tag{2.13}$$

Here K is *bulk modulus*. Since μ also turns out to be the coefficient of shear deformation of the body, it is also sometime referred as the *shear modulus*.

Further we rewrite Eq. (2.9) as

$$\sigma^{\alpha\beta} = \frac{Y}{1+\nu} \left(e^{\alpha\beta} + \frac{\nu}{1-2\nu} e^{\mu\mu} \delta^{\alpha\beta} \right), \tag{2.14}$$

where Y is *Young's modulus*, and ν is the *Poisson ratio*. The Young's modulus and Poisson ratio are related to Lamé coefficient as follows:

$$Y = \frac{9K\mu}{3K+\mu}, \tag{2.15a}$$

$$\nu = \frac{1}{2} \frac{3K-2\mu}{3K+\mu}. \tag{2.15b}$$

To understand the meaning of Young's modulus and Poisson ratio, consider a rod with force F stretching it on both ends. Relative lengthening of the rod in the longitudinal direction is F/Y. Young's modules is the ratio of applied force and change in length of the rod and Poisson ratio is the ratio of relative compression in the transverse direction and extension in longitudinal direction(see [2, section 5] and [1, section 2.4]).

2.3 Mechanical equilibrium

One possible way to solve for problems in linear elasticity, is to consider the energy $\mathcal{H}$ (Eq. (2.11)) as a functional for the deformation field $\boldsymbol{u}(\mathbf{x})$, and set

$$\frac{\delta \mathcal{H}}{\delta \boldsymbol{u}} = 0, \tag{2.16}$$

where $\delta/\delta \boldsymbol{u}$ denotes functional derivative. This gives the partial differential equation [4, Chapter 39]

$$(\lambda + \mu)\boldsymbol{\nabla}(\boldsymbol{\nabla} \cdot \boldsymbol{u}) + \mu \nabla^2 \boldsymbol{u} = 0, \tag{2.17}$$

which must be solved with the appropriate boundary conditions.

References

[1] Basile Audoly and Yves Pomeau. “Elasticity and geometry”. In: *Peyresq Lectures On Nonlinear Phenomena*. World Scientific, 2000, pp. 1–35.

[2] LD Landau and EM Lifshitz. *Mechanics*. Vol. 1. Course of Theoretical Physics. Oxford, England: Pergamon Press Ltd., 1969.

[3] Richard P Feynman. *The Feynman Lectures on Physics Vol 2*. Narosa, 1986.

[4] Richard P Feynman, Robert B Leighton, and Matthew Sands. *The Feynman Lectures on Physics: Mainly Electromagnetism and Matter, Vol. 2*. Addison-Wesley, Reading. reprinted, 1977.

3

PLATES

By definition, a plate has a very small thickness i.e. its dimension in one direction, called the transverse direction, is very small compared to the two other longitudinal directions. In this chapter, we discuss the equations governing the elasticity of plates.

Clearly for plates, the dynamical variable consists of both in-plane deformation and out-of-plane deformation. This gives two type of contribution to the total elastic energy, first, bending energy and second, stretching energy. To understand this, consider a plate with thickness h as shown in Fig. 3.1. When the plate is bent, it is compressed at some points and extended at some other points. So there should be a plane inside the plate, which does not undergo any compression or extension – we call this the neutral plane. For such deformations, where the plate has a neutral plane, total elastic energy has contribution due to the curvature of the plate (bending energy) but negligible contribution from in-plane $(\mathrm{x}^1, \mathrm{x}^2)$ deformations. Such deformations are generally called as *isometric deformation* or *pure bending deformation*. Next, we also consider that the plate is deformed in-plane only. Here, the elastic energy has contribution only due to stretching of the plate.

In section 3.1, we only consider out-of-plane deformations and formulate the expression for bending energy of plate. In section 3.2, we consider only in-plane

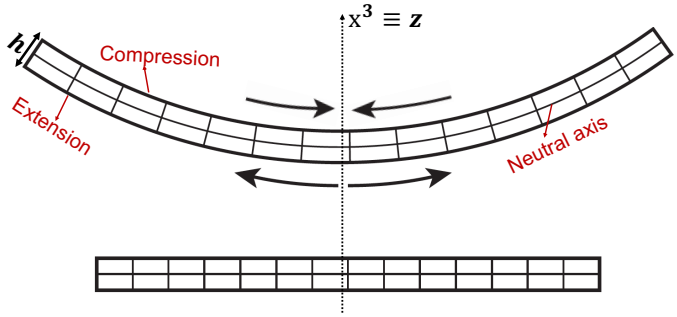

Fig. 3.1.: **A plate** with thickness h bent along x^3-axis. The plate is compressed at some points and stretched at other points. Here, neutral axis of the plate does not show any compression or extension – it is an example of isometric deformation or pure bending. Figure adapted and reprinted with permission from [1].

deformations and write down the stretching energy. Further, in section 3.3, we discuss the large deformation of plate – where the elastic energy has contributions from both in-plane and out-of-plane deformations– and subsequently arrive at the Föppl–von Kármán equations.

3.1 Bending energy of a plate

Consider a plate of thickness h, as shown in Fig. 3.1. We notice that the component of stress in x^3 direction is zero on both the top and the bottom surface of the plate. Since the plate is very thin, we assume that these stresses shall be negligible throughout the thickness of the plate. Thus we have: [2, section 11]

$$\sigma^{13} = \frac{Y}{1+\nu}\mathrm{e}^{13} = 0, \tag{3.1a}$$

$$\sigma^{23} = \frac{Y}{1+\nu}\mathrm{e}^{23} = 0, \tag{3.1b}$$

$$\sigma^{33} = \frac{Y}{(1+\nu)(1-2\nu)}\left[(1-\nu)e^{33} + \nu(e^{11}+e^{22})\right] = 0, \tag{3.1c}$$

where we have used Hooke's law (Eq. (2.14)) to write stress in terms of strain. We solve Eq. (3.1)(a,b) in the limit of small displacement (Eq. (2.6)) with the following boundary conditions

$$u^1(z=0) = u^2(z=0) = 0. \tag{3.2}$$

We get

$$u^1 = -z\frac{\partial f}{\partial x^1}; \qquad u^2 = -z\frac{\partial f}{\partial x^2}, \tag{3.3}$$

where $f \equiv u^3$ is the displacement in x^3 direction, and z is the vertical coordinate which varies from $-h/2$ to $+h/2$. A straight forward calculation for the elastic energy per unit volume (Eq. (2.11)) leads us to:

$$\mathrm{H} = z^2\frac{Y}{1+\nu}\left\{\frac{1}{2(1-\nu)}\left(\partial_1^2 f + \partial_2^2 f\right)^2 + \left[(\partial_1\partial_2 f)^2 - \partial_1^2 f\partial_2^2 f\right]\right\}, \tag{3.4}$$

where Y is Young's modulus, ν is Poisson's ratio and $\partial_i(\cdot) \equiv \partial(\cdot)/\partial x^i$. Note that, the expression of H in Eq. (3.4) contains only out-of-plane displacement term, f. This is the bending energy of the plate per unit volume. We integrate Eq. (3.4) from

$z = -h/2$ to $z = +h/2$ to get bending energy per unit surface area of the plate. The total bending energy is

$$\mathcal{H}^{\text{Bend}} = \frac{Yh^3}{24(1-\nu^2)} \int_S \left[\left(\partial_1^2 f + \partial_2^2 f \right)^2 + 2(1-\nu) \left\{ (\partial_1 \partial_2 f)^2 - \partial_1^2 f \partial_2^2 f \right\} \right] dS. \tag{3.5}$$

The first and second term in Eq. (3.5) are the mean, κ_H, and Gaussian curvature, κ_G, of plate respectively.

$$\kappa_H = \frac{1}{2} \left(\partial_1^2 f + \partial_2^2 f \right); \quad \text{and} \quad \kappa_G = (\partial_1 \partial_2 f)^2 - \partial_1^2 f \partial_2^2 f, \tag{3.6}$$

Gauss-Bonnet theorem [3, 4] implies that the contribution from κ_G to elastic energy does not change if the topology of surface is held fixed. Hence we shall drop the respective term to obtain:

$$\mathcal{H}^{\text{Bend}} = \frac{B}{2} \int \left(\nabla^2 f \right)^2 dS, \tag{3.7}$$

where

$$B = \frac{Yh^3}{24(1-\nu^2)} \tag{3.8}$$

is the bending modulus of the plate.

3.2 Stretching energy

In this section, we consider the special case where the plate has only in-plane deformations but no out-of-plane deformations. We write down the stress by being only on the surface – an intrinsic way. We follow the same logic as in three-dimensional elasticity (see Eq. (2.9)) to define stress-strain relationship using Hooke's law as

$$\sigma_{2\text{D}}^{ij} = \lambda_{2\text{D}} e_{2\text{D}}^{kk} \delta^{ij} + 2\mu_{2\text{D}} e_{2\text{D}}^{ij}, \tag{3.9}$$

where $\sigma_{2\text{D}}$ is force per unit length (as opposed to force per unit area in three dimension), $e_{2\text{D}}$ is the strain tensor for two dimensional surface,

$$e_{2\text{D}}^{ij} = \frac{1}{2} \left[\frac{\partial u^i}{\partial x^j} + \frac{\partial u^j}{\partial x^i} \right] \tag{3.10}$$

λ_{2D} and μ_{2D} are 2D Lamé coefficients. Latin indices run from 1 to 2. Here, we assumed the limit of small in-plane deformation. Stretching energy of the system is written as

$$\mathcal{H}^{\text{Stretch}} = \int_S dS \left[\frac{1}{2}\lambda_{2D} e^{kk}_{2D} e^{kk}_{2D} + \mu_{2D} e^{ij}_{2D} e^{ij}_{2D}\right], \tag{3.11}$$

where S is area of the surface.

3.2.1 2D Lamé coefficients in terms of 3D elastic coefficients:

In this section, we shall again use the equations of general elasticity theory in three dimension to compute the stretching energy of a flat surface. Consider a flat surface of thickness h, as shown in Fig. 3.1. We apply the stress free conditions on the surface of the plate as described in Eq. (3.1). We solve (3.1) to get [2, section 13]

$$e^{13} = e^{23} = 0, \qquad e^{33} = -\frac{\nu}{1-\nu}(e^{11} + e^{12}). \tag{3.12}$$

Since we want to write the stress tensor and stretching energy in terms of in-plane displacement i.e. u^1, u^2, we use Eq. (3.12) to substitute e^{13}, e^{23}, e^{33} in the expressions of $\sigma^{11}, \sigma^{12}, \sigma^{22}$ to get:

$$\sigma^{ij} = \frac{Y\nu}{1-\nu^2} e^{kk}\delta^{ij} + \frac{Y}{1+\nu} e^{ij}, \quad i,j = \{1,2\} \tag{3.13}$$

where σ is force per unit area, and σ_{2D} is force per unit length which is obtained by multiplying σ by thickness h i.e. $\sigma_{2D} = \sigma h$. We compare Eq. (3.13) with (3.9) to get

$$\lambda_{2D} = \frac{Yh\nu}{1-\nu^2}, \qquad \mu_{2D} = \frac{Yh}{1+\nu}. \tag{3.14}$$

The stretching energy is given by Eq. (3.11).

3.3 Large deformation of a plate: stretching and bending energy

Here we consider the contribution from both in-plane and out-of-plane deformation to the total elastic energy. Let us rewrite the general expression for strain tensor

$$e^{\alpha\gamma} = \frac{1}{2}\left(\frac{\partial u^\alpha}{\partial x^\gamma} + \frac{\partial u^\gamma}{\partial x^\alpha} + \frac{\partial u^1}{\partial x^\alpha}\frac{\partial u^1}{\partial x^\gamma} + \frac{\partial u^2}{\partial x^\alpha}\frac{\partial u^2}{\partial x^\gamma} + \frac{\partial f}{\partial x^\alpha}\frac{\partial f}{\partial x^\gamma}\right), \tag{3.15}$$

where u^1, u^2 are in-plane displacements in x^1, x^2 direction and $u^3 \equiv f$.

Here, as in section 2.1.1, we assume that the in-plane strain are small. Hence for x^1, x^2 direction, we ignore the quadratic term in u^1, u^2 but we must retain the quadratic term in f in Eq. (3.15). Thus we obtain:

$$e^{ij}_{\mathrm{2D}} = \frac{1}{2}\left(\frac{\partial u^i}{\partial x^j} + \frac{\partial u^j}{\partial x^i} + \frac{\partial f}{\partial x^i}\frac{\partial f}{\partial x^j}\right), \tag{3.16}$$

where $i, j = \{1, 2\}$. Total energy of the system is:

$$\mathcal{H} = \int_S dS \left[\frac{B}{2}(\nabla^2 f)^2 + \mu_{\mathrm{2D}} e^{ij} e^{ij} + \frac{\lambda_{\mathrm{2D}}}{2} e^{kk} e^{kk}\right] \tag{3.17}$$

3.3.1 The Föppl–von Kármán equation

Minimizing the energy functional (Eq. (3.17)) with respect to both f and $\boldsymbol{u}$ yields the Föppl–von Kármán equations [2, section 14] [1, section 6.5]

$$B\nabla^4 f - \frac{\partial}{\partial x^k}\left(\sigma^{ik}_{\mathrm{2D}}\frac{\partial f}{\partial x^i}\right) = P \tag{3.18a}$$

$$\frac{\partial \sigma^{ik}_{\mathrm{2D}}}{\partial x^k} = 0. \tag{3.18b}$$

Here Latin indices run from 1 to 2 and P is force per unit area on the plate in the transverse direction.

References

[1] Basile Audoly and Yves Pomeau. “Elasticity and geometry”. In: *Peyresq Lectures On Nonlinear Phenomena*. World Scientific, 2000, pp. 1–35.

[2] LD Landau and EM Lifshitz. *Mechanics*. Vol. 1. Course of Theoretical Physics. Oxford, England: Pergamon Press Ltd., 1969.

[3] Thomas R Powers. “Dynamics of filaments and membranes in a viscous fluid”. In: *Reviews of Modern Physics* 82.2 (2010), p. 1607.

[4] David Nelson, Tsvi Piran, and Steven Weinberg. *Statistical mechanics of membranes and surfaces*. World Scientific, 2004.

4

SHELLS

This chapter covers fundamental aspects of the mechanics of thin spherical shells. A shell is a two-dimensional curved surface whose thickness is small compared with its other dimension. They are different from plates because of their non-zero curvature even when they are not deformed. They are commonly found in many natural and engineering settings. Their sizes can vary over a very large range – from hundred meters, e.g., the Avicii Arena Stockholm [1] down to about hundred nanometers, e.g., viral capsules [1, 2] and exosomes [3, 4]. From an engineering perspective, a typical reason to study shells is to determine conditions under which these structures buckle or collapse [5, 6, 7, 8]. Interest in this traditional field has been rekindled in the past decades because of possible applications to medicine and nanoscience [9, 10, 11].

In this chapter, we construct an effective Hamiltonian for shells. For that, we need to use generalized curvilinear coordinate system. We start by describing kinematics of the surface.

4.1 Kinematics of a surface

Let us consider a two dimensional surface embedded in three-dimensional Euclidean space $\mathbb{R}^3$ as shown in Fig. 4.1. We define a generalized curvilinear coordinate system on the surface as $\boldsymbol{\xi} \equiv \{\xi^i; i = 1, 2\}$ – this is an intrinsic coordinate on the surface [2]. Let us also denote the position of a point P in an extrinsic way on the surface in $\mathbb{R}^3$ as

$$\mathbf{x}(\boldsymbol{\xi}) \equiv \{x^\mu(\boldsymbol{\xi}); \mu = 1, 2, 3\} \tag{4.1a}$$

$$\boldsymbol{\xi} \equiv \{\xi^i; i = 1, 2\}. \tag{4.1b}$$

[1] There are several geodesic domes with sizes ranging from 10 to 200 meters.

[2] Intrinsic coordinates are defined in such a way as if a creature is living entirely within the surface without any reference to its embedding dimension [12].

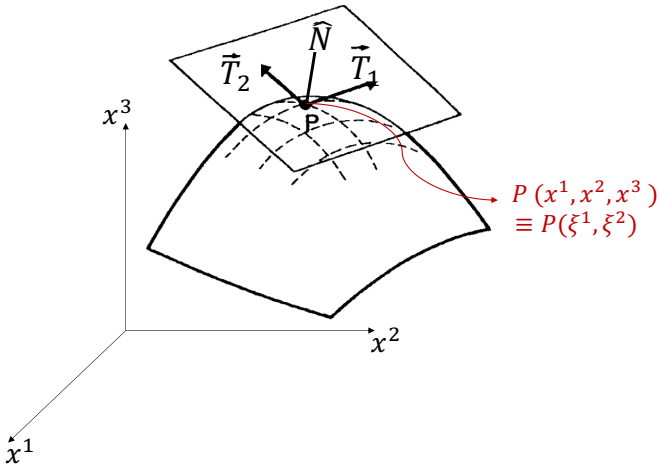

Fig. 4.1.: Tangent plane and normal vector at point P on a two dimensional surface embedded in three dimensional space. Position of P is described in two ways, first in the intrinsic surface coordinate system (ξ^1, ξ^2), and second in the extrinsic Cartesian coordinate system (x^1, x^2, x^3). Figure adapted and reprinted with permission from [13].

Here, for two dimensional coordinate system we use Latin indices and for three dimensional coordinate system we use Greek indices. A two dimensional surface has infinite number of tangent vectors at a point. We choose two linearly independent tangent vectors, $\boldsymbol{T}_i, \{i = 1, 2\}$ at any point P, which forms the basis for tangent plane [14, 13]. We write

$$\boldsymbol{T}_i \equiv T_i^\mu = \frac{\partial x^\mu}{\partial \xi^i} \equiv \frac{\partial \mathbf{x}}{\partial \xi^i} \equiv \partial_i \mathbf{x}, \tag{4.2}$$

where $i = \{1, 2\}, \mu = \{1, 2, 3\}$. In general, $\boldsymbol{T}_1, \boldsymbol{T}_2$ do not form an orthonormal basis. We define the unit normal to the surface $\widehat{\boldsymbol{N}}$ as

$$\widehat{\boldsymbol{N}} = \frac{\boldsymbol{T}_1 \times \boldsymbol{T}_2}{|\boldsymbol{T}_1 \times \boldsymbol{T}_2|}. \tag{4.3}$$

Note that, there are two normal vectors $\widehat{\boldsymbol{N}}$ and $-\widehat{\boldsymbol{N}}$. Direction of $\widehat{\boldsymbol{N}}$ is decided by the choice of an orientation on the surface. Unless there is any asymmetry, there is no reason to prefer one over another.

We calculate the infinitesimal Euclidean distance, ds, between two points on the surface, $\boldsymbol{\xi}$ and $\boldsymbol{\xi} + d\boldsymbol{\xi}$ [13, chapter 6]:

$$ds^2 = [\mathbf{x}(\boldsymbol{\xi} + d\boldsymbol{\xi}) - \mathbf{x}(\boldsymbol{\xi})]^2 = d\xi^i d\xi^j \frac{\partial \mathbf{x}}{\partial \xi^i} \frac{\partial \mathbf{x}}{\partial \xi^j} = d\xi^i d\xi^j g_{ij}(\boldsymbol{\xi}), \tag{4.4}$$

where $g_{ij}(\boldsymbol{\xi})$ is the metric tensor [15].

4.1.1 Curvature tensor

The curvature is the tangential component of the rate of change of the normal to the surface [14, Eq. 80]:

$$d\widehat{\boldsymbol{N}} \cdot d\mathbf{x} = -\kappa_{ij} d\xi^i d\xi^j, \tag{4.5}$$

where

$$\kappa_{ij} = -\frac{\partial \widehat{\boldsymbol{N}}}{\partial \xi^i} \cdot \boldsymbol{T}_j, \tag{4.6}$$

$\mu = \{1, 2, 3\}$ and $i = \{1, 2\}$.

An alternate description of the curvature is as follows. We take derivative of a tangent vector with respect to the surface coordinates [14, 13]. The component of the derivative of tangent in $\widehat{\boldsymbol{N}}$ direction, $\kappa_{ij}\widehat{\boldsymbol{N}}$, is the curvature tensor.

$$\frac{\partial \boldsymbol{T}_i}{\partial \xi^j} = \kappa_{ij}\widehat{\boldsymbol{N}} + \begin{pmatrix} \text{Other terms in} \\ \boldsymbol{T}_1, \boldsymbol{T}_2 \text{ direction} \end{pmatrix}, \tag{4.7}$$

This description allows us to write the curvature $\boldsymbol{\kappa}_{ij} \equiv \kappa_{ij}\widehat{\boldsymbol{N}}$, as a 2nd rank tensor with each element as a vector in the direction of $\widehat{\boldsymbol{N}}$ [13, Eq. 2.40]. Using Eq. (4.2), we note that κ_{ij} is symmetric. Hence its eigenvectors are orthogonal. In the frame of these eigenvectors κ_{ij} is a diagonal matrix with two curvature values, κ_1, κ_2 – known as principal curvatures. Trace κ_H and determinant κ_G of κ_{ij} is:

$$\kappa_H = \frac{\kappa_1 + \kappa_2}{2}; \quad \kappa_G = \kappa_1 \kappa_2. \tag{4.8}$$

Here κ_H and κ_G are the mean and Gaussian curvature of the surface – these are the invariants of the surface under any coordinate transformation.

4.1.2 Laplace-Beltrami operator

We shall make extensive use of $\kappa_H\widehat{\boldsymbol{N}}$, therefore we define an operator $\boldsymbol{\mathcal{L}}(\mathbf{x}) = 2\kappa_H(\mathbf{x})\widehat{\boldsymbol{N}}(\mathbf{x})$ – it is generalization of Laplacian on curvilinear coordinate system, which is also known as Laplace-Beltrami operator. The operator can be used to assign the sign of curvature at any point. The idea is to compute $\boldsymbol{\mathcal{L}}$ at the point and if it points in the direction of chosen orientation of the surface i.e. $\widehat{\boldsymbol{N}}$, κ_H is positive otherwise κ_H is negative. To understand this, let us consider a sphere under an action of some force F on point P at north-pole as shown in Fig. 4.2(a,b,c). We choose the force to be towards the center of sphere and the direction of $\widehat{\boldsymbol{N}}$ away from the center of the sphere for all the cases. Initially in Fig. 4.2, the sphere is

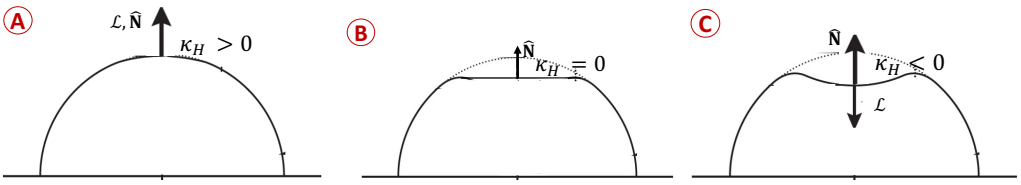

Fig. 4.2.: Change in sign of mean curvature on a sphere before and after deformation.

undeformed, $\boldsymbol{\mathcal{L}}$ at point P is in the same direction as $\widehat{\boldsymbol{N}}$ so κ_H is positive. Later in Fig. 4.2(b), κ_H and $\boldsymbol{\mathcal{L}}$ are zero at point P. In the end, in Fig. 4.2(c), the region around the point P have become inverted. Now $\boldsymbol{\mathcal{L}}$ points downwards, in the opposite direction of $\widehat{\boldsymbol{N}}$, which determines that κ_H is negative.

4.2 Bending energy of a shell

To construct an effective energy for a shell, we generalize the energy of plate (Eq. (3.5)) for curvilinear coordinates, and subtract the contribution from the curvature when sphere is not deformed. A general form of bending energy [16, 17] [13, section 4]

$$\mathcal{H}^{\text{Bend}} = \int_S \left[\frac{B}{2} \left(2\kappa_H \widehat{\boldsymbol{N}} - 2\kappa_0 \widehat{\boldsymbol{N}}_0 \right)^2 + \bar{B}\kappa_G \right] dS. \tag{4.9}$$

where $\mathcal{H}^{\text{Bend}}$ is total bending energy, B is the bending rigidity and $\bar{B}$ is the Gaussian rigidity, $\widehat{\boldsymbol{N}}_0$ is the unit normal vector on the surface before deformation, κ_0 is the curvature of the surface before deformation (also known as spontaneous curvature, for a shell $\kappa_0 = 2/d$, where d is diameter of the shell) and dS is the area of the parallelogram formed by tangent vectors,

$$dS = \widehat{\boldsymbol{N}} \cdot \left(\boldsymbol{T}_1 d\xi^1 \times \boldsymbol{T}_2 d\xi^2 \right) = \sqrt{g} d\xi^1 d\xi^2, \tag{4.10}$$

where g is the determinant of metric tensor g_{ij}. We use the similar arguments as section 3.1 that if the surface does not change its topology, we drop the term involving $\bar{B}$ to get

$$\mathcal{H}^{\text{Bend}} = \frac{B}{2} \int_S \left(2\kappa_H \widehat{\boldsymbol{N}} - 2\kappa_0 \widehat{\boldsymbol{N}}_0 \right)^2 \sqrt{g} d\xi^1 d\xi^2. \tag{4.11}$$

References

[1] Mathias Buenemann and Peter Lenz. “Elastic properties and mechanical stability of chiral and filled viral capsids”. In: *Physical Review E* 78.5 (2008), p. 051924.

[2] JP Michel, IL Ivanovska, MM Gibbons, et al. “Nanoindentation studies of full and empty viral capsids and the effects of capsid protein mutations on elasticity and strength”. In: *Proceedings of the National Academy of Sciences* 103.16 (2006), pp. 6184–6189.

[3] D Michiel Pegtel and Stephen J Gould. “Exosomes”. In: *Annual review of biochemistry* 88 (2019), pp. 487–514.

[4] Sara Cavallaro, Josef Horak, Petra Hååg, et al. “Label-free surface protein profiling of extracellular vesicles by an electrokinetic sensor”. In: *ACS sensors* 4.5 (2019), pp. 1399–1408.

[5] WT Koiter. *Progress in Applied Mechanics (The Prager Anniversary Volume)*. 1963.

[6] Koiter WT. “Current trends in theory of buckling”. In: *Buckling of structures: Symposium Cambridge/USA*. Ed. by Bernard Budiansky. Berlin, Heidelberg, New York: Springer-Verlag, 1976, pp. 1–16.

[7] John W Hutchinson. “Buckling of spherical shells revisited”. In: *Proceedings of the Royal Society A: Mathematical, Physical and Engineering Sciences* 472.2195 (2016), p. 20160577.

[8] LD Landau and EM Lifshitz. *Theory of Elasticity*. Vol. 7. Course of Theoretical Physics. Oxford, England: Pergamon Press Ltd., 1970.

[9] Ch Gao, E Donath, S Moya, V Dudnik, and H Möhwald. “Elasticity of hollow polyelectrolyte capsules prepared by the layer-by-layer technique”. In: *The European Physical Journal E* 5.1 (2001), pp. 21–27.

[10] Vernita D Gordon, Xi Chen, John W Hutchinson, et al. “Self-assembled polymer membrane capsules inflated by osmotic pressure”. In: *Journal of the American Chemical Society* 126.43 (2004), pp. 14117–14122.

[11] Gerard Adriaan Vliegenthart and Gerhard Gompper. “Mechanical deformation of spherical viruses with icosahedral symmetry”. In: *Biophysical journal* 91.3 (2006), pp. 834–841.

[12] Rutherford Aris. *Vectors, tensors and the basic equations of fluid mechanics*. Courier Corporation, 2012.

[13] David Nelson, Tsvi Piran, and Steven Weinberg. *Statistical mechanics of membranes and surfaces*. World Scientific, 2004.

[14] Thomas R Powers. “Dynamics of filaments and membranes in a viscous fluid”. In: *Reviews of Modern Physics* 82.2 (2010), p. 1607.

[15] Eric W. Weisstein. *First Fundamental Form. From MathWorld—A Wolfram Web Resource*. URL: https://mathworld.wolfram.com/FirstFundamentalForm.html.

[16] Peter B Canham. “The minimum energy of bending as a possible explanation of the biconcave shape of the human red blood cell”. In: *Journal of theoretical biology* 26.1 (1970), pp. 61–81.

[17] Alexander Polyakov. “Fine structure of strings”. In: *Nuclear Physics B* 268.2 (1986), pp. 406–412.

5

ACTIVE SHELLS

> *...living matter, while not eluding the "laws of physics" as established up to date, is likely to involve "other laws of physics" hitherto unknown, which however, once they have been revealed, will form just as integral a part of science as the former.*
>
> — **Erwin Schrödinger**
> What is life, 1944

It was realized very early in biophysics [1], that the fundamental property of living matter is that they are not in thermal equilibrium even when they are statistically stationary. They are active – they consume energy and generate entropy [2]. The statistical and mechanical properties of such matter is a current topic of considerable interest [3, 4]. Membrane of any living cell can be considered as an active shell, although not necessarily spherical, because the fluctuations of its membrane have active components, in addition to the thermal fluctuations, due to active processes occurring on the membrane (e.g., endocytosis and exocytosis) and the driving by the active cytoskeleton [5, 6, 7, 8, 9].

5.1 Shallow shell approximation

Let us simplify the energy expressions for a shell by just considering a section of the shell (see Fig. 5.1). We further assume that the shell section is weakly curved and it departs only slightly from a plane [10, section 11.2][11, section 3.15][12]. An advantage of this assumption is that we do not need to describe the shell deformations in curvilinear coordinate system and we can describe the deformations using Cartesian coordinate system.

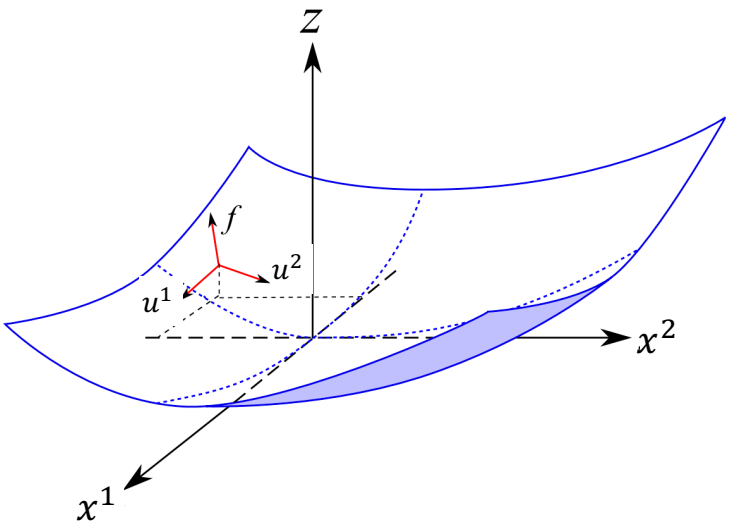

Fig. 5.1.: **A section of an undeformed sphere** is shown in Cartesian coordinate system with $x^1 - x^2$ plane as the tangential plane. The displacement vector between deformed state and undeformed state at any point P is decomposed into three mutually perpendicular direction, $u^1(x^1, x^2), u^2(x^1, x^2), f(x^1, x^2)$, as shown by red arrows. Figure adapted and reprinted with permission from Ref. [12].

Here we take the tangent vectors T_1, T_2 of the shell at origin along the Cartesian coordinate axis x^1, x^2. Thus $x^3 \equiv z$ axis is normal to the shell at origin. Now we define the height field perpendicular to x^1, x^2 plane as $z \equiv z(x^1, x^2)$, where

$$z(x^1, x^2) = R\left(1 - \sqrt{1 - \left(\frac{x^1}{R}\right)^2 - \left(\frac{x^2}{R}\right)^2}\right), \tag{5.1}$$

$Eq.\ (5.1)$ defines the undeformed state of the shell. Here we take center of the shell at $(0, 0, R)$, where R is radius of the shell. We shall make these assumptions for shallow shell theory:

1. The section of the shell is weakly curved i.e.

$$\frac{\partial z(x^1, x^2)}{\partial x^1} \sim \frac{x^1}{R} \quad ; \quad \frac{\partial z(x^1, x^2)}{\partial x^2} \sim \frac{x^2}{R} \tag{5.2}$$

2. The surface departs only slightly from the plane i.e. $z/R \ll 1$.

In addition, we assume that in-plane displacements are small as compared to out-of-plane displacement (see (3.2)). With these assumptions the undeformed state is approximately paraboloid i.e.

$$z(x^1, x^2) \approx \frac{x^1 x^1 + x^2 x^2}{2R}. \tag{5.3}$$

We decompose the displacement vector from undeformed state of the shell (Fig. 5.1) to in-plane displacement as $u^1(x^1, x^2), u^2(x^1, x^2)$ in x^1, x^2 direction, and out of plane displacement in the normal direction as $f(x^1, x^2)$. In terms of these fields, a point at (x^1, x^2, z) moves to

$$(x^1, x^2, z) \to \left(x^1 + u^1 - f\frac{\partial z}{\partial x^1}, x^2 + u^2 - f\frac{\partial z}{\partial x^2}, z + f \right). \tag{5.4}$$

We get strain tensor for this case by substituting

$$u^i \to u^i - f\frac{\partial z}{\partial x^i} \tag{5.5}$$

in the expression of strain tensor for flat surface(Eq. (3.16)). We ignore the higer order terms to get

$$e^{ij} = \frac{1}{2}\left(\frac{\partial u^i}{\partial x^j} + \frac{\partial u^j}{\partial x^i} + \frac{\partial f}{\partial x^i}\frac{\partial f}{\partial x^j} \right) - \delta^{ij}\frac{f}{R}. \tag{5.6}$$

Note that, the strain tensor for shallow shell approximation (Eq. (5.6)) differs by an additional term as compared to the strain tensor for flat surfaces in (3.16). For flat surfaces, we found that out-of-plane displacements contribute to in-plane stretching through nonlinear terms. In addition, for a shell, a purely normal displacement modifies the tangential strain.

Furthermore, a shell can also sustain pressure difference between its interior and exterior. We include an extra term for pressure to write total energy of a section of the shell:

$$\mathcal{H}[u^1, u^2, f] = \int dx^1 dx^2 \left[\frac{B}{2}(\nabla^2 f)^2 + \mu e^{ij} e^{ij} + \frac{\lambda}{2} e^{kk} e^{kk} - Pf \right], \tag{5.7}$$

where P is the difference between external and internal pressure, B is the bending rigidity and λ, μ are the Láme coefficients.

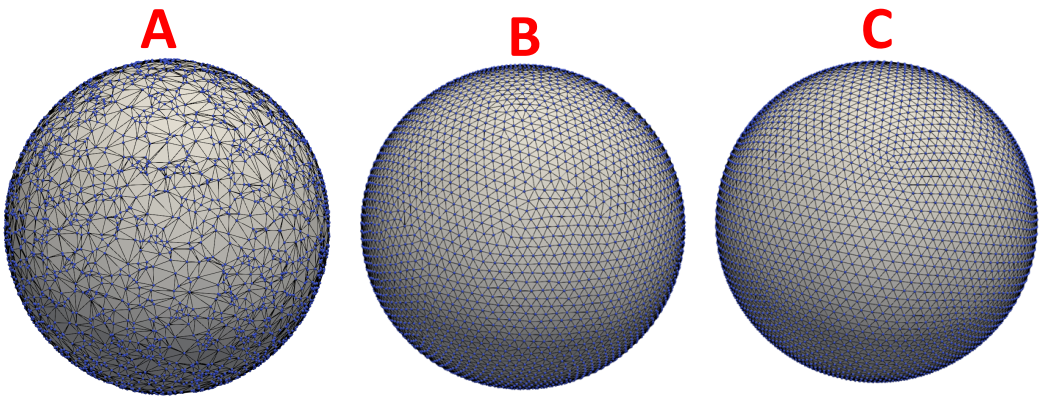

Fig. 5.2.: **Grid points on a sphere** (A)Triangulated random points on a sphere. (B) Triangulated points on sphere after 60000 SMC iteration of the initial configuration shown in (A). (C) An example of regular grid

5.2 Numerical method

Here, we discuss the numerical model for tethered shell, Monte Carlo simulation for equilibrium and non-equilibrium systems.

5.2.1 Summary of paper I – MeMC:A package for Monte Carlo simulations of spherical shells [13]

We use Monte Carlo algorithm following Refs. [12, 14] to study the elastic properties of shells. First, we start with N randomly chosen points on a sphere Fig. 5.2(A). Then, we run a Monte Carlo simulation, with a Lennard-Jones (LJ) repelling potential, of these points moving on the surface. Once the surface Monte Carlo (SMC) has reached an equilibrium, we use the algorithm in Ref. [15] to construct the Delaunay triangulation of these points, see Fig. 5.2(B). The connection between the points thus formed is kept unchanged. The distance between two neighboring nodes i and j is called ℓ_{ij}^0.

We use Monte Carlo [16] simulations to update the positions of the points ($\mathbf{x}_i$ at node i). For a pressurized shell, the total energy,

$$\mathcal{H} = \mathcal{H}^{\text{Stretch}} + \mathcal{H}^{\text{Bend}} + PV, \tag{5.8}$$

where the stretching contribution is

$$\mathcal{H}^{\text{Stretch}} = \frac{1}{2}\sum_i \frac{H}{2}\sum_{j(i)} \left(\mathbf{x}_{ij} - \ell^0_{ij}\right)^2, \quad \text{with} \tag{5.9a}$$

$$\mathbf{x}_{ij} \equiv |\mathbf{x}_i - \mathbf{x}_j|. \tag{5.9b}$$

The bending contribution is

$$\mathcal{H}^{\text{Bend}} = \frac{B}{2}\sum_i \mathcal{A}_i \left(\boldsymbol{L}_{\text{i}} - C\widehat{\boldsymbol{N}}\right)^2. \tag{5.10}$$

Here V is the volume. The Young's modulus of the membrane is given by $Y = 2H/\sqrt{3}$ [17], $\widehat{\boldsymbol{N}}$ is the outward normal to the surface, C is its spontaneous curvature, and $\mathcal{A}_i$ is the area of Voronoi dual cell at the node i [13, 18, 19]. The operator

$$\boldsymbol{L}_i = \frac{1}{\mathcal{A}_i}\sum_{j(i)} \frac{1}{2}\left[\cot(\alpha_{ij}) + \cot(\beta_{ij})\right]\mathbf{x}_{ij}, \tag{5.11}$$

is the discrete Laplacian [17, 19, 18] at the node i. Here α_{ij}, β_{ij} are the angles opposite to bond $\mathbf{x}_{ij}$ as shown in Fig. 5.3. We compute $\mathcal{A}_i$ as follows [19, 18]. Consider the triangle T in Fig. 5.3, defined by the nodes $i, j, j-1$. If T is non-obtuse, the area of shaded region in Fig. 5.3

$$\mathcal{A}_{j(i)} = \frac{1}{8}\left[\mathbf{x}^2_{ij}\cot(\alpha_{ij}) + \mathbf{x}^2_{ij-1}\cot(\beta_{ij-1})\right]. \tag{5.12}$$

If T is an obtuse triangle, the shaded region in Fig. 5.3 lies outside the triangle T then $\mathcal{A}_{j(i)} = \text{area}(T)/2$ if the angle at the vertex i of T is obtuse. Otherwise $\mathcal{A}_{j(i)} = \text{area}(T)/4$. Here $\text{area}(T) = 0.5\,|\mathbf{x}_{ij} \times \mathbf{x}_{ij-1}|$.

The area $\mathcal{A}_i$ is obtained by summing up the contributions from all the triangles similar to $\mathcal{A}_{j(i)}$, in Fig. 5.3, e.g., the contribution from the triangle T is the shaded area.

To compute the outward normal to the surface, $\widehat{\boldsymbol{N}}$, in Eq. (5.10), we sort the points about node i in a counterclockwise manner. To sort the neighbors around any node i, we rotate the coordinate system such that, the z axis passes through the point i along the vector $\mathbf{x}_i$. In this coordinate system we sort the neighbors by their azimuthal angle.

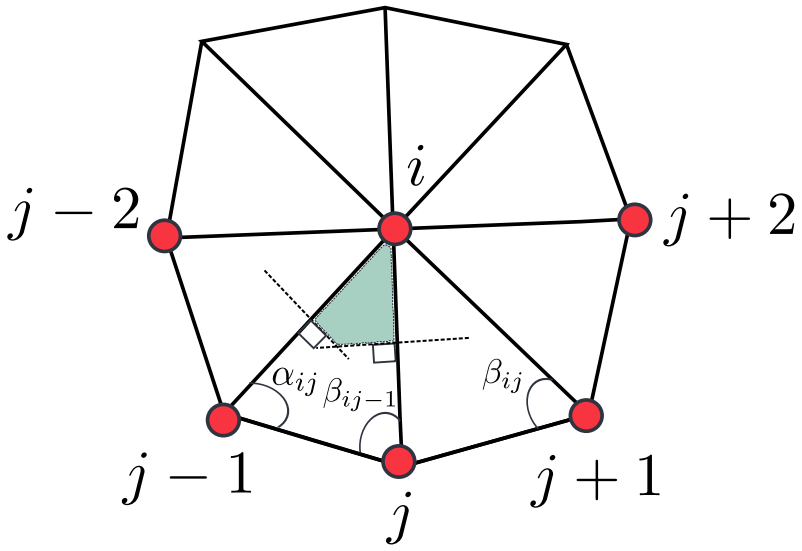

Fig. 5.3.: An example of triangulated mesh at the node i. α_{ij}, β_{ij} are the angles opposite to the bond ij. Shaded part is the Voronoi region of triangle T at the nodes $i, j-1, j$ – it lies inside as T is non-obtuse. The nodes are sorted in counterclockwise direction. The image is adapted from Ref. [13].

5.2.2 Model of activity

Over the years, many theoretical models [20, 21, 22, 23, 24, 25, 26], have been suggested to incorporate the effects of active fluctuations into models of membranes. All of these drive the membrane out of thermal equilibrium. In equilibrium Monte Carlo simulations the transition rate, W, from one state to another is given by the Metropolis algorithm:

$$W = \min[1, \exp(-\mathcal{H}/k_{\mathrm{B}}T)], \tag{5.13}$$

where k_{B} is the Boltzmann constant, T is the temperature and $\mathcal{H}$ is the difference in energy between the two states. To drive the membrane out of equilibrium, following Ref. [27], we replace $\mathcal{H}$ by $\mathcal{H} + \Delta\mathcal{H}$. This guarantees that detailed balance is broken and the amount by which it is broken is $\Delta\mathcal{H}$. If $\Delta\mathcal{H}$ is positive (negative) the probability of acceptance of large fluctuations is decreased (increased). Thus we define activity

$$A = -\frac{\Delta\mathcal{H}}{k_{\mathrm{B}}T} \tag{5.14}$$

such that simulations with positive A, *active* simulations, have higher fluctuations than equilibrium ones whereas for negative A, *quiescent* simulations, the fluctuations are less than the equilibrium ones.

5.3 Statistical-mechanics of the shells

Micro and nano vesicles, both natural and synthetic, play a crucial role in biology and medicine. The physical properties of these vesicles play an important role in their biological functions [28]. For example, consider a shell and compress it with an external pressure with no thermal fluctuations. Initially the shell contracts uniformly [11], but beyond a certain critical pressure P_0 the shell develops buckling instability. Recently Ref [12, 29] showed that for small enough shells, thermal fluctuations can decrease the critical buckling pressure by a large amount. To incorporate the effects of thermal fluctuation, instead of dealing with elastic energy, we formulate the expression for Helmholtz free-energy.

5.3.1 Free-energy

Let us consider that the shell, under the action of small enough external pressure P contracts uniformly by an amount w_0. We write

$$f(\mathbf{x}) = w_0(\mathbf{x}) + w(\mathbf{x}), \tag{5.15}$$

where $w(\mathbf{x})$ is deformation with respect to the contracted state and $\mathbf{x} = (x^1, x^2)$. An effective free energy $\mathcal{F}$ of the system is

$$\mathcal{F}[w] = -k_{\mathrm{B}}T \ln \left[\int \mathcal{D}\boldsymbol{u}(\mathbf{x}) \int dh_0 \exp\left(-\frac{\mathcal{H}[w, w_0, u^1, u^2]}{k_{\mathrm{B}}T} \right) \right] \tag{5.16}$$

Following Ref. [12, 29], we perform the functional integral in Eq. (5.16). We divide $\mathcal{F}[w]$ into harmonic ($\mathcal{F}_0[w]$) and anharmonic part ($\mathcal{F}_1[w]$),

$$\mathcal{F}[w] = \mathcal{F}_0[w] + \mathcal{F}_1[w], \tag{5.17a}$$

$$\mathcal{F}_0[w] = \frac{1}{2} \int d^2\mathbf{x} \left[B(\nabla^2 w)^2 - \frac{PR}{2} \mid \boldsymbol{\nabla} w \mid^2 + \frac{Y_{2\mathrm{D}}}{R^2} w^2 \right], \tag{5.17b}$$

$$\mathcal{F}_1[w] = \frac{Y_{2\mathrm{D}}}{2} \int d^2\mathbf{x} \left[\left(\frac{1}{2} \mathcal{P}_{ij} \frac{\partial w}{\partial x^i} \frac{\partial w}{\partial x^j} \right)^2 - \frac{w}{R} \mathcal{P}_{ij} \frac{\partial w}{\partial x^i} \frac{\partial w}{\partial x^j} \right], \tag{5.17c}$$

where $\mathbf{x} = (x^1, x^2)$, $\mathcal{P}_{ij}$ is the transverse projection operator,

$$Y_{2\mathrm{D}} = 4\mu_{2\mathrm{D}} \frac{\mu_{2\mathrm{D}} + \lambda_{2\mathrm{D}}}{2\mu_{2\mathrm{D}} + \lambda_{2\mathrm{D}}} = Yh \tag{5.18}$$

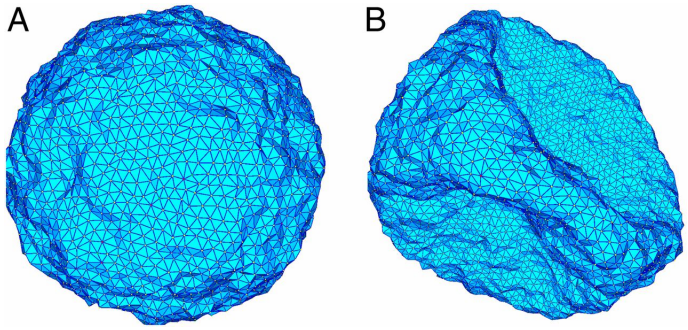

Fig. 5.4.: **Thermal buckling** for FvK $= 4616$, ET $= 27$ and $P = 0$(A), $P = 0.5P_0(B)$, where P_0 is the mechanical buckling pressure. The shell shows buckling at much lower pressure than P_0 due to thermal fluctuations. Figure adapted with permission from [12].

is two-dimensional Young's modulus, Y is three-dimensional Young's modulus, and h is thickness of the shell. We use relations in (3.14) to write the last equality in Eq. (5.18).

We define two non-dimensional numbers, the Föppl–von Kármán number and the Elasto-thermal number, respectively as

$$\text{FvK} \equiv \frac{Y_{\text{2D}} R^2}{B}, \quad \text{ET} \equiv \frac{k_{\text{B}} T}{B} \sqrt{\text{FvK}}, \tag{5.19}$$

where k_{B} is the Boltzmann constant and T is temperature. At constant temperature, the effects of anharmonicity increases with FvK whereas at constant elastic modulus the effects of thermal fluctuations increases with ET.

5.3.2 Thermal buckling

Buckling emerges in this model in the following manner. Consider just the harmonic part $\mathcal{F}_0[w]$. If we write this in Fourier space, with

$$\hat{w}(\boldsymbol{q}) \equiv \int d^2\mathbf{x} w(\mathbf{x}) \exp(i\boldsymbol{q} \cdot \mathbf{x}), \tag{5.20}$$

we obtain

$$\mathcal{F}[\hat{w}] = \frac{1}{2} \int d^2q r_{\text{q}} \hat{w}(\boldsymbol{q}) \hat{w}(-\boldsymbol{q}) \quad \text{where} \tag{5.21a}$$

$$r_{\text{q}} = Bq^4 - \frac{PR}{2} q^2 + \frac{Y_{\text{2D}}}{R^2} \tag{5.21b}$$

Using standard tools of equilibrium statistical mechanics – averaging over thermal noise – it is straightforward to obtain

$$\mathcal{C}_0 \equiv \langle \hat{w}(\boldsymbol{q})\hat{w}(-\boldsymbol{q})\rangle_0 = S\frac{k_{\rm B}T}{r_{\rm q}}. \tag{5.22}$$

Here $q > 1/R$ and S is the area of integration in the x^1–x^2 plane. We rewrite

$$r_{\rm q} = B(q+q_*)^4 - (PR/2)q^2 \tag{5.23}$$

where

$$q_* = (\ell_*)^{-1}\left(\frac{Y_{\rm 2D}}{BR^2}\right)^{1/4} = \frac{\mathrm{FvK}^{1/4}}{R}. \tag{5.24}$$

For a large Föppl–von Kármán number, FvK $\gg 1$, $\ell_* \ll R$. Hence it is valid to consider the mode $q = q_*$. We notice that for

$$P = P_0 = \frac{4B}{R}q_*^2 \tag{5.25}$$

$r_{\rm q}(q = q_*) = 0$, in other words, the equilibrium spectrum, $\mathcal{C}_0$, blows up. This is the signature of buckling. This corresponds to the well known mechanical buckling pressure of spherical shells under external pressure [11]. So far, we have discussed the emergence of mechanical buckling in this model.

Note that, the shallow shell theory can accurately predict the buckling pressure but the shape of the deformed shell after buckling can no longer be described by it. Refs. [12, 29] use renormalization group (RG) techniques to show that the effects of the anharnomic terms is to renormalize the parameters appearing in the bare theory, i.e., P, B, and $Y_{\rm 2D}$ in (5.22) must be replaced by their scale–dependent, renormalized versions, see Ref. [29, Eq. 18]. Consequently both the pressure and the critical buckling pressure are renormalized and buckling is obtained if both of these quantities are equal for a length scale which must be smaller than the radius of the sphere [29]. They find that, with thermal fluctuations, the shell buckles at much lower pressure $P < P_c$ (see Fig. 5.4) and sometime even at negative pressure i.e. shell may collapse because of thermal fluctuations alone.

5.3.3 Discussion of results from paper II – active buckling of pressurized spherical shells: Monte Carlo simulation

In this paper, we study how elastic properties of shells, in particular buckling changes if they are turned active – driven out of thermal equilibrium. We show that within

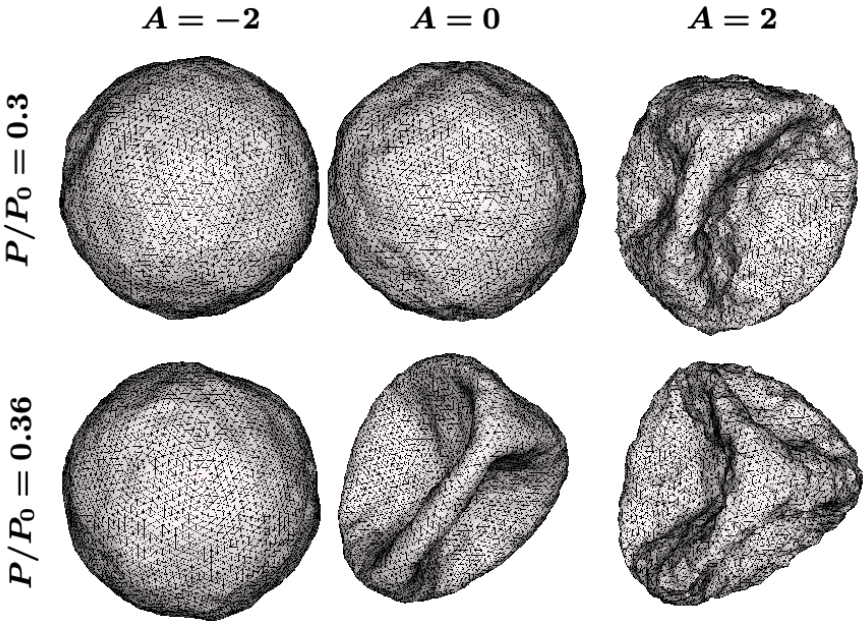

Fig. 5.5.: **Active buckling:** Typical snapshots from our simulations for activity $A = -2$, 0 and 2 (from left to right), and pressure $P = 0.30P_0$ (top row) and $0.36P_0$ (bottom row) where P_0 is the critical buckling pressure obtained from the mechanical theory of elastic shells, i.e., at zero temperature. We use FvK $= 4616$, and ET $= 8$. The middle column, $A = 0$, corresponds to shells in thermal equilibrium – an unbuckled shell buckles upon increasing P/P_0 from 0.30 to 0.36. This is consistent with the results of Refs. [12, 29]. Top row: As activity is increased to 2 (right column) the shell buckles. Bottom row: Whereas as activity is decreased to -2 (left column) the shell, that was buckled in thermal equilibrium, does not buckle at the same pressure. Figure adapted from [30].

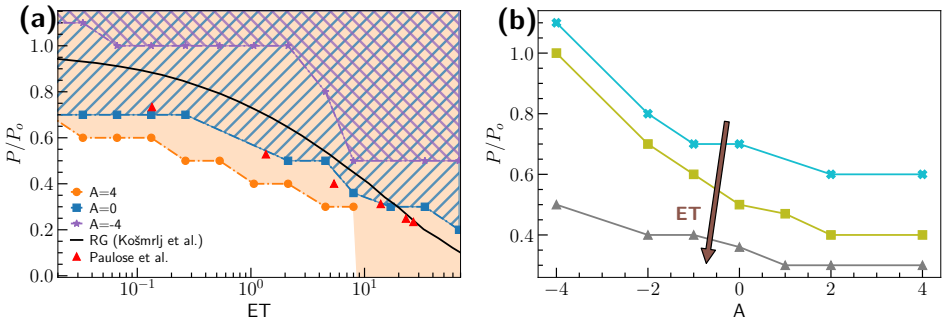

Fig. 5.6.: **Phase diagram** The phase boundary in (a) the pressure–elasto–thermal number plane for different activities and (b) in the pressure–activity plane for different elasto–thermal numbers (gray triangles for ET $= 7.99$, olive squares for ET $= 2.12$ and cyan cross for ET $= 0.03$). In (a) the region where the buckled phase is obtained in equilibrium is marked by blue lines. The region where the buckled phase is obtained for $A = 4$ is shaded in light yellow. The region where the buckled phase is obtained for $A = -4$ is marked by violet lines. In (a) the phase boundary obtained by RG calculation [29] is marked by a black line and the simulation results by Ref. [12] are represented by red triangles.

the right range of elastic parameters, a shell that is not buckled just with thermal fluctuations can be buckled if we increase its activity. Similarly a shell that is buckled in thermal equilibrium can unbuckle if we reduce its activity, see Fig. 5.5. We obtain the phase diagram for thirteen values of elasto–thermal number, for each of which we use seven values of activity. For a fixed choice of elasto–thermal number and activity we start our simulations with an initial condition where the shell is a perfect sphere. Then we choose a fixed value of external pressure and run our simulations till we reach a stationary state, which for zero activity is the equilibrium state. If the sphere in not buckled we choose a higher external pressure and start our simulations again from the same initial condition till we find the pressure where sphere buckles. This way we mark out the phase boundary in the pressure–elasto–thermal number plane for different activities and in the pressure–activity plane for different elasto–thermal numbers, see Fig. 5.6. In Fig. 5.6(a) we also plot the phase boundary, obtained through a RG calculation in Ref. [29], which agrees reasonably well with our numerical results for zero activity. Note that at small ET for the quiescent case it is possible to have the shell remain unbuckled even for pressure higher P_0, i.e., the shell is stabilized.

References

[1] Erwin Schrodinger. *What is life?: With mind and matter and autobiographical sketches*. Cambridge university press, 2012.

[2] F S Gnesotto, F Mura, J Gladrow, and C P Broedersz. “Broken detailed balance and non-equilibrium dynamics in living systems: a review”. In: *Reports on Progress in Physics* 81.6 (2018), p. 066601.

[3] M Cristina Marchetti, Jean-François Joanny, Sriram Ramaswamy, et al. “Hydrodynamics of soft active matter”. In: *Reviews of modern physics* 85.3 (2013), p. 1143.

[4] Sriram Ramaswamy. “The Mechanics and Statistics of Active Matter”. In: *The Annual Review of Condensed Matter Physics is* 1 (2010), pp. 323–45.

[5] Zhangli Peng, Xuejin Li, Igor V Pivkin, et al. “Lipid bilayer and cytoskeletal interactions in a red blood cell”. In: *Proceedings of the National Academy of Sciences* 110.33 (2013), pp. 13356–13361.

[6] Hervé Turlier, Dmitry A Fedosov, Basile Audoly, et al. “Equilibrium physics breakdown reveals the active nature of red blood cell flickering”. In: *Nature physics* 12.5 (2016), pp. 513–519.

[7] Arikta Biswas, Amal Alex, and Bidisha Sinha. “Mapping cell membrane fluctuations reveals their active regulation and transient heterogeneities”. In: *Biophysical journal* 113.8 (2017), pp. 1768–1781.

[8] Hervé Turlier and Timo Betz. “Unveiling the active nature of living-membrane fluctuations and mechanics”. In: *Annual Review of Condensed Matter Physics* 10 (2019), pp. 213–232.

[9] Sreekanth K Manikandan, Tanmoy Ghosh, Tithi Mandal, et al. “Estimate of entropy generation rate can spatiotemporally resolve the active nature of cell flickering”. In: *arXiv preprint arXiv:2205.12849* (2022).

[10] Basile Audoly and Yves Pomeau. “Elasticity and geometry”. In: *Peyresq Lectures On Nonlinear Phenomena*. World Scientific, 2000, pp. 1–35.

[11] WT Koiter. *Progress in Applied Mechanics (The Prager Anniversary Volume)*. 1963.

[12] Jayson Paulose, Gerard A Vliegenthart, Gerhard Gompper, and David R Nelson. “Fluctuating shells under pressure”. In: *Proceedings of the National Academy of Sciences* 109.48 (2012), pp. 19551–19556.

[13] Vipin Agrawal, Vikash Pandey, Hanna Kylhammar, Apurba Dev, and Dhrubaditya Mitra. “MeMC: A package for Monte Carlo simulations of spherical shells”. In: *Journal of Open Source Software* 7.74 (2022), p. 4305. URL: https://doi.org/10.21105/joss.04305.

[14] G Gompper and DM Kroll. “Triangulated-surface models of fluctuating membranes”. In: *Statistical mechanics of membranes and surfaces*. Ed. by David Nelson, Tsvi Piran, and Steven Weinberg. World Scientific, 2004, pp. 359–426.

[15] Manuel Caroli, Pedro MM de Castro, Sébastien Loriot, et al. “Robust and efficient Delaunay triangulations of points on or close to a sphere”. In: *International Symposium on Experimental Algorithms*. Springer. 2010, pp. 462–473.

[16] Artur Baumgärtner, Kurt Binder, J-P Hansen, et al. *Applications of the Monte Carlo method in statistical physics*. Vol. 36. Topics in Current Physics. Springer Science & Business Media, 2013.

[17] C Itzykson. In: *Proceedings of the GIFT seminar, Jaca 85*. Ed. by J *et al* Abad. World Scientific Singapore, 1986, pp. 130–188.

[18] Mark Meyer, Mathieu Desbrun, Peter Schröder, and Alan H Barr. “Discrete differential-geometry operators for triangulated 2-manifolds”. In: *Visualization and mathematics III*. Springer, 2003, pp. 35–57.

[19] Hans-Christian Hege and Konrad Polthier. *Visualization and mathematics III*. Springer Science & Business Media, 2003.

[20] Sriram Ramaswamy, John Toner, and Jacques Prost. “Nonequilibrium fluctuations, traveling waves, and instabilities in active membranes”. In: *Physical review letters* 84.15 (2000), p. 3494.

[21] Madan Rao and Sarasij R.C. “Active fusion and fission processes on a fluid membrane”. In: *Physical review letters* 87.12 (2001), p. 128101.

[22] Bastien Loubet, Udo Seifert, and Michael Andersen Lomholt. “Effective tension and fluctuations in active membranes”. In: *Physical Review E* 85.3 (2012), p. 031913.

[23] Ananyo Maitra, Pragya Srivastava, Madan Rao, and Sriram Ramaswamy. “Activating membranes”. In: *Physical review letters* 112.25 (2014), p. 258101.

[24] Rhoda J Hawkins and Tanniemola B Liverpool. “Stress reorganization and response in active solids”. In: *Physical review letters* 113.2 (2014), p. 028102.

[25] Sifan Yin, Bo Li, and Xi-Qiao Feng. “Bio-chemo-mechanical theory of active shells”. In: *Journal of the Mechanics and Physics of Solids* 152 (2021), p. 104419.

[26] A Goriely. “Five ways to model active processes in elastic solids: active forces, active stresses, active strains, active fibers, and active metrics”. In: *Mech. Res. Commun* 93 (2017), pp. 75–79.

[27] Manoj Kumar and Chandan Dasgupta. “Nonequilibrium phase transition in an Ising model without detailed balance”. In: *Physical Review E* 102.5 (2020), p. 052111.

[28] Rob Phillips, Jane Kondev, Julie Theriot, Hernan G Garcia, and Nigel Orme. *Physical biology of the cell*. Garland Science, 2012.

[29] Andrej Košmrlj and David R Nelson. “Statistical mechanics of thin spherical shells”. In: *Physical Review X* 7.1 (2017), p. 011002.

[30] Vipin Agrawal, Vikash Pandey, and Dhrubaditya Mitra. “Active buckling of pressurized spherical shells: Monte Carlo Simulation”. In: *arXiv preprint arXiv:2206.14172* (2022).

6

FILAMENTS

Long slender elastic bodies, filaments in short are ubiquitous in nature e.g. human hair [1], bacteria [2], carbon-nanotubes [3]. The study involving elastic properties of filaments dates back to 16th century. James Bernoulli posed the fundamental problem of elastica in 1691. The problem reads as: take a filament of uniform thickness and negligible weight. The filament is clamped at one end with force P pushing it from the other end. what is the shape of the filament? Leonhard Euler and Daniel Bernoulli found that the filament will remain straight for loads less than the critical load [1]

$$P_{cr} = \frac{\pi^2 B}{4\ell^2}, \tag{6.1}$$

where B is bending rigidity of the filament, ℓ is total length of the filament. For $P > P_{cr}$, the filament buckles rather than just longitudinally compressing itself. Solution of elastica problem has found its application in diverse felds. For example, bending of long tracks due to heat, collapsing of a tall structure under its own weight [5].

More recently, interest in studying the elastic properties of filament is rekindled because of their application in bio-physics and bio-mechanics. Few examples include, the study of twist in DNA [6], stretch-coil transition of polymers [7], actin filaments [8], flagella [9]. In this chapter, we discuss the foundation of elasticity of filaments.

The rest of this chapter is organized in the following manner. In section 6.1, we describe the kinematics of a filament. In section 6.2, we formulate the expression for total energy. We conclude the chapter by discussing equilibrium equation of a filament under external forces – known as Euler-Bernouili equation (section 4.3).

[1] A closed form solution of elastica was worked out by Saalschütz [4] in 1880.

6.1 Kinematics of a filament

Let us first consider a three-dimensional curve. We represent the curve as $\boldsymbol{R}(\xi)$. Here $\boldsymbol{R}(\xi)$ is the coordinate of every point on curve embedded in 3 dimension, with parameter ξ in some interval on real axis $\mathcal{I}$. We consider only smooth curves i.e. $d\boldsymbol{R}(\xi)/d\xi$ is well defined everywhere in $\mathcal{I}$. The length of such a curve between parameter values ξ_0 and ξ can be defined as:

$$s \equiv \psi(\xi) = \int_{\xi_0}^{\xi} \left\| \frac{d\boldsymbol{R}(\xi')}{d\xi'} \right\| d\xi' \tag{6.2}$$

Where $\|\cdot\|$ denotes the norm. $s = \psi(\xi)$ is the arc-length of the curve from ξ_0 to ξ.

Since $\psi(\xi)$ is always an increasing function , we can take its inverse and write $\xi = \psi^{-1}(s)$. We re-parametrize the curve as $\boldsymbol{R}(\psi^{-1}(s))$ with respect to arc-length s. Let us derive the relation between both notations for describing a curve. Distance between two nearby points on the curve is given by the Pythagorean theorem:

$$ds^2 = \frac{d\boldsymbol{R}(s)}{d\xi} \cdot \frac{d\boldsymbol{R}(s)}{d\xi} d\xi^2 \quad \Longrightarrow \quad \frac{ds}{d\xi} = \left\| \frac{d\boldsymbol{R}(s)}{d\xi} \right\| \tag{6.3}$$

We use this relation to write:

$$\boldsymbol{R}'(s) \equiv \frac{d\boldsymbol{R}(s)}{ds} = \frac{d\boldsymbol{R}(\xi)}{d\xi}\frac{d\xi}{ds} = \frac{d\boldsymbol{R}(\xi)/d\xi}{\|d\boldsymbol{R}(\xi)/d\xi\|} \equiv \widehat{\boldsymbol{T}}(s) \tag{6.4}$$

We denote $(\cdot)'$ as the derivative with respect to s and $\widehat{\boldsymbol{T}}$ denotes the unit tangent vector at every point on the curve.

So far we have described the curve from an extrinsic point of view i.e. we write the coordinate of every point on the curve in three-dimensional coordinate system. The curve is a one-dimensional body embedded in three-dimensional space, so it is also useful to describe its kinematics without resorting to any external co-ordinate system – this is called an intrinsic view.

6.1.1 Filament with no thickness: Frenet-Serret frame

We describe the curve in the frame of unit tangent vector ($\widehat{\boldsymbol{T}}(s)$), unit normal vector($\widehat{\boldsymbol{N}}(s)$) and unit binormal vector ($\widehat{\boldsymbol{B}}(s)$) – this is known as Frenet-Serret frame (as shown in Fig. 6.1(A). These form an orthogonal coordinate system (see Fig. 6.1(A)):

$$\widehat{\boldsymbol{B}}(s) = \widehat{\boldsymbol{T}}(s) \times \widehat{\boldsymbol{N}}(s) \tag{6.5}$$

We defined $\widehat{\boldsymbol{T}}$ in (6.4) and $\widehat{\boldsymbol{N}}$ is a vector perpendicular to $\widehat{\boldsymbol{T}}$. Notice that, if a curve is embedded in three dimension, we have infinite number of vectors perpendicular to $\widehat{\boldsymbol{T}}$. We choose one of them as a normal vector, which also fixes $\widehat{\boldsymbol{B}}$.

Frenet-Serret frame moves along the curve, from $s = 0$ to $s = L$, as shown in Fig. 6.1(A). The frame for any two nearby points differ by a small rotation $\boldsymbol{\Delta\phi}$. So we write:

$$\widehat{\boldsymbol{T}}|_{s+\Delta s} = \widehat{\boldsymbol{T}}|_s + \boldsymbol{\Delta\phi} \times \widehat{\boldsymbol{T}}|_s \quad \Longrightarrow \quad \widehat{\boldsymbol{T}}'(s) = \frac{d\boldsymbol{\phi}(\boldsymbol{s})}{ds} \times \widehat{\boldsymbol{T}}(s). \tag{6.6}$$

We can write the similar equations for $\widehat{\boldsymbol{N}}$ and $\widehat{\boldsymbol{B}}$. Equation 6.6 tells us that the $\widehat{\boldsymbol{T}}', \widehat{\boldsymbol{N}}', \widehat{\boldsymbol{B}}'$ is perpendicular to $\widehat{\boldsymbol{T}}, \widehat{\boldsymbol{N}}, \widehat{\boldsymbol{B}}$ respectively. So we choose $\widehat{\boldsymbol{N}}$ in the direction of $\widehat{\boldsymbol{T}}'$:

$$\widehat{\boldsymbol{N}} = \frac{\widehat{\boldsymbol{T}}'(s)}{\left|\left|\widehat{\boldsymbol{T}}'(s)\right|\right|} \tag{6.7a}$$

$$\widehat{\boldsymbol{T}}' = \left|\left|\widehat{\boldsymbol{T}}'(s)\right|\right| \widehat{\boldsymbol{N}} = \left|\left|\frac{d^2\boldsymbol{R}(s)}{ds^2}\right|\right| \widehat{\boldsymbol{N}} \equiv \kappa \widehat{\boldsymbol{N}} \tag{6.7b}$$

Here $\kappa(s)$ is curvature of the curve. Now we derive the same relation for $\widehat{\boldsymbol{N}}'$ and $\widehat{\boldsymbol{B}}'$. Using (6.5) and (6.6), we derive [10]:

$$\widehat{\boldsymbol{N}}' = \tau \widehat{\boldsymbol{B}} - \kappa \widehat{\boldsymbol{T}} \tag{6.8a}$$

$$\widehat{\boldsymbol{B}}' = -\tau \widehat{\boldsymbol{N}} \tag{6.8b}$$

Where τ is called the torsion of the curve. Intuitively, the curvature (κ) measures the deflection of the curve from a straight-line and torsion (τ) measures the failure of a curve to be planer[11]. Equation 6.7 and 6.8 are called the Frenet-Serret frame of equations [11] – an intrinsic description of the curve.

6.1.2 Filament with finite thickness: Darboux frame

Frenet-Serret frame describes the kinematics of a curve i.e. a filament with zero thickness, although practical filaments have a finite thickness. To describe the filaments in more accurate way, we define an orthonormal frame, $\hat{\boldsymbol{d}}_1\ \hat{\boldsymbol{d}}_2\ \hat{\boldsymbol{d}}_3$, moving along the filament, as shown in Fig. 6.1(B). We denote the centerline of the filament as $\boldsymbol{R}(s)$ and the unit tangent vector to the centerline is denoted as $\widehat{\boldsymbol{T}} = \boldsymbol{R}'(s)$.

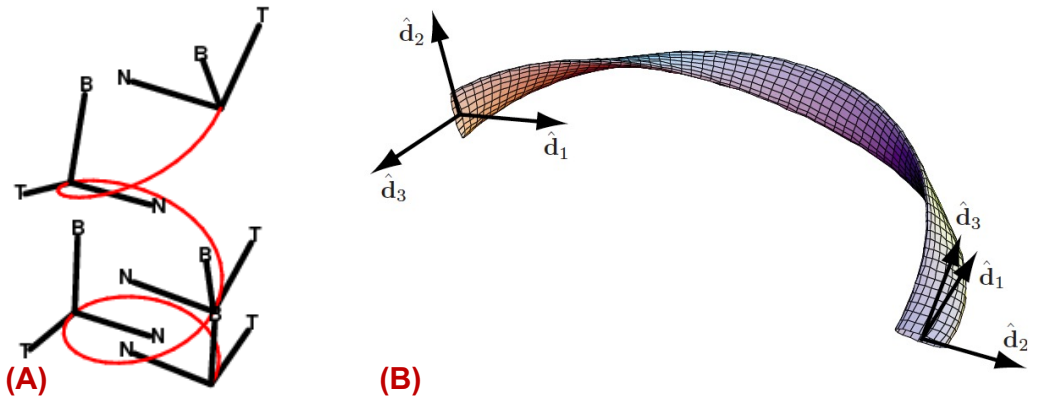

Fig. 6.1.: **(A)** The Frenet-Serret ($\widehat{T}\widehat{N}\widehat{B}$) frame moving along a helix. **(B)** Orientation of the fialment in orthonormal frame – $\hat{d}_1$, $\hat{d}_2$ and $\hat{d}_3$ is shown. The figure is reprinted with permission published by Ref. [11].

Without any loss of generality, we take $\hat{d}_3 = \widehat{T}$ and $\hat{d}_1$ is chosen arbitrarily in the cross-section perpendicular to the tangent vector, this determines the third axis $\hat{d}_2 = \hat{d}_3 \times \hat{d}_1$ – this is called the Darboux frame [1] (see Fig. 6.1(B)). The Darboux fram, $\hat{d}_a$ (a=1,2,3), for two nearby points differ by a small rotation and we write:

$$\hat{d'}_a = \mathbf{\Omega} \times \hat{d}_a \qquad (\text{a} = 1, 2, 3) \tag{6.9a}$$

where $\mathbf{\Omega} = \frac{d\phi}{dt}$ is the rotation rate of the Darboux frame. It is called the Darboux vector [1] and given as: $\mathbf{\Omega} = \Omega_1 \hat{d}_1 + \Omega_2 \hat{d}_2 + \Omega_3 \hat{d}_3$.

$$\Omega_1 = \hat{d'}_2 \cdot \hat{d}_3 \tag{6.9b}$$

Similarly, we write equations for Ω_2 and Ω_3.

Darboux vector, $\mathbf{\Omega}$, shows the rate at which the Darboux frame rotates when we follow the centerline with unit speed. Ω_1 and Ω_2 are the rotation rate of Darboux frame about $\hat{d}_1$ and $\hat{d}_2$ respectively – they are called material curvatures. Similarly, Ω_3 defines the rotation rate of the frame with respect to $\hat{d}_3$ – it is called the material twist of the filament. The components of $\mathbf{\Omega}$ – Ω_1,Ω_2,Ω_3 are shown in Fig. 6.2. Note that, Darboux frame is different from Frenet-Serret frame which is described in (6.7)eq:NhpBhp. Likewise, the material curvature (Ω_1, Ω_2) and twist (Ω_3) are different from κ and τ respectively.

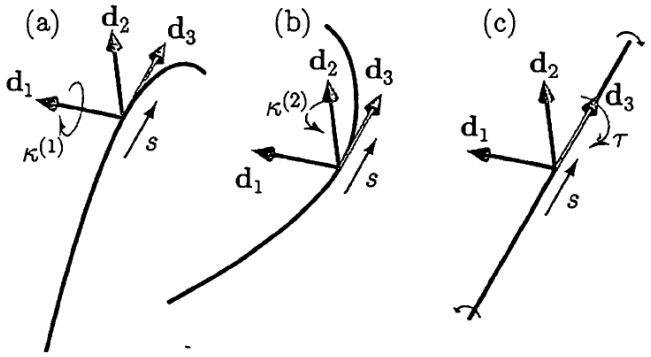

Fig. 6.2.: Three different type of deformation rate of a filament along the arc-length coordinate is shown. **(a)** Material curvature, Ω_1, which is the frame rotation rate about $\hat{\boldsymbol{d}}_1$. **(b)** Material curvature, Ω_2, – the frame rotation rate about $\hat{\boldsymbol{d}}_2$. **(c)** Twist of the filament, Ω_3 – the frame rotation rate about $\hat{\boldsymbol{d}}_3$. Figure adapted and re-printed with permission from [1]

Next, we describe relation between the Darboux frame and Frenet-Serret frame. Using (6.7), (6.8) and (6.9), we write:

$$\Omega_1^2(s) + \Omega_2^2(s) = \kappa^2(s). \tag{6.10}$$

The relation between twist Ω_3 and torsion, τ is:

$$\Omega_3 = \frac{d\theta}{dS} + \tau, \tag{6.11}$$

where θ is the angle between $\hat{\boldsymbol{d}}_2$ and $\widehat{\boldsymbol{N}}$ i.e.

$$\hat{\boldsymbol{d}}_2 \cdot \widehat{\boldsymbol{N}} = \cos(\theta) \tag{6.12}$$

6.2 Bending energy

Energy per unit length ($H(s)$) integrated over whole length gives the total elastic energy of the filament ($\mathcal{H}$). The $H(s)$, for an elastic filament has contributions due to bending i.e. Ω_1 and Ω_2 and twisting i.e. Ω_3 – For the current work, we ignore the twisting of the filament. The energy is a quadratic function of the deformation, i.e. a function of Ω_1, Ω_2[12, 1, 11, 13].

$$H(s) = \frac{YI_{11}}{2}\Omega_1^2(s) + \frac{YI_{22}}{2}\Omega_2^2(s) \tag{6.13a}$$

$$\mathcal{H}^{\text{Bend}} = \int_{s=0}^{L} H(s)\, ds \tag{6.13b}$$

where Y (unit: Pa = Kg m^{-1} s^{-2}) is the Young's modulus of the filament, $\mathcal{H}^{\text{Bend}}$ is the bending energy of the elastic filament and I_{11} and I_{22} are the second moment of inertia along the principal axes of inertia of the cross-section of the filament.

For a filament with circular cross-section, $I_{11} = I_{22} = I = \frac{\pi d^4}{64}$, where d is diameter of the filament. We define $B = YI$, as the bending rigidity of the filament, since this is the contribution due to bending of the filament. Equations (6.10) and (6.13) yields:

$$H(s) = \frac{YI}{2}\left(\Omega_1^2(s) + \Omega_2^2(s)\right) \quad = \quad \frac{B}{2}\kappa^2(s) \tag{6.14a}$$

$$\mathcal{H}^{\text{Bend}} = \frac{B}{2}\int_{s=0}^{L} \kappa^2(s) ds \tag{6.14b}$$

6.3 Euler-Bernouili equation

There are two ways to obtain an equilibrium configuration of the filament. First, we write the equation of force-balance and moment-balance on every element of the filament [12]. Second, we can use variational principle to minimize the Hamiltonian to get the equilibrium configuration of the filament [1]. We take the second approach.

Let us ignore the twist of the filament and concentrate only on the bending forces. Consider a macroscopic filament with force per unit length given as $\boldsymbol{q}(s)$. For the equilibrium configuration of the filament $\boldsymbol{R}(s)$ we write:

$$\boldsymbol{q}(s) = -\frac{\delta \mathcal{H}\left(\boldsymbol{R}''\right)}{\delta \boldsymbol{R}} = \frac{d^2}{ds^2}\left(\frac{\partial \mathcal{H}\left(\boldsymbol{R}''\right)}{\partial \boldsymbol{R}''}\right) = \frac{d^2}{ds^2}\left(-B\frac{d^2\boldsymbol{R}(s)}{ds^2}\right) = -B\frac{d^4\boldsymbol{R}(s)}{ds^4} \tag{6.15}$$

where $\frac{\delta(\cdot)}{\delta \boldsymbol{R}}$ denotes the functional derivative with respect to $\boldsymbol{R}$.

The total force on the filament is

$$\int_{s=0}^{L} \boldsymbol{q}(s) ds = \sum_{i\ \epsilon\ forces} \boldsymbol{F}_i = \boldsymbol{F} = F_1\hat{\boldsymbol{d}}_1 + F_2\hat{\boldsymbol{d}}_2 + F_3\hat{\boldsymbol{d}}_3 \tag{6.16}$$

where $\boldsymbol{F}$ is the summation over all the forces acting on the filament.

The force acting along the tangent can not bend a filament. So we do not write equations in that direction. We write down the equation in the other two direction by integrating both sides of equation 6.15:

$$-B\frac{d^3\boldsymbol{R}(s)}{ds^3}\cdot\hat{\boldsymbol{d}}_i = \boldsymbol{F}\cdot\hat{\boldsymbol{d}}_i \quad ; \quad \mathrm{i}=1,2 \tag{6.17a}$$

This can also be written as following:

$$B\frac{d\boldsymbol{R}(s)}{ds}\times\frac{d^3\boldsymbol{R}(s)}{ds^3} = \boldsymbol{F}\times\frac{d\boldsymbol{R}(s)}{ds} \tag{6.17b}$$

where $\hat{\boldsymbol{d}}_3 = \frac{d\boldsymbol{R}(s)}{ds}$. Equation 6.15 and 6.17b are the Euler-Bernoulli beam equation [14].

6.3.1 Boundary conditions on the filament

There are atleast three types of boundary conditions that are commonly used. Here we show boundary conditions at one end with $s = 0$.

- **Clamped**: The filament can not move either longitudinally or transversely i.e. the direction of the filament at the point can not change.

$$\boldsymbol{R}(s=0) = \boldsymbol{R}_0 \qquad \frac{d\boldsymbol{R}(s=0)}{ds} = \widehat{\boldsymbol{N}}_0 \tag{6.18}$$

- **Hinged**: The filament can not move, but its direction can vary

$$\boldsymbol{R}(s=0) = \boldsymbol{R}_0; \qquad \frac{d^2\boldsymbol{R}(s=0)}{ds^2} = 0 \tag{6.19}$$

- **Free end**: For this case, the force and moment at the point is zero.

$$\frac{d^2\boldsymbol{R}(s=0)}{ds^2} = 0 \qquad \frac{d^3\boldsymbol{R}(s=0)}{ds^3} = 0 \tag{6.20}$$

References

[1] Basile Audoly and Yves Pomeau. “Elasticity and geometry”. In: *Peyresq Lectures On Nonlinear Phenomena*. World Scientific, 2000, pp. 1–35.

[2] Eric Lauga and Thomas R Powers. “The hydrodynamics of swimming microorganisms”. In: *Reports on Progress in Physics* 72.9 (2009), p. 096601.

[3] M K. Jawed, NG Hadjiconstantinou, DM Parks, and Pedro M Reis. “Patterns of carbon nanotubes by flow-directed deposition on substrates with architectured topographies”. In: *Nano letters* 18.3 (2018), pp. 1660–1667.

[4] Louis Saalschütz. *Vorlesungen über die Bernoullischen Zahlen: ihren Zusammenhang mit den Secanten-Coefficienten und ihre wichtigeren Anwendungen*. Springer, 1893.

[5] S Timoshenko. “History of strength of materials McGraw-Hill book company”. In: *Inc., New York/Toronto/London* (1953).

[6] William R Bauer, Russell A Lund, and James H White. “Twist and writhe of a DNA loop containing intrinsic bends.” In: *Proceedings of the National Academy of Sciences* 90.3 (1993), pp. 833–837.

[7] PG De Gennes. “Coil-stretch transition of dilute flexible polymers under ultrahigh velocity gradients”. In: *The Journal of Chemical Physics* 60.12 (1974), pp. 5030–5042.

[8] Stephen J Kron and James A Spudich. “Fluorescent actin filaments move on myosin fixed to a glass surface.” In: *Proceedings of the National Academy of Sciences* 83.17 (1986), pp. 6272–6276.

[9] Ehssan Nazockdast, Abtin Rahimian, Denis Zorin, and Michael Shelley. “A fast platform for simulating semi-flexible fiber suspensions applied to cell mechanics”. In: *Journal of Computational Physics* 329 (2017), pp. 173–209.

[10] Hugh C Crenshaw and Leah Edelstein-Keshet. “Orientation by helical motion—II. Changing the direction of the axis of motion”. In: *Bulletin of mathematical biology* 55.1 (1993), pp. 213–230.

[11] Thomas R Powers. “Dynamics of filaments and membranes in a viscous fluid”. In: *Reviews of Modern Physics* 82.2 (2010), p. 1607.

[12] LD Landau and EM Lifshitz. “Theory of Elasticity,(Pergamon Press, Oxford, 1986)”. In: ().

[13] Stuart S Antman. “Nonlinear plasticity”. In: *Nonlinear Problems of Elasticity*. Springer, 1995, pp. 603–628.

[14] JM Gere and SP Timoshenko. “Mechanics of materials, 1997”. In: *PWS-KENT Publishing Company, ISBN 0* 534.92174 (1997), p. 4.

7

STOKES FLOW

> *Imagine that a man swimming at same Reynolds number as his own sperm. Well, you put him in a swimming pool full that is full of molasses, and then you forbid him to move any part of his body faster than* 1 *cm/min. If under these condition, you are able to move more than a few meters per week, you can qualify as low Reynolds number swimmer – and that exactly is harsh life of bacteria.*
>
> **— E.M.Purcell**
> life at low Reynolds number, 1973

Low Reynolds number flows are ubiquitous in nature ranging from the world of tiny organisms such as bacteria to the movement of glaciers. Reynolds number – the ratio of inertial to viscous forces – is used to predict the transition from laminar flow to turbulent flow [1]. For example, a swimming bacteria corresponds to a Reynolds number of about 10^{-5} – a laminar regime. Whereas a flying bird has a Reynolds number of about 10^{4} – a turbulent regime, see fig 7.1. At Re $\ll 1$, the inertial and nonlinear terms of the Navier–Stokes equation can be ignored. Such flows are called Stokes flows. Many biophysical phenomena are well described by the Stokes flows e.g. swimming of unicellular organism such as Chlamydomonas to multicellular organisms Volvox [2], human blood circulation system in capillary [3], beating of flagella [4, 5] etc. Furthermore the subject of microfluidics almost entirely (except inertial microfluidics [6]) is in Stokesian regime. In this regime, the flows obey linear equations and they are also time-reversible [7] due to absence of nonlinearities. Consequently, such flows are non-mixing. For example, if the fluid is sheared by its boundary motion that is subsequently reversed, then all the fluid elements return to their initial positions. Hence, mixing in micro-channels happens solely due to molecular diffusion and is very slow [8, 9].

7.1 Fundamental equations

Motion of an incompressible Newtonian fluid is given by Navier-Stokes equation [10, 11, 12]:

$$\partial_t \boldsymbol{v} + \boldsymbol{v} \cdot \boldsymbol{\nabla} \boldsymbol{v} = -\frac{\boldsymbol{\nabla} p}{\rho} + \frac{\eta}{\rho} \nabla^2 \boldsymbol{v} + \boldsymbol{f}_{\text{ex}}, \tag{7.1a}$$

$$\boldsymbol{\nabla} \cdot \boldsymbol{v} = 0. \tag{7.1b}$$

Here ρ is constant density of the fluid, $\boldsymbol{v}$ is the velocity, p is the pressure, η is the dynamic viscosity and $\boldsymbol{f}_{\text{ex}}$ is the external force e.g. gravity, electro-magnetic forces etc. (7.1a) is the equation for momentum conservation and 7.1b is the continuity equation. We take curl of (7.1a) and write down the vorticity equation:

$$\partial_t \boldsymbol{\varpi} + \boldsymbol{\nabla} \times (\boldsymbol{\varpi} \times \boldsymbol{v}) = \frac{\eta}{\rho} \nabla^2 \boldsymbol{\varpi} + \boldsymbol{\nabla} \times \boldsymbol{f}_{\text{ex}}, \tag{7.2}$$

where $\boldsymbol{\varpi} \equiv \boldsymbol{\nabla} \times \boldsymbol{v}$, is vorticity of the fluid. Let us introduce the dimensionless variables:

$$x = \tilde{x} L, \quad \boldsymbol{v} = U \tilde{\boldsymbol{v}}, \quad t = T \tilde{t}, \quad \partial_t = \frac{1}{T} \tilde{\partial}_{\tilde{t}}, \quad \boldsymbol{\nabla} = \frac{1}{L} \widetilde{\boldsymbol{\nabla}}, \quad \boldsymbol{f}_{\text{ex}} = F \tilde{\boldsymbol{f}}_{\text{ex}} \tag{7.3}$$

Here L is a length scale, U is a reference velocity scale, and T is a time scale, $\tilde{(\cdot)}$ denotes the dimensionless variables. We write (7.2) in non-dimensional form [13]:

$$\frac{1}{\text{St}} \tilde{\partial}_{\tilde{t}} \widetilde{\boldsymbol{\varpi}} + \widetilde{\boldsymbol{\nabla}} \times (\widetilde{\boldsymbol{\varpi}} \times \tilde{\boldsymbol{v}}) = \frac{1}{\text{Re}} \widetilde{\nabla}^2 \widetilde{\boldsymbol{\varpi}} + F \widetilde{\boldsymbol{\nabla}} \times \tilde{\boldsymbol{f}}_{\text{ex}}, \tag{7.4a}$$

$$\widetilde{\boldsymbol{\nabla}} \cdot \tilde{\boldsymbol{v}} = 0. \tag{7.4b}$$

We get two dimensionless number

$$\text{Re} = \text{Reynolds number} = \frac{UL\rho}{\eta}, \qquad \text{St} = \text{Stokes Number} = \frac{UT}{L} \tag{7.5}$$

Reynolds number is the ratio between typical inertial and viscous forces, and Stokes number characterizes the time scale of particles or any foreign body in the flow.

Let us assume that there is no external force or time-scale in the system. Then $T \sim L/U$ or $\text{St} \sim 1$. In that case, dynamics of the fluid flow is determined by only one dimensionless number, Re [13]. We visually represent the importance of Re in Fig. 7.1. Realm of microfluidics generally deals with the flows with very small characteristic length scale, L, i.e. $\text{Re} \ll 1$. We rewrite (7.4a):

$$\text{Re} \left[\tilde{\partial}_{\tilde{t}} \widetilde{\boldsymbol{\varpi}} + \widetilde{\boldsymbol{\nabla}} \times (\widetilde{\boldsymbol{\varpi}} \times \tilde{\boldsymbol{v}}) \right] = \widetilde{\nabla}^2 \widetilde{\boldsymbol{\varpi}} \tag{7.6}$$

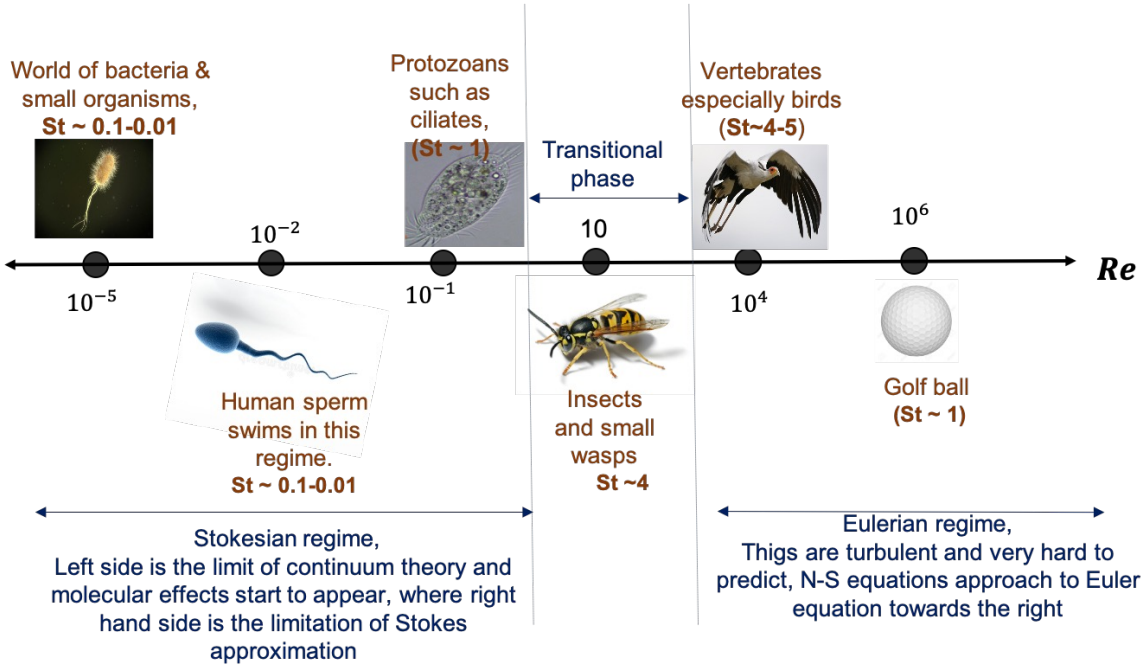

Fig. 7.1.: Reynolds and Stokes number of various examples of swimming and flying. Stokesian and turbulent regime are loosely defined based on Reynolds number. (fig not to scale)

We take the limit Re $\rightarrow 0$ to get:

$$\widetilde{\nabla}^2\widetilde{\boldsymbol{\varpi}} = \mathbf{0} \tag{7.7a}$$

$$\Rightarrow \widetilde{\nabla}^2\tilde{\boldsymbol{v}} = \widetilde{\boldsymbol{\nabla}}\phi \tag{7.7b}$$

Comparing (7.1a) and (7.7b), we note that the scalar function ϕ is proportional to p/η. Hence we write the Stokes equations in dimensional form [13]:

$$\eta\nabla^2\boldsymbol{v} = \boldsymbol{\nabla}p \qquad \boldsymbol{\nabla}\cdot\boldsymbol{v} = 0 \tag{7.8}$$

The Stokes equations are simpler than the Navier Stokes equation as they do not contain nonlinear terms. The equation has two very important features: 1) linearity 2) time independence. These two features are what defines the Stokesian realm. Due to its linearity, Stokes equation has a unique solution for given boundary conditions [14]. Since there is no time-dependent term as well, the dynamics of the flow is completely determined by the boundary condition specified at that instant i.e. the flow instantly adapts to any change in the boundary condition.

7.2 One sphere in Stokes flow

In this section, first we develop the expression for flow disturbances due to a fixed sphere in an ambient flow, $\boldsymbol{v}_\infty(\boldsymbol{X})$ [15]. Second, we calculate the forces and torques required to keep the sphere fixed. Third, we calculate the flow disturbances due to an external force, torque and stresslet in a quiescent flow.

Let us assume the ambient flow, $\boldsymbol{v}_\infty(\boldsymbol{X})$, to be a linear function of space. Then

$$v_\infty^\alpha(\boldsymbol{X}) = v_\infty^\alpha + (\Omega_\infty^{\alpha\beta} + E_\infty^{\alpha\beta})X^\beta \tag{7.9}$$

Where $\Omega_\infty^{\alpha\beta}$ and $E_\infty^{\alpha\beta}$ represent rate of rotation and rate of strain of the ambient flow respectively [15]. Einstein summation is implied. Since the Stokes equations are linear, flow disturbances due to the presence of fixed sphere in the ambient flow are sum of flow disturbances due to the presence of fixed sphere in an ambient flow with translational velocity, rotation, and strain individually. The velocity at any Eulerian point $\boldsymbol{X}$, $\boldsymbol{V}_{\text{act}}(\boldsymbol{X})$, is the sum of flow disturbances and ambient flow.

$$\boldsymbol{V}_{\text{act}}(\boldsymbol{X}) = \boldsymbol{V}(\boldsymbol{X}) + \boldsymbol{v}_\infty(\boldsymbol{X}), \tag{7.10}$$

where $\boldsymbol{V}(\boldsymbol{X})$ are the flow disturbances due to the fixed sphere which also satisfies the Stokes equations with the following boundary conditions [15]:

$$V^\alpha\left(X = |\boldsymbol{X}| = \frac{d}{2}\right) = -v_\infty^\alpha - \epsilon^{\alpha\beta\gamma}\omega_\infty^\beta X^\gamma - E_\infty^{\alpha\beta}X^\beta \tag{7.11a}$$

$$\boldsymbol{V}\left(X = |\boldsymbol{X}| \to \infty\right) = \boldsymbol{0} \tag{7.11b}$$

$$p\left(X = |\boldsymbol{X}| \to \infty\right) = 0. \tag{7.11c}$$

Here $\omega_\infty^\alpha = -\left(1/2\right)\epsilon^{\alpha\beta\gamma}\Omega^{\beta\gamma}$, d is the diameter of the sphere and $\epsilon^{\alpha\beta\gamma}$ is Levi-Civita symbol [16]. The first, second and third term in the right hand side (RHS) of the (7.11a) are the contributions from translation, rotation and straining motion respectively. The solution is (see chapter 2 of [15], chapter 2,3 of [14] for the complete derivation):

$$\begin{aligned} V^\alpha(\boldsymbol{X}) = &-\frac{3d}{8}v_\infty^\beta\left(1 + \frac{d^2}{24}\nabla^2\right)\mathcal{G}^{\alpha\beta}(\boldsymbol{X}) - \frac{d^3}{8X^3}\epsilon^{\alpha\beta\gamma}\omega_\infty^\beta X^\gamma \\ &+ \frac{5d^3}{48}\left(E_\infty^{\beta\gamma}\partial^\gamma\right)\left(1 + \frac{d^2}{24}\nabla^2\right)\mathcal{G}^{\alpha\beta}(\boldsymbol{X}) \end{aligned} \tag{7.12a}$$

$$p(\boldsymbol{X}) = -\frac{3\eta d}{2}\frac{v_\infty^\alpha X^\alpha}{X^3} + 0 - \frac{5\eta d^3}{8}\frac{X^\alpha E_\infty^{\alpha\beta}X^\gamma}{X^5} \tag{7.12b}$$

where $\mathcal{G}^{\alpha\beta}(\boldsymbol{X})$ is the Green's function (also known as Stokeslet):

$$\mathcal{G}^{\alpha\beta} = \frac{\delta^{\alpha\beta}}{X} + \frac{X^{\alpha}X^{\beta}}{X^3}. \tag{7.13}$$

Note that, the second term in the RHS of the (7.12b) is 0, to show that there is no pressure disturbance in the flow due to the rotation of the sphere. We compute the hydrodynamic force,F_{h}, on the sphere:

$$F_{\mathrm{h}}^{\alpha} = \iint_{S_{\mathrm{p}}} \sigma^{\alpha\beta}\hat{N}^{\beta} dS_{\mathrm{p}}, \tag{7.14}$$

where

$$\sigma^{\alpha\beta} \equiv -p\delta^{\alpha\beta} + \eta\left(\partial^{\alpha}V^{\beta} + \partial^{\beta}V^{\alpha}\right), \tag{7.15}$$

is the stress on the sphere due to the flow, S_{p} denote the surface of the sphere and $\widehat{\boldsymbol{N}}$ is the unit normal in the outward direction of the surface S_{p}. Only the translational part of the velocity disturbance (first term in the RHS of the (7.12)) contributes to the force on the sphere. An equal and opposite force, $\boldsymbol{F}$, is required to hold the sphere fixed i.e. $\boldsymbol{F} = -\boldsymbol{F}_{\mathrm{h}}$.

$$\boldsymbol{F} = -\boldsymbol{F}_{\mathrm{h}} = -3\pi\eta d\boldsymbol{v}_{\infty} \tag{7.16}$$

The rotation and the straining term (second and third term in RHS of the (7.12)) contributes to the first moment of force distribution which is:

$$\iint_{S} \sigma^{\alpha\gamma}X^{\beta}\hat{N}^{\gamma} dS_{\mathrm{p}} = \mathcal{A}^{\alpha\beta} + \mathcal{S}^{\alpha\beta}. \tag{7.17}$$

Here $\mathcal{A}^{\alpha\beta}$ and $\mathcal{S}^{\alpha\beta}$ are the antisymmetric and symmetric part of the first moment respectively [15]:

$$\begin{aligned} \mathcal{A}^{\alpha\beta} &= \frac{1}{2}\iint_{S}\left[\sigma^{\alpha\gamma}X^{\beta} - \sigma^{\beta\gamma}X^{\alpha}\right]\hat{N}^{\gamma} dS_{\mathrm{p}} = -\frac{1}{2}\epsilon^{\alpha\beta\gamma}T_{\mathrm{h}}^{\gamma} \\ \mathcal{S}^{\alpha\beta} &= \frac{1}{2}\iint_{S}\left[\sigma^{\alpha\gamma}X^{\beta} + \sigma^{\beta\gamma}X^{\alpha}\right]\hat{N}^{\gamma} dS_{\mathrm{p}}, \end{aligned} \tag{7.18}$$

where $\boldsymbol{T}_{\mathrm{h}}$ is the hydrodynamic torque on the sphere. If $\boldsymbol{T}$ is an external torque to hold the sphere fixed, then $\boldsymbol{T} = -\boldsymbol{T}_{\mathrm{h}}$. By substituting equation 7.12a, 7.15 in (7.18), we get:

$$\begin{aligned} \boldsymbol{T} = -\boldsymbol{T}_{\mathrm{h}} &= -\pi\eta d^3\boldsymbol{\omega} \\ \mathcal{S}^{\alpha\beta} &= \frac{5}{6}\pi\eta d^3 E_{\infty}^{\alpha\beta}. \end{aligned} \tag{7.19}$$

It is useful to express (7.12a) in terms of $F^\beta, T^\beta, \mathcal{S}^{\alpha\beta}$:

$$V^\alpha(\boldsymbol{X}) = F^\beta \left(1 + \frac{d^2}{24}\nabla^2\right) \frac{\mathcal{G}^{\alpha\beta}(\boldsymbol{X})}{8\pi\eta} + \frac{1}{8\pi\eta X^3}\epsilon^{\alpha\beta\gamma} T^\beta X^\gamma + \mathcal{S}^{\beta\gamma}\partial^\gamma \left(1 + \frac{d^2}{24}\nabla^2\right) \frac{\mathcal{G}^{\alpha\beta}(\boldsymbol{X})}{8\pi\eta} \quad (7.20)$$

Now, if we imagine an inertia-less sphere in a quiescent fluid with external force $\boldsymbol{F}$, external torque $\boldsymbol{T}$, and stresslet $\mathcal{S}^{\alpha\beta}$ such that the motion of the sphere still follows the assumption of the Stokes flow. The fluid flow due to the external $\boldsymbol{F}$,$\boldsymbol{T}$ and $\mathcal{S}^{\alpha\beta}$ on the sphere, is given by (7.20) [15].

7.2.1 A sphere in shear flow:

We consider a freely suspended sphere (i.e. the sphere is not under influence of any external force or torque) in shear flow, $\boldsymbol{v}_\infty = (Sy, 0, 0)$. We wish to determine the flow disturbances due to the sphere. For the shear flow, we write:

$$E^{\alpha\beta}_\infty = \begin{bmatrix} 0 & S/2 & 0 \\ S/2 & 0 & 0 \\ 0 & 0 & 0 \end{bmatrix}, \qquad \Omega^{\alpha\beta} = \begin{bmatrix} 0 & S/2 & 0 \\ -S/2 & 0 & 0 \\ 0 & 0 & 0 \end{bmatrix} \quad (7.21)$$

Without any loss of generality, we take the origin of shear flow at the center of the sphere. Hence, the sphere does not have any translational motion. However, the shear flow causes the sphere to rotate with an angular velocity, $\boldsymbol{\omega}$. The Stokes equations (7.8) does not contain inertia. In addition, let us assume that the sphere also does not have any inertia. Then the sphere rotates with the angular velocity of the fluid i.e. $\boldsymbol{\omega} = \boldsymbol{\omega}_\infty = -(1/2)\epsilon^{\alpha\beta\gamma}\Omega^{\beta\gamma}$. Hence, there will not be any disturbances in the flow due to the $\Omega^{\alpha\beta}_\infty$ as there is no relative angular velocity between the fluid and the sphere. Note that, by the same logic, even if the sphere is not at the origin, there are no disturbances in the flow due to translation.

The symmetric part, $E^{\alpha\beta}_\infty$, exerts no net force or torque on the sphere due to its symmetry. The flow disturbance due to $E^{\alpha\beta}_\infty$ ((7.12a)) is :

$$V^\alpha(\boldsymbol{X}) = \frac{5d^3}{48}\left(E^{\beta\gamma}_\infty \partial^\gamma\right)\left(1 + \frac{d^2}{24}\nabla^2\right)\mathcal{G}^{\alpha\beta}(\boldsymbol{X}) \quad (7.22)$$

7.3 Faxén's law

So far, we have assumed the ambient flow to be linear. If the ambient flow is not linear, there is an additional term in the expression for $\boldsymbol{F}$, $\boldsymbol{T}$ and $\mathcal{S}^{\alpha\beta}$, known as Faxén's law [17, 15, 14, 18]:

$$\boldsymbol{F} = 3\pi\eta d\left[\left(1+\frac{d^2}{24}\nabla^2\right)\boldsymbol{v}_\infty(\boldsymbol{X}=\boldsymbol{0}) - \boldsymbol{U}\right], \tag{7.23a}$$

$$\boldsymbol{T} = \pi\eta d^3\left[\boldsymbol{\omega}_\infty(\boldsymbol{X}=\boldsymbol{0}) - \boldsymbol{W}\right], \tag{7.23b}$$

$$\mathcal{S}^{\alpha\beta} = \frac{5}{6}\pi\eta d^3\left(1+\frac{d^2}{40}\right)E^{\alpha\beta}_\infty. \tag{7.23c}$$

Here $\boldsymbol{U}$ and $\boldsymbol{W}$ are the velocities and angular velocity of the sphere respectively and we take the center of the sphere to be at the origin.

7.4 Stokesian dynamics

Particles suspended in Stokes flow effect each other's motion through hydrodynamic interaction. In this section, we discuss the basics of Stokesian dynamics – a perturbative approach to compute hydrodynamic interaction between N spherical particles. The method treats the suspended particles in a discrete sense while the continuum approximation remains valid for the surrounding fluid. Stokesian dynamic approach is broadly divided in two types of problems. First, if the velocity and angular velocity of N spherical particles are specified, what is the total force, torque and stresslet on each particle – this is known as the resistance problem. Second, what is the velocity and angular velocity of N spherical particles, if forces, torques and stresslets are specified – known as mobility problem. Here, we give a short overview of only mobility problems.

7.4.1 *N* spheres in quiescent fluid

Consider N spheres each subject to an external force, $\boldsymbol{F}_i$, where i goes from 0 to N. We do not consider any external torque or external stresslet on the sphere. We

assume that the motion of spheres follows the assumption of the Stokes flow. We exploit the linearity of Stokes equations to write [14, 19]:

$$U_i^\alpha = \sum_{i=0}^{i=N} \mathcal{M}_{ij}^{\alpha\beta} F_j^\beta, \tag{7.24}$$

or in the matrix form,

$$\begin{bmatrix} U_1^\alpha \\ U_2^\alpha \\ \vdots \\ U_N^\alpha \end{bmatrix} = \begin{bmatrix} \mathcal{M}_{11}^{\alpha\beta} & \mathcal{M}_{12}^{\alpha\beta} & \ddots & \mathcal{M}_{1N}^{\alpha\beta} \\ \mathcal{M}_{21}^{\alpha\beta} & \mathcal{M}_{22}^{\alpha\beta} & \ddots & \\ \vdots & \vdots & & \vdots \\ \mathcal{M}_{N1}^{\alpha\beta} & \mathcal{M}_{N2}^{\alpha\beta} & \ddots & \mathcal{M}_{NN}^{\alpha\beta} \end{bmatrix} \begin{bmatrix} F_1^\beta \\ F_2^\beta \\ \vdots \\ F_N^\beta \end{bmatrix}. \tag{7.25}$$

Here $\boldsymbol{U}_i$ is the velocity of the i^{th} sphere, $\mathcal{M}^{\alpha\beta}$ is the mobility tensor. The Greek indices run over coordinates and the Latin indices run over the number of spheres.

No closed-form solution to the Stokes equations (7.8) with boundary conditions:

$$\int\int_{S_i} \sigma^{\alpha\beta}(\boldsymbol{X}_i)\hat{N}^\beta dS_i = F_i^\alpha \quad \text{for} \quad \boldsymbol{X} \in S_i, i = 1, \ldots N \quad , \tag{7.26a}$$

$$\boldsymbol{V}(\boldsymbol{X}_i \to \infty) = 0 \quad , \tag{7.26b}$$

$$p(\boldsymbol{X}_i \to \infty) = 0 \quad , \tag{7.26c}$$

is known for $N \geq 2$. So we find the solution by perturbative methods. The perturbation series for $\boldsymbol{U}_i$, is expanded in the powers of (d/X_{ij}), where d is diameter of the spheres, $X_{ij} = |\boldsymbol{X}_{ij}| = |\boldsymbol{X}_i - \boldsymbol{X}_j|$, and j goes from 0 to N.

Let us start with $N = 2$. We assume that the spheres are very far from each other $(d/X) \to 0$, and write the velocity of the spheres using (7.16) – this is the zeroth order approximation to the problem. The flow field at any Eulerian point is the sum of flow disturbances due to both spheres i.e. at the lowest order, we neglect the hydrodynamic interaction between them. Next, we consider that the ambient flow around the second sphere consists of flow disturbances (velocity field and stresslet) produced by the first sphere and vice-versa – this generates a correction to the earlier solution, and is the first order approximation to the problem. Similarly, we get the higher order terms in the series – this method is known as method of reflection [20, 19]. We write the final velocity $\boldsymbol{U}_i$ as:

$$\boldsymbol{U}_i = \boldsymbol{U}_i^{(0)} + \boldsymbol{U}_i^{(1)} + \ldots, \tag{7.27}$$

where the superscript (m) denotes the m^{th} order approximation.

Zeroth order approximation:

We take $N = 2$. As described earlier, for zeroth order approximation we take $(d/X_{ij}) \to 0$ i.e. we write the velocity of the sphere using (7.16):

$$\boldsymbol{U}_i^{(0)} = \frac{\boldsymbol{F}_i}{3\pi\eta d} \tag{7.28}$$

and the mobility matrix consists of only diagonal terms:

$$\mathcal{M}^{\alpha\beta} = \begin{bmatrix} \frac{1}{3\pi\eta d}\delta^{\alpha\beta} & 0 \\ 0 & \frac{1}{3\pi\eta d}\delta^{\alpha\beta} \end{bmatrix} \tag{7.29}$$

We use (7.20) (only the force part, as torque and stresslet is zero) to write the velocity field at any Eulerian point $\boldsymbol{X}$:

$$V^{(0),\alpha}(\boldsymbol{X}) = \sum_{i=1}^{2} V_i^{(0),\alpha} = \sum_{i=1}^{2} F_i^{\beta} \left(1 + \frac{d^2}{24}\nabla^2\right) \frac{\mathcal{G}^{\alpha\beta}(\boldsymbol{X} - \boldsymbol{X}_i)}{8\pi\eta}, \tag{7.30}$$

where $\boldsymbol{V}_i^{(0)}$ is the flow disturbance due to i^{th} sphere.

First order approximation:

We notice that, the zeroth order velocity on each sphere $\boldsymbol{U}_i^{(0)}$, produce exactly the prescribed forces $\boldsymbol{F}_i$. So the next correction in the velocity $\boldsymbol{U}_i$ should be such that, they do not produce any additional forces on the sphere. As described earlier, the flow field generated by the second sphere acts as an ambient flow around the first sphere. We use Faxèn's law ((7.23a)) to write:

$$\begin{aligned} U_1^{(1),\alpha} &= \left(1 + \frac{d^2}{24}\nabla^2\right) V_2^{(0),\alpha}(\boldsymbol{X}_1) \\ &= \frac{3d}{8}\boldsymbol{U}_2^{(0),\beta} \left(1 + \frac{d^2}{12}\nabla^2 + \frac{d^4}{496}\nabla^4\right) \mathcal{G}^{\alpha\beta}(\boldsymbol{X}_1 - \boldsymbol{X}_2) \end{aligned} \tag{7.31a}$$

$$\mathcal{S}_1^{(1),\alpha\beta} = \frac{5}{6}\pi\eta d^3 \left(1 + \frac{d^2}{40}\nabla^2\right) E_2^{(0),\alpha\beta}(\boldsymbol{X} = \boldsymbol{X}_1). \tag{7.31b}$$

Here $E_i^{\alpha\beta} = (1/2)[\partial^\alpha V_i^\beta + \partial^\beta V_i^\alpha]$. Similarly, the expression for $\boldsymbol{U}_2$ and $\mathcal{S}_2^{\alpha\beta}$ is also written.

The final velocity of i^{th} sphere $\boldsymbol{U}_i$ is the sum of zeroth order and first order velocities. We write the final mobility matrix for N spheres:

$$\mathcal{M}_{ij}^{\alpha\beta}(\boldsymbol{X}_{ij}) = \left\{ \begin{array}{ll} \frac{1}{8\pi\eta X_{ij}}\left[\delta^{\alpha\beta} + \frac{X_{ij}^{\alpha}X_{ij}^{\beta}}{X_{ij}^2} + \frac{d^2}{2X_{ij}^2}\left(\frac{\delta^{\alpha\beta}}{3} - \frac{X_{ij}^{\alpha}X_{ij}^{\beta}}{X_{ij}^2}\right) + O\left(\frac{d^4}{X_{ij}^4}\right)\right] & , i \neq j \\ \frac{1}{3\pi\eta d}\delta^{\alpha\beta} & , i = j \end{array} \right\}. \tag{7.32}$$

Here $i, j = \{0, 1, \ldots, N\}$, and $X_{ij} = |\boldsymbol{X}_{ij}| = |\boldsymbol{X}_i - \boldsymbol{X}_j|$. (7.32) is known as Rotne-Pragor tensor [21, 22]. The velocity field at an Eulerian point $\boldsymbol{X}$, upto first order approximation is:

$$\begin{aligned} V^{\alpha}(\boldsymbol{X}) = \sum_{i=1}^{N}\Bigg[F_i^{\beta}\left(1 + \frac{d^2}{24}\nabla^2\right)\frac{\mathcal{G}^{\alpha\beta}(\boldsymbol{X} - \boldsymbol{X}_i)}{8\pi\eta} \\ + \frac{5}{6}\pi d^3 E_i^{(0),\beta\gamma}\partial^{\gamma}\left(1 + \frac{d^2}{40}\nabla^2\right)\frac{\mathcal{G}^{\alpha\beta}(\boldsymbol{X} - \boldsymbol{X}_i)}{8\pi\eta}\Bigg] \end{aligned} \tag{7.33a}$$

$$\implies V^{\alpha}(\boldsymbol{X}) = \frac{1}{8\pi\eta X}\left[\delta^{\alpha\beta} + \frac{X^{\alpha}X^{\beta}}{X^2} + \frac{d^2}{4X^2}\left(\frac{\delta^{\alpha\beta}}{3} - \frac{X^{\alpha}X^{\beta}}{R^2}\right) + O\left(\left(\frac{d}{X}\right)^3\right)\right] \tag{7.33b}$$

Note that, the first order correction to the sphere velocity, $\boldsymbol{U}_i^{(1)}$ does not have any contribution to the flow disturbance in the ambient flow, as they do not produce any net force. Though $\mathcal{S}_1^{(1),\alpha\beta}, \mathcal{S}_2^{(1),\alpha\beta}$ has contributions to (7.33) but these terms drops faster than $O(d^4/X_{ij}^4)$.

7.4.2 *N* spheres in shear flow

Let us now consider N spheres in shear flow, $\boldsymbol{v}_{\infty}$:

$$\boldsymbol{v}_{\infty} = (Sy, 0, 0) \tag{7.34}$$

with force $\boldsymbol{F}_i$ on i^{th} particle, where $i = \{0.N\}$, and S is the shear rate. The shear flow imposes velocity, angular velocity and stresslet on all the spheres as described in section 7.2.1. There is no external torque on any sphere, so there is no flow disturbance due to the angular motion of the spheres as there is no relative angular velocity between ambient fluid and the sphere. We write the velocity of the spheres, $\boldsymbol{U}_i$ and stresslet around it, $\mathcal{S}_i^{\alpha\beta}$ as:

$$U_i^{\alpha} = v_{\infty}^{\alpha}(\boldsymbol{X}_i) + \sum_{j=0}^{i=N}\left(\mathcal{M}_{ij}^{\alpha\beta}F_j^{\beta} + \mathcal{N}_{ij}^{\alpha\beta\gamma}E_{\infty}^{\beta\gamma}(\boldsymbol{X}_j)\right) \tag{7.35}$$

We use the same technique as described in section 7.4.1.

Zeroth order interaction:

For simplicity, we first consider $N = 2$. Velocity and stresslets at the zeroth order approximation are:

$$\begin{aligned} U_i^{(0),\alpha} &= v_\infty^\alpha(\boldsymbol{X}_i) + \frac{\boldsymbol{F}_i}{3\pi\eta d} \\ \mathcal{S}_i^{(0),\alpha\beta} &= \frac{5}{6}\pi\eta d^3 E_\infty^{\alpha\beta}(\boldsymbol{X}_i) \end{aligned} \tag{7.36}$$

In the case of shear flow, the velocity field, $\boldsymbol{V}^{(0)}(\boldsymbol{X})$ at the zeroth order approximation has an additional term than the quiescent fluid ((7.30)) due to the presence of $\mathcal{S}^{(0),\alpha\beta}$:

$$V^{(0),\alpha}(\boldsymbol{X}) = \sum_{i=1}^{2}\left[F_i^\beta\left(1+\frac{d^2}{24}\nabla^2\right) + \frac{5}{6}\pi d^3 E_i^{\beta\gamma}\partial^\gamma\left(1+\frac{d^2}{40}\nabla^2\right)\right]\frac{\mathcal{G}^{\alpha\beta}(\boldsymbol{X}-\boldsymbol{X}_i)}{8\pi\eta} \tag{7.37}$$

First order interaction:

$$\begin{aligned} \boldsymbol{U}_1^{(1),\alpha} &= \left(1+\frac{d^2}{24}\nabla^2\right)V_2^{(0),\alpha}(\boldsymbol{X}_1) \\ \mathcal{S}_1^{(1),\alpha\beta} &= \frac{5}{6}\pi\eta d^3\left(1+\frac{d^2}{40}\nabla^2\right)E_2^{\alpha\beta}(\boldsymbol{X}_1) \end{aligned} \tag{7.38}$$

Similarly, we write expressions for the other sphere i.e. $\boldsymbol{U}_2^{(1),\alpha}$ and $\mathcal{S}_2^{(1),\alpha\beta}$. Upto, the first order approximation, the expression for $\mathcal{M}^{\alpha\beta}$ remains same as in quiescent fluid ((7.32)). $\mathcal{N}^{\alpha\beta\gamma}$ is:

$$\mathcal{N}_{ij}^{\alpha\beta\gamma}(\boldsymbol{X}_{ij}) = \left\{\begin{array}{ll} -\frac{5d^3}{16}\frac{X_{ij}^\alpha X_{ij}^\beta X_{ij}^\gamma}{X_{ij}^5} - \frac{d^5}{64}\left[\frac{\delta^{\alpha\beta}X_{ij}^\gamma+\delta^{\alpha\gamma}X_{ij}^\beta}{X_{ij}^5} - \frac{5X_{ij}^\alpha X_{ij}^\beta X_{ij}^\gamma}{X_{ij}^7}\right] & , i \neq j \\ 0 & , i = j \end{array}\right\}. \tag{7.39}$$

Here $i, j = \{0, 1.N\}$ The leading order term in $\mathcal{N}_{ij}^{\alpha\beta\gamma}$ drops as $O(d^3/X_{ij}^2)$.

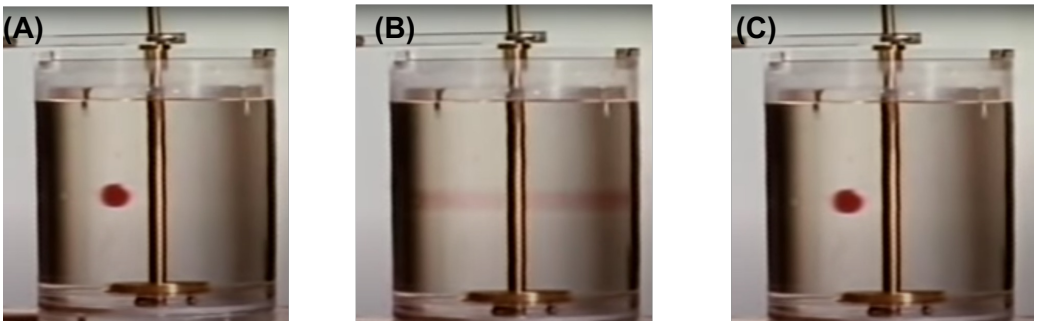

Fig. 7.2.: Kinematic reversibility of Stokes flow demonstrated by G.I.Taylor. The dye in the syrup comes back to its position after rotating the apparatus in clockwise and counterclockwise direction by same angle.

7.5 Life at low Reynolds number

So far, we exploited time-reversibility and linearity of Stokes equation to write their solution in various cases. However, we have not considered the harsh consequences of Stokes flow i.e. slow swimming of microorganisms [23], No-mixing [8].

7.5.1 Kinematic reversibility of Stokes flow

Effect of kinematic reversibility is demonstrated beautifully in G.I.Taylor's one of the lectures on *low reynolds number flows* [1] *[24]*. He starts with the Taylor-Couette apparatus with a highly viscous fluid. He describes the reversibility of the Stokes flow by putting some dye in syrup in the Taylor-Couette apparatus (Fig. 7.2). We quote G.I.Taylor:

> "The space between two concentric cylinders is filled with glycerin. Dye is introduced into the annulus which forms a compact colored volume, see Fig. 7.2(A). The inner cylinder is turned through, say, N revolutions. When observed from the side, the colored area seems to mix with the uncolored glycerin (see Fig. 7.2(B)), just as milk mixes with tea when stirred in a cup, but on reversal of the motion the dye suddenly collects into a compact mass when the cylinder has been turned exactly N turns in reverse (Fig. 7.2(C)). On reversal of the motion of the boundary, every particle retraces exactly the same path on its return journey as on the outward journey. Molecular diffusion, which is irreversible, is negligible during the time of this experiment."

[1] Video to the lecture: https://youtu.be/51-6QCJTAjU

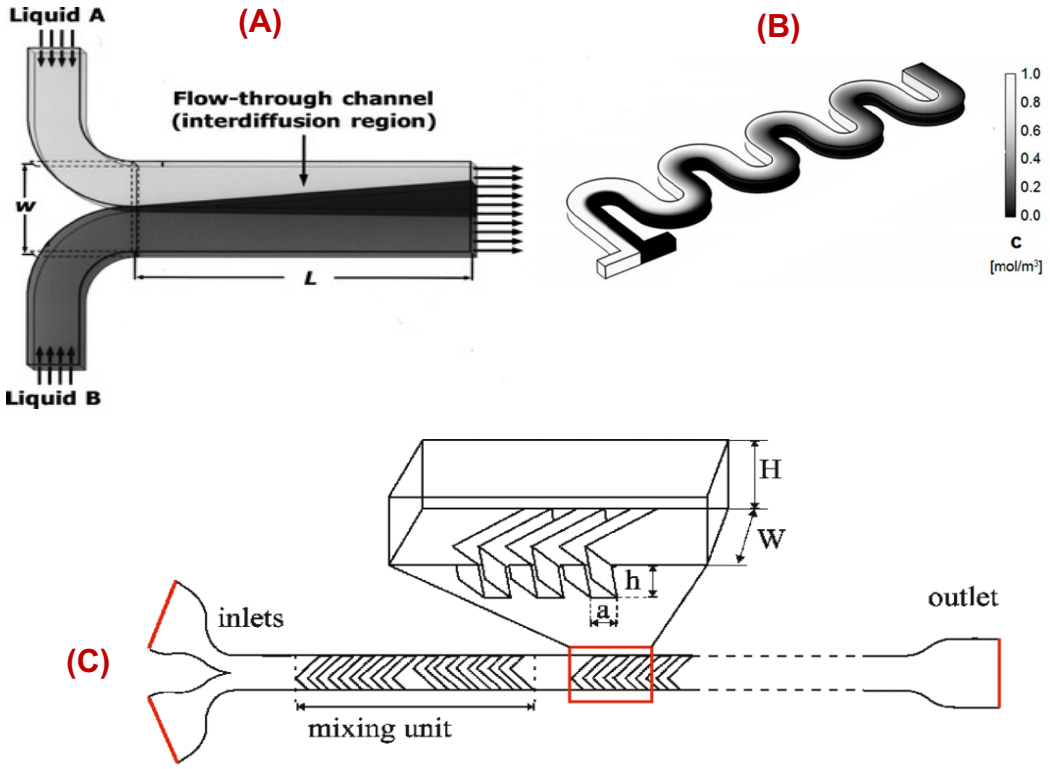

Fig. 7.3.: **(A)** Mixing of two liquids in a micro-channel solely due to diffusion. L is length and w is width of the channel. **(B)** Serpentine micromixer. **(C)** Staggered herringbone micromixer. Figure reprinted with permission from Ref. [25, 26].

7.5.2 Mixing in micro-channel

The mixing in micro-channels happens solely due to molecular diffusion and is very slow. Take a micro-channel of length L and width w, see Fig. 7.3(A). Two liquids A and B enter to the channel through two inputs. The amount of time, t_{D}, that fluid takes to traverse the width of the channel through diffusion is

$$t_{\mathrm{D}} = \frac{w^2}{D}, \tag{7.40}$$

where D is the diffusion coefficient. Length of the channel required for fluids to inter-diffuse

$$\frac{L}{w} = \frac{U t_{\mathrm{D}}}{w} = \frac{U w}{D} \approx 250 \text{ (protein)}, \tag{7.41}$$

where U is velocity of the fluid. It is clear that we need very long channels to mix two fluids in micro-channel. Most strategies to increase mixing in microfluidics rely on having a non-zero but small molecular diffusivity and by stretching and folding the fluid –they increase the surface area between the layers– hence mixing [8]. We quote Aref [8]:

For efficient mixing to be achieved, the velocity field must stir together different portions of the fluid to within a scale that is small enough for diffusion to take over and homogenize the concentrations of the advected quantities.

In recent years, there has been some progress in this direction. These solutions are practical for moderate Reynolds number flows Re $\sim 1-40$. For examples, a *serpentine* channel (see Fig. 7.3(B)) and a *staggered herringbone mixer* (see Fig. 7.3(C)) – this mixer has grooves as pattern printed on the surface of the channel which relies on clockwise and counterclockwise vortices to mix the fluids [27].

References

[1] Osborne Reynolds. "An experimental investigation of the circumstances which determine whether the motion of water shall be direct or sinuous, and of the law of resistance in parallel channels." In: *Proceedings of the royal society of London* 35.224-226 (1883), pp. 84–99.

[2] Raymond E Goldstein. "Green algae as model organisms for biological fluid dynamics". In: *Annual review of fluid mechanics* 47 (2015), pp. 343–375.

[3] Bernhard Sebastian and Petra S Dittrich. "Microfluidics to mimic blood flow in health and disease". In: *Annual review of fluid mechanics* 50 (2018), pp. 483–504.

[4] James Lighthill. "Flagellar hydrodynamics". In: *SIAM review* 18.2 (1976), pp. 161–230.

[5] Lisa J Fauci and Robert Dillon. "Biofluidmechanics of reproduction". In: *Annu. Rev. Fluid Mech.* 38 (2006), pp. 371–394.

[6] Dino Di Carlo. "Inertial microfluidics". In: *Lab on a Chip* 9.21 (2009), pp. 3038–3046.

[7] Todd M Squires and Stephen R Quake. "Microfluidics: Fluid physics at the nanoliter scale". In: *Reviews of modern physics* 77.3 (2005), p. 977.

[8] Hassan Aref, John R Blake, Marko Budišić, et al. "Frontiers of chaotic advection". In: *Reviews of Modern Physics* 89.2 (2017), p. 025007.

[9] Geoffrey Ingram Taylor and John Friedman. "Low Reynolds number flows". In: (1985).

[10] DJ Acheson. *Elementary fluid dynamics: Oxford University Press*. 1990.

[11] Cx K Batchelor and GK Batchelor. *An introduction to fluid dynamics*. Cambridge university press, 2000.

[12] Richard P Feynman. *The Feynman Lectures on Physics Vol 2*. Narosa, 1986.

[13] Stephen Childress. *Mechanics of swimming and flying*. Vol. 2. Cambridge University Press, 1981.

[14] Sangtae Kim and Seppo J Karrila. *Microhydrodynamics: principles and selected applications*. Courier Corporation, 2013.

[15] Elisabeth Guazzelli and Jeffrey F Morris. *A physical introduction to suspension dynamics*. Vol. 45. Cambridge University Press, 2011.

[16] Rutherford Aris. *Vectors, tensors and the basic equations of fluid mechanics*. Courier Corporation, 2012.

[17] Hilding Faxén. "Der Widerstand gegen die Bewegung einer starren Kugel in einer zähen Flüssigkeit, die zwischen zwei parallelen ebenen Wänden eingeschlossen ist". In: *Annalen der Physik* 373.10 (1922), pp. 89–119.

[18] GK Batchelor and J-T_ Green. "The hydrodynamic interaction of two small freely-moving spheres in a linear flow field". In: *Journal of Fluid Mechanics* 56.2 (1972), pp. 375–400.

[19] John F Brady and Georges Bossis. "Stokesian dynamics". In: *Annual review of fluid mechanics* 20.1 (1988), pp. 111–157.

[20] C Pozrikidis. "MICROHYDRODYNAMICS: PRINCIPLES AND SELECTED APPLICATIONS by Sangtae Kim, Seppo J. Karilla". In: *Chemical Engineering Education* 28.3 (1994), pp. 166–167.

[21] David Schwörer. "Rotne–Prager based hydrodynamics on GPUs". PhD thesis. Max Planck Institute for Intelligent Systems, 2015.

[22] Hirofumi Wada and Roland R Netz. "Non-equilibrium hydrodynamics of a rotating filament". In: *EPL (Europhysics Letters)* 75.4 (2006), p. 645.

[23] Eric Lauga and Thomas R Powers. "The hydrodynamics of swimming microorganisms". In: *Reports on Progress in Physics* 72.9 (2009), p. 096601.

[24] Geoffrey I Taylor. "Film notes for low-Reynolds-number flows". In: *National Committee for Fluid Mechanics Films* 21617 (1967). URL: https://youtu.be/51-6QCJTAjU.

[25] Chia-Yen Lee, Chin-Lung Chang, Yao-Nan Wang, and Lung-Ming Fu. "Microfluidic mixing: a review". In: *International journal of molecular sciences* 12.5 (2011), pp. 3263–3287.

[26] https://www.elveflow.com/microfluidic-reviews/microfluidic-flow-control/microfluidic-mixers-a-short-review/.

[27] Abraham D Stroock, Stephan KW Dertinger, Armand Ajdari, et al. “Chaotic mixer for microchannels”. In: *Science* 295.5555 (2002), pp. 647–651.

8

FILAMENT IN STOKES FLOW

The interaction between Stokesian fluid and filament holds the key to understand many natural phenomena e.g. swimming of microorganisms [1], nuclear positioning in eukaryotic cells [2], or how cells search and home to a target [3]. The dynamics of an elastic filament in a constant-in-time Stokes flow has been extensively studied, numerically and experimentally [4, 5, 6, 7, 8, 9, 10, 11, 12]. Depending on the flow, the filament either attains a complex shape, which in one case can even be helical [12], or shows a wide range of morphological transition [6] depending on its elastoviscous number $\overline{\mu} \equiv (8\pi\eta S L^4)/B$, where L is length of the filament, η is viscosity of the fluid, S is inverse time-scale, and B is the bending rigidity of the filament. For small elastoviscous number (large bending rigidity), typically, the filament behaves like a rigid one.

In section 8.1, we compare the time-scales of bending and stretching forces for a filament in Stokes flow. In section 8.2, we discuss the motion of the filament with time-periodic forcing.

8.1 Time scales

Consider a simple experiment. Take a strand of your hair and try to stretch or bend it. You shall find that bending of hair is much easier than stretching it. In this section, we elucidate this by comparing typical stretching and bending time-scales.

Consider a filament in Stokes flow i.e. viscous forces are the dominant forces on the filament which balances the bending and stretching forces on the filament. The viscous force, $\boldsymbol{F}^{\text{vis}}$, scales as (equation 7.16):

$$F^{\text{vis}} \sim \eta U_0 L, \tag{8.1}$$

where η is viscosity, U_0 is some velocity scale, L is size of the object. The bending and stretching forces scale as:

$$F^{\text{Bend}} = -\frac{\delta \mathcal{H}^{\text{Bend}}(R'')}{\delta R} \sim Y\frac{d^4}{L^2} \quad , \tag{8.2a}$$

and

$$F^{\text{Stretch}} \sim Y d^2 \quad , \tag{8.2b}$$

where $F^{\text{Bend}}, F^{\text{Stretch}}$ are forces due to bending and stretching respectively, d is diameter of the filament, L is length of the filament, $B = YI$, Y is the Young's modulus of the material and I is second moment of inertia of the filament i.e. $I \sim d^4$. The bending and stretching force (equation 8.2) balances the viscous forces (equation 8.1). We compute the relaxation time for bending and stretching:

$$\eta U_0 L = Y\frac{d^4}{L^2} \quad \Rightarrow \quad \tau^{\text{Bend}} = \frac{L}{U_0} = \frac{\eta}{Y}\left(\frac{L}{d}\right)^4 \quad , \tag{8.3a}$$

$$\eta U_0 L = Y d^2 \quad \Rightarrow \quad \tau^{\text{Stretch}} = \frac{\eta}{Y}\left(\frac{L}{d}\right)^2 \quad , \tag{8.3b}$$

$$\frac{\tau^{\text{Stretch}}}{\tau^{\text{Bend}}} = \left(\frac{d}{L}\right)^2 \ll 1 \quad . \tag{8.3c}$$

Here τ is the relaxation time. We compare the relaxation time for stretching and bending in (8.3c) and we observe the ratio to be much smaller than 1 as we generally deal with the filaments with very high aspect ratio ($L/d \gg 1$). Therefore, we say that the modulation in the extension relax much faster than the bending deformations for the filament in Stokes flow [13]. Hence, we consider the filament to be almost inextensible throughout the study.

Note that, if the inertial forces are dominant instead of viscous force i.e. $F \sim \rho U_0^2 L^2$, the ratio of stretch and bend timescales is proportional to $d/L \ll 1$instead of d^2/L^2. Although the ratio of timescales in the case, where inertial forces are dominant, is smaller than the case, where viscous forces are dominant, the assumption that the filament is easier to bend than stretch still holds.

8.2 Breaking of kinematic reversibility of Stokes flow

It has been shown that addition of elastic polymers [14, 15, 16, 17], or active objects [18, 19, 20] and mutual hydrodynamic interaction between many suspended

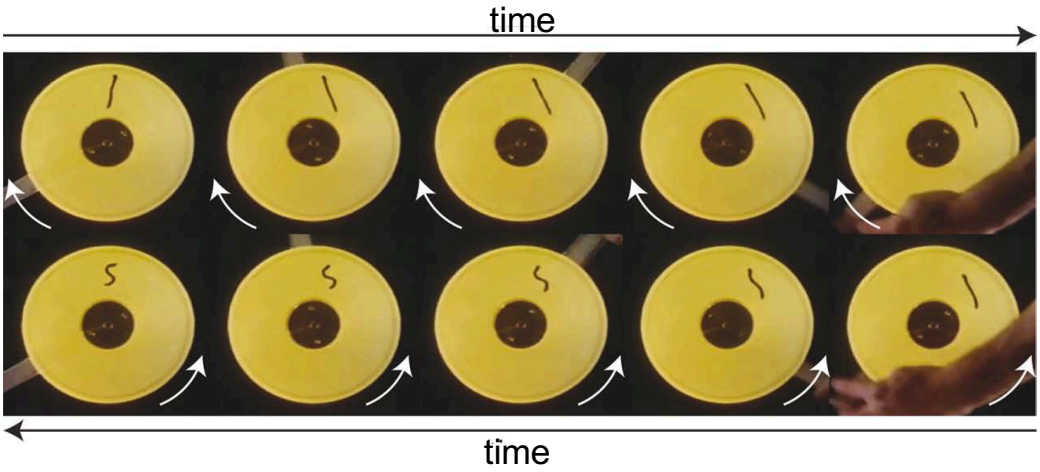

Fig. 8.1.: Breaking of kinematic reversibility: due to a flexible but inextensible filament in the Taylor-Couette apparatus. The filament breaks kinematic reversibility and does not come back to its original shape but comes back in the buckled shape after reversing the flow.

colloidal particles [21], give rise to breakdown of time-reversibility and to chaotic flows even at zero Reynolds number.

G.I. Taylor puts a flexible filament in the Taylor-Couette apparatus. He studies the effect of nonlinear elasticity of the filament in the following way [22]. We again quote him:

> The motion of a flexible body is not reversible because when the stresses in a flexible body are reversed it changes its shape. This is illustrated in Fig. 8.1, where we put a flexible body, consisting of a piece of wool in the fluid. The inner cylinder was then rotated in a clockwise direction, the wool moved round in a clockwise direction. The wool remained nearly straight, because it was in fluid which was moving in such a way as to stretch it. After the motion was reversed until the inner cylinder was in its original position, the wool curled up because on the return path the viscous stressed gave rise to a compressive stress along its length which naturally made it collapse.

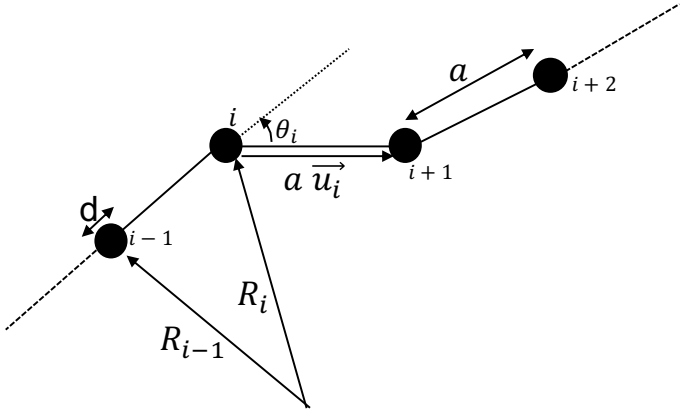

Fig. 8.2.: Schematic of a freely jointed bead-rod chain. We show $a > d$ for illustration, but we use $a = d$ for our simulation. Figure adapted and reprinted with permission from [23].

8.3 Simulation model

We use the bead-spring model to simulate the dynamics of the filament. The model consists of N spherical beads of diameter d, connected by springs of equilibrium length a, see Fig. 8.2. We assume the springs to be in the over-damped limit (see appendix A for discussion on over-damped limit in Stokes flow). The position of the center of the i-th bead is $\boldsymbol{R}_i$, where $i = 1, \dots N$. The equation of motion for the i-th bead is given by [24, 9] (see Eq. (8.17)):

$$\begin{aligned}\frac{\partial R_i^\alpha}{\partial t} &= \sum_{j=0}^{N-1}\left[-\mathcal{M}_{ij}^{\alpha\beta}(\boldsymbol{R}_{ij})\frac{\delta\mathcal{H}}{\delta R_j^\beta} + \mathcal{N}_{ij}^{\alpha\beta\gamma}(\boldsymbol{R}_{ij})E_\infty^{\beta\gamma}(\boldsymbol{R}_{ij})\right] + v_\infty^\alpha(\boldsymbol{R}_i) \quad , \\ &= \sum_{j=0}^{N-1}\Bigg[-\frac{1}{8\pi\eta R_{ij}}\left\{\delta^{\alpha\beta} + \frac{R_{ij}^\alpha R_{ij}^\beta}{R_{ij}^2} + \frac{d^2}{2R_{ij}^2}\left(\frac{\delta^{\alpha\beta}}{3} - \frac{R_{ij}^\alpha R_{ij}^\beta}{R_{ij}^2}\right)\right\}\frac{\partial\mathcal{H}}{\partial R_j^\beta} \\ &\qquad \frac{1}{N}v_\infty^\alpha(\boldsymbol{R}_i) - \frac{5d^3}{16}\frac{R_{ij}^\alpha R_{ij}^\beta R_{ij}^\gamma}{R_{ij}^5}E_\infty^{\beta\gamma}\Bigg] \quad .\end{aligned} \tag{8.4}$$

Here $\boldsymbol{R}_i$ is the position vector of the center of the i-th bead, $\boldsymbol{R}_{ij} = \boldsymbol{R}_j - \boldsymbol{R}_i$, $\mathcal{H}$ is the elastic Hamiltonian, and $\boldsymbol{v}_\infty$ is the velocity of the background flow, $\mathcal{M}^{\alpha\beta}, \mathcal{N}^{\alpha\beta\gamma}$ are the hydrodynamic interaction tensors explained in section 7.4.1,7.4.2. Note that, in Eq. (8.17) we do not include term with second derivative of position i.e. we consider the springs to be over-damped – which is a reasonable approximation for small beads in Stokes flow [25].

Let us look at the (8.17) dimensionally. We compare the terms due to the external shear and flow (terms with $E_\infty^{\alpha\beta}, \boldsymbol{v}_\infty$), and terms due to elastic forces ($\delta\mathcal{H}/\delta R_j^\beta$) separately. We write:

$$\frac{\partial R_i^\alpha}{\partial t} \sim \frac{1}{\eta R_{ij}} \left[O(1) + O(1) + O\left(\frac{d^2}{R_{ij}^2}\right) \right] \frac{\delta \mathcal{H}}{\delta R_j^\beta} + SX_{ij} \left[O(1) + O\left(\frac{d^3}{R_{ij}^3}\right) \right] \quad . \tag{8.5}$$

In our model, we do not consider the terms of higher order than $O(d^2/R_{ij}^2)$ to obtain:

$$\frac{\partial R_i^\alpha}{\partial t} = -\sum_{j=0}^{N-1} \mathcal{M}_{ij}^{\alpha\beta}(\boldsymbol{R}_{ij}) \frac{\delta \mathcal{H}}{\delta R_j^\beta} + v_\infty^\alpha(\boldsymbol{R}_i) \quad , \tag{8.6}$$

The Hamiltonian of the system, $\mathcal{H}$, is $\mathcal{H} = \mathcal{H}^{\text{Bend}} + \mathcal{H}^{\text{Stretch}}$ – we do not consider twisting. Here $\mathcal{H}^{\text{Bend}}$ and $\mathcal{H}^{\text{Stretch}}$ are from bending [26, 27]and stretching [24, 28] respectively. The bending energy of a filament for a discrete bead-rod model [29, 27, 26]:

$$\mathcal{H}^{\text{Bend}} = aB \sum_{i=0}^{N-1} \kappa_i^2 = \frac{B}{a} \sum_{i=0}^{N-1} \widehat{\boldsymbol{T}}_i \cdot \widehat{\boldsymbol{T}}_{i-1} = \frac{B}{a} \sum_{i=0}^{N-1} \cos\theta_i, \tag{8.7}$$

where

$$\kappa_i = \frac{2}{a} \tan\left(\frac{\theta_i}{2}\right) \approx \frac{\sin(\theta_i)}{a} = \frac{\left|\widehat{\boldsymbol{T}}_{\text{i}} \times \widehat{\boldsymbol{T}}_{i-1}\right|}{a}, \tag{8.8a}$$

$$\widehat{\boldsymbol{T}}_i = \frac{\boldsymbol{R}_{i+1} - \boldsymbol{R}_i}{|\boldsymbol{R}_{i+1} - \boldsymbol{R}_i|} \quad , \tag{8.8b}$$

and θ_{i} is the angle between two consecutive unit vectors $\widehat{\boldsymbol{T}}_i$ and $\widehat{\boldsymbol{T}}_{i-1}$ (see Fig. 8.2A). In the second step of equation 8.7, we have dropped a constant term. In the last step of equation 8.8a, we have used small-angle approximation [26]. This is a discrete approximation of contribution to the bending energy (equation 6.13) from curvature.

The stretching energy is: [24, 28]

$$\mathcal{H}^{\text{Stretch}} = \frac{k}{2a} \sum_{i=0}^{N-1} (|\boldsymbol{R}_{i+1} - \boldsymbol{R}_i| - a)^2, \tag{8.9}$$

where k is the stretching modulus. We ignore thermal fluctuations. Expression for $\delta\mathcal{H}/\delta R_{ij}^\beta$ is given in the section 8.3.1. We use the adaptive Runge-Kutta method [30] with cash-karp parameters [31, 32] to evolve the system. We use time-step, Δt, such that

$$\tilde{\Delta} = \frac{B\Delta t}{8\pi\eta\ell^4} = 10^{-11} - 10^{-12} \tag{8.10}$$

We use numerical accuracy of order 10^{-6} [30, 31, 32]. We use CUDA to parallelize the code [1].

8.3.1 Discretized bending and stretching force

Total force on any bead is the sum of the bending force and stretching force:

$$\boldsymbol{F} = \boldsymbol{F}^{\text{Bend}} + \boldsymbol{F}^{\text{Stretch}} = \frac{\partial \mathcal{H}^{\text{Bend}}}{\partial \boldsymbol{R}_i} + \frac{\partial \mathcal{H}^{\text{Stretch}}}{\partial \boldsymbol{R}_i} = \sum_{i=0}^{N-1} \left[\frac{B}{a} \widehat{\boldsymbol{T}}_i \cdot \widehat{\boldsymbol{T}}_{i-1} + \frac{k}{2a} \left(|\boldsymbol{R}_{i+1} - \boldsymbol{R}_i| - a \right)^2 \right] \tag{8.11}$$

where $\mathcal{H}^{\text{Bend}}$ and $\mathcal{H}^{\text{Stretch}}$ are the Hamiltonian for bending and stretching respectively.

Bending force:

$$\boldsymbol{F}_i^{\text{Bend}} = \frac{B}{a} \left[\frac{\widehat{\boldsymbol{T}}_{i-2} + \widehat{\boldsymbol{T}}_i}{b_{i-1}} - \frac{\widehat{\boldsymbol{T}}_{i+1} + \widehat{\boldsymbol{T}}_{i-1}}{b_i} + (\hat{T}_i^\alpha \hat{T}_{i-1}^\alpha + \hat{T}_i^\alpha \widehat{\boldsymbol{T}}_{i+1}^\alpha) \left(\frac{\widehat{\boldsymbol{T}}_i}{b_i} \right) - \left(\hat{T}_{i-1}^\alpha \widehat{\boldsymbol{T}}_{i-2}^\alpha + \hat{T}_{i-1}^\alpha \hat{T}_i^\alpha \right) \left(\frac{\widehat{\boldsymbol{T}}_{i-1}}{b_{i-1}} \right) \right], \quad \text{for } i \neq 0, 1, N-1, N-2. \tag{8.12a}$$

The bending force for boundary points are:

$$\boldsymbol{F}_i^{\text{Bend}} = \frac{B}{a} \left[-\frac{\widehat{\boldsymbol{T}}_{i+1}}{b_i} + \left(\hat{T}_i^\alpha \widehat{\boldsymbol{T}}_{i+1}^\alpha \right) \frac{\widehat{\boldsymbol{T}}_i}{b_i} \right], \qquad i = 0 \tag{8.12b}$$

$$\boldsymbol{F}_i^{\text{Bend}} = \frac{B}{a} \left[\frac{\widehat{\boldsymbol{T}}_{\text{k}}}{b_{\text{k}-1}} - \frac{\widehat{\boldsymbol{T}}_{i+1} + \widehat{\boldsymbol{T}}_{i-1}}{b_i} + (\hat{T}_i^\alpha \hat{T}_{i-1}^\alpha + \hat{T}_i^\alpha \widehat{\boldsymbol{T}}_{i+1}^\alpha) \left(\frac{\widehat{\boldsymbol{T}}_i}{b_i} \right) - \left(\hat{T}_{i-1}^\alpha \hat{T}_i^\alpha \right) \left(\frac{\widehat{\boldsymbol{T}}_{i-1}}{b_{i-1}} \right) \right], \qquad i = 1 \tag{8.12c}$$

$$\boldsymbol{F}_i^{\text{Bend}} = \frac{B}{a} \left[\frac{\widehat{\boldsymbol{T}}_{i-2} + \widehat{\boldsymbol{T}}_i}{b_{i-1}} - \frac{\widehat{\boldsymbol{T}}_{i-1}}{b_i} + (\hat{T}_i^\alpha \hat{T}_{i-1}^\alpha) \left(\frac{\widehat{\boldsymbol{T}}_i}{b_i} \right) - \left(\hat{T}_{i-1}^\alpha \widehat{\boldsymbol{T}}_{i-2}^\alpha + \hat{T}_{i-1}^\alpha \hat{T}_i^\alpha \right) \left(\frac{\widehat{\boldsymbol{T}}_{i-1}}{b_{i-1}} \right) \right], \qquad i = N-2 \tag{8.12d}$$

[1] Our code is available here: https://github.com/dhrubaditya/ElasticString

$$\boldsymbol{F}_i^{\text{Bend}} = \frac{B}{a}\left[\left(\hat{T}_{i-1}^{\alpha}\widehat{\boldsymbol{T}}_{i-2}^{\alpha}\right)\left(\frac{\widehat{\boldsymbol{T}}_{i-1}}{b_{i-1}}\right)\right], \qquad i = N-1 \tag{8.12e}$$

Here

$$b_i = |\boldsymbol{R}_{i-1} - \boldsymbol{R}_i| \tag{8.13}$$

Stretching force:

$$\boldsymbol{F}_i^{\text{Stretch}} = \frac{k}{a}\left[\widehat{\boldsymbol{T}}_i\,(b_i - a) - \widehat{\boldsymbol{T}}_{i-1}(b_{i-1} - a)\right], \qquad i \neq 0, N-1 \tag{8.14a}$$

$$\boldsymbol{F}_i^{\text{Stretch}} = \frac{k}{a}\left[\widehat{\boldsymbol{T}}_i(b_i - a)\right], \qquad i = 0 \tag{8.14b}$$

$$\boldsymbol{F}_i^{\text{Stretch}} = -\frac{k}{a}\left[\widehat{\boldsymbol{T}}_{i-1}(b_{i-1} - a)\right], \qquad i = N-1 \tag{8.14c}$$

8.4 Filament driven in time-periodic manner

Elongation and compression of flexible filament gives rise to buckling instability [5, 6, 7, 12]. The intensity of elongational and compressional forces determines the morphology of the filament. For a filament in fluid, typically, these forces are the result of fluid-filament interaction. Thus for a time-dependent forcing, it is possible to control the buckling of filament by controlling the amount of time filament spends in elongation and compression regime. Furthermore, such a driving of the filament can also act as a stirrer to mix flows at very small Reynolds number.

8.4.1 summary of paper III – chaos and irreversibility of a flexible filament in periodically driven Stokes flow [33]

In paper III [33], we consider a freely suspending filament in plane-Couette flow as shown in Fig. 8.3(A). The ambient flow is

$$v_\infty = \dot{\gamma} y \hat{x}, \tag{8.15}$$

where strain rate $\dot{\gamma} = S\sin(\omega t)$, $S = 2s^{-1}$, ω is rate of change of the flow, and t is time. The filament extends for the first-half of the cycle and compresses for second-half of the cycle. If the bending rigidity of the filament is very large, such that the filament behaves effectively like a rigid body, we expect the filament to rotate away and back to its original position and shape . Once the bending rigidity

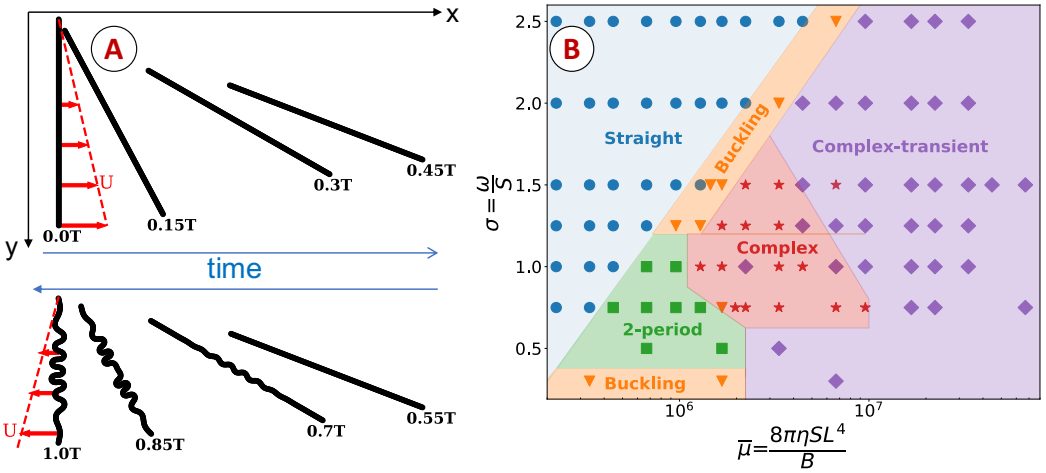

Fig. 8.3.: **(A) Sketch of numerical experiment**: Initially the filament is straight. It rotates and translates while advected by $v_\infty = \dot{\gamma} y \hat{x}$ with $\dot{\gamma} = S\sin(\omega t)$ over the first-half of the cycle. In the second half the filament rotates and translates back but in addition buckles if its elastoviscous number is large enough. The flow v_∞ at $t = T/4$ (top panel) and $t = 3T/4$ (bottom panel) are shown as red arrows. **(B) Phase diagram** from time-dependent numerical simulation of (8.6) in $\bar{\mu}$–$\tilde{t} = \omega/S$ parameter space. We show five different dynamical phases in the system represented by five symbols. Straight (●); Periodic buckling (▼); Two-period (■) ; Complex(★); Complex–transients(⧫). Figure adapted and reprinted with permission from [23].

is below a threshold, we find that the filament buckles (similar to Fig. 8.1) – it does not return to its original shape. If the bending rigidity is decreased further we find that the elastic nonlinearities play a more and more dominant role in the dynamics thereby giving rise to higher order buckling.

Overall, we identify five types of dynamical phase (see Fig. 8.3(B)), each characterized by the shape of the filament – as described by its curvature as a function of its arc length – at late times [33, see section IIIA, appendix C]:

1. **Straight**:- The filament comes back to the initial position in the straight configuration after every period.

2. **Periodic buckling**:- The filament comes back in the buckled configuration after every period.

3. **Two-period**:- The filament repeats its configuration not after every but after two-period.

4. **Complex**:- The filament buckles into complex shape with very high mode of buckling instability and it never repeats itself.

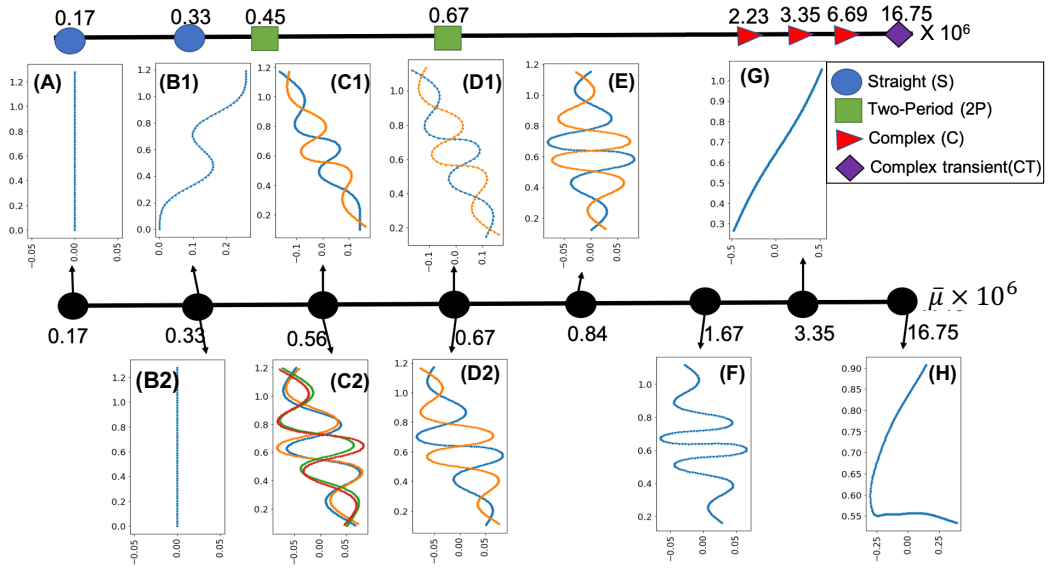

Fig. 8.4.: **Solutions of stroboscopic map** in real space for $\tilde{t} = 0.75$ for different values of $\overline{\mu}$. We find multiple co-existing solutions as we increase $\overline{\mu}$ (black symbols from left to right) indicating the complexity of the system. We compare this solutions with the solutions obtained at late times from the evolution code at the same points in the phase diagram. Figure adapted and reprinted with permission from [23].

5. **Complex–transients**:- Filament shows long transients with complex shape but at late times, the shape of the filament (almost) repeats itself. At late times the filament settles down to a complicated shape which changes very slowly. The boundary between the complex and complex-transient phase is difficult to clearly demarcate.

We characterize the chaos using fixed-point analysis of the iterative stroboscopic map by integrating the dynamical equation for exactly one period [33, see section IIIB]. We define the stroboscopic map

$$\kappa(s, pT) = \mathcal{F}\kappa(s, 0), \tag{8.16}$$

where $\kappa(s, T)$ is curvature of the filament as a function of its arc-length, s (see (8.8a)) at time T, where $T = 2\pi/\omega$ and n is an integer. This converts the non-autonomous system described by (8.6) to an autonomous map in N-dimensional space where N is the total number of beads. we study the chaos by obtaining the fixed points We use look for solution of (8.16) for different values of p i.e. different periods [33, see appendixD1].

In Fig. 8.4 we show the co-existence of many periodic orbits and fixed points for a fixed $\tilde{t} = 0.75$ as a function of $\overline{\mu}$. For small $\overline{\mu} = 0.17 \times 10^6$ we obtain only one fixed point and it corresponds to $\kappa(s) = 0$, i.e., a straight filament. At $\overline{\mu} = 0.33 \times 10^6$ in

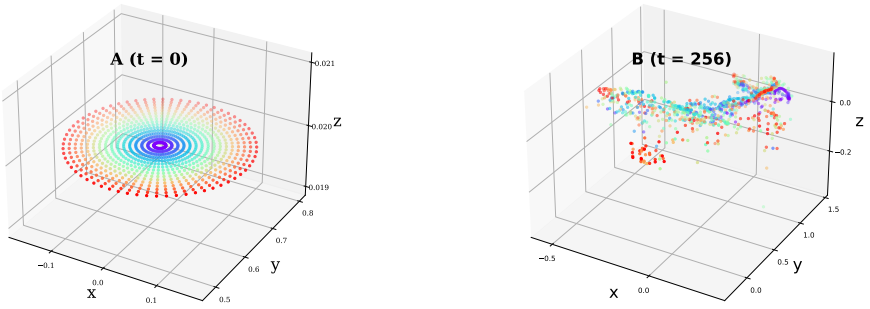

Fig. 8.5.: Mixing of passive tracer: (A) to (B) Positions of tracer particles at $t = 0T, 256T$ respectively for the filament in complex phase ($\overline{\mu} = 3.3 \times 10^6$, $\tilde{t} = 1.5$). Initially, the tracers are placed on concentric circles, color coded by their distance from the center of the circles. The mixing of the colors show the mixing of the scalars. Figure adapted and reprinted with permission from [23].

addition to the straight filament a new fixed point appears, where κ is zero at one end, changes sign once roughly at the middle of the filament and has two maximas. We show the shape of the filament in Fig. 8.4(B1). Next at $\overline{\mu} = 0.33 \times 10^6$ we no longer find any fixed points. We find two periodic orbits, one that is a two–period Fig. 8.4(C1) and one with four periods Fig. 8.4(C2). The two solutions in the two-period solution are mirror images of each other. At the same place in the phase diagram the evolution code finds the same two–period solution. Increasing $\overline{\mu}$ to 0.84×10^6 we find that the four-period solution has disappeared, two two–period solutions exist, Fig. 8.4(D). At even higher values of $\overline{\mu}$ we start to obtain many solutions. We show a few examples in Fig. 8.4(F), Fig. 8.4(G), and Fig. 8.4(H). This is the region of phase space where complex and complex-transient dynamical phases are seen.

Next we demonstrate that if we choose $\overline{\mu}$ and $\tilde{t}$ inside the complex phase then the filament acts as an effective mixer of passive tracers [33, see section C]. Once the filament has reached a statistically stationary state we introduce N_p tracers placed on concentric circles in the x–y plane, Fig. 8.5(A). The equation of motion of a passive tracer is given by (7.33). At $t = 256T$, we find the tracer particles are well mixed with each other (see Fig. 8.5(B)). To obtain a quantitative measure of mixing we compute the net displacement of the k-th tracer particle, $\Delta \boldsymbol{X}_\mathrm{j}^\mathrm{k}$, over the j-th cycle – $t = jT$ to $t = (j+1)T$, where j is an integer. Furthermore, we calculate the cumulative probability density function (CPDF) for each component of the displacement $\Delta \boldsymbol{X}_\mathrm{j}^\mathrm{k}$. For the out-of-plane component this CPDF has an exponential tail. For the in-plane components we obtain a power-law tail of exponent of -3. This implies that the probability density function (PDF) of each component of the

displacement $\Delta \boldsymbol{X}_{\mathrm{j}}^{\mathrm{k}}$ is such that its second moment is well defined. Hence by the central limit theorem, we expect the tracers to mix diffusively.

8.4.2 Summary of paper IV – flexible filament in time-periodic viscous flow: shape chaos and period three [23]

There are two types of nonlinearities in (8.6). First, the elastic nonlinearities in the system and second, the nonlinear filament-fluid interaction. It has been shown that the time-reversible motion of many particle suspended in shear flow breaks the kinematic reversibility and shows chaos solely due to the nonlinear hydrodynamic interactions between the particles [21]. Hence it becomes important to ask that, if we assume the local approximation to the flow–structure interaction, can an elastic filament still show the chaotic behavior? After ignoring the nonlocal fluid–filament interaction in (8.6), the equation of motion is:

$$\frac{\partial R_{\mathrm{i}}^{\alpha}}{\partial t} = -\frac{1}{3\pi\eta d}\frac{\partial \mathcal{H}}{\partial R_{\mathrm{i}}^{\alpha}} + v_{\infty}^{\alpha}(\boldsymbol{R}_i) \quad . \tag{8.17}$$

The background shear flow is given by (8.15).

We evolve the filament from a straight configuration similar to what is shown in Fig. 8.3(A). The evolution phase diagram is shown in Fig. 8.6A. We have observed the same qualitative behavior for the case where the viscous forces are modeled by the non-local Rotne-Prager tensor, with three quantitative differences. First, the instabilities appear at lower $\overline{\mu}$ for a given $\tilde{t}$, second, the appearance of three-period solution, third, we obtained complex transients for large enough $\overline{\mu}$ in the case of nonlocal interaction, whereas here we observe the reappearance of the complex phase for the higher $\overline{\mu}$s. Nevertheless, we conclude that the model with local viscosity is able to capture the feature of the problem we consider essential – a rich dynamical phase diagram that includes complex shapes.

The computational complexity of this model in $\mathcal{O}(N)$, where N is the total number of beads, as opposed to the nonlocal case where the computational complexity is $\mathcal{O}(N^2)$. This allows us to run our simulations for much longer times than it was possible in the case of nonlocal interactions. Here for any fixed value of $\overline{\mu}$ and $\tilde{t}$ we obtain many periodic orbits. We list all of them in table 8.1.

Further we attempt an arbitrary dimensional reduction to construct a one-dimensional map. We draw the straight line that connects the top end of the filament to the bottom one and call Θ the angle this line makes with the tangent to the filament at its top

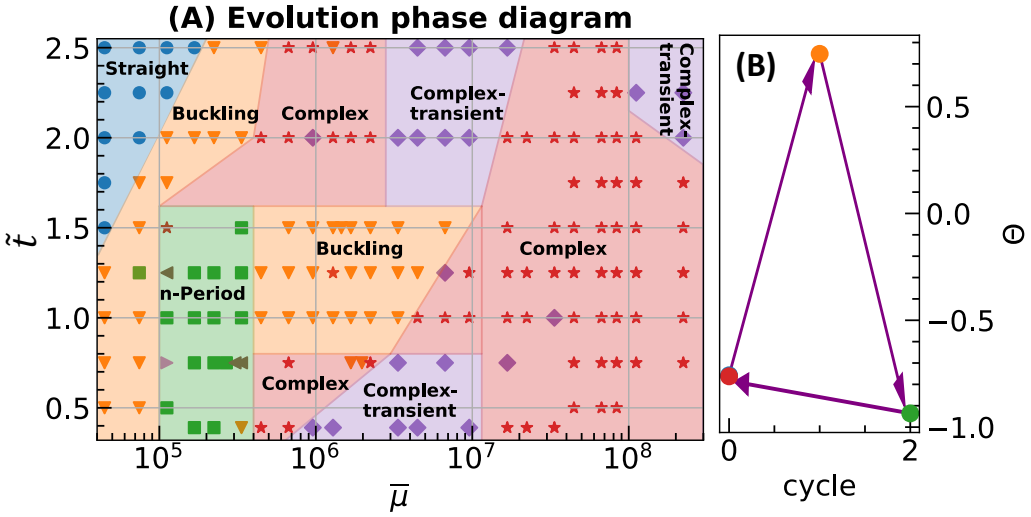

Fig. 8.6.: **(A):Phase diagram** in the $\overline{\mu}$–$\tilde{t}$ plane; We find 5 different qualitatively different dynamical phases: Straight(●); periodic (▼) with n-period, where n=2(■), 3(◀), 4(▶); complex (★) complex-transients (⧫). **(B) An example of three period solution**: for $(\tilde{t} = 0.75, \overline{\mu} = 3.35 \times 10^5)$ in 1D Θ-space (C). The Θ is defined as the angle between the lines connecting the top and bottom end of the filament to the tangent to the filament at its top point.

point, see Fig. 8.6(B). We find period three solution of Θ for $\tilde{t} = 0.75, \overline{\mu} = 3.35 \times 10^5$. This is a one-dimensional map for which Sharkovskiˇi's theorem [34] and the Li and Yorke theorem [35] is valid – existence of orbits of period three implies not only the existence of orbits of all periods but also the sensitive dependence on initial condition. Thus by demonstrating that the Θ map has three period we show that this map is chaotic. We also show that, in the chaotic phase, the tracers are mixed diffusively.

References

[1] Eric Lauga and Thomas R Powers. "The hydrodynamics of swimming microorganisms". In: *Reports on Progress in Physics* 72.9 (2009), p. 096601.

[2] Michael J Shelley. "The dynamics of microtubule/motor-protein assemblies in biology and physics". In: *Annual review of fluid mechanics* 48 (2016), pp. 487–506.

[3] Deepak Krishnamurthy and Manu Prakash. "Emergent Programmable Behavior and Chaos in Dynamically Driven Active Filaments". In: *bioRxiv* (2022).

$\overline{\mu}$ \ $\tilde{t}$	**0.75**	**1.0**	**1.25**
3.35×10^4	1	1	1
4.47×10^4	1	1	1
6.67×10^4	1,16	1	1
9.57×10^4	1,4,20,22,23,27	2,4,11	1,2,3,12,13,24,25
1.67×10^5	1,2,10,14,33	1,2,3	1,2
2.23×10^5	1,2	1,2,3	1,2
3.35×10^5	1,2,3,4,5,7,9, 10,15,19,22,23,31	1,2	1,2,7
4.47×10^5	1	1,2,3,5,6,7, 13,19,37,41	1
6.70×10^5	1,2,5,7,12,25,32,41,47 50,68,76,85,100,104	1	1,2
9.57×10^5	1,126	1,4,9	1,2
1.67×10^6	1,50,54,62,65,66, 70,80,86,108,132	1,2,3,4,5, 7,9,22,44	1
2.23×10^6	1,11,12,28	1,2,45	1
3.34×10^6	1,2,4,32	1,4	1
6.67×10^6	1^*	1,17	1
1.67×10^7	1^*	1^*	1^*
3.35×10^7	1^*	1^*	1^*

Tab. 8.1.: **Cycles of the stroboscopic map** in (8.16). In some of these cases the evolution equation shows chaotic solution but so far we have obtained one or two periodic orbits of small periods, these are marked by $*$.

[4] Leif E Becker and Michael J Shelley. “Instability of elastic filaments in shear flow yields first-normal-stress differences”. In: *Physical Review Letters* 87.19 (2001), p. 198301.

[5] Laura Guglielmini, Amit Kushwaha, Eric SG Shaqfeh, and Howard A Stone. “Buckling transitions of an elastic filament in a viscous stagnation point flow”. In: *Physics of Fluids* 24.12 (2012), p. 123601.

[6] Yanan Liu, Brato Chakrabarti, David Saintillan, Anke Lindner, and Olivia Du Roure. “Morphological transitions of elastic filaments in shear flow”. In: *Proceedings of the National Academy of Sciences* 115.38 (2018), pp. 9438–9443.

[7] John LaGrone, Ricardo Cortez, Wen Yan, and Lisa Fauci. “Complex dynamics of long, flexible fibers in shear”. In: *Journal of Non-Newtonian Fluid Mechanics* 269 (2019), pp. 73–81.

[8] AM Slowicka, Howard A Stone, and Maria L Ekiel-Jezewska. “Flexible fibers in shear flow: attracting periodic solutions”. In: *arXiv preprint arXiv:1905.12985* (2019).

[9] Paweł J Żuk, Agnieszka M Słowicka, Maria L Ekiel-Jeżewska, and Howard A Stone. “Universal features of the shape of elastic fibres in shear flow”. In: *Journal of Fluid Mechanics* 914 (2021).

[10] Steve Kuei, Agnieszka M Słowicka, Maria L Ekiel-Jeżewska, Eligiusz Wajnryb, and Howard A Stone. “Dynamics and topology of a flexible chain: knots in steady shear flow”. In: *New Journal of Physics* 17.5 (2015), p. 053009.

[11] Shi-Yuan Hu, Jun-Jun Chu, Michael J Shelley, and Jun Zhang. “Lévy Walks and Path Chaos in the Dispersal of Elongated Structures Moving across Cellular Vortical Flows”. In: *Physical Review Letters* 127.7 (2021), p. 074503.

[12] Brato Chakrabarti, Yanan Liu, John LaGrone, et al. “Flexible filaments buckle into helicoidal shapes in strong compressional flows”. In: *Nature Physics* (2020), pp. 1–6.

[13] Thomas R Powers. “Dynamics of filaments and membranes in a viscous fluid”. In: *Reviews of Modern Physics* 82.2 (2010), p. 1607.

[14] Alexander Groisman and Victor Steinberg. “Efficient mixing at low Reynolds numbers using polymer additives”. In: *Nature* 410.6831 (2001), pp. 905–908.

[15] Alexander Groisman and Victor Steinberg. “Elastic turbulence in a polymer solution flow”. In: *Nature* 405.6782 (2000), pp. 53–55.

[16] Victor Steinberg. “Elastic turbulence: an experimental view on inertialess random flow”. In: *Annual Review of Fluid Mechanics* 53 (2021), pp. 27–58.

[17] Abraham D Stroock, Stephan KW Dertinger, Armand Ajdari, et al. “Chaotic mixer for microchannels”. In: *Science* 295.5555 (2002), pp. 647–651.

[18] Christopher Dombrowski, Luis Cisneros, Sunita Chatkaew, Raymond E Goldstein, and John O Kessler. “Self-concentration and large-scale coherence in bacterial dynamics”. In: *Physical review letters* 93.9 (2004), p. 098103.

[19] Henricus H Wensink, Jörn Dunkel, Sebastian Heidenreich, et al. “Meso-scale turbulence in living fluids”. In: *Proceedings of the national academy of sciences* 109.36 (2012), pp. 14308–14313.

[20] Jörn Dunkel, Sebastian Heidenreich, Knut Drescher, et al. “Fluid dynamics of bacterial turbulence”. In: *Physical review letters* 110.22 (2013), p. 228102.

[21] David J Pine, Jerry P Gollub, John F Brady, and Alexander M Leshansky. “Chaos and threshold for irreversibility in sheared suspensions”. In: *Nature* 438.7070 (2005), pp. 997–1000.

[22] Geoffrey Ingram Taylor and John Friedman. “Low Reynolds number flows”. In: (1985).

[23] Vipin Agrawal and Dhrubaditya Mitra. *Flexible filament in time-periodic viscous flow: shape chaos and period three*. 2022. arXiv: 2210.04781 [cond-mat.soft].

[24] Hirofumi Wada and Roland R Netz. “Non-equilibrium hydrodynamics of a rotating filament”. In: *EPL (Europhysics Letters)* 75.4 (2006), p. 645.

[25] P Chaikin and TC Lubensky. *Introduction to Condensed Matter Physics*. 1995.

[26] Alberto Montesi, David C Morse, and Matteo Pasquali. “Brownian dynamics algorithm for bead-rod semiflexible chain with anisotropic friction”. In: *The Journal of chemical physics* 122.8 (2005), p. 084903.

[27] Miklós Bergou, Basile Audoly, Etienne Vouga, Max Wardetzky, and Eitan Grinspun. “Discrete viscous threads”. In: *ACM Transactions on Graphics (TOG)* 29.4 (2010), pp. 1–10.

[28] Hirofumi Wada and Roland R Netz. “Stretching helical nano-springs at finite temperature”. In: *EPL (Europhysics Letters)* 77.6 (2007), p. 68001.

[29] Miklós Bergou, Max Wardetzky, Stephen Robinson, Basile Audoly, and Eitan Grinspun. “Discrete elastic rods”. In: *ACM SIGGRAPH 2008 papers*. 2008, pp. 1–12.

[30] William H Press, Saul A Teukolsky, William T Vetterling, and Brian P Flannery. *Numerical recipes 3rd edition: The art of scientific computing*. Cambridge university press, 2007.

[31] William H Press and Saul A Teukolsky. “Adaptive Stepsize Runge-Kutta Integration”. In: *Computers in Physics* 6.2 (1992), pp. 188–191.

[32] Jeff R Cash and Alan H Karp. “A variable order Runge-Kutta method for initial value problems with rapidly varying right-hand sides”. In: *ACM Transactions on Mathematical Software (TOMS)* 16.3 (1990), pp. 201–222.

[33] Vipin Agrawal and Dhrubaditya Mitra. “Chaos and irreversibility of a flexible filament in periodically driven Stokes flow”. In: *Physical Review E* 106.2 (2022), p. 025103.

[34] Aleksandr Nikolaevich Sharkovskii. “COEXISTENCE OF CYCLES OF A CONTINUOUS MAP OF THE LINE INTO ITSELF”. In: *International Journal of Bifurcation and Chaos* 05 (1995), pp. 1263–1273.

[35] Tien-Yien Li and James A Yorke. “Period three implies chaos”. In: *The theory of chaotic attractors*. Springer, 2004, pp. 77–84.

9

SUMMARY AND OUTLOOK

In this thesis, we have investigated the elastic properties of shells and filament and their interaction with fluid.

9.1 Filament interactions with fluid

One part of the thesis which concerns with filaments is motivated by an important problem in the field "how to mix two fluids at zero Reynolds number." Our work [1, 2], has provided a way to solve the issue. We consider a freely-floating elastic filament in a linear shear flow that changes periodically with time, at zero Reynolds number. We do not consider thermal fluctuations, although for a small enough filament, e.g., a single large polymer molecule, thermal effects that we have ignored, may be important. We have ignored them for two reasons. First, in many experimental situations [3] the filament is large enough that the thermal fluctuations may not be crucial. Second, we want to address the fundamental question of emergence of chaotic behavior due to elastic nonlinearities in the absence of any external stochastic fluctuations. We show that the motion of such a filament is chaotic.

There are two nonlinear effects, which can be the cause of chaos in such system. First, the elastic nonlinearities and second, the nonlinear filament–fluid interaction or *nonlocal viscosity*. We also consider a model where we ignore the nonlocal interaction between filament and the fluid, we call this *local viscosity*. We show that such a system also show chaotic behavior which are solely the results of elastic nonlinearities. For both cases, local and nonlocal viscosity, we characterize the chaos using fixed-point analysis of the iterative stroboscopic map by integrating the dynamical equation for exactly one period. We show the co-existence of periodic orbits and fixed points at any point in the phase space of $\overline{\mu} = 8\pi\eta SL^4/B, \tilde{t} = \omega/S$, where L is length of the filament, η is viscosity of the fluid, S is inverse time-scale, B

is the bending rigidity of the filament, ω is frequency by which the flow is reversed and S is strain rate. For the case of local viscosity, we consider a one-dimensional stroboscopic map which we define as the angle between the ray connecting first and second bead and the ray connecting first and last bead. We prove chaos by showing the existence of very high periods and more importantly three-period of one-dimensional map [4, 5]. For both cases, in the chaotic regime, tracers are mixed diffusively.

9.1.1 Further progress

These two following papers [6, 7], which appeared in arxiv shortly after our paper [8], also study the dynamics of filament when it is driven in a time-periodic manner.

1. Bonacci [6] et al. explores the morphology of the filament for half a oscillation period using experiments and weakly nonlinear Landau model. First, they show that the morphology of the filament is sensitive to the initial orientation θ_0, $\overline{\mu}$ and $\tilde{t}$. Depending on $\tilde{t}, \overline{\mu}$ and θ_0, they find rich variety of deformation modes as shown in Fig. 9.1(a,b,c). It is in contrast to the filament in constant flow field – where the filament shows either *C* mode or tank-treading motion [3]. Second, they find the absence of observable buckling at high oscillation frequencies even when the maximum elastoviscous number is greater than the buckling threshold for steady shear.

2. Krishnamurthy and Prakash [7] consider an active filament clamped on one end instead of a freely suspending passive filament. This is a numerical model of the flagella of certain unicellular organism such as *L.olor* The filament is made active with a bead on the tip with periodic phases of extensional and compressive tip-follower forces as shown in Fig. 9.1(d). The filament shows chaotic motion for certain range of activity strength and period of oscillation.

9.1.2 Future work

Our work is a first-step towards a potential microfluidic device to mix fluid. However it is not a very practical solution. Following future extensions lead us towards that goal.

1. To simulate the dynamics of an elastic filament in a flow with boundaries [9, 10].

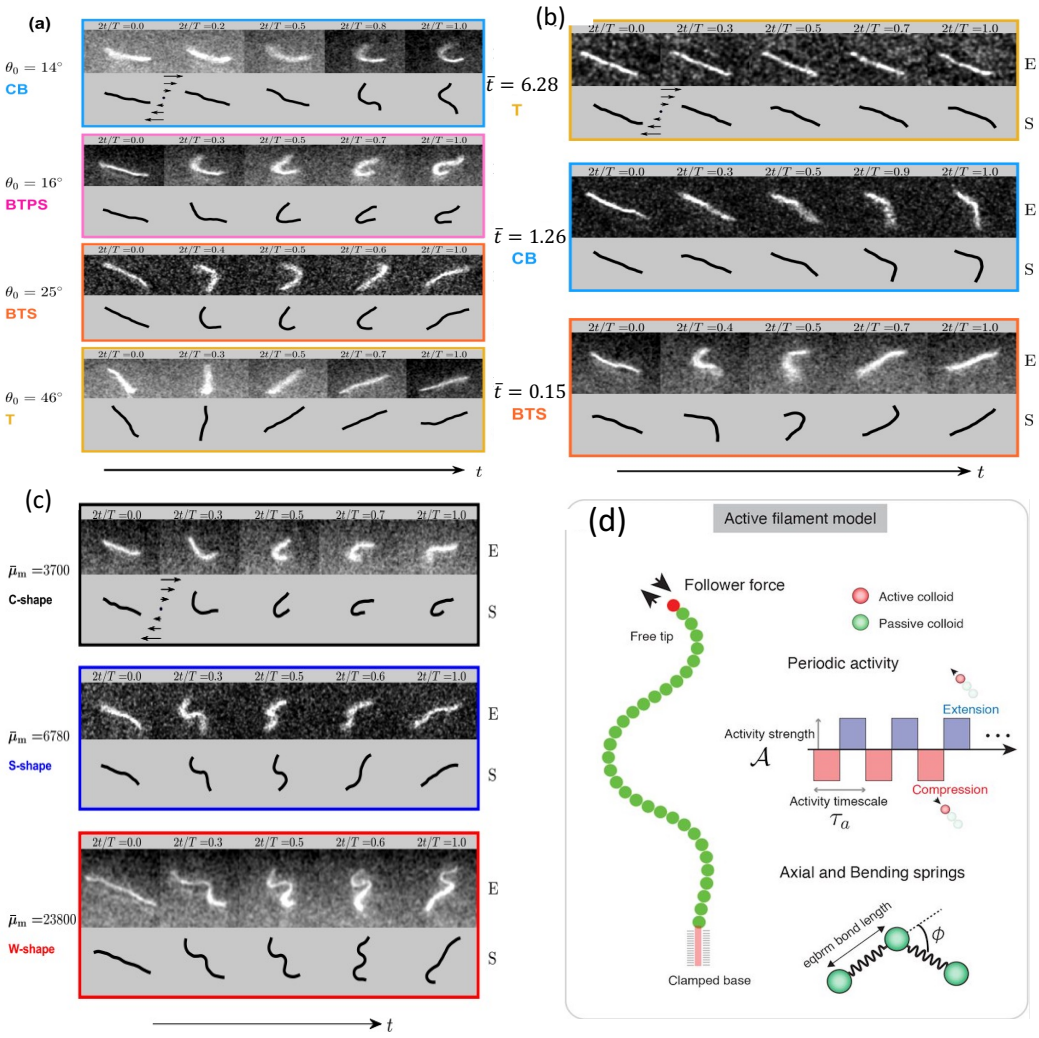

Fig. 9.1.: Filament driven in time-periodic manner: (a,b,c): Dynamics of the filament in oscillatory shear flows based on initial orientation θ_0 **(a)**, $\tilde{t}$ **(b)** and $\overline{\mu}_m = \overline{\mu}/(1 + 2\ln(d) - 2\ln(e))$ **(c)**. Here *(CB)*, *(BTPS)*, *(BTS)* and *(T)* are abbreviations of continuous buckling, buckling then partial stretching, buckling then stretching and tumbling. *E* and *S* means experimental and simulation results respectively. **(d):** Model of the active filament by Ref. [7]. The green beads are passive and red beads are active. The activity of the bead is time-periodic. Figure adapted with permission from [6, 7].

2. Instead of the background flow, activity can induce mixing at zero Reynolds number. Consider a device with a few, but not too many, filament clamped at one of walls. Such a device, when irradiated with certain frequency of light [11, 12], can be an efficient mixer.

9.2 Elastic properties of shells

We became interested in studying elastic properties of shells, due to a very general but important question: "how much are the physical properties affected by the fact that most cells are not in equilibrium" [13, 14, 15, 16, 17]? To understand this, we considered one of the fundamental problems in the theory of shells that how is buckling affected with an inclusion of activity. We realized the need of an open source software for Monte Carlo simulation of spherical shells [1] due to growing interest in elasticity in biological systems. The package is written in C++ and Python and we have released it under the GNU GPL-3.0 license. The package is helpful for biophysicists working on Cells, Nano-vesicles, etc.

We further add the modification to this package to perform Monte Carlo simulations for shells which are not in equilibrium. We show that, for the same set of elastic parameters, a shell that is not buckled in thermal equilibrium can be buckled if turned active. Similarly a shell that is buckled in thermal equilibrium can unbuckle if turned quiescent. The results are interesting from a fundamental point of view, but they also points us towards an intriguing possibility that it is possible to experimentally design microscopic elastic shells whose buckling can be optically controlled. In such devices it may be possible to drive flows at microscopic scales by buckling and unbuckling of shells, optically. Future extensions are as follows. 1) synthetic membranes that can be turned active ($A > 0$) optically, has been already realized by embedding certain proteins in a bi-lipid membranes – proteins that act as active pumps when irradiated with light of certain frequency [11, 12]. In such cases, only a fraction of points on the shell are active. This can be incorporated in a straightforward manner in our code and it would be interesting to see how the critical buckling pressure changes as we change the fraction of active points. 2) bi–lipid membranes are semi-permeable [18]. As the shell buckles the fraction of solute increases, increasing the partial pressure inside the shell. Experimentally, this can be avoided by using shell with holes in them. We expect in such cases the buckling pressure may change by a small amount.

References

[1] Vipin Agrawal, Vikash Pandey, Hanna Kylhammar, Apurba Dev, and Dhrubaditya Mitra. "MeMC: A package for Monte Carlo simulations of spherical shells". In: *Journal of Open Source Software* 7.74 (2022), p. 4305. URL: https://doi.org/10.21105/joss.04305.

[2] Vipin Agrawal and Dhrubaditya Mitra. *Flexible filament in time-periodic viscous flow: shape chaos and period three*. 2022. arXiv: 2210.04781 [cond-mat.soft].

[3] Yanan Liu, Brato Chakrabarti, David Saintillan, Anke Lindner, and Olivia Du Roure. "Morphological transitions of elastic filaments in shear flow". In: *Proceedings of the National Academy of Sciences* 115.38 (2018), pp. 9438–9443.

[4] Tien-Yien Li and James A Yorke. "Period three implies chaos". In: *The theory of chaotic attractors*. Springer, 2004, pp. 77–84.

[5] Aleksandr Nikolaevich Sharkovskii. "COEXISTENCE OF CYCLES OF A CONTINUOUS MAP OF THE LINE INTO ITSELF". In: *International Journal of Bifurcation and Chaos* 05 (1995), pp. 1263–1273.

[6] Francesco Bonacci, Brato Chakrabarti, David Saintillan, Olivia du Roure, and Anke Lindner. "Dynamics of flexible filaments in oscillatory shear flows". In: *arXiv preprint arXiv:2205.08361* (2022).

[7] Deepak Krishnamurthy and Manu Prakash. "Emergent Programmable Behavior and Chaos in Dynamically Driven Active Filaments". In: *bioRxiv* (2022).

[8] Vipin Agrawal and Dhrubaditya Mitra. "Chaos and irreversibility of a flexible filament in periodically driven Stokes flow". In: *Physical Review E* 106.2 (2022), p. 025103.

[9] Charles S Peskin. "The immersed boundary method". In: *Acta numerica* 11 (2002), pp. 479–517.

[10] Thomas T Bringley and Charles S Peskin. "Validation of a simple method for representing spheres and slender bodies in an immersed boundary method for Stokes flow on an unbounded domain". In: *Journal of Computational Physics* 227.11 (2008), pp. 5397–5425.

[11] P Girard, J Prost, and P Bassereau. "Passive or active fluctuations in membranes containing proteins". In: *Physical review letters* 94.8 (2005), p. 088102.

[12] P Manneville. "Turbulent patterns made simple?" In: *Journal of Fluid Mechanics* 796 (2016), pp. 1–4.

[13] Zhangli Peng, Xuejin Li, Igor V Pivkin, et al. “Lipid bilayer and cytoskeletal interactions in a red blood cell”. In: *Proceedings of the National Academy of Sciences* 110.33 (2013), pp. 13356–13361.

[14] Hervé Turlier, Dmitry A Fedosov, Basile Audoly, et al. “Equilibrium physics breakdown reveals the active nature of red blood cell flickering”. In: *Nature physics* 12.5 (2016), pp. 513–519.

[15] Arikta Biswas, Amal Alex, and Bidisha Sinha. “Mapping cell membrane fluctuations reveals their active regulation and transient heterogeneities”. In: *Biophysical journal* 113.8 (2017), pp. 1768–1781.

[16] Hervé Turlier and Timo Betz. “Unveiling the active nature of living-membrane fluctuations and mechanics”. In: *Annual Review of Condensed Matter Physics* 10 (2019), pp. 213–232.

[17] Sreekanth K Manikandan, Tanmoy Ghosh, Tithi Mandal, et al. “Estimate of entropy generation rate can spatiotemporally resolve the active nature of cell flickering”. In: *arXiv preprint arXiv:2205.12849* (2022).

[18] Rob Phillips, Jane Kondev, Julie Theriot, Hernan G Garcia, and Nigel Orme. *Physical biology of the cell*. Garland Science, 2012.

PART II

APPENDIX

A

OVERDAMPED HARMONIC OSCILLATOR

In this appendix, we comment on the validity of overdamping limit in Stokes flow. We consider a harmonic oscillator immersed in a fluid. We further consider the oscillator to move so slowly such that the drag from the fluid is well approximated by the Stokes drag. This is given as (see chapter 7 of [1]):

$$m\frac{\partial^2 R}{\partial t^2} + \alpha\frac{\partial R}{\partial t} + kR = f \tag{A.1}$$

where m is mass of the particle, α is the friction coefficient, k is the spring constant and R is the position. First term, $m\partial^2 R/\partial t^2$ in the equation (A.1) represents inertial effects, $\alpha\partial R/\partial t$ is the dissipation in the system, f is an external fore and kR is the conservative force.

Consider setting up $\alpha = 0$ in (A.1), the system performs an oscillatory motion infinitely for some initial perturbation from equilibrium position – This is an undamped state of the system. For $\alpha \neq 0$, oscillation in the system gradually decays towards zero amplitude or attenuate. Equation A.1 also reads as:

$$\frac{\partial^2 R}{\partial t^2} + 2\omega_0\zeta\frac{\partial R}{\partial t} + \omega_0^2 R = \frac{f}{m} \tag{A.2}$$

where

$$\omega_0^2 = k/m, \qquad \zeta = \frac{\alpha}{2\sqrt{km}}$$

is the damping ratio of the system. For this system, we take ζ to be always positive – which is a fair assumption for a particle in viscous flow. Let us not worry about external force, and consider an ansatz $R = \exp(\mathrm{i}\omega t)$ which is put in (A.2) to give the following relation [1]:

$$-\omega^2 + \omega_0^2 + 2\mathrm{i}\zeta\omega_0\omega = 0 \tag{A.3}$$

with solutions

$$\omega = \omega_0\left(\mathrm{i}\zeta \pm \sqrt{1-\zeta^2}\right) = \omega_0\mathrm{i}\zeta \pm \omega_1 \tag{A.4}$$

If the system has damping ratio $\zeta < 1$, ω_1 is real and the system oscillates with frequency ω_1 but the amplitude of oscillation decays to zero – this is called an underdamped oscillator. If $\zeta > 1$, ω_1 is imaginary, the system does not oscillates but decays exponentially – this is called an overdamped oscillator. If $\zeta = 1$, the equation A.3 has two repeated roots, the system decays exponentially as well in this case but faster than the overdamped case [1, 2].

For a particle in fluid,

$$\zeta \sim \frac{\eta}{\sqrt{k\rho d}}$$

and if we consider the d to be very small, $\zeta \gg 1$ which is a reasonable assumption. For the overdamped case, the inverse decay times (inverse of frequency) are:

$$\tau_f^{-1} = \omega_0 \left(\zeta + \sqrt{\zeta^2 - 1}\right) \xrightarrow{\zeta \gg 1} 2\omega_0\zeta = \frac{\alpha}{m} \tag{A.5a}$$

$$\tau_s^{-1} = \omega_0 \left(\zeta - \sqrt{\zeta^2 - 1}\right) \xrightarrow{\zeta \gg 1} \frac{1}{2\zeta} = \frac{k}{\alpha} \tag{A.5b}$$

If $\zeta \gg 1$, the fast decay time, τ_f is very small as compared to the slow time decay, τ_s. Thus, for this limit, for long times compared to τ_f, this mode can be ignored. This is also same as neglecting the mass term in the equation A.1, A.2.

$$\alpha \frac{\partial R}{\partial t} = -kR \tag{A.6a}$$

$$\frac{\partial R}{\partial t} = -\frac{k}{\alpha}R = -\mu \frac{\partial \mathcal{H}_T}{\partial R} \tag{A.6b}$$

where $\mu = \alpha^{-1}$ is the total dissipation in the system from various sources, $\mathcal{H}_T$ is the total energy of the system.

References

[1] P Chaikin and TC Lubensky. *Introduction to Condensed Matter Physics*. 1995.

[2] H Goldestein. *Classical mechanics, Massachusetts*. 1980.

Part III

Papers

1

MeMC: A package for monte-carlo simulations of spherical shells

Vipin Agrawal[1,2], **Vikash Pandey**[1] **Dhrubaditya Mitra**[1]

[1] Nordita, KTH Royal Institute of Technology and Stockholm University, Roslagstullsbacken 23, 10691 Stockholm, Sweden

[2] Department of Physics, Stockholm university, Stockholm,Sweden.

Journal of Open Source Software (2022), vol. 7 (74), 4305

The MeMC is an open-source software package for monte-carlo simulation of elastic shells. It is designed as a tool to interpret the force-distance data generated by indentation of biological nano-vesicles by atomic force microscopes. The code is written in c++ and python. The code is customizable – new modules can be added in a straightforward manner.

1. Statement of need and purpose of software

Micro and nano vesicles, both natural and synthetic, play a crucial role in biology and medicine. The physical properties of these vesicles play an important role in their biological functions (Phillips *et al.* 2012). Hence it is important to be able to measure their elastic constants, in particular the Young's modulus and the bending rigidity. One way to measure the elastic constants of biological objects, e.g., a red blood cell (RBC), is to poke them with an atomic force microscope (AFM) to obtain a force-distance curve. Then we must model the biological object as an elastic material and by fitting this model to the experimental force-distance curve to estimate the parameters of the elastic model, i.e., the elastic constants. As an example, consider a force-distance curve obtained by AFM measurements of an RBC. The RBC is modeled as a linear elastic material with a Young's modulus, $Y_{3\mathrm{d}}$. Typically a Hertzian model of elastic bodies in contact (Landau and Lifshitz 1970, section 9) is used to measure $Y_{3\mathrm{d}}$. Nano vesicles differ from (micro-meter scale) cells in two important ways

1. The nano-vesicles are much smaller hence thermal fluctuations may effectively renormalize the elastic coefficients (Paulose *et al.* 2012; Košmrlj and Nelson 2017).
2. Cell membranes are strongly coupled to an underlying cytoskelton. Hence they may be modeled by a solid body (HW *et al.* 2002) but nano-vesicles must be modeled as liquid filled elastic membranes.

Hence, to be able to interpret the force-distance curve of nano-vesicles, we need to solve for the elastic response of a thermally fluctuating elastic shell.

There are commercial packages, e.g., COMSOL (COMSOL), to calculate the force-distance curve of solid bodies and closed membranes with fluids inside under the action of external forces but to the best of our knowledge there is no package that includes thermal effects, which are important in nano-vesicles. Monte-carlo simulations of elastic membranes, that does include thermal fluctuations, have been done for more than three decades (Goetz *et al.* 1999; Bowick *et al.* 2001; Auth and Gompper 2005; Paulose *et al.* 2012), see also (Gompper and Kroll 2004, for a review). But to the best of our knowledge there is no open-source code available. The goal of this package is to fill this gap in open-source software.

2. Theoretical background

Our model of nano-vesicles is an homogeneous amorphous membrane enclosing an incompressible fluid (Vorselen *et al.* 2017). Unlike a solid ball, the force-distance relationship for such a model is linear for small deformation (Vorselen *et al.* 2017; Paulose *et al.* 2012) if we ignore thermal fluctuations. Ref. (Vorselen

et al. 2017) uses a similar model, ignoring thermal fluctuations, to interpret AFM measurement of nano-vesicles.

Let us consider a (three dimensional) material with Young's modulus Y_{3d} and Poisson's ratio σ_{3d} and make a membrane out of it. Then the bending modulus and the in-plane Young's modulus are (Landau and Lifshitz 1970, section 13 and 14)

$$B = \frac{Y_{3d}h^3}{12(1-\sigma_{3d}^2)} \quad \text{and} \quad Y = Y_{3d}h, \tag{1}$$

where h is the thickness of the membrane. This need not necessarily hold for biological membranes. Nevertheless consider a fluid enclosed by a solid membrane, as done in (Paulose *et al.* 2012). We consider an elastic energy of the form

$$\mathcal{E}[w, \boldsymbol{u}] = \int d^2x \left[\frac{B}{2}\left(\nabla^2 w\right)^2 + \mu u_{ij}^2 + \frac{\lambda}{2}u_{kk}^2 - pw\right] \tag{2a}$$

$$u_{ij} = \frac{1}{2}\left(\partial_i u_j + \partial_j u_i + \partial_i w \partial_j w\right) - \delta_{ij}\frac{w}{R} \tag{2b}$$

where w is the out-of-plane deformation of the shell, and $\boldsymbol{u}$ is the in-plane deformation, p is the pressure, λ and μ are the two in-plane Láme coefficients and B is the bending modulus. The Láme coefficients are related to other elastic constant in the following manner (Landau and Lifshitz 1970)

$$K = \lambda + \frac{2}{3}\mu \tag{3a}$$

$$Y = \frac{9K\mu}{3K+\mu} \tag{3b}$$

$$\sigma = \frac{1}{2}\frac{3K-2\mu}{3K+\mu} \tag{3c}$$

Here K is the volume compressibility, Y the Young's modulus, and σ the Poisson ratio.

If we consider the material to be incompressible, $K \to \infty$ and $\sigma = 1/2$, then there are two elastic constant, the bending rigidity B and the Young's modulus Y. Consequently, there are two dimensionless numbers, the Föppl–von-Karman number

$$\mathrm{FvK} = \frac{YR^2}{B} \tag{4}$$

and the Elasto-Thermal number:

$$\mathrm{ET} = \frac{k_B T}{B}\sqrt{\mathrm{FvK}} \tag{5}$$

where R is the radius of the spherical shell.

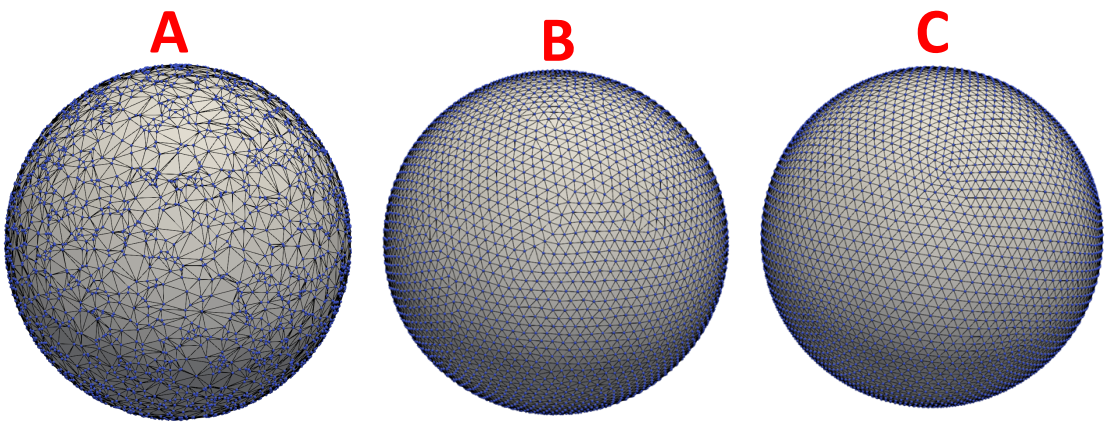

Figure 1: **Grid points on a sphere** (A)Triangulated random points on a sphere. (B) Triangulated points on sphere after 60000 SMC iteration of the initial configuration shown in (A). (C) An example of regular grid

Using values of Y and B from molecular dynamics simulations of lipid bilayers (Boek *et al.* 2005), $Y = 1.7\text{N/m}$ and $B = 5k_{\text{B}}T$ and $R = 100$ nano meter, we have FvK $\approx 0.3 \times 10^7$ which is close to the Föppl–von-Karman number for Graphene sheets and ET $\approx 10^3$.

3. Numerical implementation

3.1. Grid

Following Ref. (Gompper and Kroll 2004), we use a triangulated-network grid in the following manner. We start with N randomly chosen points on a sphere Fig. (1A). Then, we run a Monte-Carlo simulation, with a Lennard-Jones (LJ) repelling potential, of these points moving on the surface. Once the surface Monte-Carlo (SMC) has reached an equilibrium, we use the algorithm in Ref. (Caroli *et al.* 2009) to construct the Delaunay triangulation of these points. The connection between the points thus formed is kept unchanged. In the rest of this paper we call this the *initial configuration*. A different snapshot from the same equilibrium gives an equivalent but differently triangulated grid.

An alternative is to use a regular grid (Vliegenthart and Gompper 2006; Buenemann and Lenz 2008). This is achieved by approximating the sphere with geodesic polyhedron [Fig. (1C)] . They can be generated using *Meshzoo* library (A simple and fast mesh generator). In this paper we use $N = 5120$ for the random grid and $N = 5292$ for the regular grid.

3.2. Energy

The basic algorithm of the Monte-Carlo simulations is straightforward and well-known (see, e.g., Baumgärtner *et al.* 2013). We randomly choose a point on the grid and move it by a random amount. We calculate the change in energy due to this movement. We accept or reject the move by the standard Metropolis algorithm. In our code the energy has the following contributions

$$E = E_{\rm s} + E_{\rm bend} + E_{\rm bulk} \tag{6}$$

where $E_{\rm s}$ is the contribution from stretching, $E_{\rm bend}$ is the contribution from bending, and $E_{\rm bulk}$ is the contribution from the bulk modulus. Below, we describe each one of them in turn.

3.2.1. *Stretching*

In the initial configuration, two neighboring points with coordinates $\boldsymbol{R}_{\rm i}$ and $\boldsymbol{R}_{\rm j}$ are connected by a bond of length $\ell^0_{\rm ij}$. When the i-th point is moved, all its bonds with the neighbors change from their initial length. We model each of these bonds by a harmonic spring and calculate the stretching energy by

$$E_{\rm s}\frac{1}{2}\sum_i \frac{H}{2}\sum_{j(i)}\left(R_{\rm ij}-\ell^0_{\rm ij}\right)^2 \quad \text{where} \tag{7a}$$

$$R_{\rm ij} \equiv |\boldsymbol{R}_{\rm i} - \boldsymbol{R}_{\rm j}|. \tag{7b}$$

Here the notation $j(i)$ denotes that the sum is over all the nearest neighbors of the i-th point.

The Láme coefficients (λ, μ) and the Young's modulus (Y) are given by (Seung and Nelson 1988)

$$\lambda = \mu = \frac{\sqrt{3}}{4}H, \quad Y = \frac{2}{\sqrt{3}}H. \tag{8}$$

3.2.2. *Bending*

To calculate the bending contribution, we need to calculate the curvature. In the continuum limit, i.e. $N \to \infty$, bending energy (Nelson *et al.* 2004) is:

$$E_{\rm B} = \frac{B}{2}\int (\nabla^2 \boldsymbol{R})^2 dS, \tag{9}$$

where $\boldsymbol{R}$ is the vector of a point on the surface of the sphere, $\nabla^2\boldsymbol{R}$ is Laplacian of $\boldsymbol{R}$ on the surface of the sphere.

A general introduction to discretization of Laplacian on a triangulated mesh is given in Refs.(Itzykson 1986; Hege and Polthier 2003). Laplacian on a 2D

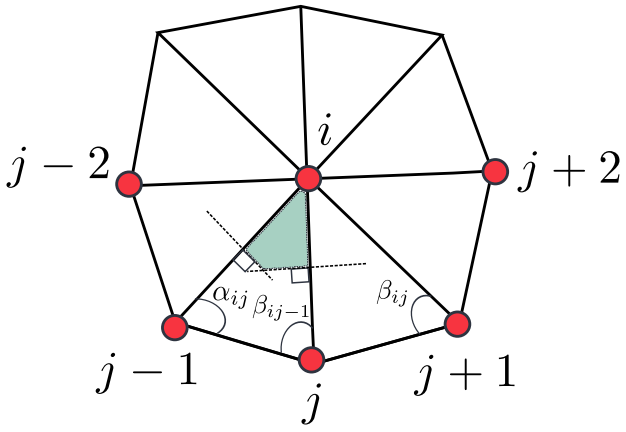

Figure 2: An example of triangulated mesh at the node i. $\alpha_{\rm ij}, \beta_{\rm ij}$ are the angles opposite to the bond ij. Shaded part is the Voronoi region of triangle T which is defined by the nodes $(i, j-1, j)$. Here, we consider that the triangle T is acute.

manifold embedded in $\mathbb{R}^3$ is:

$$\boldsymbol{L}(\boldsymbol{R}) = 2\kappa(\boldsymbol{R})\hat{\boldsymbol{m}}(\boldsymbol{R}), \tag{10}$$

where $\kappa(\boldsymbol{R})$ is the mean curvature, and $\hat{\boldsymbol{m}}(\boldsymbol{R})$ is the normal to the surface at $\boldsymbol{R}$. Note that, $\hat{\boldsymbol{m}}(\boldsymbol{R})$ is a local property of a point P with coordinates $\boldsymbol{R}$ and it is not necessarily the outward normal of the closed surface. In the discrete form (Hege and Polthier 2003; Meyer *et al.* 2003),

$$\boldsymbol{L}_i = \frac{1}{\mathcal{A}_i} \sum_{j(i)} \frac{1}{2} \left[\cot(\alpha_{\rm ij}) + \cot(\beta_{\rm ij})\right] \boldsymbol{R}_{\rm ij}. \tag{11}$$

Here, $\mathcal{A}_i$ is the area of Voronoi dual cell at the node i, and $\alpha_{\rm ij}, \beta_{\rm ij}$ are the angles opposite to bond ij as shown in Fig. (2). Consider the triangle T in Fig. (2) defined by its vertices $(i, j-1, j)$. If T is non-obtuse its circumcenter lies within it, hence so does the Voronoi region. Let $\mathcal{A}^{\rm c}$ be the area of shaded region in Fig. (2) given by (Meyer *et al.* 2003; Hege and Polthier 2003),

$$\mathcal{A}^{\rm c} = \frac{1}{8}\left[R_{\rm ij}^2 \cot(\alpha_{\rm ij}) + R_{\rm ij-1}^2 \cot(\beta_{ij-1})\right]. \tag{12}$$

If there is an obtuse angle in triangle T, the Voronoi region is not necessarily enclosed by the triangle (Hege and Polthier 2003). For such cases, instead of $\mathcal{A}^{\rm c}$, we use $\mathcal{A}^{\rm b}$, defined as (Hege and Polthier 2003; Meyer *et al.* 2003):

$$\mathcal{A}^{\rm b} = \left\{ \begin{array}{l} \frac{\rm area(T)}{2}, \text{angle of T at i is obtuse} \\ \frac{\rm area(T)}{4}, \text{any other angle is obtuse} \end{array} \right\}, \tag{13}$$

where area$(T) = 0.5\,|\boldsymbol{R}_{\mathrm{ij}} \times \boldsymbol{R}_{\mathrm{ij}-1}|$ is the area of the triangle T. The area $\mathcal{A}_i$ is obtained by summing up the contributions from all the triangles in Fig. (2), e.g., the contribution from the triangle T is the shaded area.

For a closed surface, the bending energy must be calculated relative to the spontaneous curvature, i.e., its discretised form is

$$E_{\mathrm{B}} = \frac{B}{2}\sum_{i} \mathcal{A}_i \left(\boldsymbol{L}_i - C\hat{\boldsymbol{n}}\right)^2 . \tag{14a}$$

where C is the spontaneous curvature, for a sphere $C = 2/R$, where R is radius of the sphere and $\hat{\boldsymbol{n}}$ is the outward normal to the surface. Hence not only the magnitude but also the vector nature of the surface Laplacian must be determined. For every triangle in the initial configuration, i.e., when all the points lie on the surface of a sphere, the outward unit normal can be calculated in a straightforward manner. For example, for the triangle T in Fig. (2) it can be calculated by finding out the unit vector that points along $\boldsymbol{R}_{\mathrm{ij}-1} \times \boldsymbol{R}_{\mathrm{ij}}$. Hence, at any time, if we access the points around the node i in counterclockwise manner when viewed from outside we are guaranteed to obtain the outward normal. We ensure this by sorting appropriately the points around every node in the initial configuration. As the connectivity of the mesh remains unchanged this property is preserved at all future times.

To sort the neighbors around any node i, we rotate the coordinate system such that, the z axis passes through the point i along the vector $\boldsymbol{R}_i$. In this coordinate system we sort the neighbors by their azimuthal angle.

Note that unlike Ref. (Gompper and Kroll 2004) we do not incorporate self-avoidance.

3.2.3. *Bulk*

We assume that the liquid inside the vesicle is incompressible [1]. This is implemented by adding a energy cost to the volume change. At any point, the total contribution to the bulk energy is

$$E_{\mathrm{bulk}} = K\left(\frac{V}{V_0} - 1\right)^2 , \tag{15}$$

where K is bulk modulus, V is current volume, and V_0 is the undeformed initial volume of the vesicle. As we move the point i by a random amount, the change

[1] This is different from assuming a semi-permeable membrane, as done in Ref. (Vorselen *et al.* 2017), in which case the liquid can flow in or out and the osmotic pressure of solutes decreases and increases accordingly.

in bulk energy is

$$\Delta E_{\rm bulk} = 2K \left(\frac{\Delta V (V - V_0)}{V_0^2} + \left(\frac{\Delta V}{V_0} \right)^2 \right), \tag{16}$$

where ΔV is the change in volume due to the move.

3.2.4. *Pressure*

With addition of contribution from pressure difference from inside and outside the shell our code can also be used for pressurized shells.

3.3. Sticking to a solid surface

As a specific example of nano-vesicle, we consider an exosome. We quote from Ref. (Pegtel and Gould 2019) " Exosomes are small, single-membrane, secreted organelles of $\sim$ 30 to $\sim$ 200 nm in diameter that have the same topology as the cell and are enriched in selected proteins, lipids, nucleic acids, and glycoconjugates. " The exosomes that we consider here were collected from immortalized cell line and extracted following the procedures as described in Ref. (Cavallaro *et al.* 2019). To measure the force-distance curve, it is necessary to fix an exosome on a transparent coverslip. This was done by electrostatic coupling to a PLL coated surface by incubating them at room temperature for one hour, see Ref (Cavallaro *et al.* 2019). As an illustration, in Fig. (3), we show a typical experimental measurement of the height above a flat surface as measured by the AFM. After being stuck to the flat surface the free surface forms a spherical cap. To reproduce such experiments as closely as possibly we need to fix the vesicle to a flat surface. This is implemented by the Lennard-Jones potential:

$$V_{\rm LJ}(r) \equiv 4\epsilon_{\rm w} \left[\left(\frac{\sigma_{\rm w}}{r} \right)^{12} - \left(\frac{\sigma_{\rm w}}{r} \right)^{6} \right] \tag{17}$$

What fraction of the vesicle is fixed to the flat surface is parametrized by the angle Θ_0 (see Fig. (3B)) which is a parameter in our code. We choose a system of coordinates with its origin at the center of the vesicle and the z axis pointing radially outward through the north pole. All the grid points on the surface whose polar angle is greater than Θ_0 are selected such that the sticking potential acts only on them, see Fig. (3B).

3.4. AFM tip

To model the interaction between AFM tip and the vesicle, We model the shape of tip as paraboloid and we use only the repelling part of the Lennard-Jones potential:

$$V_{\rm RLJ}(r) \equiv 4\epsilon_{\rm A} \left(\frac{\sigma_{\rm A}}{r} \right)^{12} \tag{18}$$

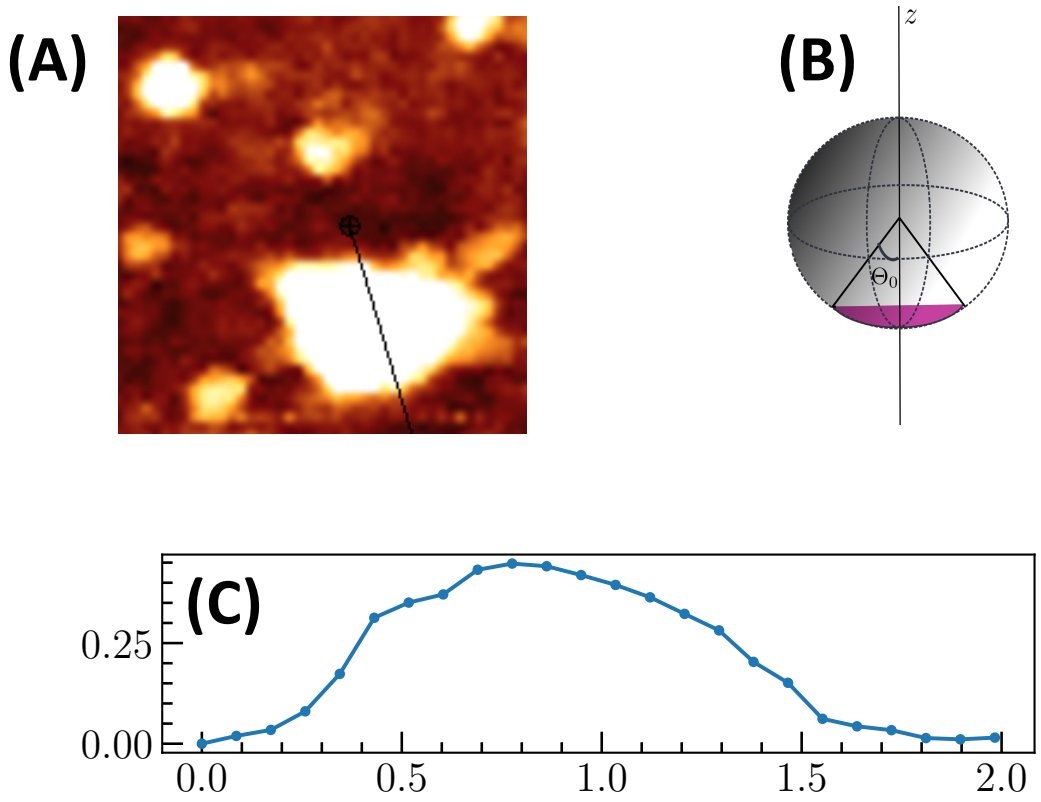

Figure 3: (A) A colormap of the height as measured by the AFM. (B) Illustration of the vesicle stuck to a flat surface by an angle Θ_0. (C) The height plotted along the line shown in (A).

For every point on the vesicle we calculate the shortest distance of this point to the paraboloid and use this distance as the argument of function V_{RLJ} in (18).

4. Dependencies

The code requires the following:

- A c++ compiler. We have tested the code with gnu g++ version 11.2.0 on x86_64 CPU.
- Hdf5 libraries for reading and writing data.
- Python version 3.8 with scipy, numpy, h5py and numpy-quaternion installed.
- For three-dimensional visualization we use VisIt (Childs *et al.* 2012).

5. Typical workflow and test

We have tested our code in LINUX operating system. We expect it to work without any problem in any similar environment. It may also work with WINDOWS although we have not tested this aspect.

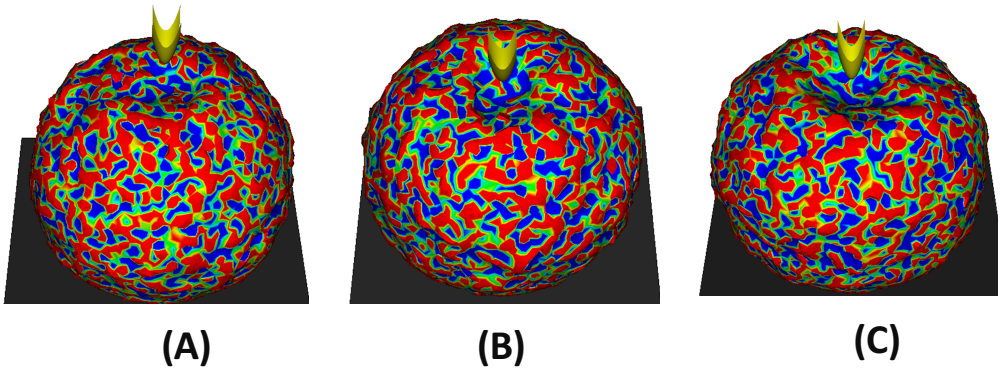

Figure 4: Representative snapshots from our code for three different positions (t_z) of the AFM tip. The origin of our coordinate system is at the center of the undeformed sphere and the radius of the undeformed sphere is unity. The colormap shows the signed curvature (10); red(positive) and blue (negative). (A) $t_z = 1.05$, (B) $t_z = 0.9$, (C) $t_z = 0.75$.

The github repository (Monte-Carlo for elastic shells) contains a a file named `README.md` that contains instructions to install and run the code. In Fig. (4) we show three typical snapshots from our code for three different positions of the AFM tip.

In the github repository, we also provide a subdirectory called `Examples`. By executing the shell script `execute.sh` in that directory the user can run the code (without the AFM tip and the bottom plate). It takes almost 30 minutes on Intel(R) Core(TM) i5-8265U CPU. The run produces a probability distribution function (PDF) of the total energy after 50,000 number of Monte -carlo steps. By running `gnuplot plot.gnu` (this requires the software gnuplot) the user can compare the PDF obtained by their run with the PDF that we provide.

References

Rob Phillips, Jane Kondev, Julie Theriot, Hernan G Garcia, and Nigel Orme, *Physical biology of the cell* (Garland Science, 2012).

LD Landau and EM Lifshitz, *Theory of Elasticity*, Course of Theoretical Physics, Vol. 7 (Pergamon Press Ltd., Oxford, England, 1970).

Jayson Paulose, Gerard A Vliegenthart, Gerhard Gompper, and David R Nelson, "Fluctuating shells under pressure," Proceedings of the National Academy of Sciences **109**, 19551–19556 (2012).

Andrej Košmrlj and David R Nelson, "Statistical mechanics of thin spherical shells," Physical Review X **7**, 011002 (2017).

Gerald Lim HW, Michael Wortis, and Ranjan Mukhopadhyay, "Stomatocyte–discocyte–echinocyte sequence of the human red blood cell: Evidence for the bilayer–couple hypothesis from membrane mechanics," Proceedings of the National Academy of Sciences **99**, 16766–16769 (2002).

COMSOL, https://www.comsol.com.

Rüdiger Goetz, Gerhard Gompper, and Reinhard Lipowsky, "Mobility and elasticity of self-assembled membranes," Physical review letters **82**, 221 (1999).

Mark J Bowick, Angelo Cacciuto, Gudmar Thorleifsson, and Alex Travesset, "Universality classes of self-avoiding fixed-connectivity membranes," The European Physical Journal E **5**, 149–160 (2001).

Thorsten Auth and Gerhard Gompper, "Fluctuation spectrum of membranes with anchored linear and star polymers," Physical Review E **72**, 031904 (2005).

G Gompper and DM Kroll, "Triangulated-surface models of fluctuating membranes," in *Statistical mechanics of membranes and surfaces*, edited by David Nelson, Tsvi Piran, and Steven Weinberg (World Scientific, 2004) pp. 359–426.

Daan Vorselen, Fred C MacKintosh, Wouter H Roos, and Gijs JL Wuite, "Competition between bending and internal pressure governs the mechanics of fluid nanovesicles," Acs Nano **11**, 2628–2636 (2017).

ES Boek, JT Padding, Wouter K den Otter, and Willem J Briels, "Mechanical properties of surfactant bilayer membranes from atomistic and coarse-grained molecular dynamics simulations," The Journal of Physical Chemistry B **109**, 19851–19858 (2005).

Manuel Caroli, Pedro Machado Manhães de Castro, Sebastien Loriot, Olivier Rouiller, Monique Teillaud, and Camille Wormser, *Robust and Efficient Delaunay triangulations of points on or close to a sphere*, Ph.D. thesis, INRIA (2009).

Gerard Adriaan Vliegenthart and Gerhard Gompper, "Mechanical deformation of spherical viruses with icosahedral symmetry," Biophysical journal **91**, 834–841 (2006).

Mathias Buenemann and Peter Lenz, "Elastic properties and mechanical stability of chiral and filled viral capsids," Physical Review E **78**, 051924 (2008).

A simple and fast mesh generator, https://github.com/meshpro/meshzoo.

Artur Baumgärtner, Kurt Binder, J-P Hansen, MH Kalos, K Kehr, DP Landau, D Levesque, H Müller-Krumbhaar, C Rebbi, Y Saito, *et al.*, *Applications of the Monte Carlo method in statistical physics*, Topics in Current Physics, Vol. 36 (Springer Science & Business Media, 2013).

Hyunjune Sebastian Seung and David R Nelson, "Defects in flexible membranes with crystalline order," Physical Review A **38**, 1005 (1988).

David Nelson, Tsvi Piran, and Steven Weinberg, *Statistical mechanics of membranes and surfaces* (World Scientific, 2004).

C Itzykson, in *Proceedings of the GIFT seminar, Jaca 85*, edited by J *et al* Abad (World Scientific Singapore, 1986) pp. 130–188.

Hans-Christian Hege and Konrad Polthier, *Visualization and mathematics III* (Springer Science & Business Media, 2003).

Mark Meyer, Mathieu Desbrun, Peter Schröder, and Alan H Barr, "Discrete differential-geometry operators for triangulated 2-manifolds," in *Visualization and mathematics III* (Springer, 2003) pp. 35–57.

This is different from assuming a semi-permeable membrane, as done in Ref. Vorselen *et al.* (2017), in which case the liquid can flow in or out and the osmotic pressure of solutes decreases and increases accordingly.

D Michiel Pegtel and Stephen J Gould, "Exosomes," Annual review of biochemistry **88**, 487–514 (2019).

Sara Cavallaro, Josef Horak, Petra Haag, Dhanu Gupta, Christiane Stiller, Siddharth S Sahu, Andre Gorgens, Hithesh K Gatty, Kristina Viktorsson, Samir El Andaloussi, *et al.*, "Label-free surface protein profiling of extracellular vesicles by an electrokinetic sensor," ACS sensors **4**, 1399–1408 (2019).

Hank Childs, Eric Brugger, Brad Whitlock, Jeremy Meredith, Sean Ahern, David Pugmire, Kathleen Biagas, Mark Miller, Cyrus Harrison, Gunther H. Weber, Hari Krishnan, Thomas Fogal, Allen Sanderson, Christoph Garth, E. Wes Bethel, David Camp, Oliver Rübel, Marc Durant, Jean M. Favre, and Paul Navrátil, "VisIt: An End-User Tool For Visualizing and Analyzing Very Large Data," in *High Performance Visualization–Enabling Extreme-Scale Scientific Insight* (2012) pp. 357–372.

Monte-Carlo for elastic shells, https://github.com/vipinagrawal25/MeMC

2

Active buckling of pressurized spherical shells : Monte Carlo Simulation

Vipin Agrawal[1,2], **Vikash Pandey**[1] **Dhrubaditya Mitra**[1]

[1] Nordita, KTH Royal Institute of Technology and Stockholm University, Roslagstullsbacken 23, 10691 Stockholm, Sweden

[2] Department of Physics, Stockholm university, Stockholm,Sweden.

arXiv:2206.14172

We study the buckling of pressurized spherical shells by Monte Carlo simulations in which the detailed balance is explicitly broken – thereby driving the shell active, out of thermal equilibrium. Such a shell typically has either higher (active) or lower (quiescent) fluctuations compared to one in thermal equilibrium depending on how the detailed balance is broken. We show that, for the same set of elastic parameters, a shell that is not buckled in thermal equilibrium can be buckled if turned active. Similarly a shell that is buckled in thermal equilibrium can unbuckle if turned quiescent. Based on this result, we suggest that it is possible to experimentally design microscopic elastic shells whose buckling can be optically controlled.

Thin spherical shells are commonly found in many natural and engineering settings. Their sizes can vary over a very large range – from hundred meters, e.g., the Avicii Arena Stockholm [2] down to about hundred nanometers, e.g., viral capsules (Buenemann and Lenz 2008,?; Michel *et al.* 2006) and exosomes (Pegtel and Gould 2019; Cavallaro *et al.* 2019). The elastic properties of shells, including conditions under which buckling can occur, have been extensively studied (Love 2011; Landau and Lifshitz 1970; Koiter 1963; WT 1976; Pogorelov 1988; Hutchinson 2016). Interest in this traditional field of applied mathematics has been rekindled in the past decades because of possible applications to biology and nanoscience (Vliegenthart and Gompper 2006; Gao *et al.* 2001; Gordon *et al.* 2004). For example, one of the most-used methods to determine the elastic modulii of microscopic shells is to measure their force–distance curves while poking them with an atomic force microscope (AFM) and then interpreting the data in the light of the theory of elastic shells (Buenemann and Lenz 2008; Vella *et al.* 2012; Vorselen *et al.* 2017; Wu *et al.* 2018; Vorselen *et al.* 2020; Cavallaro *et al.* 2021; Michel *et al.* 2006; Zoldesi *et al.* 2008). More recently, it has been shown that for small enough shells thermal fluctuations can decrease the critical buckling pressure by a large amount (Paulose *et al.* 2012; Košmrlj and Nelson 2017). This opens up the intriguing possibility of how the elastic properties of shells, in particular buckling, will change if they are turned active – driven out of thermal equilibrium.

It was realized very early in biophysics (Schrödinger 2012), that the fundamental property of living matter is that they are not in thermal equilibrium even when they are statistically stationary. They are active – they consume energy and generate entropy (Gnesotto *et al.* 2018). The statistical and mechanical properties of such matter is a current topic of considerable interest (Marchetti *et al.* 2013; Ramaswamy 2010). Membrane of any living cell can be considered as an active shell, although not necessarily spherical, because the fluctuations of its membrane have active components, in addition to the thermal fluctuations, due to active processes occurring on the membrane (e.g., endo–cytosis and exo–cytosis) and the driving by the active cytoskeleton (Peng *et al.* 2013; Turlier *et al.* 2016; Biswas *et al.* 2017; Turlier and Betz 2019; Manikandan *et al.* 2022). Active shells can also be synthetically designed, e.g., by embedding certain proteins in a bi-lipid membranes – proteins that act as active pumps when irradiated with light of certain frequency (Girard *et al.* 2005; Manneville *et al.* 2001). Shells made out of hard–magnetic elastomers can be turned active by an external magnetic field (Yan *et al.* 2021). In this paper we study the buckling of pressurized active spherical shells by Monte Carlo (MC) simulations (Kumar

[2]There are several geodesic domes with sizes ranging from 10 to 200 meters.

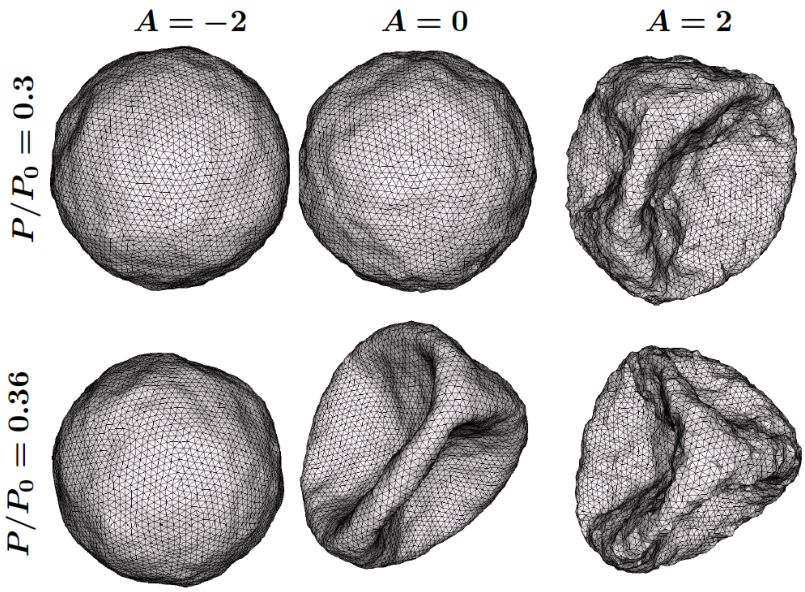

Figure 1: **Active buckling:** Typical snapshots from our simulations for activity $A = -2$, 0 and 2 (from left to right), and pressure $P = 0.30P_0$ (top row) and $0.36P_0$ (bottom row) where P_0 is the critical buckling pressure obtained from the mechanical theory of elastic shells, i.e., at zero temperature. We use $N = 5120$, FvK $= 4616$, and ET $= 8$. The middle column, $A = 0$, corresponds to shells in thermal equilibrium – an unbuckled shell buckles upon increasing P/P_0 from 0.30 to 0.36. This is consistent with the results of Refs. (Paulose *et al.* 2012; Košmrlj and Nelson 2017). Top row: As activity is increased to 2 (right column) the shell buckles. Bottom row: Whereas as activity is decreased to -2 (left column) the shell, that was buckled in thermal equilibrium, does not buckle at the same pressure.

and Dasgupta 2020) in which detailed balance is explicitly broken – thereby driving the shell active, out of thermal equilibrium. Such a shell typically has either higher or lower fluctuations than thermal ones depending on how the detailed balance is broken. We call such non-equilibrium stationary states *active* and *quiescent* respectively. We show that, within the right range of elastic parameters, a shell that is not buckled in thermal equilibrium can be buckled if turned active. Similarly a shell that is buckled in thermal equilibrium can unbuckle if turned quiescent, see Fig. (1). Based on this, we suggest that it is possible to experimentally design microscopic elastic shells whose buckling can be optically controlled.

Let us briefly summarize, following Refs. (Paulose *et al.* 2012; Košmrlj and Nelson 2017) the model and the key results of theory of thin elastic shells in *thermal equilibrium*. A pressurized elastic shell is described by an effective

Hamiltonian, $G_{\text{eff}} = G_0 + G_1$ where,

$$G_0[f] = \frac{1}{2}\int \mathrm{d}^2x \left[B(\nabla^2 f)^2 - \frac{PR}{2} \mid \boldsymbol{\nabla} f \mid^2 + \frac{Y}{R^2} f^2\right], \text{ and} \tag{1a}$$

$$G_1[f] = \frac{Y}{2}\int \mathrm{d}^2x \left[\left(\frac{1}{2}\mathcal{P}_{ij}\partial_i f \partial_j f\right)^2 - \frac{f}{R}\mathcal{P}_{ij}\partial_i f \partial_j f\right]. \tag{1b}$$

Here $\boldsymbol{x} = (x_1, x_2)$ is a two-dimensional Cartesian coordinate system and $\mathcal{P}_{ij} \equiv \delta_{ij} - \partial_i\partial_j/\nabla^2$ is the transverse projection operator. The out-of-plane displacement is $h(\boldsymbol{x}) = f_0(\boldsymbol{x}) + f(\boldsymbol{x})$ where $f_0(\boldsymbol{x})$ is the uniform contraction of the sphere in response to the external pressure. The difference between the external and the internal pressure is P. The part G_0 is harmonic and the part G_1 is anharmonic. In this model, we assume the shell to be amorphous and homogeneous with radius R, bending modulus B and (two–dimensional) Young's modulus Y. Two non-dimensional numbers determine the elastic behavior of such shells, the Föppl–von-Karman number and the Elasto-thermal number, defined respectively as

$$\mathrm{FvK} \equiv \frac{YR^2}{B}, \quad \mathrm{ET} \equiv \frac{k_{\mathrm{B}}T}{B}\sqrt{\mathrm{FvK}}, \tag{2}$$

where k_{B} is the Boltzmann constant and T is temperature. At constant ET, the effects of anharmonicity increases with FvK whereas at constant elastic modulii the effects of thermal fluctuations increases with ET. Ignoring the anharmonic contribution, using standard tools of equilibrium statistical mechanics it is straightforward (Paulose *et al.* 2012, Eq. 4) to calculate the spectrum of fluctuations

$$S(\boldsymbol{q}) \equiv \left\langle \hat{f}(\boldsymbol{q})\hat{f}(-\boldsymbol{q})\right\rangle = \frac{ak_{\mathrm{B}}T}{Bq^4 - \frac{PRq^2}{2} + \frac{Y}{R^2}}, \tag{3}$$

where $\hat{f}(\boldsymbol{q})$ is the Fourier transform of $f(\boldsymbol{x})$ and a is the area of integration in the (x_1, x_2) plane. In equilibrium, the symbol $\langle\cdot\rangle$ denotes thermal averaging; whereas for active cases, it denotes averaging over the non–equilibrium stationary states. Note that $S(\boldsymbol{q})$ blows-up for

$$P = P_0 \equiv \frac{4B}{R}q_*^2, \quad \text{where} \tag{4a}$$

$$q_* \equiv \left(\frac{Y}{BR^2}\right)^{1/4} = \frac{\mathrm{FvK}^{1/4}}{R}, \tag{4b}$$

where P_0 is the buckling pressure, independent of temperature, obtained within the traditional theory (Hutchinson 2016) of buckling of pressurized shells. For a large Föppl–von-Karman number, $q_* > 1/R$. is the buckling mode. Refs. (Paulose *et al.* 2012; Košmrlj and Nelson 2017) used renormalization

group (RG) techniques to show that the effects of the anharnomic terms is to renormalize the parameters appearing in the bare theory, i.e., P, B, and Y in (3) must be replaced by their scale–dependent, renormalized versions, see Ref. (Košmrlj and Nelson 2017, Eq. 18). Consequently both the pressure and the critical buckling pressure are renormalized and buckling is obtained if both of these quantities are equal for a length scale which must be smaller than the radius of the sphere (Košmrlj and Nelson 2017). The results of this RG analysis were validated by Monte Carlo simulations of spherical shell, randomly triangulated with N grid points, with discretized bending and stretching energies that translate directly into a macroscopic elastic modulii (Paulose *et al.* 2012; Gompper and Kroll 2004; Itzykson 1986). Our Monte Carlo code, described in detail in Ref. (Agrawal *et al.* 2022), closely follows that of Ref. (Paulose *et al.* 2012), and faithfully reproduces these results [3]. We incorporate activity into this model in the following manner.

Over the years, many theoretical models (Ramaswamy *et al.* 2000; Rao and R.C. 2001; Loubet *et al.* 2012; Maitra *et al.* 2014; Hawkins and Liverpool 2014; Yin *et al.* 2021; Goriely 2017), have been suggested to incorporate the effects of active fluctuations into models of membranes. All of these drive the membrane out of thermal equilibrium. In equilibrium Monte Carlo simulations the transition rate, W, from one state to another is given by the Metropolis algorithm:

$$W = \min[1, \exp(-E/k_{\mathrm{B}}T)], \tag{5}$$

where k_{B} is the Boltzmann constant, T is the temperature and E is the difference in energy between the two states. To drive the membrane out of equilibrium, following Ref. (Kumar and Dasgupta 2020), we replace E by $E + \Delta E$. This guarantees that detailed balance is broken and the amount by which it is broken is ΔE. If ΔE is positive (negative) the probability of acceptance of large fluctuations is decreased (increased). Thus we define $A = -\Delta E/(k_{\mathrm{B}}T)$ such that simulations with positive A, *active* simulations, have higher fluctuations than equilibrium ones whereas for negative A, *quiescent* simulations, the fluctuations are less than the equilibrium ones. For membranes in thermal equilibrium, micropipet aspiration shows $\Delta\alpha \propto (k_{\mathrm{B}}T/4\pi B)\ln\sigma$ where $\Delta\alpha$ is the areal strain and σ is the surface tension. This result can be obtained using standard techniques of equilibrium statistical mechanics (Turlier and Betz 2019). For active membranes the same proportionality holds but the constant of proportionality is different. This experimental result was captured by the model in Ref. (Prost and Bruinsma 1996) which adds an additional Ornstein–Uhlenbeck noise to the model of thermal membranes. We test our active Monte Carlo scheme,

[3] See Supplemental Material

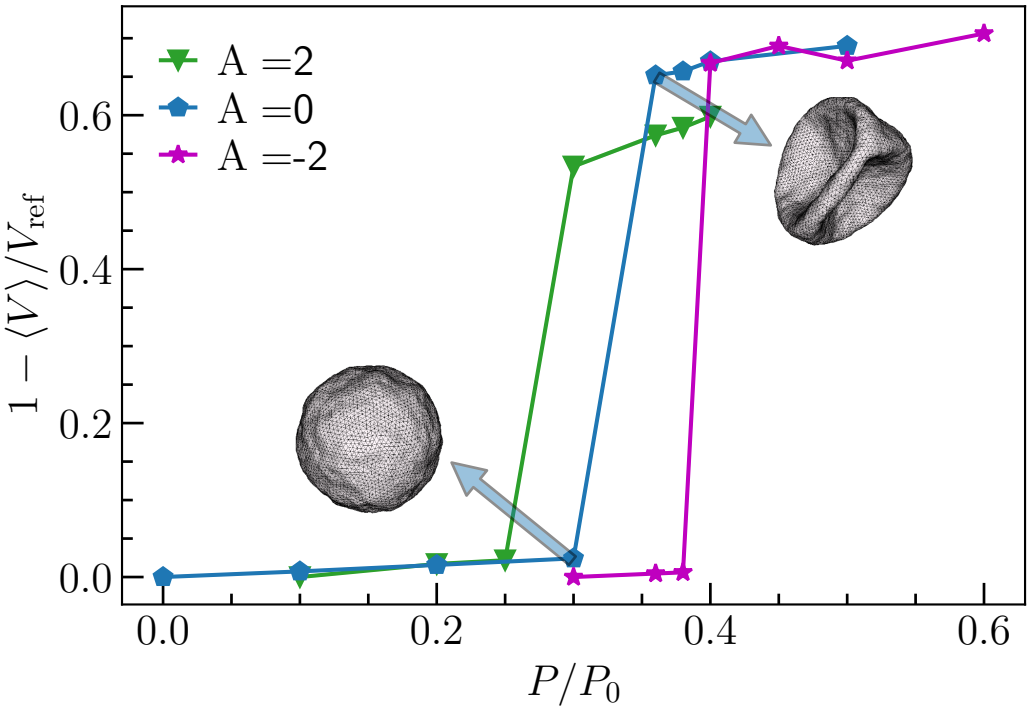

Figure 2: **Buckling under pressure:** Normalized change in volume as a function of external pressure for (blue) a shell in thermal equilibrium, (green) active ($A = 2$), and (magenta) quiescent ($A = -2$) for simulations with ET = 8 and FvK = 4616 and number of grid points $N = 5120$. Here $\langle V \rangle$ is the ensemble average of volume, and $V_{\rm ref}$ is the average volume at the smallest pressure difference. The error in $\langle V \rangle$ are the shades around the solid lines – they are too small to be visible. The signature of buckling is the sudden large change in volume. The critical buckling pressure for the thermal case is consistent with Refs (Paulose *et al.* 2012; Košmrlj and Nelson 2017).

in planar membranes [4] to reproduce the results of, Ref. (Prost and Bruinsma 1996) and also the experimental result of Ref. (Manneville *et al.* 2001). In summary, we incorporate the technique of active Monte Carlo (Kumar and Dasgupta 2020) into the Monte Carlo algorithm for spherical shells in thermal equilibrium (Paulose *et al.* 2012; Gompper and Kroll 2004; Agrawal *et al.* 2022) to simulate active shells. In our simulations we set the length scale $R = 1$ and the energy scale $k_{\rm B}T = 1$. A complete list of parameters are shown in table (1).

In Fig. (2) we show a typical plot of how the volume, V, of the spherical shell changes as the external pressure is increased from a very small value. The simulations are done in a constant pressure ensemble, hence volume is a

[4] A. Fragkiadoulakis, S.K. Manikandan, and D. Mitra, unpublished.

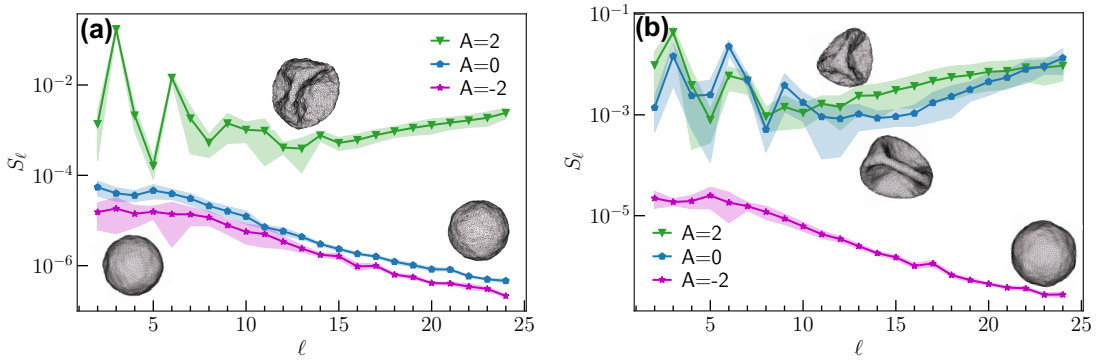

Figure 3: **Spectra:** The spectra, $S_{\ell,m}$, (6), for $m = 0$, $\ell \geq 2$ and (a) $P = 0.3P_0$ and (b) $P = 0.36P_0$ for thermal (blue) active (green, $A = 2$) and quiescent (magenta, $A = -2$). The solid lines and the shaded regions are the means and variances of spectra over many snapshots. Appearance of a peak at small ℓ signifies buckling.

fluctuating quantity. Henceforth, by volume we mean the average volume $\langle V \rangle$. The average volume at the smallest pressure difference, is the reference volume $V_{\rm ref}$. The error in $\langle V \rangle$, shown by the shaded regions in Fig. (2) are the variances – they are too minute to be visible. First consider the shell under thermal equilibrium. Buckling shows up as a sharp decrease in volume accompanied by a typical buckled shape, as shown in Fig. (1). The critical buckling pressure, $P_{\rm c}$, that we obtain is consistent with the results of Refs. (Paulose *et al.* 2012; Košmrlj and Nelson 2017). We show the results of the simulations for both the active, $A = 2$, and the quiescent, $A = -2$ cases. For the former the critical buckling pressure decreases while for the latter the critical buckling pressure increases.

Next we decompose the fluctuating height field, $f(\theta, \phi)$ in spherical harmonics, $\mathcal{Y}_{\ell,m}(\theta, \phi)$:

$$f(\theta,\phi) = \sum_{\ell,m} \tilde{f}_{\ell,m} \mathcal{Y}_\ell^m(\theta,\phi), \quad \text{and define} \tag{6a}$$

$$S_{\ell,m} = \left\langle |\tilde{f}_{\ell,m}|^2 \right\rangle \tag{6b}$$

In Fig. (3a) we plot the spectra $S_{\ell,m}$ for $P = 0.3P_0$ for the thermal ($A = 0$, blue), active ($A = 2$, red) and quiescent ($A = -2$, green) case. In Fig. (3b) we plot the same for $P = 0.36P_0$. The error in $S_{\ell,m}$, shown by the shaded regions in Fig. (3) are the variances. In particular, for the thermal case, we notice that the case $P = 0.3P_0$ has no prominent peak for small ℓ values and is not buckled, whereas for $P = 0.36P_0$ we observe buckling accompanied by a peak in $S_{\ell,m}$ at a small ℓ value. For the equilibrium case, buckling as a function

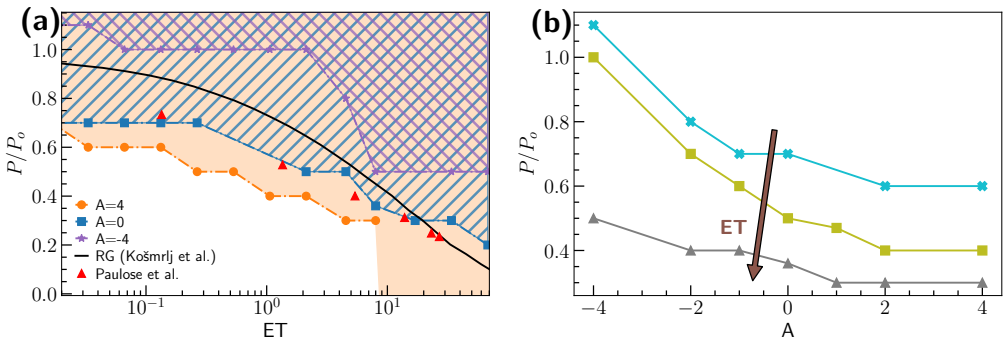

Figure 4: **Phase diagram** The phase boundary in (a) the pressure–elasto–thermal number plane for different activities and (b) in the pressure–activity plane for different elasto–thermal numbers (gray triangles for ET = 7.99, olive squares for ET = 2.12 and cyan cross for ET = 0.03). In (a) the region where the buckled phase is obtained in equilibrium is marked by blue lines. The region where the buckled phase is obtained for $A = 4$ is shaded in light yellow. The region where the buckled phase is obtained for $A = -4$ is marked by violet lines. In (a) the phase boundary obtained by RG calculation (Košmrlj and Nelson 2017) is marked by a black line and the simulation results by Ref. (Paulose *et al.* 2012) are represented by red triangles.

of external pressure is an equilibrium phase transition with the amplitude of the peak of $S_{\ell,m}$ at small ℓ as the order parameter (Paulose *et al.* 2012). But buckling at the fixed P and ET as a function of activity is not an equilibrium phase transition but can be considered as a dynamical one. Nevertheless, we can still characterize buckling by appearance of a peak in $S_{\ell,m}$ for small ℓ.

At thermal equilibrium, the phase boundary, that separates the buckled state from the unbuckled one, in the pressure–elasto–thermal number plane was marked out in Refs. (Paulose *et al.* 2012; Košmrlj and Nelson 2017). To obtain the phase diagram we use thirteen values of elasto–thermal number, for each of which we use seven values of activity. For a fixed choice of elasto–thermal number and activity we start our simulations with an initial condition where the shell is a perfect sphere. Then we choose a fixed value of external pressure and run our simulations till we reach a stationary state, which for zero activity is the equilibrium state. Whether the shell is buckled or not is decided by three checks: (a) significant decrease of volume (b) a peak at small ℓ for $S_{\ell,m}$ (c) visual inspection. If the sphere in not buckled we choose a higher external pressure and start our simulations again from the same initial condition. The buckling pressure, P_c obtained for a set of parameters is given in table (1). This way we mark out the phase boundary in the pressure–elasto–thermal number plane for different activities and in the pressure–activity plane for different elasto–thermal numbers, see Fig. (4). In Fig. (4a) we also plot the phase boundary, obtained

ET \ A	4	2	1	0	-1	-2	-4
1.65×10^{-2}	0.70	0.70	–	0.70	0.70	0.80	1.10
3.32×10^{-2}	0.60	0.60	–	0.70	0.70	0.80	1.10
6.63×10^{-2}	0.60	0.60	0.60	0.70	0.70	0.80	1.00
1.33×10^{-1}	0.60	0.60	0.60	0.70	0.70	0.80	1.00
2.65×10^{-1}	0.50	0.60	0.60	0.70	0.70	0.80	1.00
5.31×10^{-1}	0.50	0.50	0.60	–	0.70	0.80	1.00
1.06	0.40	0.40	0.50	–	0.60	0.80	1.00
2.12	0.40	0.40	0.47	0.50	0.60	0.70	1.00
4.53	0.30	0.30	–	0.50	0.50	0.60	0.80
7.99	0.30	0.30	0.30	0.36	0.40	0.40	0.50
16.99	-2.8	–	–	0.30	0.40	0.40	–
33.97	<-4	-2.5	–	0.30	0.30	0.40	0.50
67.94	<-4	<-4	-0.10	0.20	0.30	0.30	0.50

Table 1: **Buckling pressure (P_c/P_0):** for different values of elasto–thermal number (ET) and activity (A) obtained from the simulation with FvK=4616, $N = 5120$, $R = 1$ and $k_BT = 1$, where N is the number of grid points, R is radius of the shell, k_B is the Boltzmann constant and T is the temperature. We repeated some of the simulations for $N = 20252$ and obtained the same buckling pressure. To reach a stationary state, typically, we need to run for $10^6 - 3 \times 10^6$ Monte Carlo steps, where in one Monte Carlo step, we perform $2N$ Monte Carlo iterations to attempt to update the position a random point.

through a RG calculation in Ref. (Košmrlj and Nelson 2017), which agrees reasonably well with our numerical results for zero activity. Note that for large enough values of ET and A we reach a part of the phase diagram where the shell is unstable at zero external pressure and can be made stable only with positive internal pressure. This part of the phase diagram is not shown in Fig. (4) although the relevant data are included in table (1). Note that at small ET for the quiescent case it is possible to have the shell remain unbuckled even for pressure higher P_0, i.e., the shell is stabilized.

Several comments are now in order: One, most of our simulations use $N = 5120$. We have repeated some of our simulations with $N = 20252$ and obtained the same buckling pressure. Two, to obtain the buckling pressure we always start from the same initial condition and imposed a fixed external pressure. Hence, the lines of phase separation we show, Fig. (4), are not continuous and will be improved if the phase diagram is sampled in a finer resolution. Three, experimentally, it is unclear how to implement the quiescent regime, negative A. Nevertheless, synthetic membranes that can be turned active ($A > 0$) optically, has been already realized by embedding certain proteins

in a bi-lipid membranes – proteins that act as active pumps when irradiated with light of certain frequency (Girard *et al.* 2005; Manneville *et al.* 2001). In such cases, only a fraction of points on the shell are active. This can be incorporated in a straightforward manner in our code and it would be interesting to see how the critical buckling pressure changes as we change the fraction of active points. Four, bi–lipid membranes are semi-permeable (Phillips *et al.* 2012). As the shell buckles the fraction of solute increases, increasing the partial pressure inside the shell. Experimentally, this can be avoided by using shell with holes in them. We expect, in such cases the buckling pressure may change by a small amount.

Finally, our simulations point towards the intriguing possibility that within the right range of elastic parameters, a shell that is not buckled in thermal equilibrium can be buckled if turned optically active. Based on this, we suggest that it is possible to experimentally design microscopic elastic shells whose buckling can be optically controlled. In such devices it may be possible to drive flows at microscopic scales by buckling and unbuckling of shells, optically.

Acknowledgements

We thank Apurba Dev, A. Fragkiadoulakis, Sreekanth M. Manikandan, Pinaki Chaudhuri and Bidisha Sinha for useful discussions. We gratefully acknowledge the use of the following free software packages: meshzoo (Caroli *et al.* 2010; A simple and fast mesh generator), matplotlib (Hunter 2007) and VisIt (Childs *et al.* 2012). The simulations were performed on resources provided by the Swedish National Infrastructure for Computing (SNIC) at PDC center for high performance computing and the HPC facility supported by the Technical Division at the Department of Physics, Stockholm University. For the latter, we gratefully acknowledge generous help from Mikica Kocic. We acknowledge the financial support of the Swedish Research Council through grants 638-2013-9243 and 2016-05225.

Code and data availability

The source code used for the simulations of the study is freely available at `https://github.com/vipinagrawal25/MeMC/releases/tag/v1.1` (Agrawal *et al.* 2022). The simulation setup and the corresponding data are freely available on Zenodo with DOI: 10.5281/zenodo.6772570. Python scripts are included with the data to generate all the figures.

Appendix A. Monte Carlo simulation of elastic shells in thermal equilibrium

We use a Monte Carlo algorithm following Refs. Paulose *et al.* (2012); Gompper and Kroll (2004) to study the elastic properties of shells. A version of our

code, which performs thermal simulation of elastic shells, is already available as an open source software Agrawal *et al.* (2022). In this appendix, for the sake of completeness, we describe the algorithm in brief and compare the results for elastic properties of shells in thermal equilibrium with those obtained in Ref. Paulose *et al.* (2012). How we adapt the same algorithm to study shells out of equilibrium is described in the main body of this paper.

A.1. Algorithm

First, we start with N randomly chosen points on a sphere. Then, we run a Monte Carlo simulation, with a repulsive Lennard-Jones (LJ) potential, of these points moving on the surface. Once the surface Monte Carlo (SMC) has reached an equilibrium, we triangulate the points using the algorithm described in Ref. Caroli *et al.* (2010). This is our initial configuration. The distance between two neighboring nodes i and j is called $\ell^0_{\rm ij}$.

We use Monte Carlo Baumgärtner *et al.* (2013) simulations to update the positions of the points ($\boldsymbol{X}_{\rm i}$ at node i). For a pressurized shells, the total energy,

$$E = E_{\rm stretch} + E_{\rm bend} + PV, \tag{7}$$

where the stretching contribution is

$$E_{\rm stretch} = \frac{1}{2}\sum_i \frac{H}{2}\sum_{j(i)} \left(\boldsymbol{X}_{\rm ij} - \ell^0_{\rm ij}\right)^2, \quad \text{with} \tag{8a}$$

$$X_{\rm ij} \equiv |\boldsymbol{X}_{\rm i} - \boldsymbol{X}_{\rm j}|. \tag{8b}$$

The bending contribution is

$$E_{\rm bend} = \frac{B}{2}\sum_i \mathcal{A}_i \left(\boldsymbol{L}_i - C\hat{\boldsymbol{n}}\right)^2. \tag{9}$$

Here P is the pressure difference between outside and inside the shell, and V is the volume. The Young's modulus of the membrane is given by $Y = 2H/\sqrt{3}$ Itzykson (1986). The bending modulus is B, $\hat{\boldsymbol{n}}$ is the outward normal to the surface, C is its spontaneous curvature, and $\mathcal{A}_i$ is the area of Voronoi dual cell at the node i Agrawal *et al.* (2022); Meyer *et al.* (2003); Hege and Polthier (2003). The operator

$$\boldsymbol{L}_i = \frac{1}{\mathcal{A}_i}\sum_{j(i)} \frac{1}{2}\left[\cot(\alpha_{\rm ij}) + \cot(\beta_{\rm ij})\right]\boldsymbol{X}_{\rm ij}, \tag{10}$$

is the discrete Laplacian Itzykson (1986); Hege and Polthier (2003); Meyer *et al.* (2003) at the node i. Here $\alpha_{\rm ij}, \beta_{\rm ij}$ are the angles opposite to bond $\boldsymbol{X}_{\rm ij}$ as

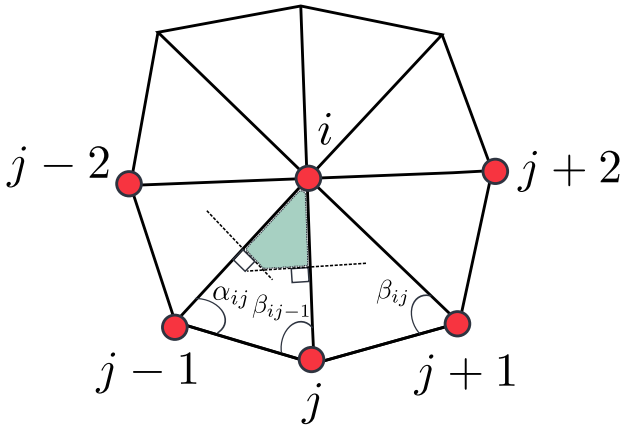

Figure 5: An example of triangulated mesh at the node i. $\alpha_{\rm ij}, \beta_{\rm ij}$ are the angles opposite to the bond ij. Shaded part is the Voronoi region of triangle T at the nodes $i, j-1, j$ – it lies inside as T is non-obtuse. The nodes are sorted in counterclockwise direction. The image is adapted from Ref. Agrawal *et al.* (2022).

shown in Fig. (5). We compute $\mathcal{A}_i$ as follows Hege and Polthier (2003); Meyer *et al.* (2003). Consider the triangle T in Fig. (5), defined by the nodes $i, j, j-1$. If T is non-obtuse, the area of shaded region in Fig. (5)

$$\mathcal{A}_{j(i)} = \frac{1}{8}\left[X_{\rm ij}^2 \cot(\alpha_{\rm ij}) + X_{\rm ij-1}^2 \cot(\beta_{ij-1})\right]. \tag{11}$$

If T is an obtuse triangle, the shaded region in Fig. (5) lies outside the triangle T then $\mathcal{A}_{j(i)} = \text{area(T)}/2$ if the angle at the vertex i of T is obtuse. Otherwise $\mathcal{A}_{j(i)} = \text{area(T)}/4$. Here $\text{area}(T) = 0.5\,|\boldsymbol{X}_{\rm ij} \times \boldsymbol{X}_{\rm ij-1}|$.

Here $\text{area}(T) = 0.5\,|\boldsymbol{X}_{\rm ij} \times \boldsymbol{X}_{\rm ij-1}|$. The area $\mathcal{A}_i$ is obtained by summing up the contributions from all the triangles similar to $\mathcal{A}_{j(i)}$, in Fig. (5), e.g., the contribution from the triangle T is the shaded area.

To compute the outward normal to the surface, $\hat{\boldsymbol{n}}$, in Eq. (9), we sort the points about node i in a counterclockwise manner. To sort the neighbors around any node i, we rotate the coordinate system such that, the z axis passes through the point i along the vector $\boldsymbol{X}_{\rm i}$. In this coordinate system we sort the neighbors by their azimuthal angle. Note that unlike Ref. Gompper and Kroll (2004) we do not incorporate self-avoidance.

A.2. Comparison with Paulose et al.

In Fig. (6A), we plot the spectra $S_{\ell,m}$ for $m = 0$ and for three different value of bending modulus B, such that $k_{\rm B}T/B = 7 \times 10^{-4}$ (blue), 0.07 (red) and 0.18

Parameters	our simulation	Paulose et al.simulation
Number of grid points, N	$5120 - 20252$	$5530 - 41816$
Activity, A	$-4 - 4$	0
P/P_c,	$-4 - 1$	$0.2 - 1$
Elasto thermal number, ET	$1.65 \times 10^{-2} - 68$	$10^{-6} - 10^{2}$
FvK, FvK	4616	$650 - 35000$
Total MC steps	$10^{6} - 10^{7}$	1.25×10^{8}
MC iterations in one MC step	$10^{4} - 4 \times 10^{4}$	Attempt to update the position of all nodes

Table 2: Comparison between our simulation parameters and Ref. Paulose *et al.* (2012).

(orange). We take the number of points $N = 20252$, FvK $= YR^2/B = 4616$, and $k_{\mathrm{B}}T = 1$. The continuous line shows the theoretical prediction calculated using RG by Paulose *et al.* (2012) – we find reasonable agreement with the theory. Next, following Paulose *et al.* (2012) we measure the mechanical response a thermal shell by deforming it with a point-like indentation. This is implemented by two harmonic springs that are attached to the north and south pole of the shell. In Fig. (6B) we compare the force–deformation curve from our simulations with those obtained in Ref. Paulose *et al.* (2012). We obtain quite reasonable agreement.

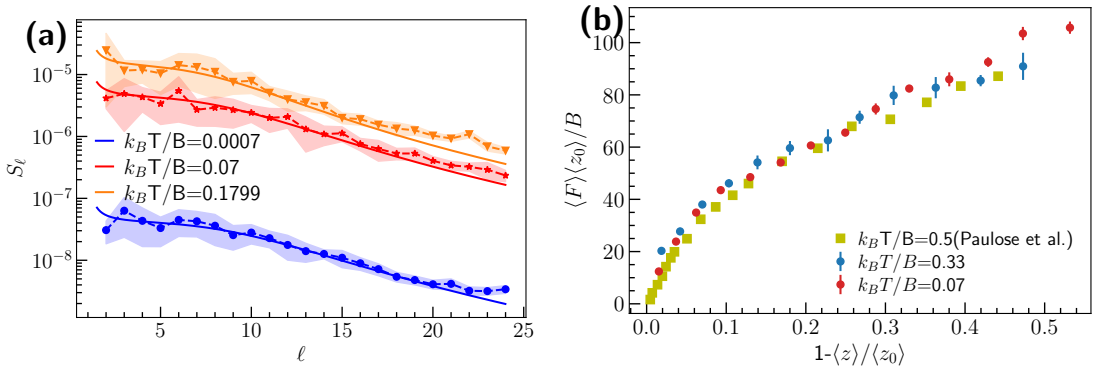

Figure 6: **Comparison with Ref Paulose *et al.* (2012):** (a) Fluctuation spectrum $S_{\ell,m}$ for $m = 0$ versus ℓ for different values of bending modulus B. The solid lines are theoretical predictions Paulose *et al.* (2012). The lines with symbols are from our simulations. The shaded area shows the variance. (b) Force–deformation curve from our simulations compared with Ref. Paulose *et al.* (2012) (yellow squares). We use $N = 20292$ and FvK $= 4616$.

References

There are several geodesic domes with sizes ranging from 10 to 200 meters.

Mathias Buenemann and Peter Lenz, "Elastic properties and mechanical stability of chiral and filled viral capsids," Physical Review E **78**, 051924 (2008).

JP Michel, IL Ivanovska, MM Gibbons, WS Klug, CM Knobler, GJL Wuite, and CF Schmidt, "Nanoindentation studies of full and empty viral capsids and the effects of capsid protein mutations on elasticity and strength," Proceedings of the National Academy of Sciences **103**, 6184–6189 (2006).

D Michiel Pegtel and Stephen J Gould, "Exosomes," Annual review of biochemistry **88**, 487–514 (2019).

Sara Cavallaro, Josef Horak, Petra Haag, Dhanu Gupta, Christiane Stiller, Siddharth S Sahu, Andre Gorgens, Hithesh K Gatty, Kristina Viktorsson, Samir El Andaloussi, *et al.*, "Label-free surface protein profiling of extracellular vesicles by an electrokinetic sensor," ACS sensors **4**, 1399–1408 (2019).

Augustus Edward Hough Love, *A treatise on the mathematical theory of elasticity* (Dover Publications; 4th edition, 2011).

LD Landau and EM Lifshitz, *Theory of Elasticity*, Course of Theoretical Physics, Vol. 7 (Pergamon Press Ltd., Oxford, England, 1970).

WT Koiter, "Progress in applied mechanics (the prager anniversary volume)," (1963).

Koiter WT, "Current trends in theory of buckling," in *Buckling of structures: Symposium Cambridge/USA*, edited by Bernard Budiansky (Springer-Verlag, Berlin, Heidelberg, New York, 1976) pp. 1–16.

Alekse Vasilevich Pogorelov, *Bendings of surfaces and stability of shells*, Vol. 72 (American Mathematical Soc., 1988).

John W Hutchinson, "Buckling of spherical shells revisited," Proceedings of the Royal Society A: Mathematical, Physical and Engineering Sciences **472**, 20160577 (2016).

Gerard Adriaan Vliegenthart and Gerhard Gompper, "Mechanical deformation of spherical viruses with icosahedral symmetry," Biophysical journal **91**, 834–841 (2006).

Ch Gao, E Donath, S Moya, V Dudnik, and H Möhwald, "Elasticity of hollow polyelectrolyte capsules prepared by the layer-by-layer technique," The European Physical Journal E **5**, 21–27 (2001).

Vernita D Gordon, Xi Chen, John W Hutchinson, Andreas R Bausch, Manuel Marquez, and David A Weitz, "Self-assembled polymer membrane capsules inflated by osmotic pressure," Journal of the American Chemical Society **126**, 14117–14122 (2004).

Dominic Vella, Amin Ajdari, Ashkan Vaziri, and Arezki Boudaoud, "The indentation of pressurized elastic shells: from polymeric capsules to yeast cells," Journal of the Royal Society Interface **9**, 448–455 (2012).

Daan Vorselen, Fred C MacKintosh, Wouter H Roos, and Gijs JL Wuite, "Competition between bending and internal pressure governs the mechanics of fluid nanovesicles," Acs Nano **11**, 2628–2636 (2017).

Pei-Hsun Wu, Dikla Raz-Ben Aroush, Atef Asnacios, Wei-Chiang Chen, Maxim E Dokukin, Bryant L Doss, Pauline Durand-Smet, Andrew Ekpenyong, Jochen Guck, Nataliia V Guz, *et al.*, "A comparison of methods to assess cell mechanical properties," Nature methods **15**, 491–498 (2018).

Daan Vorselen, Melissa C Piontek, Wouter H Roos, and Gijs JL Wuite, "Mechanical characterization of liposomes and extracellular vesicles, a protocol," Frontiers in molecular biosciences **7**, 139 (2020).

Sara Cavallaro, Federico Pevere, Fredrik Stridfeldt, André Görgens, Carolina Paba, Siddharth S Sahu, Doste R Mamand, Dhanu Gupta, Samir El Andaloussi, Jan Linnros, *et al.*, "Multiparametric profiling of single nanoscale extracellular vesicles by combined atomic force and fluorescence microscopy: correlation and heterogeneity in their molecular and biophysical features," Small **17**, 2008155 (2021).

CI Zoldesi, IL Ivanovska, C Quilliet, GJL Wuite, and A Imhof, "Elastic properties of hollow colloidal particles," Physical Review E **78**, 051401 (2008).

Jayson Paulose, Gerard A Vliegenthart, Gerhard Gompper, and David R Nelson, "Fluctuating shells under pressure," Proceedings of the National Academy of Sciences **109**, 19551–19556 (2012).

Andrej Košmrlj and David R Nelson, "Statistical mechanics of thin spherical shells," Physical Review X **7**, 011002 (2017).

Erwin Schrödinger, *What is life?: With mind and matter and autobiographical sketches* (Cambridge university press, 2012).

F S Gnesotto, F Mura, J Gladrow, and C P Broedersz, "Broken detailed balance and non-equilibrium dynamics in living systems: a review," Reports on Progress in Physics **81**, 066601 (2018).

M Cristina Marchetti, Jean-François Joanny, Sriram Ramaswamy, Tanniemola B Liverpool, Jacques Prost, Madan Rao, and R Aditi Simha, "Hydrodynamics of soft active matter," Reviews of modern physics **85**, 1143 (2013).

Sriram Ramaswamy, "The mechanics and statistics of active matter," The Annual Review of Condensed Matter Physics is **1**, 323–45 (2010).

Zhangli Peng, Xuejin Li, Igor V Pivkin, Ming Dao, George E Karniadakis, and Subra Suresh, "Lipid bilayer and cytoskeletal interactions in a red blood cell," Proceedings of the National Academy of Sciences **110**, 13356–13361 (2013).

Hervé Turlier, Dmitry A Fedosov, Basile Audoly, Thorsten Auth, Nir S Gov, Cécile Sykes, J-F Joanny, Gerhard Gompper, and Timo Betz, "Equilibrium physics breakdown reveals the active nature of red blood cell flickering," Nature physics **12**, 513–519 (2016).

Arikta Biswas, Amal Alex, and Bidisha Sinha, "Mapping cell membrane fluctuations reveals their active regulation and transient heterogeneities," Biophysical journal **113**, 1768–1781 (2017).

Hervé Turlier and Timo Betz, "Unveiling the active nature of living-membrane fluctuations and mechanics," Annual Review of Condensed Matter Physics **10**, 213–232 (2019).

Sreekanth K Manikandan, Tanmoy Ghosh, Tithi Mandal, Arikta Biswas, Bidisha Sinha, and Dhrubaditya Mitra, "Estimate of entropy generation rate can spatiotemporally resolve the active nature of cell flickering," arXiv preprint arXiv:2205.12849 (2022).

P Girard, J Prost, and P Bassereau, "Passive or active fluctuations in membranes containing proteins," Physical review letters **94**, 088102 (2005).

J-B Manneville, P Bassereau, S Ramaswamy, and J Prost, "Active membrane fluctuations studied by micropipet aspiration," Physical Review E **64**, 021908 (2001).

Dong Yan, Matteo Pezzulla, Lilian Cruveiller, Arefeh Abbasi, and Pedro M Reis, "Magneto-active elastic shells with tunable buckling strength," Nature communications **12**, 1–9 (2021).

Manoj Kumar and Chandan Dasgupta, "Nonequilibrium phase transition in an ising model without detailed balance," Physical Review E **102**, 052111 (2020).

G Gompper and DM Kroll, "Triangulated-surface models of fluctuating membranes," in *Statistical mechanics of membranes and surfaces*, edited by David Nelson, Tsvi Piran, and Steven Weinberg (World Scientific, 2004) pp. 359–426.

C Itzykson, in *Proceedings of the GIFT seminar, Jaca 85*, edited by J *et al* Abad (World Scientific Singapore, 1986) pp. 130–188.

Vipin Agrawal, Vikash Pandey, Hanna Kylhammar, Apurba Dev, and Dhrubaditya Mitra, "Memc: A package for monte carlo simulations of spherical shells," Journal of Open Source Software **7**, 4305 (2022).

Sriram Ramaswamy, John Toner, and Jacques Prost, "Nonequilibrium fluctuations, traveling waves, and instabilities in active membranes," Physical review letters **84**, 3494 (2000).

Madan Rao and Sarasij R.C., "Active fusion and fission processes on a fluid membrane," Physical review letters **87**, 128101 (2001).

Bastien Loubet, Udo Seifert, and Michael Andersen Lomholt, "Effective tension and fluctuations in active membranes," Physical Review E **85**, 031913 (2012).

Ananyo Maitra, Pragya Srivastava, Madan Rao, and Sriram Ramaswamy, "Activating membranes," Physical review letters **112**, 258101 (2014).

Rhoda J Hawkins and Tanniemola B Liverpool, "Stress reorganization and response in active solids," Physical review letters **113**, 028102 (2014).

Sifan Yin, Bo Li, and Xi-Qiao Feng, "Bio-chemo-mechanical theory of active shells," Journal of the Mechanics and Physics of Solids **152**, 104419 (2021).

A Goriely, "Five ways to model active processes in elastic solids: active forces, active stresses, active strains, active fibers, and active metrics," Mech. Res. Commun **93**, 75–79 (2017).

J Prost and R Bruinsma, "Shape fluctuations of active membranes," EPL (Europhysics Letters) **33**, 321 (1996).

A. Fragkiadoulakis, S.K. Manikandan, and D. Mitra, unpublished.

Rob Phillips, Jane Kondev, Julie Theriot, Hernan G Garcia, and Nigel Orme, *Physical biology of the cell* (Garland Science, 2012).

Manuel Caroli, Pedro MM de Castro, Sébastien Loriot, Olivier Rouiller, Monique Teillaud, and Camille Wormser, "Robust and efficient delaunay triangulations of points on or close to a sphere," in *International Symposium on Experimental Algorithms* (Springer, 2010) pp. 462–473.

A simple and fast mesh generator, `https://github.com/meshpro/meshzoo`.

J. D. Hunter, "Matplotlib: A 2d graphics environment," Computing in Science & Engineering **9**, 90–95 (2007).

Hank Childs, Eric Brugger, Brad Whitlock, Jeremy Meredith, Sean Ahern, David Pugmire, Kathleen Biagas, Mark Miller, Cyrus Harrison, Gunther H. Weber, Hari Krishnan, Thomas Fogal, Allen Sanderson, Christoph Garth, E. Wes Bethel, David Camp, Oliver Rübel, Marc Durant, Jean M. Favre, and Paul Navrátil, "VisIt: An End-User Tool For Visualizing and Analyzing Very Large Data," in *High Performance Visualization–Enabling Extreme-Scale Scientific Insight* (2012) pp. 357–372.

Artur Baumgärtner, Kurt Binder, J-P Hansen, MH Kalos, K Kehr, DP Landau, D Levesque, H Müller-Krumbhaar, C Rebbi, Y Saito, *et al.*, *Applications of the Monte Carlo method in statistical physics*, Topics in Current Physics, Vol. 36 (Springer Science & Business Media, 2013).

Mark Meyer, Mathieu Desbrun, Peter Schröder, and Alan H Barr, "Discrete differential-geometry operators for triangulated 2-manifolds," in *Visualization and mathematics III* (Springer, 2003) pp. 35–57.

Hans-Christian Hege and Konrad Polthier, *Visualization and mathematics III* (Springer Science & Business Media, 2003)

3

Chaos and irreversibility of a flexible filament in periodically–driven Stokes flow

Vipin Agrawal[1,2] **and Dhrubaditya Mitra**[1]

[1] Nordita, KTH Royal Institute of Technology and Stockholm University, Roslagstullsbacken 23, 10691 Stockholm, Sweden

[2] Department of Physics, Stockholm university, Stockholm,Sweden.

Phys. Rev. E 106, 025103

(Published 12 August 2022)

The flow of Newtonian fluid at low Reynolds number is, in general, regular and time-reversible due to absence of nonlinear effects. For example, if the fluid is sheared by its boundary motion that is subsequently reversed, then all the fluid elements return to their initial positions. Consequently, mixing in microchannels happens solely due to molecular diffusion and is very slow. Here, we show, numerically, that the introduction of a single, freely-floating, flexible filament in a time-periodic linear shear flow can break reversibility and give rise to chaos due to elastic nonlinearities, if the bending rigidity of the filament is within a carefully chosen range. Within this range, not only the shape of the filament is spatiotemporally chaotic, but also the flow is an efficient mixer. Overall, we find five dynamical phases: the shape of a stiff filament is time-invariant – either straight or buckled; it undergoes a period-two bifurcation as the filament is made softer; becomes spatiotemporally chaotic for even softer filaments but, surprisingly, the chaos is suppressed if bending rigidity is decreased further.

1. Introduction

Flows at very small Reynolds number play a key role in biology Purcell (1977); Lauga and Powers (2009); Phillips *et al.* (2012); Taylor (1951) and microfluidics Squires and Quake (2005); Kirby (2010); Stone *et al.* (2004). In the presence of rigid boundaries, such flows are typically laminar and reversible. For example, consider the fluid between two concentric cylinders sheared by rotating the outer one slowly. If the rotation is reversed the fluid particles come back to their original positions (ignoring the small fluctuations due to Brownian motion) Taylor (1967). Consequently, mixing by periodic stirring is in general catastrophically slow in microfluidic flows although Lagrangian chaos is possible in pressure–driven flows through rigid but complex boundaries Aref *et al.* (2017). Addition of elastic polymers Groisman and Steinberg (2000, 2001, 2000); Stroock *et al.* (2002); Steinberg (2021), or active objects Dombrowski *et al.* (2004); Wensink *et al.* (2012); Dunkel *et al.* (2013) and mutual hydrodynamic interaction between many suspended colloidal particles Pine *et al.* (2005), can also give rise to breakdown of time-reversibility and to chaotic flows.

Here we consider a neutrally–buoyant inextensible, elastic filament, of length L and bending rigidity B, subject to a linear shear flow $\boldsymbol{U}_0(x, y) = \dot{\gamma} y \hat{\mathrm{x}}$. The strain-rate $\dot{\gamma}$ is time-periodic with a period T, $\dot{\gamma} = S \sin(\omega t)$, where $\omega = 2\pi/T$. Initially the filament is placed along the y direction, see Figure. 1. The flow parameters, S, T, and dynamic viscosity of the fluid, η, are chosen such that the Reynolds number is very small. This corresponds to, for example, the demonstration by G.I. Taylor where he puts a small thread in a Taylor-Couette apparatus filled with syrup, turns the outer cylinder in one direction and then reverses it exactly back to its starting position Taylor (1967) This experiment does break time-reversal invariance – the thread is buckled at the end of the cycle. Here our aim is to study the same phenomena in a numerical setup For simplicity, we consider a plane Couette flow without boundaries.

An elastic filament, of length L, in a constant-in-time flow has been extensively studied, numerically and experimentally Becker and Shelley (2001); Guglielmini *et al.* (2012); Liu *et al.* (2018); LaGrone *et al.* (2019); Slowicka *et al.* (2019); Żuk *et al.* (2021); Kuei *et al.* (2015); Hu *et al.* (2021); Chakrabarti *et al.* (2020) for the last two decades. Depending on the flow, the filament either attains a complex shape, which is one case can even be helical Chakrabarti *et al.* (2020), or shows a wide range of morphological transition Liu *et al.* (2018) depending on its elastoviscous number $\overline{\mu} \equiv (8\pi\eta S L^4)/B$ For small elastoviscous number (large bending rigidity), typically, the filament behaves like a rigid one. Hence we expect that in our case, if the bending rigidity of the filament is very large, the filament would rotate away and back to its original position without

any change in shape. We also expect that once the bending rigidity is below a threshold, (or $\overline{\mu}$ is above a threshold) the filament would buckle – it would not return to its original shape. The time reversibility would be broken. If the bending rigidity is decreased further we expect elastic nonlinearities to play a more and more dominant role in the dynamics thereby giving rise to complex morphologies. Repeating the experiments over many cycles can potentially give rise to spatiotemporaly chaotic behaviour of the filament.

2. Model

We use the bead-spring model for the numerical simulation of the filament in a Stokes flow Larson *et al.* (1999); Wada and Netz (2006); Guglielmini *et al.* (2012); Nazockdast *et al.* (2017); Slowicka *et al.* (2019); Żuk *et al.* (2021). The model consists of N spherical beads of diameter d, connected by overdamped springs of equilibrium length a. The equation of motion for the i-th bead is given by Wada and Netz (2006):

$$\partial_t R_{\mathrm{i}}^{\alpha} = -\sum_{j=0}^{N-1} M_{\mathrm{ij}}^{\alpha\beta}(\boldsymbol{R}_{\mathrm{ij}}) \frac{\partial \mathcal{H}}{\partial R_{\mathrm{j}}^{\beta}} + U_0^{\alpha}(\boldsymbol{R}_{\mathrm{i}}) \quad , \tag{1a}$$

$$\begin{aligned} M_{\mathrm{ij}}^{\alpha\beta}(\boldsymbol{R}) &= \frac{1}{8\pi\eta R}\Big[\delta^{\alpha\beta} + \frac{R^{\alpha}R^{\beta}}{R^2} \\ &\quad + \frac{d^2}{2R^2}\left(\frac{\delta^{\alpha\beta}}{3} - \frac{R^{\alpha}R^{\beta}}{R^2}\right)\Big], \quad \text{for} \quad \mathrm{i} \neq \mathrm{j} \\ &= \frac{1}{3\pi\eta d}\delta^{\alpha\beta} \quad \text{for} \quad \mathrm{i} = \mathrm{j} \end{aligned} \tag{1b}$$

Where $\boldsymbol{R}_{\mathrm{i}}$ is the position vector of the center of the i-th bead, $\boldsymbol{R}_{\mathrm{ij}} \equiv \boldsymbol{R}_{\mathrm{j}} - \boldsymbol{R}_{\mathrm{i}}$, $\boldsymbol{U}$ is the velocity of the background shear flow, and η is the dynamic viscosity of the fluid.

The hydrodynamic interaction between the beads is described by the Rotne–Prager mobility tensor $M_{\mathrm{ij}}(\boldsymbol{R})$ Rotne and Prager (1969); Brady and Bossis (1988); Guazzelli and Morris (2011); Kim and Karrila (2013) derived by solving the Stokes equation, i.e., our simulations are at zero Reynolds number. The Latin indices run from 1 to N, the total number of beads, and the greek indices run from 1 to D, where $D = 3$ is dimensionality of space. Repeated greek indices are summed.

The elastic Hamiltonian, $\mathcal{H}$, contains contribution from both bending and stretching but not torsion: $\mathcal{H} = \mathcal{H}_{\mathrm{B}} + \mathcal{H}_{\mathrm{S}}$, where $\mathcal{H}_{\mathrm{B}}$ and $\mathcal{H}_{\mathrm{S}}$ are contributions from bending Montesi *et al.* (2005); Bergou *et al.* (2010) and stretching Wada and Netz (2006, 2007) respectively. The bending energy of a continuous filament

is given by Powers (2010):

$$\mathcal{H}_{\mathrm{B}} = \frac{B}{2}\int \kappa^2(s)\mathrm{ds}, \tag{2}$$

where B is the bending modulus, κ is curvature, and s is the material coordinate. As we use a discrete bead–spring model, hence we must discretize the Hamiltonian, see appendix Appendix A.

We define three dimensionless parameters: the elastoviscous number, $\overline{\mu}$, the non-dimensional frequency, σ, and the ratio of stretching to bending, K, defined respectively as

$$\overline{\mu} = \frac{8\pi\eta S L^4}{B}, \quad \sigma = \frac{\omega}{S}, \quad \text{and} \quad K = \frac{Hd^2}{B}. \tag{3}$$

The elastoviscous number measures the relative strength of the elastic forces due to bending and the visous forces.

In appendix Appendix A, we give a comprehensive description of the model, its numerical implementation, and the parameters of simulations. The elastoviscous number of our simulations includes in the same range as the experiments in Ref. Liu *et al.* (2018). Our code reproduces their experimental results, see appendix Appendix A.

The velocity of the flow at any Eulerian point $\boldsymbol{r} = (x, y, z)$ is given by

$$U^{\alpha}(\boldsymbol{r}) = U_0^{\alpha}(\boldsymbol{r}) + \mathcal{G}^{\alpha\beta}(\boldsymbol{r} - \boldsymbol{R}_{\mathrm{i}})F_{\mathrm{i}}^{\beta}, \quad \text{, where} \tag{4a}$$

$$F_{\mathrm{i}}^{\alpha} = -\frac{\partial \mathcal{H}}{\partial R_{\mathrm{i}}^{\alpha}}, \quad \text{and} \tag{4b}$$

$$\mathcal{G}^{\alpha\beta}(\boldsymbol{R}) = \frac{1}{8\pi\eta R}\left[\delta^{\alpha\beta} + \frac{R^{\alpha}R^{\beta}}{R^2} + \frac{d^2}{4R^2}\left(\frac{1}{3}\delta^{\alpha\beta} - \frac{R^{\alpha}R^{\beta}}{R^2}\right)\right] \tag{4c}$$

In (4a) $U_0^{\alpha}(\boldsymbol{r})$ is the background linear shear flow and $\mathcal{G}^{\alpha\beta}$ is the Green's function given in (4c).

3. Results

Initially, the filament is placed along the y direction with its head at $y = 0$, see Figure. 1. We use $N = 256$, $K = 16$ and $a = d$ in all our simulations and vary both σ and $\overline{\mu}$ to explore a variety of dynamical behaviour.

As we impose an external linear flow with a period T, it is useful to look at *stroboscopic* snapshots of the filament separated by time T. We note that in some cases filament does not return to its original position at the end of a cycle. When that happens time-reversal invariance is already broken even if the shape of the filament remains unchanged. We call this *swimming*. In this paper we focus not on swimming but on how the shape of the filament changes.

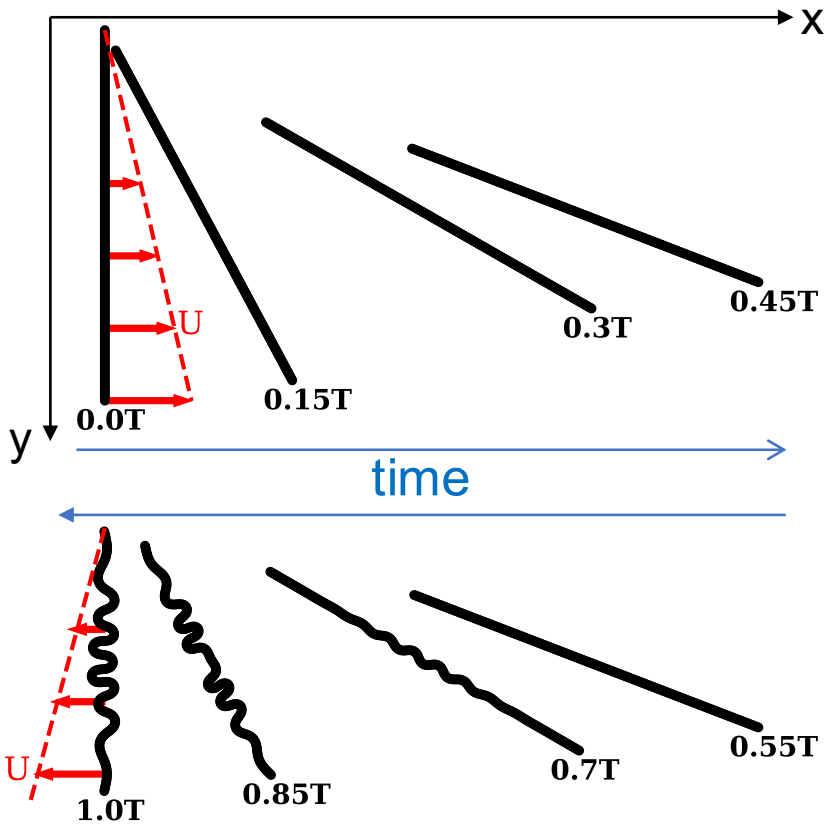

Figure 1: **Sketch of numerical experiment**: Initially the filament is straight. It rotates and translates while advected by $\boldsymbol{U} = \dot{\gamma} y \hat{\mathrm{x}}$ with $\dot{\gamma} = S \sin(\omega t)$ over the first-half of the cycle. In the second half the filament rotates and translates back but in addition buckles if its elastoviscous number is large enough. The flow $\boldsymbol{U}$ at $t = T/4$ (top panel) and $t = 3T/4$ (bottom panel) are shown as red arrows.

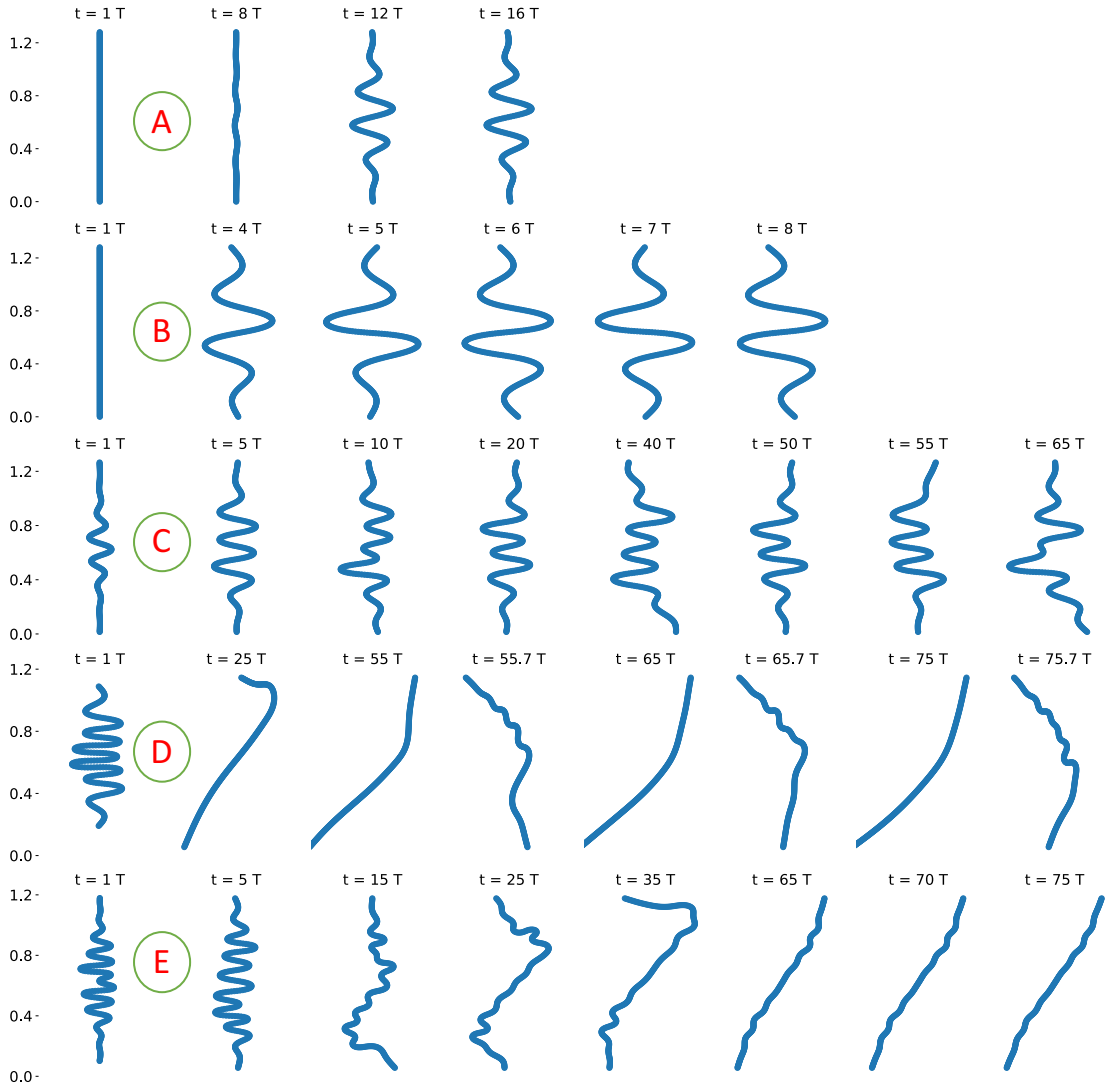

Figure 2: **Kaleidoscope of dynamical behavior**: (A) **Periodic buckling** ($\overline{\mu} = 1.46 \times 10^6$, $\sigma = 1.5$): The filament is buckled after 8 cycles and repeats itself after every cycle afterwards. Till cycle 8 the filament is not straight but slightly deformed from its initial straight shape. This small deformation is barely noticeable in this figure. (B) **Two-period** ($\overline{\mu} = 0.67 \times 10^6$, $\sigma = 0.75$): The shape of the filament is either of two shapes, which are mirror images of each other, at odd and even cycles. (C) and (D) The two types of **Complex** phases: (C)For $\overline{\mu} = 3.35 \times 10^6$, $\sigma = 1.5$: The filament never repeats itself. (D) For $\overline{\mu} = 6.7 \times 10^6$, $\sigma = 0.75$: The filament shows spatiotemporally complex behavior but for late cycles, the filament (almost) repeats at the end of every cycle (nT) ($t = 55T, 65T, 75T$) but not at any other time. To illustrate, we show the snapshots at $t = 55.7T, 65.7T, 75.7T$ – the shape of the filament is different from one another. Note, the filament shows maximum buckling, not at the end of a cycle, but at times in-between the cycles, i.e., at $t = (n + p)T$, where n is an integer and $0 < p < 1$. (E) **Complex transients**($\overline{\mu} = 16.75 \times 10^6$, $\sigma = 1.5$): Filament shows complex behavior for early periods but repeats itself at late times.

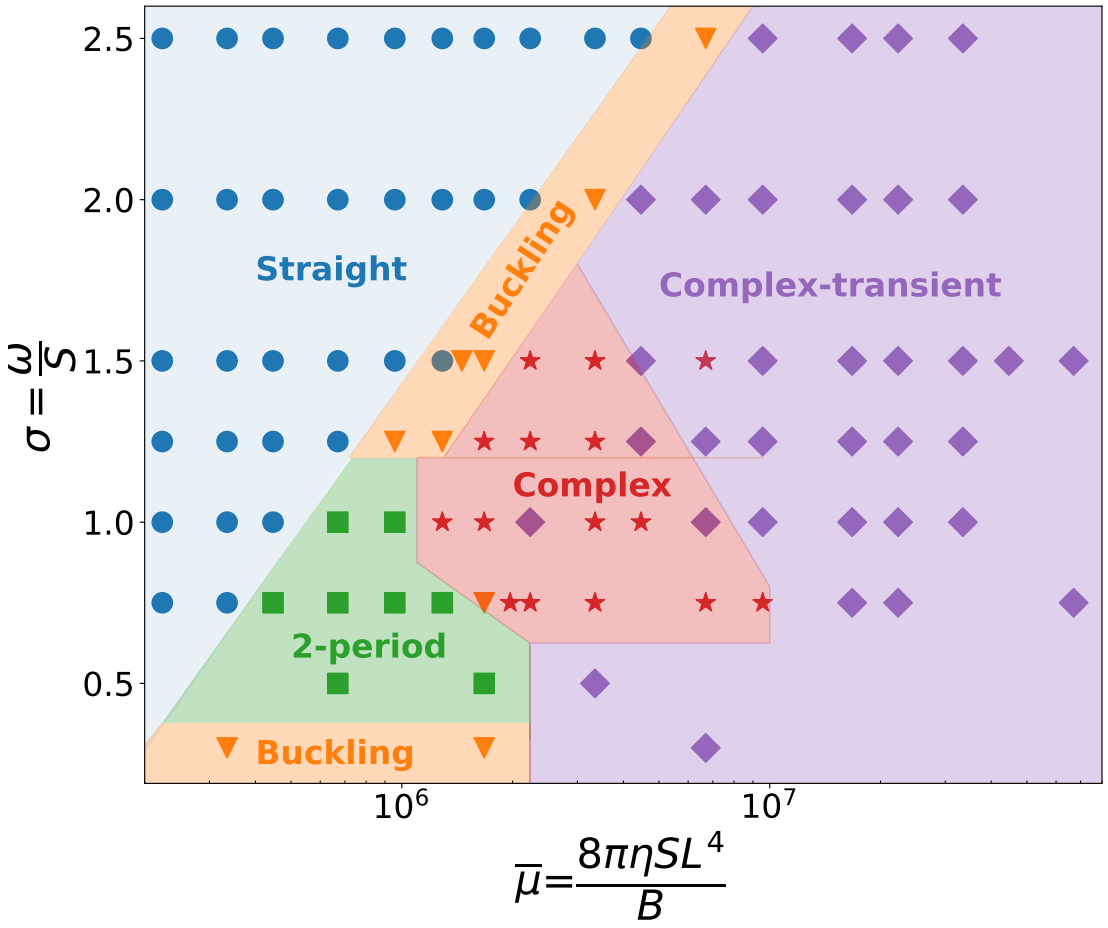

Figure 3: **Phase diagram** from time-dependent numerical simulations in the $\overline{\mu}$–σ parameter space; $\left(\sigma = \frac{\omega}{S}, \overline{\mu} = \frac{8\pi\eta SL^4}{B}\right)$. Here ω is rate of change of strain, S is strain rate, η is the viscosity, L is length of the filament, and B is the bending modulus. Initially, the filament is freely suspended in the shear flow, see Figure. 1. We show five different dynamical phases in the system represented by five symbols. **Straight** (•) : The filament comes back to the initial position in the straight configuration after every period. **Periodic buckling** (▼):- The filament comes back in the buckled configuration after every period. **Two-period (■)** : The filament repeats its configuration not after every but after two-period. **Complex**(★): The filament buckles into complex shape with very high mode of buckling instability. **Complex–transients**(⧫) : Filament shows long transients with complex shape but at late times, the shape of the filament repeats itself. The boundary between the complex and complex-transient phase is difficult to clearly demarcate.

3.1. Dynamical phases

Based on the shape, a kaleidoscope of qualitative behavior emerges that we classify into five different dynamical phases. For small elastoviscous number

($\overline{\mu}$) the filament comes back to its original position undeformed at the end of every period (not shown in Fig. 2). As $\overline{\mu}$ is increased, the filament is buckled at the end of every period; see Fig. 2 panel A. On increasing $\overline{\mu}$ further we reach a phase where two buckled states, which are mirror images of each other, alternate at the end of even and odd periods – *a period–two solution*; see Fig. 2 panel B. At even higher $\overline{\mu}$ the shape of the filament at the end of every cycle is different – the filament never repeats itself. We continue these simulations to long times. In some cases the shape of the filament never repeats itslf, see Figure. 2 panel C. In some other cases, the shape of the filament is almost repeated at the end of every period, but the shape is different at all other times, e.g., consider the snapshots in Figure. 2 panel D. The shape of the filament at $65T$ and $75T$ are almost the same. But the shapes at $65.7T$ and $75.7T$ are not. We do not make a distinction between these two dynamical behavior – we call both of them complex. Finally, for large $\overline{\mu}$ we find that the shape of the filament shows complex spatiotemporal behaviour till intermediate times $t < 60T$ but almost settles (it comes very close but does not repeat itself) to a fixed spatially complex shape at late times; see Fig. 2 panel E. By surveying a range of values for $\overline{\mu}$ and σ we construct a phase diagram in Fig. 3. We find that the straight phase can go unstable in two ways, depending on the value of σ. It can either undergo a bifurcation to a two-period solution or go to a buckled phase which repeats itself. The buckled solution appears at end of every period, it is a time-reversible solution, the two-period solution is not. The boundary between the phases can be clearly demarcated except the boundary between the complex and the complex-transient phase. Thus it may be possible that there is a fractal boundary between these two phases. Fractal boundaries are not an uncommon occurance in many dynamical systems including transition to turbulence in pipe flows Schneider *et al.* (2007), different forms of spiral-wave dynamics in mathematical models of cardiac tissues Shajahan *et al.* (2007), and onset of dynamo in shell-models Sahoo *et al.* (2010). We have not explored this aspect in any detail in this paper. Except the region of the phase diagram where we find straight solutions, swimming solutions appear everywhere else.

3.1.1. *Complex Phase*

Let us first discuss in detail a representative simulation in the complex phase. As we focus on the shape of the filament we describe the filament in its intrinsic coordinates – its curvature (κ) as a function of material coordinate (s). We calculate curvature using a discrete approximation, see appendix Appendix A. In Fig. 4 we plot κ versus s for early times, at $t = T, 10T, 19T$ and $28T$, in Fig. 4(A) and for late times in Fig. 4(C), at t=$35T, 45T, 55T$ and $75T$. At all times, the curvature is zero at the two end of the filament, as dictated by the boundary conditions, and changes sign several times, i.e., a quite complex

morphology is observed, as we show in Fig. 4(B) and Fig. 4(D) respectively. The minimum value of the radius of curvature is approximately $10d$ where d is the diameter of each bead or alternatively the thickness of the filament. A sine transform of the $\kappa(s)$ to $\hat{\kappa}(q)$ shows several peaks, For $q \gtrapprox 20$ the $\hat{\kappa}$ is practically zero, see Appendix Appendix C. This demonstrates that our simulations are well resolved to capture the phenomena we observe. As the filament moves in the fluid it changes the background flow. In Fig. 4(E) and Fig. 4(F) we plot a typical phase-potrait of the velocity of the flow (after subtracting out the background velocity) at a fixed Eulerian point. For small $\overline{\mu}$, in the part of the phase diagram where the filament always remain straight, the phase potrait is a simple closed curve as shown in orange in Fig. 4(E) and Fig. 4(F). For the case where the filament is in the complex phase we obtain a non-trivial attractor.

There is another intriguing feature seen in some of the runs in the complex phase: although the filament never repeat itself exactly in the κ–s space it comes very close to periodic behavior with a large period, in one case $30T$.

3.1.2. *Complex–Transient phase*

Next we turn to the phase we call *Complex–Transient*. Here the behavior is the same as the *Complex* phase upto quite late times, e.g., $60T$ after which the filament comes to almost the same shape at the end of every period. Here also the dynamics of the filament is not strictly periodic. The shapes, which are complex, change but very slowly over time. This slow drift in the configuration space can be measured by calculating

$$K(p-m) = \left[\int \mid \kappa(s,pT) - \kappa(s,mT) \mid^2 ds\right]^{1/2} \tag{5}$$

where $m > 60$ is a period where the filament has already reached its late time behavior. We find $K(p-m) \sim (p-m)$, for not too large values of $p-m$. i.e., an algebraic growth. We perform another numerical experiment. We take the filament in its late almost stationary configuration and add a small perturbation and then evolve again. The perturbation goes to zero very quickly, the filament goes back to its almost stationary configuration.

3.2. Stroboscopic map

So far we have studied the different dynamical phases through time-stepping our numerical code. Potentially, both the complex and complex-transient phase are spatiotemporally chaotic. But a time-stepping code however accurate accumulates error which grows with the number of time-steps taken. To investigate the fate of the filament at late times we do have to integrate over long times. Hence we need additional evidence to confirm the existence of chaos in this problem.

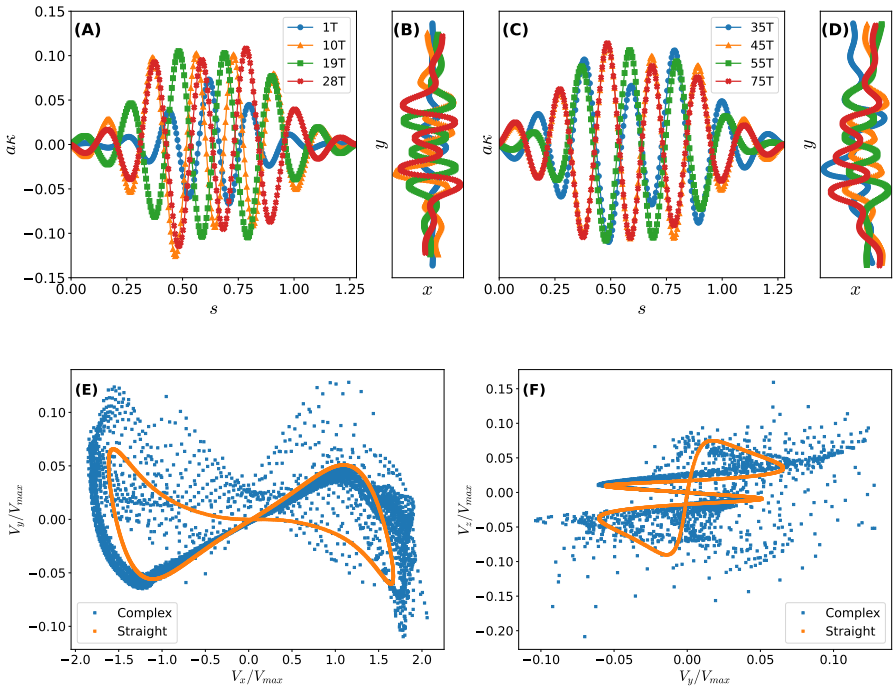

Figure 4: **Evolution in the complex phase**: ($\overline{\mu} = 3.35 \times 10^6$, $\sigma = 1.5$) The filament shows complex behavior and does not repeat in real space or configuration space ($t < 45T$) 9. (A) Curvature (κ) as a function of material coordinate, s, of the filament at early cycles, $t = T, 10T, 19T$ and $28T$. (B) Image of the filament at the same times. (C) and (D) Same as (A) and (B) but for late times. (E,F) Phase portrait of tracer velocity at a fixed Eulerian point for late cycles $t = 45T$–$75T$.

We start by defining the stroboscopic map, $\mathcal{F}$,

$$\kappa(s, T) = \mathcal{F}\kappa(s, 0) \tag{6}$$

The dynamical system obeyed by the filament, equation (1a), is non-autonomous because the external flow $\boldsymbol{U}$ is an explicit function of time, the map $\mathcal{F}$, which is generated by integrating (1a) over exactly one time period T, is autonomous. This is a map of N-dimensional space onto itself where N is the number of beads. The function $\kappa(s, t)$ at $t = nT$ and $t = (n + 1)T$ are related by one iteration of this map. We proceed to study the fixed points and periodic orbits of this map as a function of the parameters, $\overline{\mu}$ and σ, following Refs. Auerbach *et al.* (1987); Cvitanovic *et al.* (2005). Such techniques have been used widely to study transition to turbulence in high-dimensional flows Kerswell (2005); Suri *et al.* (2020); Page *et al.* (2020) and has also been applied to other fields of fluid dynamics Franco-Gómez *et al.* (2018); Gaillard *et al.* (2021). The detailed numerical techniques are described in appendix Appendix A.

In Fig. 5 we show several examples of the solutions we obtain, for a fixed $\sigma = 0.75$ as a function of $\overline{\mu}$. For small $\overline{\mu} = 0.17 \times 10^6$ we obtain only one fixed point and it corresponds to $\kappa(s) = 0$, i.e., a straight filament. At $\overline{\mu} = 0.33 \times 10^6$ in addition to the straight filament a new fixed point appears, where κ is zero at one end, changes sign once roughly at the middle of the filament and has two maximas. We show the shape of the filament in Fig. 5(B1). At exactly this point in the phase diagram, see top line in Fig. 5, obtained from the evolution code, we find a straight filament. This implies, either of the two possibilities: one, the new solution is unstable; two both the solutions are stable but the evolution code lands up in the straight one because of the initial condition we chose. Next at $\overline{\mu} = 0.33 \times 10^6$ we no longer find any fixed points. We find two periodic orbits, one that is a two–period Fig. 5(C1) and one with four periods Fig. 5(C2). The two solutions in the two-period solution are mirror images of each other. At the same place in the phase diagram the evolution code finds the same two–period solution. Increasing $\overline{\mu}$ to 0.84×10^6 we find that the four-period solution has disappeared, two two–period solutions exist, Fig. 5(D). At even higher values of $\overline{\mu}$ we start to obtain many solutions. We show a few examples in Fig. 5(F), Fig. 5(G), and Fig. 5(H). This is the region of phase space where complex and complex-transient dynamical phases are seen.

To summarize, by turning our system of coupled non-autonomous differential equations, (1a) to an autonomous stroboscopic map and by studying the solutions of the map we find further support of breakdown of time reversibiity and appearence of chaos that we had already seen from the evolution of the differential equations. We demonstrate that the first appearence of breakdown of time-reversibility is through a period-two bifurcation. The map has many solutions and the number of solutions increases as we increase $\overline{\mu}$.

3.3. Mixing of passive tracer

Next we study how passive tracers are transported by the flow generated by the presence of the filament for parameters in the complex phase. The velocity of the flow, $\boldsymbol{U}(\boldsymbol{r})$, at any Eulerian point, $\boldsymbol{r} = (x, y, z)$ is given in (4a). The equation of motion of a passive tracer, whose position at time t is given by $\boldsymbol{X}(t)$, is

$$\frac{d\boldsymbol{X}}{dt} = \boldsymbol{U}(\boldsymbol{r})\delta(\boldsymbol{r} - \boldsymbol{X}). \tag{7}$$

We solve (7) simultaniously with (4a) and for N_p tracers. The tracers are introduced into the flow on concentric circles in the x–y plane, Fig. 6(A), after approximately 10 cycles, when the flow has reached a statistically stationary They are colored by radius of the circle on which they lie on at the initial time. After 8 periods, $t = 8T$, we find that the outer rings are still somewhat intact

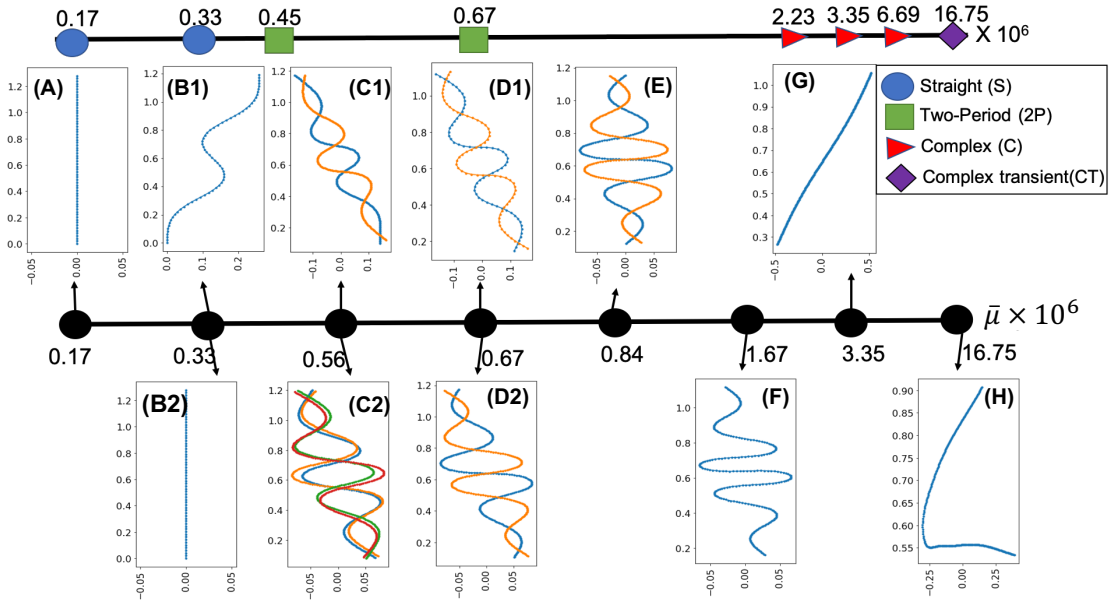

Figure 5: **Solutions of stroboscopic map** in real space for $\sigma = 0.75$ for different values of $\overline{\mu}$. We find multiple co-existing solutions as we increase $\overline{\mu}$ (black symbols from left to right) indicating the complexity of the system. We compare this solutions with the solutions obtained at late times from the evolution code at the same points in the phase diagram.

but the inner rings have somewhat merged with each other and also moved out of the x–y plane. At even later time, $t = 256T$, we find the tracer particles are well mixed with each other.

In the rest of this section, we set $t = 0$ at the time the tracers are introduced. To obtain a quantitative measure of mixing we define

$$\Delta \boldsymbol{X}^{\mathrm{k}}_{\mathrm{j}} \equiv \boldsymbol{X}^{\mathrm{k}}((j+1)T) - \boldsymbol{X}^{\mathrm{k}}(jT) \quad , \tag{8}$$

the net displacement of the k-th tracer particle over the j-th cycle – $t = jT$ to $t = (j+1)T$, where j is an integer. The net displacement of the k-th tracer after q cycles is

$$\boldsymbol{\rho}^{\mathrm{k}}(q) = \sum_{j=1}^{q} \Delta \boldsymbol{X}^{\mathrm{k}}_{\mathrm{j}}. \tag{9}$$

The total mean square displacement, averaged over all the tracers, at the end of q cycles is given by

$$\left\langle \rho^2(q) \right\rangle \equiv \frac{1}{N_{\mathrm{p}}} \sum_{\mathrm{k}=1}^{N_{\mathrm{p}}} |\boldsymbol{\rho}^{\mathrm{k}}(q)|^2 \tag{10}$$

If the tracers diffuse then we expect $\langle \rho^2(q) \rangle \sim q$ for large q Taylor (1922). In Fig. 6(D) we plot $\langle \rho^2(q) \rangle$ versus q in log-log scale. Clearly $\langle \rho^2(q) \rangle$ increases faster than q but slower than q^2! Could it be possible that the tracers show Levy-like superdiffusion ?

If this is true then the probability distribution function (PDF), $\mathcal{P}$, of the displacement $\Delta X_{\mathrm{j}}^{\mathrm{k}}$ must have a power-law tail with an exponent $\gamma \geq -2$. We probe this by calculating the cumulative probability distribution (CDF) function for $\Delta X_{\mathrm{j}}^{\mathrm{k}}$ for all j and k. We calculate the CDF using rank-order method. The advantace of using the CDF is that unlike the PDF it is not plagued by binning error. The CDF of $\Delta X_{\mathrm{j}}^{\mathrm{k}}$ is different for each of its components. The CDF of the out-of-plane component, X_3, has an exponential tail. The CDF of the two in-plane components are qualitatively similar, hence we calculate $\Delta s = \sqrt{X_1^2 + X_2^2}$ and plot its CDF, $\mathcal{Q}(\Delta s)$, calculated by the rank-order method, in Fig. 6(E). The tail of the CDF has a slope approximately equal to -3, which implies that the tail of the corresponding PDF has a slope of approximately -4. Thus, by the central limit theorem we conclude that the tracers to show diffusion, not superdiffusion. However, as the PDF has power-law tail we expect that very long averaging over very many number of tracer particles is necessary for convergence. This explains why we do not observe clear evidence of diffusion from the mean square displacement.

4. Conclusion

To summarize, we numerically study the motion of a freely-floating elastic filament in a linear shear flows that changes periodically with time, at zero Reynolds number. We find that elastic nonlinearies of the filament are responsible for breakdown of time-reversal symmetry. The first signature of this breakdown, which appears as we increase the elasto-viscous number, is that the filament starts to *swim* – it does not return to its initial poistion after one period, although it returns to the same shape. As the elastoviscous number is increased we find period-two bifurcation and eventually what could be spatiotemporally chaotic behavior of the shape of the filament. Surprisingly, at quite large elastoviscous number we find that chaos is suppressed at late times – the filament returns to the same shape at the end of every period but does not repeat itself between the periods. We also demonstrate that such a filament is an efficient mixer of a passive scalar. Few comments are now in order.

Our numerical experiments corresponds, roughly, to the same range of elastoviscous parameters as the recent experiments Liu *et al.* (2018) of flexible filaments in constant-in-time shear flow and our code reproduces the behaviour seen in these experiments. Hence we expect it will be possible to experimentally

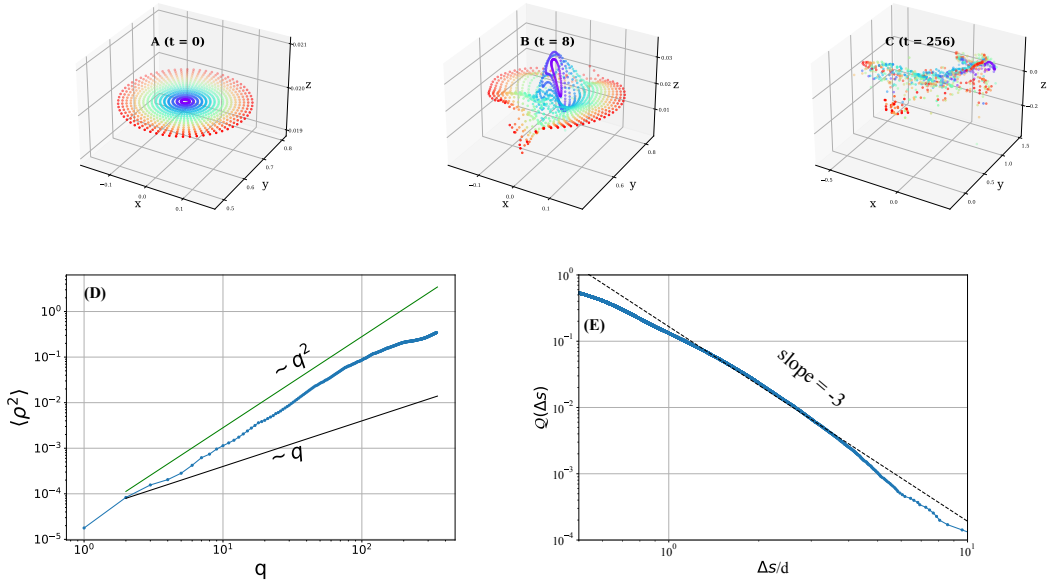

Figure 6: **Mixing of passive tracer**: (A) to (C) Positions of tracer particles at different times for the filament in complex phase ($\overline{\mu} = 3.3 \times 10^6$, $\sigma = 1.5$). Initially, the tracers are placed on concentric circles, color coded by their distance from the center of the circles. The mixing of the colors show the mixing of the scalars. (D) Mean squre displacment (MSD), $\langle \rho^2 \rangle (qT)$, defined in (10), as a function of q in log-log scale. We also plot two lines with slopes 1 and 2. (E) Cumulative probability distribution function, $1 - \mathcal{Q}(\Delta s)$ as a function of $\Delta s = \sqrt{X_1^2 + X_2^2}$ (X_1 and X_2 are in-plane coordinate of the tracers).

confirm our results, at least qualitatively. Intriguingly, the spatiotemporally chaotic behavior is observed within a window of values of the elastoviscous number for a fixed value of σ.

We have not confined the numerical solution of our problem to two dimensions. The filament could, in principle, bend out-of-plane when buckled, but it never does. We expect, if torsion is included the filament will bend out of the plane and also break the reflection symmetry. However, the passive tracers driven by the filament do move out of the plane.

In addition to elastic nonlinearity, we have included non-local viscous interaction. In its simplest approximation a filament in a viscous flow can be described by including only the diagonal term (i = j) in the Rotne–Prager tensor Goldstein *et al.* (1998) in (1b). We have checked that for such a model we also find spatiotemporally chaotic behavior, which will be reported elsewhere.

Spatiotemporally chaotic systems are rare in nonlinear systems in one space dimension, e.g., the one-dimensional Burgers equation does not show chaotic behavior. When described in terms of its intrinsic coordinates our filament could, naively, considered to be, a spatiotemporally chaotic one dimensional

system. However, this is not true because the external shear cannot be captured only with the intrinsic coordinates.

A single rigid ellipsoid in a shear flow shows low-dimensional chaotic motion for appropriate choice of parameters Radhakrishnan *et al.* (1999); Lundell (2011); Nilsen and Andersson (2013). Hence, from a fundamental point of view, it is not a surprise that a deformable thread in a time-dependent shear can show spatiotemporally chaotic behaviour. However, it has never been demonstrated before.

For a small enough filament, e.g., a single large polymer molecule, thermal effects that we have ignored, may be important. We have ignored them for two reasons. First, in many experimental situations Liu *et al.* (2018) the filament is large enough that the thermal fluctuations may not be crucial. Second, we want to address the fundamental question of emergence of chaotic behavior due to elastic nonlinearities in the absence of any external stochastic fluctuations. We further emphasize that most strategies of increasing mixing in microfluidics rely on having a non-zero but small molecular diffusivity – " For efficient mixing to be achieved, the velocity field must stir together different portions of the fluid to within a scale that is small enough for diffusion to take over and homogenize the concentrations of the advected quantities." Aref *et al.* (2017). By contrast, we operate at zero molecular diffusivity – our system is diffusive even at infinite Peclet number.

Acknowledgements

We acknowledge the support of the Swedish Research Council Grant No. 638-2013-9243 and 2016-05225. The figures in this paper are plotted using the free software matplotlib (Hunter 2007). The simulations were performed on resources provided by the Swedish National Infrastructure for Computing (SNIC) at PDC center for high performance computing.

Appendix A. Model and Method

A.1. Model

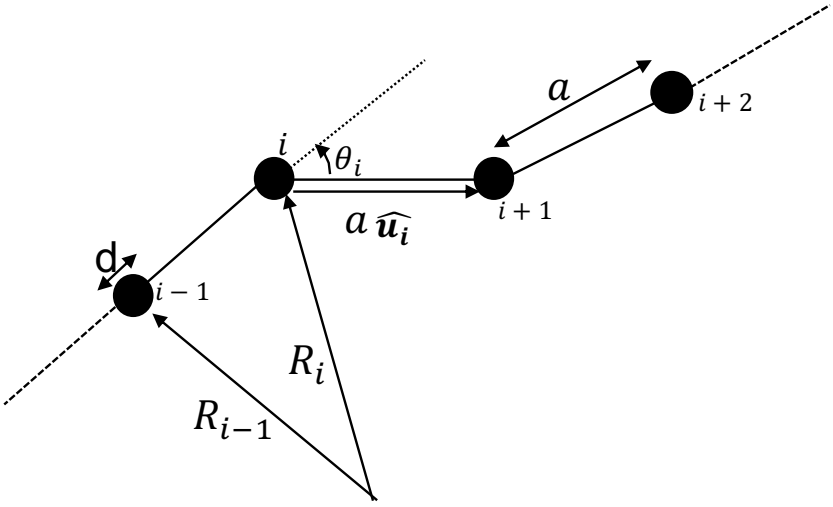

Figure 7: **Schematic** of a freely jointed bead-rod chain. We show $a > d$ for illustration, but we use $a = d$ for our simulation.

We use the bead-spring model for the numerical simulation of the filament in a flow Larson *et al.* (1999); Guglielmini *et al.* (2012); Nazockdast *et al.* (2017); Slowicka *et al.* (2019); Wada and Netz (2006); Żuk *et al.* (2021). The model consists of N spherical beads of diameter d, connected by overdamped springs of equilibrium length a, see Fig. 7. The total length of the filament is L. The position of the center of the i-th bead is $\boldsymbol{R}_{\mathrm{i}}$, where $i = 1, \ldots N$. The equation of motion for the i-th bead is given by Wada and Netz (2006):

$$\partial_t R^{\alpha}_{\mathrm{i}} = -\sum_{j=0}^{N-1} M^{\alpha\beta}_{\mathrm{ij}}(\boldsymbol{R}_{\mathrm{ij}}) \frac{\partial \mathcal{H}}{\partial R^{\beta}_{\mathrm{j}}} + U^{\alpha}_{0}(\boldsymbol{R}_{\mathrm{i}}) \quad . \tag{11}$$

Where $\boldsymbol{R}_{\mathrm{ij}} = \boldsymbol{R}_{\mathrm{j}} - \boldsymbol{R}_{\mathrm{i}}$, $\mathcal{H}$ is the elastic hamiltonian, $\partial(\cdot)/\partial(\cdot)$ denotes the partial derivative, the greek indices run from 1 to D, where $D = 3$ is dimensionality of space. Repeated greek indices are summed. The velocity of the background flow, $\boldsymbol{U}_0$ is given by

$$\boldsymbol{U}_0(x, y) = \dot{\gamma} y \hat{\mathrm{x}}, \quad \text{with} \quad \dot{\gamma} = S \sin(\omega t), \tag{12}$$

being the time–periodic strain—rate and $\omega \equiv 2\pi/T$.

The hydrodynamic interaction between the beads is encoded by the Rotne–Prager mobility tensor $M_{\mathrm{ij}}(\boldsymbol{R})$ Rotne and Prager (1969); Guazzelli and Morris

(2011); Brady and Bossis (1988); Kim and Karrila (2013):

$$M_{\mathrm{ij}}^{\alpha\beta}(\boldsymbol{R}) = \left\{ \begin{array}{ll} \frac{1}{8\pi\eta R}\left[\delta^{\alpha\beta} + \frac{R^\alpha R^\beta}{R^2} + \frac{d^2}{2R^2}\left(\frac{\delta^{\alpha\beta}}{3} - \frac{R^\alpha R^\beta}{R^2}\right)\right] & ,\mathrm{i} \neq \mathrm{j} \\ \frac{1}{3\pi\eta d}\delta^{\alpha\beta} & ,\mathrm{i} = \mathrm{j} \end{array} \right\}. \tag{13}$$

Here η is viscosity of the fluid, and $R = |\boldsymbol{R}|$.

The Hamiltonian of the system, $\mathcal{H}$, is $\mathcal{H} = \mathcal{H}_{\mathrm{B}} + \mathcal{H}_{\mathrm{S}}$ – we do not consider torsion. Here $\mathcal{H}_{\mathrm{B}}$ and $\mathcal{H}_{\mathrm{S}}$ are contributions from bending Montesi *et al.* (2005); Bergou *et al.* (2010) and stretching Wada and Netz (2006, 2007) respectively. The bending energy of a filament is given by Powers (2010):

$$\mathcal{H}_{\mathrm{B}} = \frac{B}{2}\int \kappa^2(s)ds, \tag{14}$$

where B is the bending modulus, κ is curvature, and s is the material coordinate. The discrete form of $\mathcal{H}_{\mathrm{B}}$ is Bergou *et al.* (2008, 2010); Montesi *et al.* (2005):

$$\mathcal{H}_{\mathrm{B}} = aB\sum_{i=0}^{N-1}\kappa_i^2 = \frac{B}{a}\sum_{i=0}^{N-1}\hat{\boldsymbol{u}}_i\cdot\hat{\boldsymbol{u}}_{i-1} = \frac{B}{a}\sum_{i=0}^{N-1}\cos\theta_i, \tag{15}$$

where

$$\kappa_{\mathrm{i}} = \frac{2}{a}\tan\left(\frac{\theta_{\mathrm{i}}}{2}\right) \approx \frac{\sin(\theta_{\mathrm{i}})}{a} = \frac{|\hat{\boldsymbol{u}}_{\mathrm{i}}\times\hat{\boldsymbol{u}}_{\mathrm{i}-1}|}{a}, \tag{16a}$$

$$\hat{\boldsymbol{u}}_{\mathrm{i}} = \frac{\boldsymbol{R}_{\mathrm{i}+1}-\boldsymbol{R}_{\mathrm{i}}}{|\boldsymbol{R}_{\mathrm{i}+1}-\boldsymbol{R}_{\mathrm{i}}|} \quad , \tag{16b}$$

and θ_{i} is the angle between two consecutive unit vectors $\hat{\boldsymbol{u}}_{\mathrm{i}}$ and $\hat{\boldsymbol{u}}_{\mathrm{i}-1}$ (see Fig. 1(A)). In the second step of (15), we have dropped a constant term. In the last step of (16a), we have used the small-angle approximation Montesi *et al.* (2005).

The stretching energy is discretized Wada and Netz (2006, 2007) as:

$$\mathcal{H}_{\mathrm{S}} = \frac{H}{2a}\sum_{\mathrm{i}=0}^{N-1}(|\boldsymbol{R}_{\mathrm{i}+1}-\boldsymbol{R}_{\mathrm{i}}|-a)^2, \tag{17}$$

where H is the stretching modulus. We ignore thermal fluctuations.

A.2. Non–dimensionalization

We use L and $1/S$ as our characteristic scales for length and time, respectively. The evolution equation in non-dimensional form is:.

$$\partial_{\tilde{t}}\widetilde{R}_{\mathrm{i}}^{\alpha} = -\frac{1}{\overline{\mu}}\sum_{j=0}^{N-1}\widetilde{M}_{\mathrm{ij}}^{\alpha\beta}(\widetilde{R}_{\mathrm{ij}})\left[\frac{\partial\widetilde{\mathcal{H}}_{\mathrm{B}}}{\partial\widetilde{R}_{\mathrm{j}}^{\beta}} + K\left(\frac{L}{d}\right)^{3}\left(\frac{d}{a}\right)\frac{\partial\widetilde{\mathcal{H}}_{\mathrm{S}}}{\partial\widetilde{R}_{\mathrm{j}}^{\beta}}\right] + \tilde{y}\sin\sigma\tilde{t} \quad . \tag{18}$$

Here $\tilde{(\cdot)}$ denotes non-dimensional quantities. We get the following dimensionless parameters: The elasto-viscous number,

$$\overline{\mu} \equiv \frac{8\pi\eta S L^{4}}{B}, \tag{19}$$

the non-dimensional frequency,

$$\sigma \equiv \frac{\omega}{S}, \tag{20}$$

and the ratio of stretching to bending,

$$K \equiv \frac{Hd^{2}}{B}. \tag{21}$$

All the parameter values are shown in table 1.

Appendix B. Numerical Implementation

We use the adaptive Runge-Kutta method Press *et al.* (2007) with cash-karp parameters Press and Teukolsky (1992); Cash and Karp (1990) to evolve the system. We use time-step, Δt, such that

$$\tilde{\Delta} = \frac{B\Delta t}{8\pi\eta L^{4}} = 10^{-11} - 10^{-12} \tag{22}$$

We use numerical accuracy of order 10^{-6} Press *et al.* (2007); Press and Teukolsky (1992); Cash and Karp (1990). We use CUDA to parallelize the code [5].

The dimensionless frequency, σ, must be small enough such that the Stokesian approximation remains valid. We use $K = 16$ (see table 1) for all the simulations. Note that (15) is exact for an inextensible filament. In our case, the total length of the filament changes at most by 2% – the filament is practically inextensible. Hence (15) remains a reasonable approximation. Our code reproduces the experimental results by Liu et. al. Liu *et al.* (2018) (see Fig. 8).

[5]Our code is available here: https://github.com/dhrubaditya/ElasticString

Parameters	Simulation values
Number of beads, N	256
Equilibrium distance between beads, a	0.005
Filament diameter, d	0.005
Filament length, L	1.28
Bending modulus, B	2×10^{-5}–8×10^{-3}
Strain Rate amplitude, S	2
Viscosity, η	10
Rate of change of strain rate, ω	1–6
Time-step, Δ	10^{-4}–10^{-6}
Elasto-viscous number, $\overline{\mu} = \frac{8\pi\eta SL^4}{B}$	1.7×10^5–6.8×10^7
Frequency parameter, $\sigma = \frac{\omega}{S}$	0.5–3
Stretching-bending modulus ratio, $K = \frac{Ha^2}{B}$	16

Table 1: Parameters of simulation. Earlier studies have used $N = 20 - 40$ Wada and Netz (2006), $N = 40$ Slowicka *et al.* (2019), N=400 Chakrabarti *et al.* (2020)

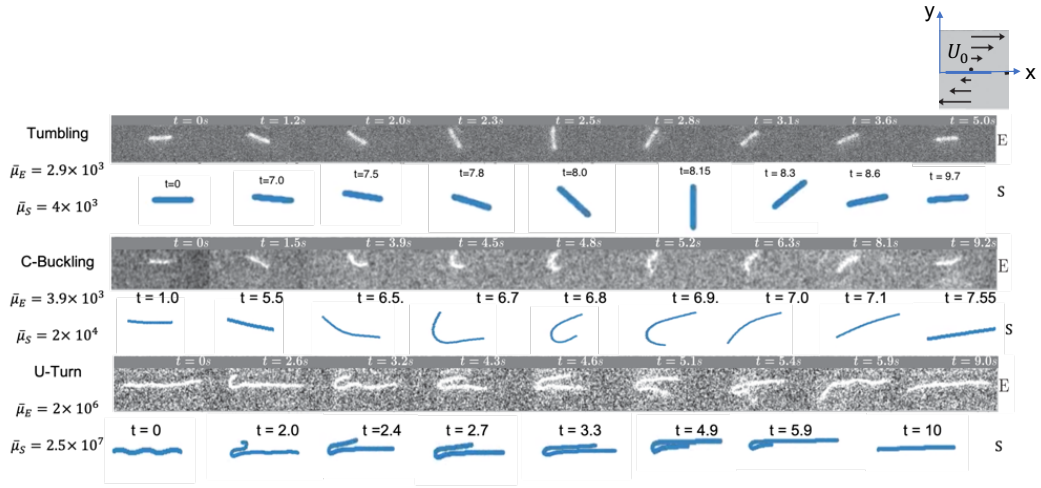

Figure 8: **Comparison with experimental results:** We reproduce the experimental results of Ref. Liu *et al.* (2018). The filament lies along the x-axis. It is advected by a flow $\boldsymbol{U} = (\dot{\gamma}y, 0)$, where $\dot{\gamma}$ is the shear rate. The flow is constant in time. We observe different dynamical behavior for different $\overline{\mu}$. The grey background are figures from Ref. Liu *et al.* (2018), and the white background are results of our simulation. Initially, we add small perturbation to the filament but ignore thermal fluctuations. The $\overline{\mu}_{\mathrm{E}}$ and $\overline{\mu}_{\mathrm{S}}$ are the values of $\overline{\mu}$ from experiments and our simulations respectively.

Appendix C. Detailed description of the dynamical phases

Our simulations reveal five different dynamical phases which we call – straight, buckling, two-period, complex and complex–transients (see Fig. 3 from main text).

For each case, we describe the dynamics through the morphology of the filament. This we do in two ways:

1. Extrinsic (real space) – actual shape of the filament.
2. Intrinsic (configurational space) – curvature (κ) of the filament as a function of the material coordinate(s). Our classification of dynamical phase is based on the intrinsic coordinates. Conversion between extrinsic to intrinsic coordinates is done using (16) – this conversion is unique. Although the inverse is not true. To impose uniqueness, we fix the position of the first bead and slope of the bond to the next one.

C.1. Straight (S)

The filament does not buckle but remains straight all through its evolution, the curvature remains zero always.

C.2. Periodic buckling (B)

The filament develops buckling instability. The filament settles into periodic behavior after initial transients and repeats itself stroboscopically (after every cycle) both extrinsically and intrinsically.

C.3. Two-period (2P)

The filament does not repeat itself after every period but after every two periods. Also, the filament does not come back to its position but is rotated after two-cycles – which we call *swimming*.

C.4. Complex (C)

The filament rotates in the first half of the cycle (see Fig. 1). In the second half, it buckles. In Fig. 9 (A), we plot the filament at the end of 1st, 10th, 19th and 28th cycle for $\overline{\mu} = 3.35 \times 10^6$, $\sigma = 1.5$) – the filament never repeats itself. In Fig. 9 (B), we plot the curvature (κ) of the filament as a function of arc-length (s) at the same times. This shows too that the shape of the filament never repeats at the end of each cycle. Even at late times $t > 60T$, the filament does not repeat itself at the end of a cycle – see Fig. 9(C) where we plot the shape of the filament at $t = 35T, 45T, ..., 75T$. The corresponding plot of κ versus s is shown in Fig. 9(D). Here it may seem that the filament comes close to

its previous shapes but a careful look tells us that it never completely repeats itself. Note that, the $\kappa - s$ plot for $t = 35T$ is very close to the one at $t = 65T$, although not exactly the same. The same is true for $t = 45T$ and $t = 75T$. This suggests that there maybe a very high period solution to the stroboscopic map. A sine transform of the $\kappa(s)$ to $\hat{\kappa}(q)$ shows several peaks, For $q \gtrapprox 20$ the $\hat{\kappa}$ is practically zero (Fig. 10) This demonstrates that our simulations are well resolved to capture the phenomena we observe.

Note that, in some cases of this complex phase, at late times, the filament achieves the most buckled state (as measured by total elastic energy) not at the end of the cycle but somewhere in between. One such case is shown in Fig. 11 for $\overline{\mu} = 6.7 \times 10^6$ and $\sigma = 0.75$. The κ–s plot at the end of every cycle comes very close to repeating itself – Fig. 11(B). The corresponding plots of the filament in real space, is shown in Fig. 11(A), are also very close to one another although do not overlap everywhere. However, if we loook at intermediate times e.g. at $t = 65.7T...75.7T$, we find that the filament does not repeat itself, Fig. 11(C,D).

To measure the disturbances in the flow due to moving filament, we calculate the time series of flow disturbance $(\boldsymbol{U} - \boldsymbol{U}_0)$ at an Eulerian point $\boldsymbol{r} = [0, L/2, 2d]$. The numerical method is described in the main body of the paper, see also chapter 8 of Ref. Kim and Karrila (2013). The Eulerian point is chosen to be just above the XY plane such that the filament does not overlap with it. We show the phase portraits of fluctuating velocity at late times ($t = 40T$ to $t = 75T$) in Fig. 9, Fig. 11(E,F) respectively. Note that, the velocity values are larger compared to the straight phase (Fig. 9(E,F)).

C.5. Complex transients:

The filament shows high mode of buckling. We compare the filament extrinsically and intrinsically at the end of 24th, 34th, 44th cycle for $\overline{\mu} = 3.35 \times 10^7, \sigma = 1.5$ respectively in Fig. 12(A,B). The filament shows complex behavior and does not repeat itself for early periods ($t < 60T$), similar to the complex phase. However, the complex behavior is transient and the filament comes very close to itself for late periods – at the end of a cycle ($t = 80T, 90T, 100T$, see Fig. 12(C)) and intermediate times between cycle where the filament shows maximum buckling ($t = 80.8T, 90.8T, 100.8T$, see Fig. 12(E)). The corresponding plots of κ–s are shown in Fig. 12 (D)(F) – this also shows the almost–periodic behavior of filament at late times. In Fig. 12(G), we show the shapes at $t = 80T, 130T, 180T$ and $230T$. Over such a long time scale, the shape does change. The corresponding s–κ plots are shown in Fig. 12(H) In Fig. 12(I) and (J) we show the phase portrait of Eulerian velocity at $\boldsymbol{r} = [0, L/2, 2d]$ for late times ($t > 80T$).

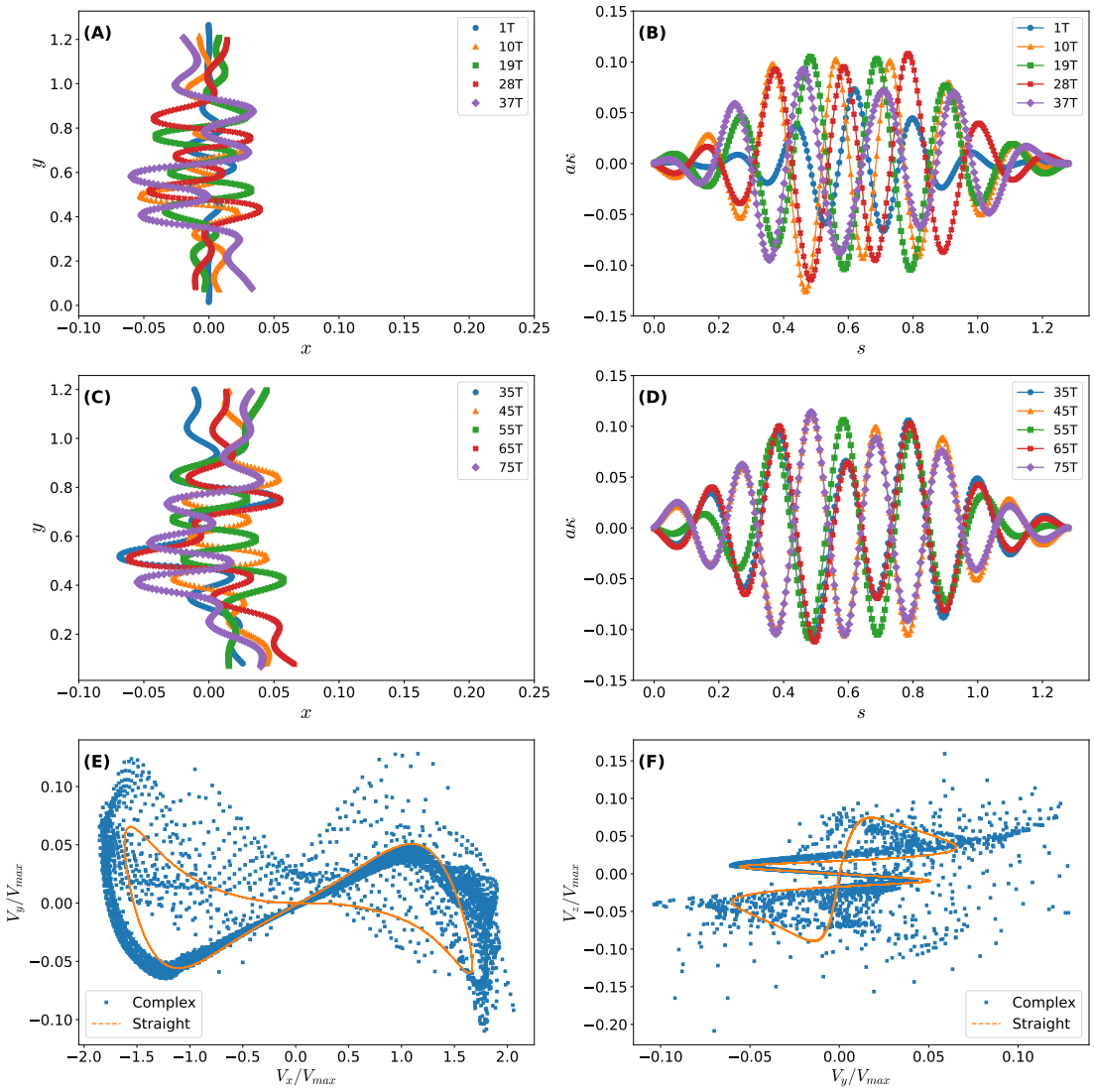

Figure 9: **Evolution of the filament in complex phase** ($\overline{\mu} = 3.35 \times 10^6$, $\sigma = 1.5$) The filament shows complex behavior for cycles at intermediate times, (A) real space; (B) configurational space. (C,D) For late cycles also, the filament either does not repeat itself or comes close to repeating itself with very high time-period. The filament shows maximum compression at the end of cycle. (E,F) Phase portrait of tracer velocity late cycles $t = 45T$–$75T$. For comparison we also show the phase potrait for a case in the straight phase (organge).

Appendix D. Stroboscopic map

We take a dynamical system approach to analyze the complex dynamics we observe. Such techniques have been used widely to study highly turbulent flows Kerswell (2005); Suri *et al.* (2020); Page *et al.* (2020) and has also been applied to other fields of fluid dynamics Franco-Gómez *et al.* (2018); Gaillard

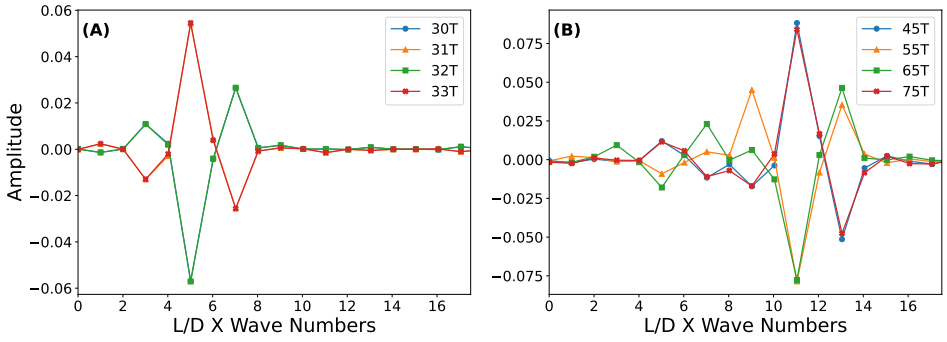

Figure 10: **Discrete sine transform** for two-period phase (A), and complex phase (B).

et al. (2021). Let us define an operator $\mathcal{F}$ such that:

$$\boldsymbol{\kappa}(T) = \mathcal{F}\boldsymbol{\kappa}(0) \tag{23a}$$

$$\mathcal{F}^{\mathrm{p}} = \mathcal{F}\mathcal{F}...\text{p times}...\mathcal{F}, \tag{23b}$$

where $\boldsymbol{\kappa} = [\kappa_1, \kappa_2, \ldots \kappa_{\mathrm{i}} \ldots \kappa_N]$, where κ_{i} is the curvature at point i. For a given $\boldsymbol{\kappa}$, the operator, $\mathcal{F}$, returns the values of $\boldsymbol{\kappa}$ after evolving the system for exactly one time-period. We look for fixed points and periodic orbits of this map Cvitanovic *et al.* (2005) by solving $\boldsymbol{\kappa} = \mathcal{F}^{\mathrm{p}}\boldsymbol{\kappa}$. The task is now to calculate the solutions of set of the non-linear equations:

$$\mathcal{N}_{\mathrm{p}}\boldsymbol{\kappa} \equiv (\mathcal{F}^{\mathrm{p}} - 1)\,\boldsymbol{\kappa} = 0 \tag{24}$$

For example, $\boldsymbol{\kappa} = \mathbf{0}$, $\mathrm{p} = 1$, is a solution for straight phase. The periodic buckling and two–period have non–zero curvature ($\boldsymbol{\kappa}$) solution respectively for $\mathrm{p} = 1$ and $\mathrm{p} = 2$. We use the Newton-Krylov method Knoll and Keyes (2004) based on Generalized Minimal Residual Method (GMRES) Saad and Schultz (1986) in jacobian–free way to find the solutions. It is described next.

D.1. Newton–Krylov

The flow-chart of the algorithm is shown in Fig. 13. We start with a guess for the curvature, $\boldsymbol{\kappa}(0)$. Then we calculate the positions of the beads given by $\boldsymbol{y} \equiv [y_1, ...y_{2j-1}, y_{2j}, ...y_{2N}] \equiv [R_1^1, ..., R_j^1, R_j^2, ...R_N^2]$. We call this transformation $\boldsymbol{\kappa}$ to $\boldsymbol{y}$, $\mathbb{K}^{-1}$, such that:

$$\boldsymbol{y}(0) = \mathbb{K}^{-1}\boldsymbol{\kappa}(0) \tag{25}$$

Then we evolve in time from $t = 0$ to $t = \mathrm{p}T$ by solving (11) to obtain $\boldsymbol{y}(\mathrm{p}T)$. Then we apply the inverse transformation, $\mathbb{K}$, to obtain

$$\boldsymbol{\kappa}(\mathrm{p}T) = \mathbb{K}(\boldsymbol{y}(\mathrm{p}T)) \tag{26}$$

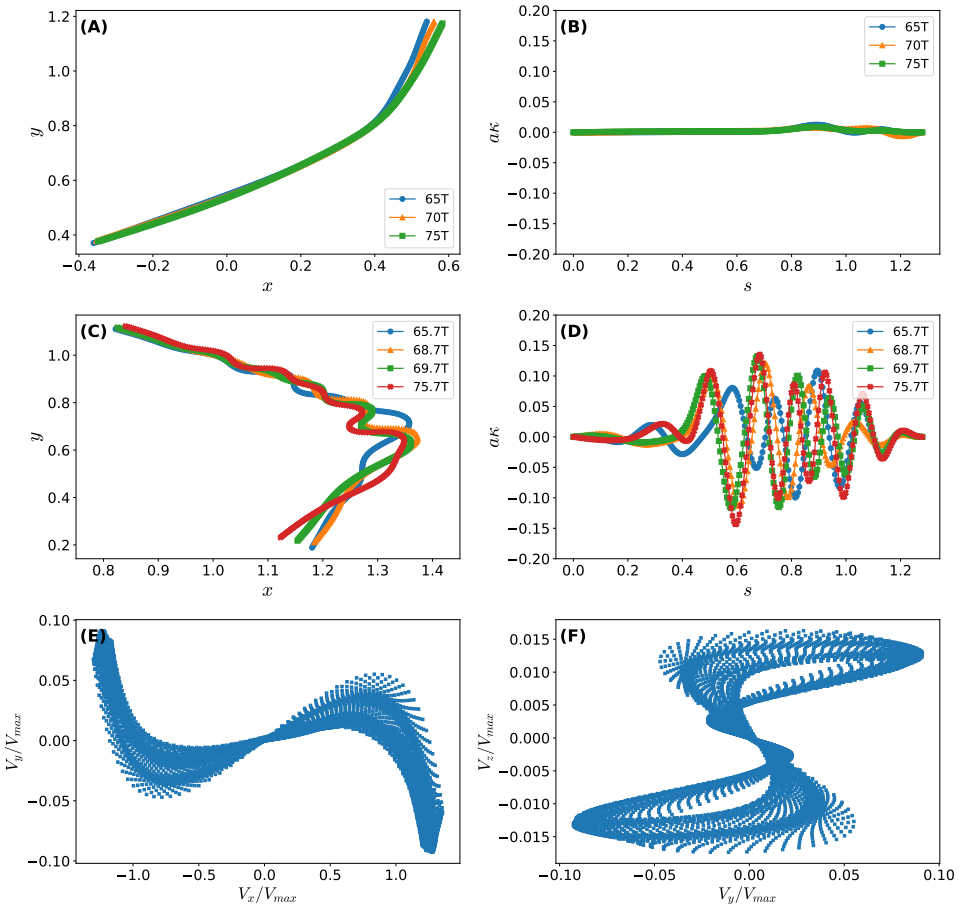

Figure 11: **Evolution of the filament in the complex phase** ($\overline{\mu} = 6.7 \times 10^6$, $\sigma = 0.75$) The filament shows complex behavior at early cycles respectively in real space and configuration space. However, for late times ($t = 65T, 70T, 75T$), the filament almost repeats itself at nT, where n is an integer (A,B). Also note that, highest bending energy of the filament is at $(n+p)T$, $p \neq 0$ instead of nT (C,D). The filament is shown stroboscopically for $p = 0.7$ respectively in real space and configuration space. We observe that the filament does not repeat itself. (E,F) Phase portrait in (x, y) and (y, z) of Eulerian velocity at one point.

Then we check how accurately (24) is satisfied, i.e. we define

$$\text{error} = \frac{||\mathcal{N}_{\text{p}}\boldsymbol{\kappa}||_2}{||\boldsymbol{\kappa}(0)||_2}. \tag{27}$$

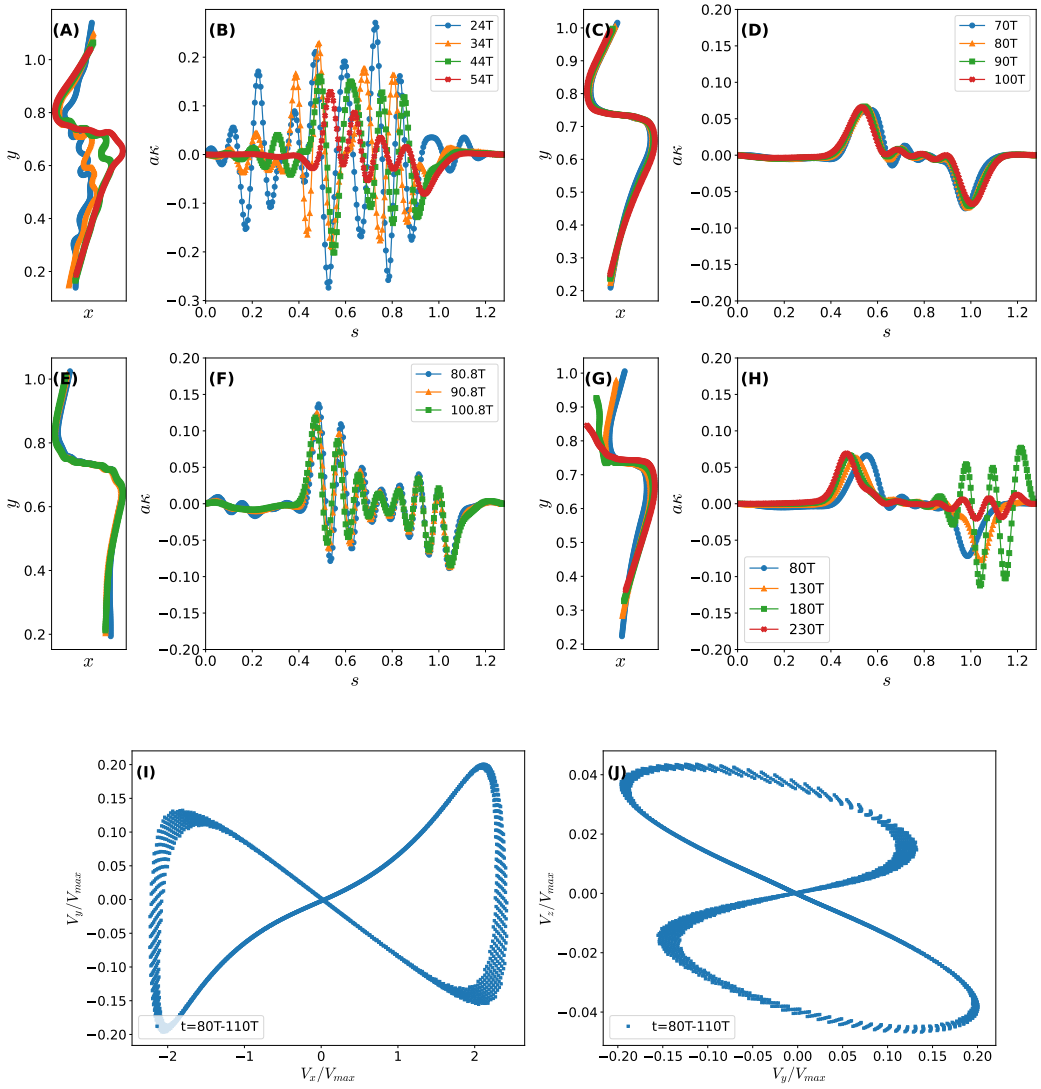

Figure 12: **Evolution in the complex–transient phase**: ($\overline{\mu} = 3.35 \times 10^7$, $\sigma = 1.5$). The shape of the filament in (A)(C)(E) and the corresponding curvature is shown in (B)(D)(F). For early cycles (t $\leq$ 60T), the filament shows complex behavior and does not repeat itself (A,B), similar to the complex phase (see Fig. 9). For late cycles (t=70T ... 100T), although the filament does not repeat itself, it comes very close after every cycle (C,D,E,F). The filament shape, from the end of one cycle to next, changes very slowly, e.g. (E) shows the shape at $t = 80.8T, 90.8T, 100.8T$. In (G), we show the shapes at $t = 80T, 130T \ldots$. Over such a long time scale, the shape does change. (I)(J) Phase portrait of velocity at an Eulerian point for the late cycles.

The case for straight solution is dealt specially because in this case $\boldsymbol{\kappa} = 0$. Here we use:

$$\text{error} = \frac{||\mathcal{N}_{\text{p}}\boldsymbol{\kappa}||_2}{N * \text{tol}} \tag{28}$$

If the error is less than a preset tolerance, then we accept the guess ($\boldsymbol{\kappa}(0)$) as a solution, otherwise, we generate a new guess by

$$\boldsymbol{\kappa}(0) = \boldsymbol{\kappa}(0) + \delta\boldsymbol{\kappa}, \tag{29a}$$

such that

$$\mathcal{J} \cdot \delta\boldsymbol{\kappa} = -\mathcal{N}_{\mathrm{p}}\boldsymbol{\kappa}(0). \tag{29b}$$

Here $\mathcal{J}$ is jacobian matrix of the operator $\mathcal{N}_{\mathrm{p}}$ computed at $\boldsymbol{\kappa}(0)$. We do not calculate $\mathcal{J}$, instead we calculate:

$$\mathcal{J} \cdot \delta\boldsymbol{\kappa} = \frac{\mathcal{N}_{\mathrm{p}}(\boldsymbol{\kappa}(0) + \varepsilon\delta\boldsymbol{\kappa}) - \mathcal{N}_{\mathrm{p}}(\boldsymbol{\kappa}(0) - \varepsilon\delta\boldsymbol{\kappa})}{2\varepsilon}. \tag{30}$$

Here ε is a step size Knoll and Keyes (2004). We use the GMRES Saad and Schultz (1986); Guennebaud *et al.* (2010) method in matrix-free way using (30) to find solutions of (29b). The operator $\mathcal{N}_{\mathrm{p}}$ is implemented as described in Figure. 13. The value of ε should be small enough such that (30) is well approximated and large enough such that the floating point round–off errors are not too large Knoll and Keyes (2004). We compute ε in the following way:

$$\varepsilon = \varepsilon_{\mathrm{rel}} \left(1 + \frac{||\boldsymbol{\kappa}(0)||_2}{||\delta\boldsymbol{\kappa}(0)||_2}\right), \tag{31}$$

where $||\cdot||$ is the 2nd norm, and $\varepsilon_{\mathrm{rel}} = 10^{-4}$.

Note that, the conversion from curvature space to real space ($\mathbb{K}^{-1}$) is not unique. However, if we fix the position of the first bead and slope of the bond to the next one, it is unique. One advantage of using this method is that, it accounts for all the continuous symmetries (translation in x,y direction) present in the system Cvitanovic *et al.* (2005).

Also note that the $\boldsymbol{\kappa}$ is the same for two filaments which has the same shape but are rotated with respect to each other. But the evolution of two such filaments are not the same, in principle, because the ambient flow depends on space. In some cases, we find the solutions such that the filament comes to the same shape as before but rotated. We call these solutions "swimming solutions".

References

Edward M Purcell, "Life at low reynolds number," American journal of physics **45**, 3–11 (1977).

Eric Lauga and Thomas R Powers, "The hydrodynamics of swimming microorganisms," Reports on Progress in Physics **72**, 096601 (2009).

Rob Phillips, Jane Kondev, Julie Theriot, Hernan G Garcia, and Nigel Orme, *Physical biology of the cell* (Garland Science, 2012).

Geoffrey Ingram Taylor, "Analysis of the swimming of microscopic organisms," Proceedings of the Royal Society of London. Series A. Mathematical and Physical Sciences **209**, 447–461 (1951).

Todd M Squires and Stephen R Quake, "Microfluidics: Fluid physics at the nanoliter scale," Reviews of modern physics **77**, 977 (2005).

Brian J Kirby, *Micro-and nanoscale fluid mechanics: transport in microfluidic devices* (Cambridge university press, 2010).

Howard A Stone, Abraham D Stroock, and Armand Ajdari, "Engineering flows in small devices: microfluidics toward a lab-on-a-chip," Annu. Rev. Fluid Mech. **36**, 381–411 (2004).

Geoffrey I Taylor, "Film notes for low-reynolds-number flows," National Committee for Fluid Mechanics Films **21617** (1967).

Hassan Aref, John R Blake, Marko Budišić, Silvana SS Cardoso, Julyan HE Cartwright, Herman JH Clercx, Kamal El Omari, Ulrike Feudel, Ramin Golestanian, Emmanuelle Gouillart, *et al.*, "Frontiers of chaotic advection," Reviews of Modern Physics **89**, 025007 (2017).

Alexander Groisman and Victor Steinberg, "Elastic turbulence in a polymer solution flow," Nature **405**, 53–55 (2000).

Alexander Groisman and Victor Steinberg, "Efficient mixing at low reynolds numbers using polymer additives," Nature **410**, 905–908 (2001).

Abraham D Stroock, Stephan KW Dertinger, Armand Ajdari, Igor Mezić, Howard A Stone, and George M Whitesides, "Chaotic mixer for microchannels," Science **295**, 647–651 (2002).

Victor Steinberg, "Elastic turbulence: an experimental view on inertialess random flow," Annual Review of Fluid Mechanics **53**, 27–58 (2021).

Christopher Dombrowski, Luis Cisneros, Sunita Chatkaew, Raymond E Goldstein, and John O Kessler, "Self-concentration and large-scale coherence in bacterial dynamics," Physical review letters **93**, 098103 (2004).

Henricus H Wensink, Jörn Dunkel, Sebastian Heidenreich, Knut Drescher, Raymond E Goldstein, Hartmut Löwen, and Julia M Yeomans, "Meso-scale turbulence in living fluids," Proceedings of the national academy of sciences **109**, 14308–14313 (2012).

Jörn Dunkel, Sebastian Heidenreich, Knut Drescher, Henricus H Wensink, Markus Bär, and Raymond E Goldstein, "Fluid dynamics of bacterial turbulence," Physical review letters **110**, 228102 (2013).

David J Pine, Jerry P Gollub, John F Brady, and Alexander M Leshansky, "Chaos and threshold for irreversibility in sheared suspensions," Nature **438**, 997–1000 (2005).

Leif E Becker and Michael J Shelley, "Instability of elastic filaments in shear flow yields first-normal-stress differences," Physical Review Letters **87**, 198301 (2001).

Laura Guglielmini, Amit Kushwaha, Eric SG Shaqfeh, and Howard A Stone, "Buckling transitions of an elastic filament in a viscous stagnation point flow," Physics of Fluids **24**, 123601 (2012).

Yanan Liu, Brato Chakrabarti, David Saintillan, Anke Lindner, and Olivia Du Roure, "Morphological transitions of elastic filaments in shear flow," Proceedings of the National Academy of Sciences **115**, 9438–9443 (2018).

John LaGrone, Ricardo Cortez, Wen Yan, and Lisa Fauci, "Complex dynamics of long, flexible fibers in shear," Journal of Non-Newtonian Fluid Mechanics **269**, 73–81 (2019).

AM Slowicka, Howard A Stone, and Maria L Ekiel-Jezewska, "Flexible fibers in shear flow: attracting periodic solutions," arXiv preprint arXiv:1905.12985 (2019).

Paweł J Żuk, Agnieszka M Słowicka, Maria L Ekiel-Jeżewska, and Howard A Stone, "Universal features of the shape of elastic fibres in shear flow," Journal of Fluid Mechanics **914** (2021).

Steve Kuei, Agnieszka M Słowicka, Maria L Ekiel-Jeżewska, Eligiusz Wajnryb, and Howard A Stone, "Dynamics and topology of a flexible chain: knots in steady shear flow," New Journal of Physics **17**, 053009 (2015).

Shi-Yuan Hu, Jun-Jun Chu, Michael J Shelley, and Jun Zhang, "Lévy walks and path chaos in the dispersal of elongated structures moving across cellular vortical flows," Physical Review Letters **127**, 074503 (2021).

Brato Chakrabarti, Yanan Liu, John LaGrone, Ricardo Cortez, Lisa Fauci, Olivia du Roure, David Saintillan, and Anke Lindner, "Flexible filaments buckle into helicoidal shapes in strong compressional flows," Nature Physics , 1–6 (2020).

RG Larson, Hua Hu, DE Smith, and S Chu, "Brownian dynamics simulations of a dna molecule in an extensional flow field," Journal of Rheology **43**, 267–304 (1999).

Hirofumi Wada and Roland R Netz, "Non-equilibrium hydrodynamics of a rotating filament," EPL (Europhysics Letters) **75**, 645 (2006).

Ehssan Nazockdast, Abtin Rahimian, Denis Zorin, and Michael Shelley, "A fast platform for simulating semi-flexible fiber suspensions applied to cell mechanics," Journal of Computational Physics **329**, 173–209 (2017).

Jens Rotne and Stephen Prager, "Variational treatment of hydrodynamic interaction in polymers," The Journal of Chemical Physics **50**, 4831–4837 (1969).

John F Brady and Georges Bossis, "Stokesian dynamics," Annual review of fluid mechanics **20**, 111–157 (1988).

Elisabeth Guazzelli and Jeffrey F Morris, *A physical introduction to suspension dynamics*, Vol. 45 (Cambridge University Press, 2011).

Sangtae Kim and Seppo J Karrila, *Microhydrodynamics: principles and selected applications* (Courier Corporation, 2013).

The length of the filament changes by at most 2% in the worst case.

William H Press, Saul A Teukolsky, William T Vetterling, and Brian P Flannery, *Numerical recipes 3rd edition: The art of scientific computing* (Cambridge university press, 2007).

William H Press and Saul A Teukolsky, "Adaptive stepsize runge-kutta integration," Computers in Physics **6**, 188–191 (1992).

Jeff R Cash and Alan H Karp, "A variable order runge-kutta method for initial value problems with rapidly varying right-hand sides," ACM Transactions on Mathematical Software (TOMS) **16**, 201–222 (1990).

Tobias M Schneider, Bruno Eckhardt, and James A Yorke, "Turbulence transition and the edge of chaos in pipe flow," Physical review letters **99**, 034502 (2007).

TK Shajahan, Sitabhra Sinha, and Rahul Pandit, "Spiral-wave dynamics depend sensitively on inhomogeneities in mathematical models of ventricular tissue," Physical Review E **75**, 011929 (2007).

Ganapati Sahoo, Dhrubaditya Mitra, and Rahul Pandit, "Dynamo onset as a first-order transition: Lessons from a shell model for magnetohydrodynamics," Physical Review E **81**, 036317 (2010).

Ditza Auerbach, Predrag Cvitanović, Jean-Pierre Eckmann, Gemunu Gunaratne, and Itamar Procaccia, "Exploring chaotic motion through periodic orbits," Physical Review Letters **58**, 2387 (1987).

Predrag Cvitanovic, Roberto Artuso, Ronnie Mainieri, Gregor Tanner, Gábor Vattay, Niall Whelan, and Andreas Wirzba, "Chaos: classical and quantum," ChaosBook. org (Niels Bohr Institute, Copenhagen 2005) **69**, 25 (2005).

RR Kerswell, "Recent progress in understanding the transition to turbulence in a pipe," Nonlinearity **18**, R17 (2005).

Balachandra Suri, Logan Kageorge, Roman O Grigoriev, and Michael F Schatz, "Capturing turbulent dynamics and statistics in experiments with unstable periodic orbits," Physical Review Letters **125**, 064501 (2020).

Jacob Page, Yves Dubief, and Rich R Kerswell, "Exact traveling wave solutions in viscoelastic channel flow," Physical Review Letters **125**, 154501 (2020).

Andrés Franco-Gómez, Alice B Thompson, Andrew L Hazel, and Anne Juel, "Bubble propagation in hele-shaw channels with centred constrictions," Fluid Dynamics Research **50**, 021403 (2018).

Antoine Gaillard, Jack S Keeler, Grégoire Le Lay, Grégoire Lemoult, Alice B Thompson, Andrew L Hazel, and Anne Juel, "The life and fate of a bubble in a geometrically perturbed hele-shaw channel," Journal of Fluid Mechanics **914** (2021).

G.I. Taylor, "Diffusion by continious movements," Proc. London. Math. Soc. **s2-20**, 196–212 (1922).

Raymond E Goldstein, Thomas R Powers, and Chris H Wiggins, "Viscous nonlinear dynamics of twist and writhe," Physical Review Letters **80**, 5232 (1998).

K Radhakrishnan, K Asokan, J Dasan, C Chandrashekara Bhat, and TR Ramamohan, "Numerical evidence for the existence of a low-dimensional attractor and its

implications in the rheology of dilute suspensions of periodically forced slender bodies," Physical Review E **60**, 6602 (1999).

Fredrik Lundell, "The effect of particle inertia on triaxial ellipsoids in creeping shear: from drift toward chaos to a single periodic solution," Physics of Fluids **23**, 011704 (2011).

Christopher Nilsen and Helge I Andersson, "Chaotic rotation of inertial spheroids in oscillating shear flow," Physics of Fluids **25**, 013303 (2013).

J. D. Hunter, "Matplotlib: A 2d graphics environment," Computing in Science & Engineering **9**, 90–95 (2007).

Alberto Montesi, David C Morse, and Matteo Pasquali, "Brownian dynamics algorithm for bead-rod semiflexible chain with anisotropic friction," The Journal of chemical physics **122**, 084903 (2005).

Miklós Bergou, Basile Audoly, Etienne Vouga, Max Wardetzky, and Eitan Grinspun, "Discrete viscous threads," ACM Transactions on Graphics (TOG) **29**, 1–10 (2010).

Hirofumi Wada and Roland R Netz, "Stretching helical nano-springs at finite temperature," EPL (Europhysics Letters) **77**, 68001 (2007).

Thomas R Powers, "Dynamics of filaments and membranes in a viscous fluid," Reviews of Modern Physics **82**, 1607 (2010).

Miklós Bergou, Max Wardetzky, Stephen Robinson, Basile Audoly, and Eitan Grinspun, "Discrete elastic rods," in *ACM SIGGRAPH 2008 papers* (2008) pp. 1–12.

Our code is available here: https://github.com/dhrubaditya/ElasticString.

Dana A Knoll and David E Keyes, "Jacobian-free newton–krylov methods: a survey of approaches and applications," Journal of Computational Physics **193**, 357–397 (2004).

Youcef Saad and Martin H Schultz, "Gmres: A generalized minimal residual algorithm for solving nonsymmetric linear systems," SIAM Journal on scientific and statistical computing **7**, 856–869 (1986).

Gaël Guennebaud, Benoît Jacob, Philip Avery, Abraham Bachrach, Sebastien Barthelemy, *et al.*, "Eigen v3," (2010)

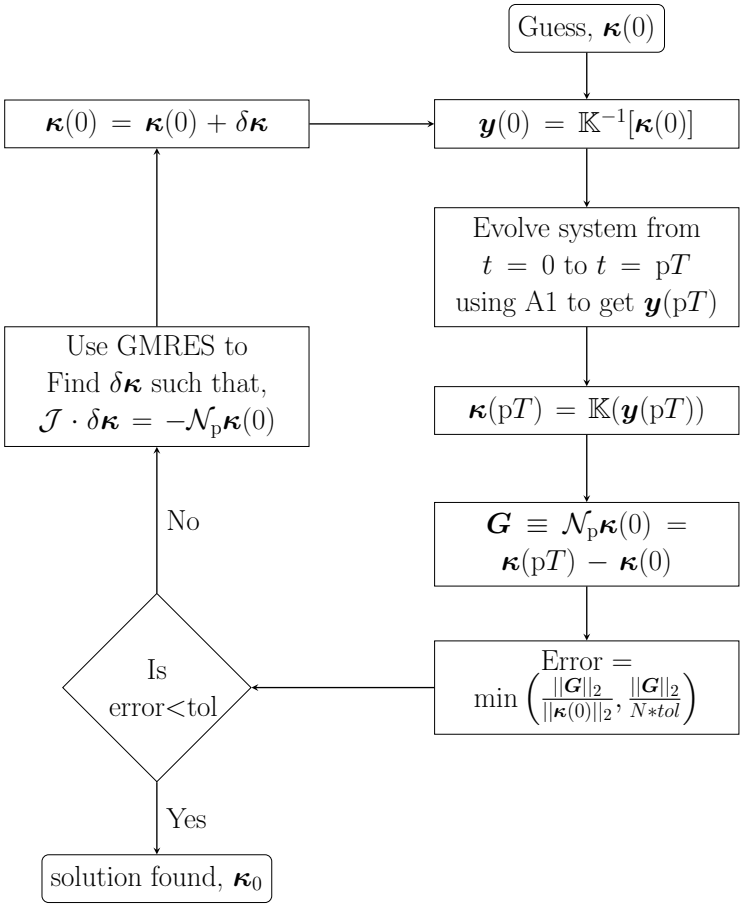

1

Figure 13: Flowchart for Newton–Krylov iteration. $\mathbb{K}$ is co-ordinate transformation from real to curvature space using equation (16). Similarly, $\mathbb{K}^{-1}$ is the inverse coordinate transformation from curvature to real space. We use the notation: $\mathcal{J}$ is jacobian of the operator $\mathcal{N}$, described in (24). We use tol = 0.01

4

Flexible filament in time–periodic viscous flow : shape chaos and period three

Vipin Agrawal[1,2] **and Dhrubaditya Mitra**[1]

[1] Nordita, KTH Royal Institute of Technology and Stockholm University, Roslagstullsbacken 23, 10691 Stockholm, Sweden

[2] Department of Physics, Stockholm university, Stockholm,Sweden.

arXiv:2210.04781

We study a single, freely–floating, inextensible, elastic filament in a linear shear flow: $\boldsymbol{U}_0(x, y) = \dot{\gamma} y \hat{x}$. In our model: the elastic energy depends only on bending; the rate–of–strain, $\dot{\gamma} = S \sin(\omega t)$ is a periodic function of time, t; and the interaction between the filament and the flow is approximated by a local isotropic drag force. Based on the shape of the filament we find five different dynamical phases: straight, buckled, periodic (with period two, period three, period four, etc), chaotic and one with chaotic transients. In the chaotic phase, we show that the iterative map for the angle, which the end–to–end vector of the filament makes with the tangent its one end, has period three solutions; hence it is chaotic. Furthermore, in the chaotic phase the flow is an efficient mixer.

1. Introduction

The dynamics of flexible filaments in flows plays a crucial role in many biological and industrial processes Duprat (2022). A canonical example is that of cilia and flagella Brennen and Winet (1977); Sleigh (2016) that takes part in wide variety of biological tasks, e.g., swimming of microorganisms, feeding and breathing of marine invertebrates. In such cases, although the flow nonlinearities can often be safely ignored, due to its elastic nonlinearities and flow–structure interactions a single isolated filament can show surprisingly complex dynamics in flows. Both active and passive filament, anchored or freely floating, in various steady flows have been studied extensively, see Ref. Du Roure *et al.* (2019); Bruot and Cicuta (2016) and references therein. In steady flows, a single passive filament has quite complex transient dynamics Becker and Shelley (2001); Guglielmini *et al.* (2012); Liu *et al.* (2018); LaGrone *et al.* (2019); Slowicka *et al.* (2019); Żuk *et al.* (2021); Kuei *et al.* (2015); Hu *et al.* (2021); Chakrabarti *et al.* (2020). For active filaments, the focus has been on how a periodic driving can give rise to symmetry breaking, e.g., swimming Wiggins *et al.* (1998) or whirling Wolgemuth *et al.* (2000); Lim and Peskin (2004); Wada and Netz (2006). This year, three papers have focussed on, how periodic driving, either of the flow or the filament, can give rise to secondary instabilities Bonacci *et al.* (2022) or statistically stationary state with chaotic/complex dynamics Agrawal and Mitra (2022); Krishnamurthy and Prakash (2022). For the latter, the shape of the filament, as described by its curvature as a function of its arc length, is a spatiotemporally chaotic function. Henceforth we call this phenomena *shape chaos*. Such chaotic solutions are particularly interesting because they have the potential to be used to generate efficient mixing in microfluidics. Two effects determine the fate of an elastic filament in flow. One is the elastic nonlinearity of the filament and the other is the viscous interaction between the filament and the flow. The latter, in all its glory, gives rise to non–local and nonlinear interaction between two different parts of the same filament. Nevertheless, theoretical studies Doi and Edwards (1986); Goldstein and Langer (1995); Goldstein *et al.* (1998); Wolgemuth *et al.* (2000) have often approximated the viscous effect as a local, linear, isotropic drag. Can this local approximation to the flow–structure interaction still capture the shape chaos of a freely-floating filament ? As we show in the rest of this paper, the answer is yes; we prove shape chaos using Sharkovskii and Li and Yorke's famous result Alligood *et al.* (1996) – existence of period orbits of period three implies not only the existence of orbits of all periods but also senstive dependence on initial condition.

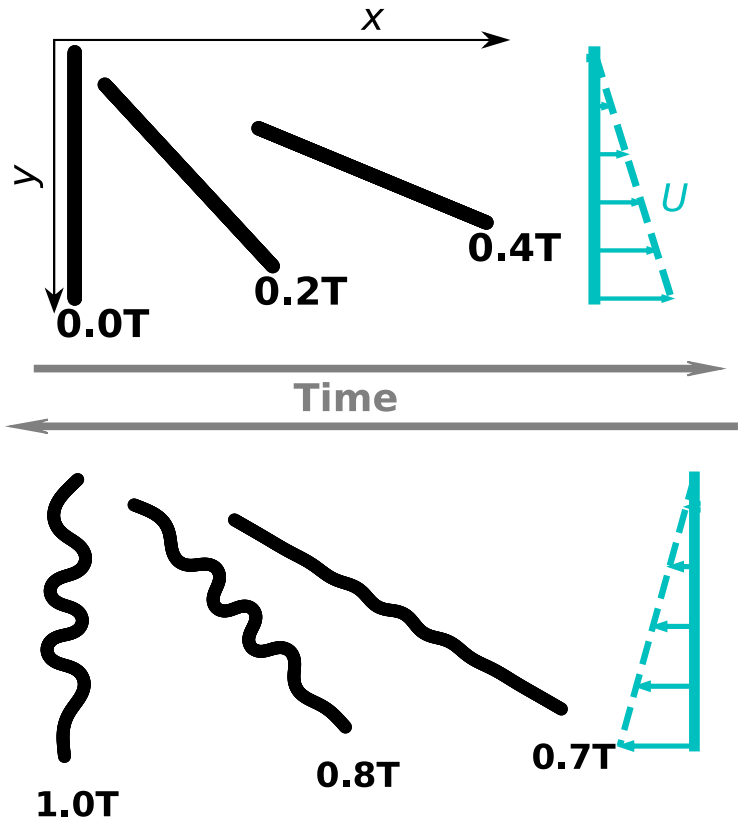

Figure 1: **Sketch of our numerical experiment**. Initially the filament is straight and is aligned vertically. The background shear flow, Equation (1) is shown as arrow: $t = T/4$ (top panel) and $t = 3T/4$ (bottom panel).

In Figure. 1 we show a sketch of our numerical experiment. Initially the filament is aligned vertically. The background shear flow is given by

$$\boldsymbol{U}_0(x, y) = \dot{\gamma} y \hat{\mathrm{x}}, \quad \text{and} \quad \dot{\gamma} = S \sin(\omega t). \tag{1}$$

Here $T = 2\pi/\omega$ is the time period of the periodic shear and S is a constant.

2. Model

We model the filament using the bead-spring model Larson *et al.* (1999); Guglielmini *et al.* (2012); Nazockdast *et al.* (2017); Slowicka *et al.* (2019); Wada and Netz (2006); Żuk *et al.* (2021): identical spherical beads of diameter d are connected by over-damped springs of equilibrium length a. The position of the center of the i-th bead is $\boldsymbol{R}_\mathrm{i}$, where $i = 1 \ldots N$, the total number of beads. The equation of motion is:

$$\frac{\partial R_\mathrm{i}^\alpha}{\partial t} = -\frac{1}{3\pi\eta d}\frac{\partial \mathcal{H}}{\partial R_\mathrm{i}^\alpha} + U_0^\alpha(\boldsymbol{R}_\mathrm{i}), \tag{2}$$

where U_0 is given in (1). Here η is viscosity of the fluid, $\partial(\cdot)/\partial(\cdot)$ denotes partial derivative, $\boldsymbol{U}_0$ is the velocity of the background shear, and $\mathcal{H}$ is the elastic Hamiltonian of the filament. The Greek indices run from 1 to D, the dimensionality of the space, and the Latin indices run from 1 to N. The elastic Hamiltonian Wada and Netz (2006, 2007), has contributions from bending ($\mathcal{H}_\mathrm{B}$) and stretching ($\mathcal{H}_\mathrm{S}$):

$$\mathcal{H} = \mathcal{H}_\mathrm{B} + \mathcal{H}_\mathrm{S} \quad \text{where} \tag{3a}$$

$$\mathcal{H}_\mathrm{B} = aB \sum_{\mathrm{i}=0}^{N-1} \kappa_\mathrm{i}^2 \quad \text{and} \tag{3b}$$

$$\mathcal{H}_\mathrm{S} = \frac{H}{2a} \sum_{\mathrm{i}=0}^{N-1} \left(|\boldsymbol{R}_{\mathrm{i}+1} - \boldsymbol{R}_\mathrm{i}| - a\right)^2; \quad \text{where} \tag{3c}$$

$$\kappa_\mathrm{i} = \frac{1}{a}|\hat{\boldsymbol{u}}_\mathrm{i} \times \hat{\boldsymbol{u}}_{\mathrm{i}-1}| \quad \text{and} \tag{3d}$$

$$\hat{\boldsymbol{u}}_\mathrm{i} = \frac{\boldsymbol{R}_{\mathrm{i}+1} - \boldsymbol{R}_\mathrm{i}}{|\boldsymbol{R}_{\mathrm{i}+1} - \boldsymbol{R}_\mathrm{i}|}. \tag{3e}$$

Here B is the bending modulus of the filament and H is its stretching modulus. We ignore thermal fluctuations and torsion. Three dimensionless parameters determine the dynamics. We call them, the elasto–viscous parameters, the dimensionless frequency and the ratio of stretching to bending defined respectively as:

$$\overline{\mu} \equiv \frac{8\pi\eta S L^4}{B}, \tag{4a}$$

$$\sigma \equiv \frac{\omega}{S}, \quad \text{and} \tag{4b}$$

$$K \equiv \frac{Ha^2}{B}. \tag{4c}$$

In practice, the filaments are inextensible Powers (2010), which we implement by choosing appropriately high value of K. We evolve Equation (2) using adaptive Runge-Kutta Press and Teukolsky (1992) method with cash-karp parameters Cash and Karp (1990). Our code is freely available [6] and has been benchmarked against experimental results Agrawal and Mitra (2022). A complete list of the parameters of the simulation is given in table 1. We study the problem for a large range of $\overline{\mu}$ and σ all within experimentally realizable range. Note that, with the local approximation of viscous forces it is possible for the filament to cross itself. Such unphysical solutions do appear in our simulations but for values of $\overline{\mu}$ other than that has been considered in this paper.

[6] https://github.com/dhrubaditya/ElasticString

The computational complexity of the model, where the viscous interaction is modelled by the non–local Rotne–Pregor tensor Agrawal and Mitra (2022), is $\mathcal{O}(N^2)$ where N is the number of beads, whereas the computational complexity of the model with local viscosity is $\mathcal{O}(N)$. This allows us to run our simulations for much longer times than it was possible in Ref. Agrawal and Mitra (2022).

3. Results

A rigid ellipsoid in a periodic shear may show chaotic three–dimensional rotation under certain conditions Ramamohan *et al.* (1994); Kumar *et al.* (1995); Lundell (2011); Nilsen and Andersson (2013). Such behavior emerges due to the nonlinearities present in the Euler's equations of rigid body rotation. Here we consider a filament with no inertia, hence such chaotic solutions are not present in our system. For a filament with high bending rigidity (small $\overline{\mu}$) we find that the filament merely translates and rotates coming back to its initial position and shape at the end of every period.

For a fixed dimensionless frequency (σ) as the bending rigidity is decreased ($\overline{\mu}$ is increased) an kaleidoscope of dynamic behavior emerges. We show an example in Figure. 1. During the first half-period the flow is extensional and the filament rotates. In the second half the flow is compressional and the filament can undergo buckling transition – the shape of the filament after one period is no longer straight but buckled. Furthermore, it may not come back to its initial position but may come back translated or rotated, neither of which are of interest to us in this paper – we focus on the shape of the filament. Under subsequent iterations of the periodic shear the buckled filament can go through many changes in shape.

We show a dynamic phase diagram in Fig. 2(A). Overall, at late times, the following possibilities exists:

1. The filament is always straight.
2. The filament reaches the same buckled shape at the end of each period.
3. The shape of the filament shows periodic behaviour with two-cycle, three-cycle, four-cycle, etc.
4. The shape of the filament is spatiotemporally chaotic. In Fig. 2(A) such solutions are marked *complex*.
5. The filament shows chaotic behavior for a long time but such behavior turns out to be transient. At late times the filament settles down to a complicated shape which changes very slowly. In Fig. 2(A) such solutions are marked *complex transients*.

We have observed the same qualitative behavior before Agrawal and Mitra (2022), for the case where the viscous forces are modeled by the non-local Rotne-Pregor tensor, with two crucial quantitative differences. We did not observe any

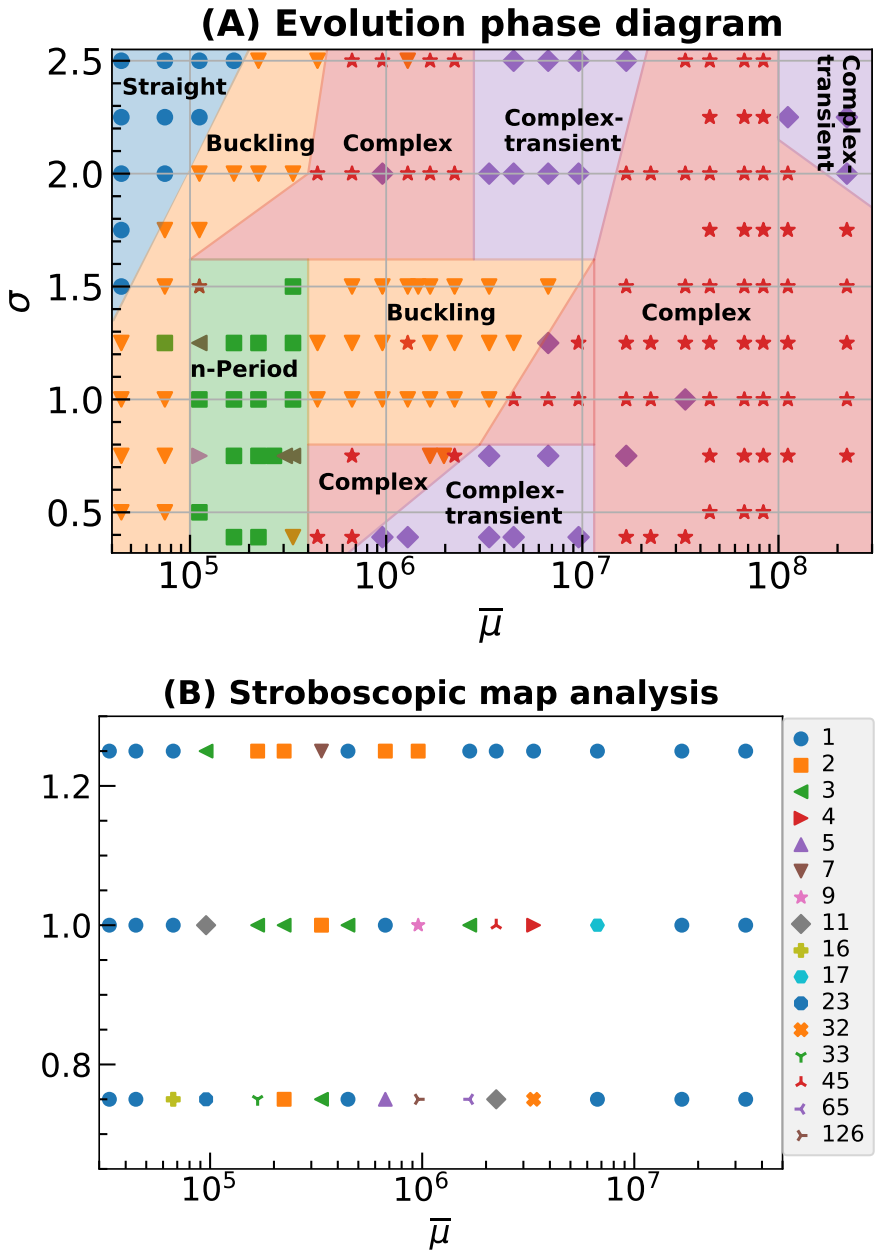

Figure 2: **(A):Phase diagram** in the $\overline{\mu}$–σ plane; We find 5 different qualitatively different dynamical phases: Straight(•); periodic (▼) with n-period, where n=2(■), 3(◀), 4(▶); complex (★) complex-transients (♦) **(B) Solutions of stroboscopic map**: The stroboscopic map has many periodic solutions at every point in $\overline{\mu}$–σ plane. We show time period of the lowest cycle in Sharvoskii ordering.

three–period solution before and for large $\overline{\mu}$ we obtained complex transients for all values of σ we used whereas here we observe the reappearance of the complex phase for the higher $\overline{\mu}$s. Nevertheless, we conclude that the model

with local viscosity is able to capture the feature of the problem we consider essential – a rich dynamical phase diagram that includes complex shapes.

3.1. Stroboscopic map

The dynamical system described by (2) is non-autonomous because $\dot{\gamma}$ is an explicit function of time. Integrating (2) over exactly one time period T gives us the position of every bead of the filament at $t = T$. Recall that the shape of the filament is fully specified by its curvature κ as a function of arc length s. Thus we can define the stroboscopic map, $\mathcal{F}$, that allows us to obtain $\kappa(s, T)$ from $\kappa(s, 0)$:

$$\kappa(s, T) = \mathcal{F}\kappa(s, 0). \tag{5}$$

The stroboscopic map is no longer an explicit function of time. Following Refs. Auerbach *et al.* (1987); Cvitanovic *et al.* (2005), we study the shape-chaos by obtaining the fixed points and periodic orbits of the stroboscopic map using the Newton–Krylov method, which is described in detail in appendix D1 of our earlier paper Agrawal and Mitra (2022). In general, for any fixed value of $\overline{\mu}$ and σ we obtain many periodic orbits. We list all of them in table 4. We sort the cycles using Sharkovskiĭ's ordering Sharkovski (1995):

$$\begin{aligned} 3 &\prec 5 \prec 7 \prec 9 \prec 11 \ldots \prec 2 \cdot 3 \prec 2 \cdot 5 \prec \ldots \\ \ldots &\prec 2^2 \cdot 3 \prec 2^2 \cdot 5 \ldots \prec 2^3 \cdot 3 \prec 2^3 \cdot 5 \prec \ldots \\ \ldots &\prec 2^3 \prec 2^2 \prec 2 \prec 1, \end{aligned} \tag{6}$$

In Fig. 2(B) we show the leading period of stroboscopic map, as it appears in Sharkovskii's ordering, as a function of $\overline{\mu}$ and σ – we do find orbits of period three. Although many periodic orbits appear as solutions of the map most of them are not stable and do not appear in the solution of dynamical equation. Let us recall the Sharkovskiĭ's theorem Alligood *et al.* (1996): Consider a continuous map f on an interval with a period p orbit. If $p \prec q$, where q appears in the Sharkovskiĭ's ordering, then f has a period-q orbit. This implies that if f possess a period 3 orbit it has all orbits of all other periods. Although this shows that the map has very complex dynamical behavior it does not necessarily proves the existence of chaos. Nevertheless, existence of period three does imply chaos as was proved by Li and Yorke Li and Yorke (2004). Unfortunatley neither Sharkovskiĭ's theorem nor the result of Li and Young is valid for maps in dimensions higher than unity[7] Hence we conclude that although we demonstrate the rich complexity of the solutions of the stroboscopic map and we have not yet conclusively proven the existence of chaotic solutions.

[7] As a counterexample Kloeden and Li (2006), consider the two dimensional map that rotates every point in the $x - y$ plane by an angle of $2\pi/3$ in the counter-clockwise direction. Clearly this map has a period three solution but it is not chaotic.

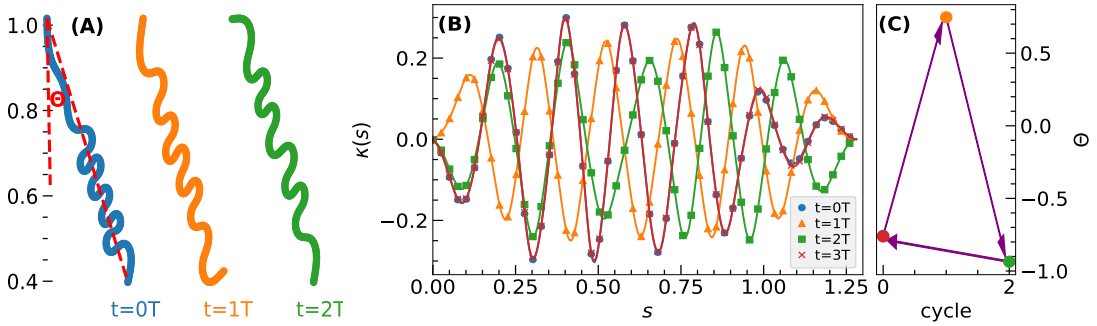

Figure 3: **Example of a three period solution** (for $\sigma = 1, \overline{\mu} = 1.67 \times 10^6$) in real space (A) and curvature space (B) and for ($\sigma = 0.75, \overline{\mu} = 3.35 \times 10^5$) in 1D Θ-space (C). We start from $t = 0$ and evolve the filament for three cycles. In (A,B), blue, orange and green curves shows the filament at $t = 0, 1T$, and $2T$ respectively. In (B), the $\kappa(s)$ plots for $t = 0$ and $3T$ (blue, red) lie on top of each other.

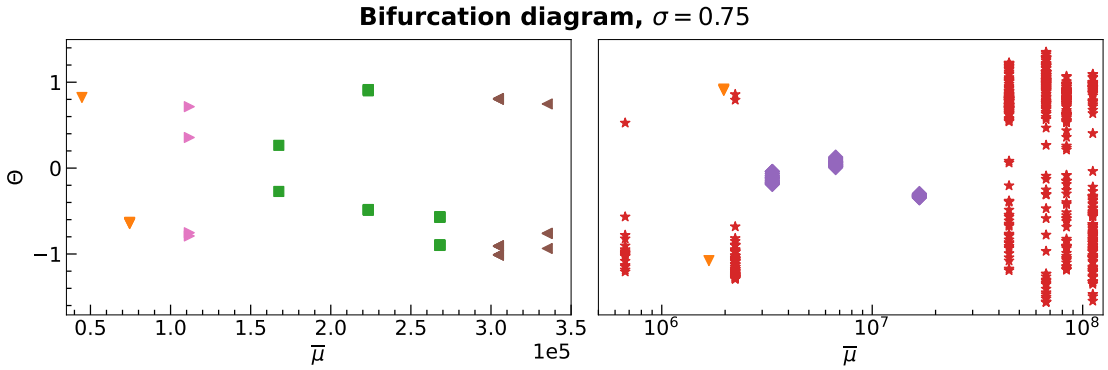

Figure 4: **Bifurcation diagram** of Θ for $\sigma = 0.75$. The system shows chaos at high enough $\overline{\mu}$, except certain isolated ranges of $\overline{\mu}$, where Θ settles into periodic behavior – a behavior similar to island of order for bifurcation diagram of the logistic map Alligood *et al.* (1996).

3.2. Period three and the Θ map

The existence of period three solutions for both the evolution equations and the stroboscopic map is a key result in this problem. It behooves us to study it in greater detail. We choose the period-three solution that appears as a solution of stroboscopic map for $\sigma = 1$ and $\overline{\mu} = 1.6 \times 10^6$. This is shown in Fig. 2(B) as a green triangle. In Fig. 3(A,B) we show the three solutions in real and curvature space respectively.

Now we attempt an arbitrary dimensional reduction to construct a one-dimensional map. We draw the straight line that connects the top end of the

filament to the bottom one and call Θ the angle this line makes with the tangent to the filament at its top point, see Fig. 3(A). Defined this way, Θ does not depend on the position or orientation of the overall filament, but only its shape. In some cases, if shape of the filament shows a period three solution, so does Θ. One such case is shown in Fig. 3(C) for $\sigma = 0.75, \overline{\mu} = 3.35 \times 10^5$ [8]. From the stroboscopic map we can construct a map for Θ. This is a one dimensional map for which the Li and Yorke theorem is valid. Thus by demonstrating that the Θ map has three period we show that this map is chaotic. Further evidence of chaos is obtained by plotting the bifurcation diagram for Θ in Fig. 4. We find period two, period four and period three solutions and also chaotic ones.

3.3. Mixing of passive tracers

Next we demonstrate that if we choose $\overline{\mu}$ and σ inside the complex phase, see Fig. 2(A), then the filament acts as an effective mixer of passive tracers. We use the same notation and technique used in our earlier paper Agrawal and Mitra (2022).

Once the filament has reached a statistically stationary state we introduce N_p tracers placed on concentric circles in the x–y plane, Fig. 5(A). They are colored by radius of the circle on which they lie on at the initial time. For the rest of this section the time when the tracers are introduced is $t = 0$. The equation of motion of the k-th tracer particle whose position at time t is given by $\boldsymbol{X}^\mathrm{k}(t)$, is

$$\frac{d\boldsymbol{X}^\mathrm{k}}{dt} = \boldsymbol{U}(\boldsymbol{r})\delta(\boldsymbol{r} - \boldsymbol{X}^\mathrm{k}). \tag{7}$$

Here $\boldsymbol{U}(\boldsymbol{r})$, the velocity of the flow at $\boldsymbol{r} = (x, y, z)$, is a superposition of the background flow velocity $\boldsymbol{U}_0(\boldsymbol{r})$ and the contributions from all the beads in the filament Rotne and Prager (1969); Brady and Bossis (1988); Guazzelli and Morris (2011); Kim and Karrila (2013):

$$U^\alpha(\boldsymbol{r}) = U_0^\alpha(\boldsymbol{r}) + \mathcal{G}^{\alpha\beta}(\boldsymbol{r} - \boldsymbol{R}_\mathrm{i})F_\mathrm{i}^\beta, \quad \text{, where} \tag{8a}$$

$$F_\mathrm{i}^\alpha = -\frac{\partial \mathcal{H}}{\partial R_\mathrm{i}^\alpha}, \quad \text{and} \tag{8b}$$

$$\mathcal{G}^{\alpha\beta}(\boldsymbol{R}) = \frac{1}{8\pi\eta R}\left[\delta_{\alpha\beta} + \frac{R_\alpha R_\beta}{R^2} + \frac{d^2}{4R^2}\left(\frac{1}{3}\delta_{\alpha\beta} - \frac{R_\alpha R_\beta}{R^2}\right)\right] \tag{8c}$$

At $t = 8T$, we find that most of the tracers have moved out of the plane and have become somewhat mixed, Fig. 5(B). At even later time, $t = 128T$ (not

[8] It is also possible that the shape shows period three solution but the Θ shows a fixed point or a period–two solution. Conversely, it is possible for Θ to have a period–three solution without the shape having a period-three solution.

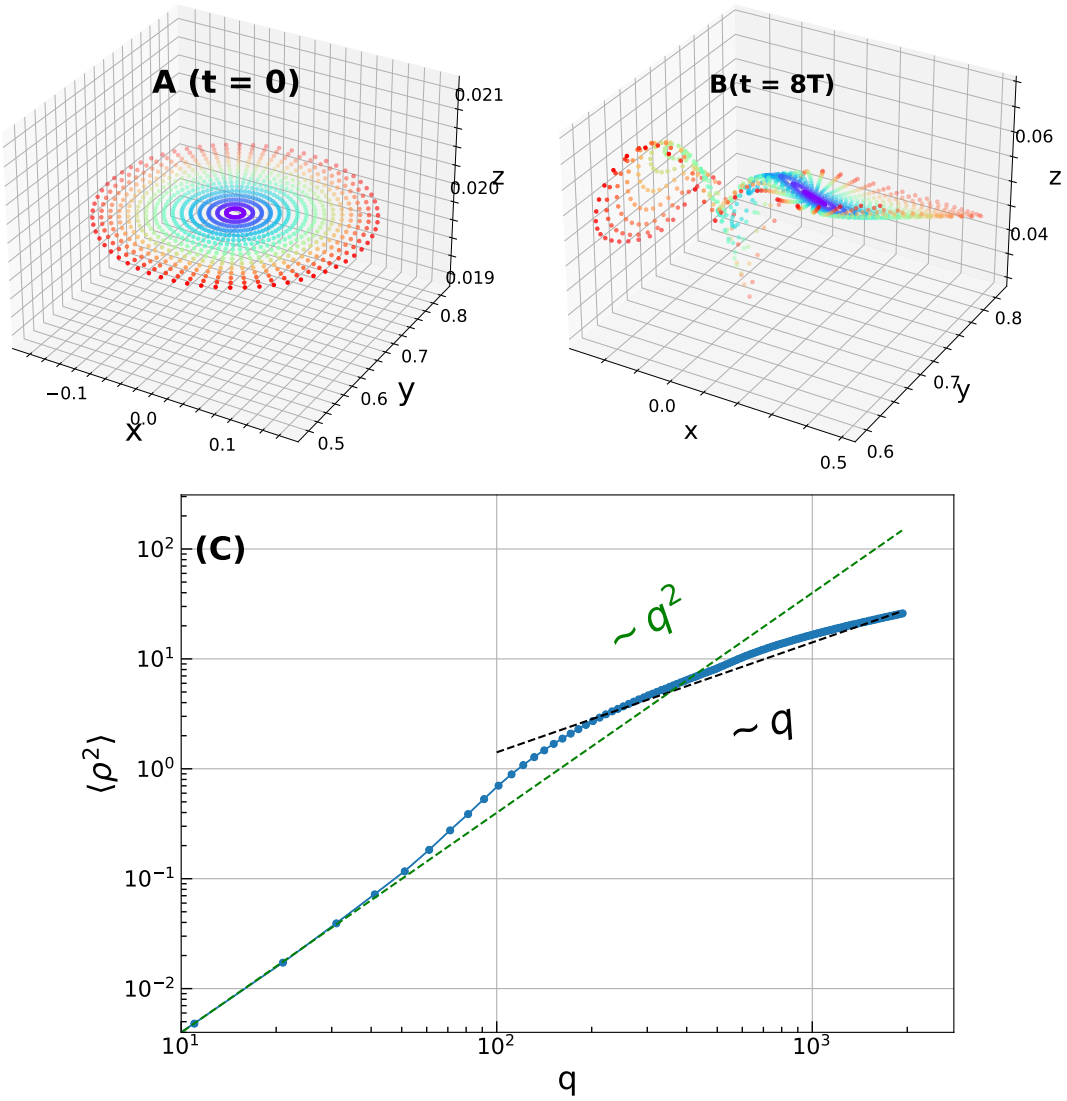

Figure 5: **Mixing of passive tracer**: (A) and (B) Positions of tracer particles at $t = 0$ and $t = 8T$. The parameters $\sigma = 0.75$ and $\overline{\mu} = 6.7 \times 10^7$ are chosen such that we are in the complex phase. Initially, the tracers are placed on concentric circles, color coded by their distances from the center of the circles. The mixing of the colors show the mixing of the tracers. (C) Mean square displacement (MSD), $\langle \rho^2 \rangle (qT)$, defined in (11), as a function of q in log-log scale. We also plot two lines with slopes 1 and 2.

shown), we find the tracer particles are well mixed. To obtain a quantitative measure of mixing we define

$$\Delta \boldsymbol{X}_{\mathrm{j}}^{\mathrm{k}} \equiv \boldsymbol{X}^{\mathrm{k}}((j+1)T) - \boldsymbol{X}^{\mathrm{k}}(jT) \quad , \tag{9}$$

the net displacement of the k-th tracer particle over the j-th cycle – $t = jT$ to $t = (j+1)T$, where j is an integer. The net displacement of the k-th tracer after q cycles is

$$\boldsymbol{\rho}^{\mathrm{k}}(q) = \sum_{j=1}^{q} \Delta \boldsymbol{X}_{\mathrm{j}}^{\mathrm{k}}. \tag{10}$$

The total mean square displacement, averaged over all the tracers, at the end of q cycles is given by

$$\left\langle \rho^2(q) \right\rangle \equiv \frac{1}{N_{\mathrm{p}}} \sum_{\mathrm{k}=1}^{N_{\mathrm{p}}} |\boldsymbol{\rho}^{\mathrm{k}}(q)|^2 \tag{11}$$

In Fig. 5(C) we plot $\left\langle \rho^2(q) \right\rangle$ versus q in log-log scale. If the tracers diffuse then we expect $\left\langle \rho^2(q) \right\rangle \sim q$ for large q Taylor (1922), which is what we obtain. Furthermore, we calculate the cumulative probability density function (CPDF) for each component of the displacement $\Delta \boldsymbol{X}_{\mathrm{j}}^{\mathrm{k}}$. For the out-of-plane component this CPDF has an exponential tail. For the in-plane components we obtain a power-law tail of exponent of -3. This implies that the probability density function (PDF) of each component of the displacement $\Delta \boldsymbol{X}_{\mathrm{j}}^{\mathrm{k}}$ is such that its second moment is well defined. Hence by the central limit theorem the probability density function of $\rho^2(q)$ is a Gaussian and we expect simple diffusive behavior. However, as the PDF (of displacement) has power-law tail we expect that very long averaging over very many number of tracer particles is necessary for convergence. This explains why we observe not-so-clear evidence of diffusion.

4. Conclusion

In this paper we consider a simplified model for a flexible filament in a viscous flow driven in a time–periodic manner. In particular, the simplicity lies is approximating the viscous forces by a local drag. We show that the shape of the filament is spatiotemporally chaotic. This model has only the elastic nonlinearity of the filament, hence it is solely the elastic nonlinearity that is responsible for chaos. This is the central message of this paper. An additional advantage of using the simplified model for viscous forces is that it may be possible to make theoretical progress following Goldstein and Langer Goldstein and Langer (1995).

The dimensionless parameters that we consider are within a range that is experimentally accessible. Although we do not expect exact quantitative agreement with experiment, We hope that, together with our previous work Agrawal and Mitra (2022), we have now presented convincing evidences that a single flexible filament in periodically driven Stokes flow can give chaotic solutions that is able to effectively mix passive scalars even at infinite Peclet number.

N	256
a	0.005
d	0.005
L	1.28
B	6×10^{-6}–4×10^{-2}
S	2
η	10
ω	1–6
Δ	10^{-4}–10^{-6}
$\overline{\mu}$	12560–8.37×10^{7}
σ	0.5–3
K	16

Table 1: Parameters of simulation: Number of beads, N, equilibrium distance between beads, a, bead diameter d, filament length L Bending modulus B, viscosity η, time-step, Δ. The quantities S and ω defined in (1) determined the space-time dependence of the background flow. The dimensionless parameters $\overline{\mu}$, σ and K are defined in (4).

$\overline{\mu}$ \ σ	0.75	1.0	1.25
3.35×10^4	1	1	1
4.47×10^4	1	1	1
6.67×10^4	1,16	1	1
9.57×10^4	1,4,20,22,23,27	2,4,11	1,2,3,12,13,24,25
1.67×10^5	1,2,10,14,33	1,2,3	1,2
2.23×10^5	1,2	1,2,3	1,2
3.35×10^5	1,2,3,4,5,7,9,10,15,19,22,23,31	1,2	1,2,7
4.47×10^5	1	1,2,3,5,6,7,13,19,37,41	1
6.70×10^5	1,2,5,7,12,25,32,41,47,50,68,76,85,100,104	1	1,2
9.57×10^5	1,126	1,4,9	1,2
1.67×10^6	1,50,54,62,65,66,70,80,86,108,132	1,2,3,4,5,7,9,22,44	1
2.23×10^6	1,11,12,28	1,2,45	1
3.34×10^6	1,2,4,32	1,4	1
6.67×10^6	1^*	1,17	1
1.67×10^7	1^*	1^*	1^*
3.35×10^7	1^*	1^*	1^*

Table 2: **Cycles of the stroboscopic map**. In some of these cases the evolution equation shows chaotic solution but so far we have obtained one or two periodic orbits of small periods, these are marked by $*$.

References

C Duprat, "Moisture in textiles," Annual Review of Fluid Mechanics **54**, 443–467 (2022).

Christopher Brennen and Howard Winet, "Fluid mechanics of propulsion by cilia and flagella," Annual Review of Fluid Mechanics **9**, 339–398 (1977).

Michael A Sleigh, *The biology of Cilia and Flagella: international series of monographs on pure and applied biology: zoology, vol. 12*, Vol. 12 (Elsevier, 2016).

Olivia Du Roure, Anke Lindner, Ehssan N Nazockdast, and Michael J Shelley, "Dynamics of flexible fibers in viscous flows and fluids," Annual Review of Fluid Mechanics **51**, 539–572 (2019).

Nicolas Bruot and Pietro Cicuta, "Realizing the physics of motile cilia synchronization with driven colloids," Annual Review of Condensed Matter Physics **7**, 323–348 (2016).

Leif E Becker and Michael J Shelley, "Instability of elastic filaments in shear flow yields first-normal-stress differences," Physical Review Letters **87**, 198301 (2001).

Laura Guglielmini, Amit Kushwaha, Eric SG Shaqfeh, and Howard A Stone, "Buckling transitions of an elastic filament in a viscous stagnation point flow," Physics of Fluids **24**, 123601 (2012).

Yanan Liu, Brato Chakrabarti, David Saintillan, Anke Lindner, and Olivia Du Roure, "Morphological transitions of elastic filaments in shear flow," Proceedings of the National Academy of Sciences **115**, 9438–9443 (2018).

John LaGrone, Ricardo Cortez, Wen Yan, and Lisa Fauci, "Complex dynamics of long, flexible fibers in shear," Journal of Non-Newtonian Fluid Mechanics **269**, 73–81 (2019).

AM Slowicka, Howard A Stone, and Maria L Ekiel-Jezewska, "Flexible fibers in shear flow: attracting periodic solutions," arXiv preprint arXiv:1905.12985 (2019).

Paweł J Żuk, Agnieszka M Słowicka, Maria L Ekiel-Jeżewska, and Howard A Stone, "Universal features of the shape of elastic fibres in shear flow," Journal of Fluid Mechanics **914** (2021).

Steve Kuei, Agnieszka M Słowicka, Maria L Ekiel-Jeżewska, Eligiusz Wajnryb, and Howard A Stone, "Dynamics and topology of a flexible chain: knots in steady shear flow," New Journal of Physics **17**, 053009 (2015).

Shi-Yuan Hu, Jun-Jun Chu, Michael J Shelley, and Jun Zhang, "Lévy walks and path chaos in the dispersal of elongated structures moving across cellular vortical flows," Physical Review Letters **127**, 074503 (2021).

Brato Chakrabarti, Yanan Liu, John LaGrone, Ricardo Cortez, Lisa Fauci, Olivia du Roure, David Saintillan, and Anke Lindner, "Flexible filaments buckle into helicoidal shapes in strong compressional flows," Nature Physics , 1–6 (2020).

Chris H Wiggins, D Riveline, Albrecht Ott, and Raymond E Goldstein, "Trapping and wiggling: elastohydrodynamics of driven microfilaments," Biophysical journal **74**, 1043–1060 (1998).

Charles W Wolgemuth, Thomas R Powers, and Raymond E Goldstein, "Twirling and whirling: Viscous dynamics of rotating elastic filaments," Physical Review Letters **84**, 1623 (2000).

Sookkyung Lim and Charles S Peskin, "Simulations of the whirling instability by the immersed boundary method," SIAM Journal on Scientific Computing **25**, 2066–2083 (2004).

Hirofumi Wada and Roland R Netz, "Non-equilibrium hydrodynamics of a rotating filament," EPL (Europhysics Letters) **75**, 645 (2006).

Francesco Bonacci, Brato Chakrabarti, David Saintillan, Olivia du Roure, and Anke Lindner, "Dynamics of flexible filaments in oscillatory shear flows," arXiv preprint arXiv:2205.08361 (2022).

Vipin Agrawal and Dhrubaditya Mitra, "Chaos and irreversibility of a flexible filament in periodically driven stokes flow," Physical Review E **106**, 025103 (2022).

Deepak Krishnamurthy and Manu Prakash, "Emergent programmable behavior and chaos in dynamically driven active filaments," bioRxiv (2022).

M Doi and SF Edwards, "The theory of polymer dynamics," (1986).

Raymond E Goldstein and Stephen A Langer, "Nonlinear dynamics of stiff polymers," Physical review letters **75**, 1094 (1995).

Raymond E Goldstein, Thomas R Powers, and Chris H Wiggins, "Viscous nonlinear dynamics of twist and writhe," Physical Review Letters **80**, 5232 (1998).

Kathleen T Alligood, Tim D Sauer, and James A Yorke, *Chaos: An introduction to dynamical systems* (Springer, New York, 1996).

RG Larson, Hua Hu, DE Smith, and S Chu, "Brownian dynamics simulations of a dna molecule in an extensional flow field," Journal of Rheology **43**, 267–304 (1999).

Ehssan Nazockdast, Abtin Rahimian, Denis Zorin, and Michael Shelley, "A fast platform for simulating semi-flexible fiber suspensions applied to cell mechanics," Journal of Computational Physics **329**, 173–209 (2017).

Hirofumi Wada and Roland R Netz, "Stretching helical nano-springs at finite temperature," EPL (Europhysics Letters) **77**, 68001 (2007).

Thomas R Powers, "Dynamics of filaments and membranes in a viscous fluid," Reviews of Modern Physics **82**, 1607 (2010).

William H Press and Saul A Teukolsky, "Adaptive stepsize runge-kutta integration," Computers in Physics **6**, 188–191 (1992).

Jeff R Cash and Alan H Karp, "A variable order runge-kutta method for initial value problems with rapidly varying right-hand sides," ACM Transactions on Mathematical Software (TOMS) **16**, 201–222 (1990).

https://github.com/dhrubaditya/ElasticString.

TR Ramamohan, S Savithri, R Sreenivasan, and C Chandra Shekara Bhat, "Chaotic dynamics of a periodically forced slender body in a simple shear flow," Physics Letters A **190**, 273–278 (1994).

CV Kumar, K Satheesh Kumar, and TR Ramamohan, "Chaotic dynamics of periodically forced spheroids in simple shear flow with potential application to particle separation," Rheologica acta **34**, 504–511 (1995).

Fredrik Lundell, "The effect of particle inertia on triaxial ellipsoids in creeping shear: from drift toward chaos to a single periodic solution," Physics of Fluids **23**, 011704 (2011).

Christopher Nilsen and Helge I Andersson, "Chaotic rotation of inertial spheroids in oscillating shear flow," Physics of Fluids **25**, 013303 (2013).

Ditza Auerbach, Predrag Cvitanović, Jean-Pierre Eckmann, Gemunu Gunaratne, and Itamar Procaccia, "Exploring chaotic motion through periodic orbits," Physical Review Letters **58**, 2387 (1987).

Predrag Cvitanovic, Roberto Artuso, Ronnie Mainieri, Gregor Tanner, Gábor Vattay, Niall Whelan, and Andreas Wirzba, "Chaos: classical and quantum," ChaosBook. org (Niels Bohr Institute, Copenhagen 2005) **69**, 25 (2005).

AN Sharkovski, "Coexistence of cycles of a continuous map of the line into itself," International journal of bifurcation and chaos **5**, 1263–1273 (1995).

Tien-Yien Li and James A Yorke, "Period three implies chaos," in *The theory of chaotic attractors* (Springer, 2004) pp. 77–84.

As a counterexample Kloeden and Li (2006), consider the two dimensional map that rotates every point in the $x-y$ plane by an angle of $2\pi/3$ in the counter-clockwise direction. Clearly this map has a period three solution but it is not chaotic.

It is also possible that the shape shows period three solution but the Θ shows a fixed point or a period–two solution. Conversely, it is possible for Θ to have a period–three solution without the shape having a period-three solution.

Jens Rotne and Stephen Prager, "Variational treatment of hydrodynamic interaction in polymers," The Journal of Chemical Physics **50**, 4831–4837 (1969).

John F Brady and Georges Bossis, "Stokesian dynamics," Annual review of fluid mechanics **20**, 111–157 (1988).

Elisabeth Guazzelli and Jeffrey F Morris, *A physical introduction to suspension dynamics*, Vol. 45 (Cambridge University Press, 2011).

Sangtae Kim and Seppo J Karrila, *Microhydrodynamics: principles and selected applications* (Courier Corporation, 2013).

Geoffrey I Taylor, "Diffusion by continuous movements," Proceedings of the london mathematical society **2**, 196–212 (1922).

Peter Kloeden and Zhong Li, "Li–yorke chaos in higher dimensions: A review," Journal of Difference Equations and Applications **12**, 247–269 (2006)